

Efficient methods for the operation of active distribution networks in unsymmetric and uncertain states

Présentée le 16 décembre 2022

Faculté des sciences et techniques de l'ingénieur
Laboratoire des systèmes électriques distribués
Programme doctoral en génie électrique

pour l'obtention du grade de Docteur ès Sciences

par

Sherif Alaa Salaheldin FAHMY

Acceptée sur proposition du jury

Prof. D. Dujic, président du jury
Prof. M. Paolone, directeur de thèse
Dr K. Knezovic, rapporteuse
Prof. F. Sossan, rapporteur
Dr R. Cherkaoui, rapporteur

Never forget that only dead fish
swim with the stream.
— Malcolm Muggeridge

To my family (blood and chosen).

Acknowledgements

My EPFL journey started back in 2011. Throughout my bachelor's, master's and Ph.D. years I have met many individuals whose help/support was detrimental for me to be where I am today. In this acknowledgement, it is impossible to list them all. However, even though some might not see their names explicitly written in this section, I would like to ensure you that your help and support are not and will never be forgotten.

First, I would like to thank my mentor and friend Professor Mario Paolone. You have been in my life for most of my adult life. We practically started our journey in Switzerland together back in 2010/11 and ever since we met that first time during my third year at EPFL, I knew that we would have many interactions in the coming years. Little did I know back then that you would be my Ph.D. supervisor and thesis director and that you'd do everything in your power to help me through my journey by constantly transferring your knowledge *free of charge* as you always do. For that, I thank you as I would have never done it without you.

Moving onto the lab. Working at the Distributed-Electrical-Systems-Laboratory (DESL) is an incredible experience. I have had the chance to arrive at the lab during a transitional period when some people were graduating and others were starting. As a result, I have met many many people who all contributed one way or another for me to be here today. I would like to extend a big thank you for all members but a special thanks to: (i) Dr. Lorenzo Reyes Chamorro who helped me integrate the lab and get accustomed to the lab infrastructure, (ii) Dr. Andreas Martin Kettner (the founder of the *Trinity*) who constantly supported me by sharing his strong theoretical knowledge, his acute reviewer comments and many, many funny memes, (iii) Drs. Asja Derviskadic, Guglielmo Frigo, Enrica Scolari, Antonio Zecchino, Antonio Sunjerga, Yihui Zuo, Mohsen Kalantar Neyestanaki, Zhaoyang Wang, Emil Namor, Amirhossein Mostajabi and Hossein Mahmoudimanesh whose warm welcome quickly made me feel at home in the lab, (iv) Soon-to-be Dr. Rahul Kumar Gupta one of the members of the *Trinity*, a huge thanks to you my friend as it was only through our many conversations, late nights and collaborations that I was able to finish this thesis, (v) the new generation: Alexandra Karpilow, Johanna Becker, Ji-Hyun Yi, Denis Tudor, Francesco Gerini, Vladimir Sovljanski, Willem Lambrichts, Simone Rametti, Ehsan Mansouri, Hamidreza Karami and Plouton Grammatikos, for all the pleasant memories and fun times (vi) the lab secretariat: Mrs. Sophie Flynn, Mrs. Lora Kasabaqi and Mrs. Eulalia Durussel, that constantly makes our lives easier, and (vii) last but not least the

Acknowledgements

brain and brawn behind most of the lab's infrastructure Mr. Sylvain Robert and Mr. Stephane Burri for their constant infinite support. I would also like to thank the many former students with whom I collaborated, especially: Engs. Quentin Walger, Max Chevron and Enea Figini for their rigor, creativity and immense help in finalizing different parts of my thesis. I cannot end this paragraph concerning the DESL lab without personally thanking Dr. Rachid Cherkaoui for being a constant source of light and wisdom for all lab members.

Regarding other labs around campus, I cannot go through these acknowledgements without thanking the LCA2 members. Specifically: (i) Prof. Jean-Yves LeBoudec for his theoretical support, (ii) Dr. Roman Rudnik for all our fruitful collaborations and discussions, and (iii) Dr. Wajeb Saab together with Roman for their friendship and support. I would also like to thank all unmentioned researchers, faculty and doctoral school staff (at EPFL or in other universities and companies I have visited) that helped me throughout my journey.

Moving on to life beyond the EPFL campus, I would like to express my gratitude to the Allani-Salietti family for their immense constant support and love. A special thanks to Mohamed/Emmanuelle and their two little princesses Alma and Fiona that are always capable of letting you forget all your worries. I would like to also thank the Errougani family for their tremendous support. A special thanks to Ilham who has supported me unconditionally, especially in the closing stages of this incredible journey. I haven't mentioned everyone but I also haven't forgotten the fantastic support that I have received throughout my Ph.D. years from my friends in Switzerland (Lausanne/Geneva), my friends in Munich, my friends in Cairo (the Mahmouds, Mohameds and everyone in between), my football friends, and my friends from The Consulting Society. Thank you all, dearly.

Last but *certainly* not least, I would like to extend my deepest thanks to all the members of my family. A special thanks to my parents: Dr. Alia Shoeib and Eng. Alaa Fahmy, my sister: Farida Fahmy, my grandparents, my cousins and my aunt for their unconditional love, support and wisdom. I would not be here without you.

Thank you Mom & Dad.

Cairo, November 9, 2022

S. F.

Abstract

The increasing penetration of stochastic renewable distributed generation, energy storage systems and novel loads (e.g. electric-vehicles (EVs)) in active-distribution-networks (ADNs) or microgrids has triggered the need to develop real-time (e.g. minutes to sub-second) control frameworks to avoid grid-operational problems. These can be split into two main categories of active constraints: *static* and *power-quality*. *Static* constraints refer to branches' capacity limitations, nodal voltage magnitudes' security-bounds as well as resources' limitations (e.g. MV-LV substation transformer apparent power limitations, power converters' capability curves and general constraints of the internal states of energy storage systems). *Power-quality* constraints refer to the quality-of-service for the end-users that must be guaranteed by the power distribution utility.

Within this context, this thesis focuses on the development of *real-time* ADN controls, in the form of frameworks or control-enabling methodologies, that take into account the above-mentioned power-grid operational constraints while considering grid *uncertainties* and *unbalances*. In its first part, the thesis focuses on a general, i.e. resource-agnostic, methodology to linearize the power-flow equations and showcases its real-time control-enabling advantages through two sub-second-scale control-application-examples. Then, in the second part, a deeper focus is given to the operational challenges raised by the large presence of electric-vehicles charging-stations (EVCSs) in ADNs.

More specifically, here below the contributions of both parts of the thesis are listed.

1. *Part 1 - Efficient methods for the control of multiple unsymmetric and uncertain ADN resources*

- First, an analytical method for computing general-three-phase sensitivity coefficients (SCs), considering voltage-dependent nodal power injections, is presented. SCs are the partial derivatives of any electrical quantity w.r.t. control variables (e.g. nodal active power injections and nodal voltage magnitudes at PV-nodes). The proposed method assumes the knowledge of the grid-model, i.e. grid topology and branch parameters, and relies on the resolution of unique and full-rank linear systems of equations to compute nodal voltage SCs. Finally, knowing the nodal voltage SCs and the grid model, one can compute all other auxiliary SCs that can, for instance, be leveraged to linearize the power-flow equations, rendering the resolution of security-constrained optimal-power-flow (OPF) problems highly efficient.

- Second, an application example of SCs is presented. More specifically, the problem of securely reconnecting unbalanced islanded ADNs to their upstream grids at the point of common coupling (PCC) is tackled. The process is usually called *resynchronization* and is split into two sub-processes: (i) steering the downstream PCC nodal voltages towards their upstream counterparts and, (ii) asserting nodal voltage phasors' alignment on both sides of the PCC to close the PCC-breaker. An algorithm is proposed for each process. The first leverages SCs to approximately solve a three-phase OPF. The second makes use of the enhanced-Interpolated-Discrete-Fourier-Transform (e-IpDFT) to extract and compare the per-phase nodal voltage phasors at both sides of the PCC. Both processes are experimentally validated on a real-scale laboratory microgrid.
- Third, a second application example of SCs is presented. More specifically, a novel technique to render an intractable OPF problem solvable, is presented. The proposed algorithms account for the uncertainties due to set-point implementation by the resources' controllers. The result of the proposed methods is the computation of optimal control setpoints that are admissible i.e. satisfies grid and resource operational constraints for all uncertainties realizations. The algorithms are numerically tested on MATLAB using a modified IEEE-34 node test distribution feeder.

1. Part 2 - Efficient methods for the safe operation of electric-vehicle-charging-stations

- First, a specific analysis is presented to quantify: (i) how uncontrolled EV charging can affect ADN static operational constraints, (ii) how some EVCS can increase grid-load-unbalances, and (iii) EV on-board controller reaction times. The analysis leverages (i) a Monte-Carlo load-flow framework, and (ii) a small-scale experiment using a non-commercial Type-2 EVCS connected to a real-scale laboratory microgrid.
- Second, a distributed real-time, i.e. seconds to minute scale, control framework for EVCSs is presented. The framework consists in solving a three-phase OPF that is: (i) *augmented*, i.e. accounts for EV user needs, (ii) *approximated*, i.e. leverages SCs to linearize the power-flow equations, and (iii) *distributed*, i.e. uses the alternating direction method of multipliers (ADMM) algorithm. The presented framework is numerically validated on MATLAB using a modified IEEE-34 node test distribution feeder.
- Third, a day-ahead ADN dispatch-plan (DP) generator is presented. The presented algorithm accounts for next-day load and generation stochasticity through scenario-based optimization. It further considers that, unlike what can be found in the literature, both energy-storage systems *and* EVCSs are controllable entities. The generated DP is experimentally validated on a real-scale laboratory microgrid.

Key words: active distribution networks, microgrids, load flow, optimal power flow, sensitivity

coefficients, voltage-dependent nodal power injections, unbalanced power grids, island resynchronization, synchronism check, unbalanced three-phase control, uncertainties, feasible network operation, uncertain three-phase control, electric vehicles charging stations, real-time (distributed) control, grid operational constraints, power quality, day-ahead dispatching.

Résumé

La prolifération croissante des producteurs d'énergie renouvelable non-centralisés, des systèmes de stockage d'énergie et des nouveaux consommateurs (e.g. les véhicules électriques (EVs)) dans les réseaux de distribution actifs (ADN) ou les micro-réseaux a déclenché le besoin de développer des algorithmes de contrôle en temps réel pour éviter des problèmes de fonctionnement du réseau. Ces derniers peuvent être catégorisés en des contraintes *statiques* et des contraintes liées à la *qualité de l'alimentation*. Les contraintes *statiques* font référence aux limites de capacité des lignes électriques, aux limites de sécurité des modules des tensions aux nœuds ainsi qu'aux limites des ressources (e.g. les limites de puissance apparente des transformateurs des sous-stations MT-BT, les courbes de capacité des convertisseurs de puissance et les contraintes générales des états internes des systèmes de stockage d'énergie). Les contraintes liées à la *qualité de l'alimentation* font plutôt référence à la qualité de la tension fournie aux utilisateurs finaux qui doit être garantie par les gérants des réseaux de distribution.

Dans ce contexte, cette thèse se focalise sur le développement d'algorithmes de contrôle d'ADN en temps réel qui prennent en compte les contraintes opérationnelles mentionnées ci-dessus tout en considérant les incertitudes et les déséquilibres du réseau. Dans sa première partie, la thèse présente une méthodologie générale pour linéariser les équations de flux de puissances et illustre ses avantages en termes de contrôle en temps réel à travers deux exemples d'application avec des périodes de contrôle de l'ordre de moins d'une seconde. Ensuite, dans sa deuxième partie, une attention plus approfondie est accordée aux défis opérationnels soulevés par la présence importante de bornes de recharge pour véhicules électriques dans les ADNs.

Plus précisément, les contributions de chaque partie de la thèse sont énumérées ci-dessous.

1. *Partie 1 - Méthodes efficaces pour le contrôle de multiples ressources asymétriques et incertaines connectées à un ADN*

- Tout d'abord, en considérant que les injections de puissance aux nœuds dépendent des modules des tensions aux nœuds, une méthode analytique pour calculer les coefficients de sensibilité (SCs) triphasés est présentée. Les SCs sont les dérivées partielles de toute quantité électrique par rapport aux variables de contrôle (e.g. les

injections de puissance active et les modules de tension aux nœuds producteurs (PV)). La méthode proposée suppose la connaissance du modèle de réseau (i.e. la topologie du réseau et les paramètres des branches) et repose sur la résolution de systèmes d'équations linéaires uniques de rangs complets pour calculer les SCs des tensions aux nœuds. En effet, en connaissant les SCs de tension aux nœuds et le modèle du réseau, on peut calculer tous les autres SCs auxiliaires souhaités (e.g. les SCs des modules des courants de lignes). Ces derniers peuvent, par exemple, être utilisés pour linéariser les équations de flux de puissance dans le cadre d'un problème de flux de puissance optimal (OPF) rendant sa résolution beaucoup plus efficace.

- Deuxièmement, un exemple d'application des SCs est présenté. Plus précisément, le sujet abordé est celui de reconnecter des ADN isolés et déséquilibrés à leurs réseaux en amont au point de couplage commun (PCC). Ce dernier est généralement appelé *resynchronisation* et se définit par deux processus : (i) diriger les tensions aux nœuds en aval du PCC d'un ADN isolé vers leurs homologues amont, et (ii) affirmer l'alignement des phases de tension aux nœuds des deux côtés du PCC pour fermer le disjoncteur du PCC. Un algorithme est proposé pour chaque processus. Le premier utilise les SCs pour résoudre approximativement un OPF triphasé. Le second fait appel à la transformée de Fourier améliorée (e-IPDFT) pour extraire et comparer, par phase, les phaseurs de tension aux nœuds des deux côtés du PCC. Les deux processus sont validés expérimentalement sur un micro-réseau de laboratoire à échelle réelle.
- Troisièmement, un deuxième exemple d'application des SCs est présenté. Plus précisément, une nouvelle technique pour rendre résoluble un OPF intraitable est présentée. Les algorithmes proposés tiennent compte des incertitudes dues à l'implémentation des consignes par les contrôleurs des ressources. Le résultat des méthodes proposées est le calcul de points de consigne de contrôle optimaux qui sont admissibles, c'est-à-dire qui satisfont les contraintes opérationnelles du réseau et des ressources pour toutes les réalisations d'incertitudes possibles. Les algorithmes sont testés numériquement sur MATLAB en utilisant une version modifiée du réseau de distribution de test IEEE-34.

2. Partie 2 - Méthodes efficaces pour l'exploitation sûre des bornes de recharge pour véhicules électriques

- Premièrement, une analyse spécifique est présentée pour quantifier : (i) comment la recharge incontrôlée des EVs peut influencer les contraintes opérationnelles statiques d'un ADN, (ii) comment certaines EVCSs peuvent augmenter les déséquilibres de la charge du réseau, et (iii) les différents temps de réaction des contrôleurs embarqués des EVs. L'analyse s'appuie sur : (i) une analyse de flux de charge basée sur la méthode statistique de simulations Monte-Carlo, et (ii) une expérience à petite échelle utilisant une EVCS non-commerciale de Type-2 connectée à un micro-réseau de laboratoire à échelle réelle.

- Deuxièmement, un algorithme de contrôle en temps réel, i.e. à l'échelle de quelques secondes à quelques minutes, de EVCSs est présenté. L'algorithme consiste à résoudre une OPF triphasée qui est : (i) *augmentée*, c'est-à-dire qu'elle tient compte des besoins des utilisateurs des EVs, (ii) *approximée*, c'est-à-dire qu'elle utilise les SCs pour linéariser les équations de flux de puissance, et (iii) *distribuée*, c'est-à-dire que sa méthode de résolution se base sur la technique ADMM (méthode des multiplicateurs à direction alternée). L'algorithme présenté est validé numériquement sur MATLAB en utilisant une version modifiée du réseau de distribution de test IEEE-34.
- Troisièmement, un outil qui génère des plans de répartition (DP) d'ADN du jour suivant est présenté. L'algorithme présenté tient compte des charges et productions stochastiques du lendemain en utilisant une formulation d'un problème d'optimisation basée sur des scénarios. Il considère en outre que, contrairement à ce que l'on trouve dans la littérature, les systèmes de stockage d'énergie *et* les EVCS sont des entités contrôlables. Le DP généré est validé expérimentalement sur un micro-réseau de laboratoire à échelle réelle.

Mots clefs : réseaux de distribution actifs, micro-réseaux, flux de charge, flux de puissance optimal, coefficients de sensibilité, injections de puissance de nœud qui dépendent des modules des tensions des nœuds, réseaux électriques déséquilibrés, resynchronisation d'îlots, vérification du synchronisme, commande triphasée déséquilibrée, incertitudes, commande triphasée incertaine, stations/bornes de recharge de véhicules électriques, commande (distribuée) en temps réel, contraintes opérationnelles du réseau, qualité de l'alimentation, répartition des réseaux de distribution actifs pour le jour suivant.

Contents

Acknowledgements	i
Abstract (English/Français)	iii
List of figures	xv
List of tables	xix
Nomenclature	xxiv
Thesis Introduction	1
I Efficient methods for the control of multiple unsymmetric and uncertain active distribution network resources	5
1 Context	7
1.1 Introduction & Motivations	7
1.2 Contributions of the next chapters of Part I	8
2 Analytical Computation of Power Grids' Sensitivity Coefficients with Voltage-Dependent Injections	11
2.1 Introduction & Literature Review	11
2.2 Problem Formulation	12
2.2.1 Grid Model	12
2.2.2 Voltage-Dependent Power Injections Model	13
2.2.3 Voltage SCs for all node types	14
2.2.4 Auxiliary SCs	14
2.2.5 Complex, magnitude and phase-angle SCs	14
2.3 Method	15
2.4 Computational Complexity & Scalability	20
2.5 Validation	21
2.6 Conclusion	21
	xi

3	Resynchronization of Islanded Unbalanced ADNs: Control, Synchrocheck and Experimental Validation	25
3.1	Introduction & Literature Review	25
3.2	Schematic Overview	27
3.3	PCC-Control	28
3.3.1	Control framework: Assumptions and Overview	28
3.3.2	Problem formulation	31
3.3.3	Optimization problem resolution	36
3.3.4	PCC-Control synthesis and scalability	37
3.4	Synchrocheck	38
3.4.1	IpDFT-based phasor extraction	39
3.4.2	Full Synchrocheck algorithm	40
3.5	Experimental Validation	40
3.5.1	Setup	40
3.5.2	Experimental Notes	41
3.5.3	Results	43
3.6	Conclusion	45
4	Efficient Computation of Admissible Power-Grid-Control-Setpoints for Heterogeneous, Unbalanced, Stochastic & Uncertain Energy Resources	47
4.1	Preamble on Uncertainty Models & Methods	47
4.1.1	Uncertainty Models	48
4.1.2	How to deal with different uncertainties	48
4.2	Introduction	51
4.3	Problem Formulation	51
4.4	Method	54
4.4.1	Admissibility Test	54
4.4.2	Computation of the closest admissible setpoint	58
4.5	Resource Models	64
4.5.1	Slack Nodes	64
4.5.2	Resource Nodes	64
4.5.3	Energy Storage	66
4.5.4	Electric Loads	66
4.5.5	Power Generators	67
4.6	Numerical Simulations	67
4.6.1	4-Node Network	68
4.6.2	IEEE 34 Test Distribution Feeder	70
4.7	Conclusion	73

II	Efficient methods for the safe operation of electric-vehicle-charging-stations	77
5	Context & Motivations	79
5.1	Introduction	79
5.2	Two Motivating Simulations & Experiments	80
5.2.1	Macro-effects of electric-vehicle charging on low-voltage power grids . .	80
5.2.2	A deeper look into EVs: Controllability and Local effects on the grid . . .	105
5.3	Contributions of the next chapters of Part II	112
6	Grid-aware Distributed Control of Electric Vehicle Charging Stations in Active Distribution Grids	113
6.1	Introduction & Literature Review	113
6.2	Problem Formulation	115
6.2.1	Grid sub-problem	115
6.2.2	EV sub-problem	118
6.2.3	Centralised Full Optimization Problem	121
6.3	Distributed Optimization	122
6.4	Comparative Simulation	125
6.4.1	Grid model and data used in the simulation	125
6.4.2	EV users model and data used in the simulation	126
6.4.3	Results of the simulation	128
6.5	Conclusion	130
7	EV-aware Day-Ahead Power-Grid-Dispatch: Theory and Experimental Validation	135
7.1	Introduction	135
7.2	Problem Statement & Overview	136
7.3	Day-ahead stage	137
7.3.1	Scenario Generation	138
7.3.2	Optimization Problem	145
7.3.3	Recap & Problem Resolution	148
7.3.4	Numerical Simulations	150
7.4	Real-time stage	163
7.5	Experimental Validation	165
7.5.1	Experimental Setup: EPFL-DESL microgrid	165
7.5.2	Experimental Notes	165
7.5.3	Results	170
7.6	Conclusion	173
	Thesis Conclusions	175
	Appendix	179
	A - Affine-Transformable-Functions	179
	A.1 – $\min\{a, b\}$	179
	A.2 – $\max\{a, b\}$	179

Contents

Bibliography	189
Curriculum Vitae	191

List of Figures

2.1	Schematic representation of a generic 3-phase network branch	13
2.2	RMS and max differences between Alg. 1 and second benchmark	23
3.1	Resynchronization schematic overview	27
3.2	Schematic illustration of the proposed PCC-control framework for the resynchronization of islanded ADNs using explicit set-points	30
3.3	EPFL-DESL microgrid schematic diagram. Greyed-out resources were not used in the experiment of Sec. 3.5.3	42
3.4	PCC voltage magnitudes, phase-angles and frequency	44
3.5	Voltage and branch current magnitudes - phase a	44
3.6	Three-phase resources' nodal power injections	45
4.1	Schematic diagram of the problem formulation together with the contributions. \mathbf{u}_{in} and \mathbf{u}_{out} are vectors of setpoints (c.f. (4.1))	52
4.2	Illustration of all possible cases for $t_m^{\phi, \hat{\Gamma}}(\mathbf{u})$ for a resource $m \in \mathcal{R}$ and a given phase $\phi \in \{a, b, c\}$ when the control setpoint is \mathbf{u} . The green dashed line represent the active (top) or reactive (bottom) power levels at which the resulting Γ will be the highest.	56
4.3	Qualitative illustration of convergence of Alg. 5 for a generic resource m and phase ϕ (superscript omitted to alleviate notation).	61
4.4	Schematic illustration of different capacity and uncertainty sets for a resource connected to node $i \in \mathcal{R}$ on phase $\phi \in \{a, b, c\}$. \mathcal{A}_i^ϕ are the regions delimited by grey lines. \mathcal{B}_i^ϕ are either the red lines, areas or dots. $\tilde{\mathcal{B}}_i^\phi$ are either the pink lines, areas or dots. Different setpoints u_i^ϕ are shown as blue dots.	65
4.5	4-Node network topology	68
4.6	4-node network: <i>Branch Current Constraint Violation</i> simulation	71
4.7	4-node network: <i>Branch Current, Nodal Voltage and Slack Constraints Violations</i> simulation	72
4.8	IEEE-34 network: <i>Nodal Voltage and Branch Current Constraint Violations</i> simulation	74
5.1	Schematic representation of the creation of the input CDFs	81
5.2	Pseudo-code for the LFMCSs algorithm	83

List of Figures

5.3	Rolle Gare grid - network topology	85
5.4	Inputted non-EV active and reactive nodal injection profiles	86
5.5	Inputted EV active (charging) nodal injection profiles	86
5.6	Nodal voltage magnitudes - min, mean and max over all NUM_SIM simulations - without EV chargers	87
5.7	Nodal voltage magnitudes - min, mean and max over all NUM_SIM simulations - only home EV chargers	88
5.8	Nodal voltage magnitudes - min, mean and max over all NUM_SIM simulations - home-and-POIs EV chargers	88
5.9	Branches currents magnitudes - min, mean and max over all NUM_SIM simula- tions - without EV chargers	89
5.10	Branches currents magnitudes - min, mean and max over all NUM_SIM simula- tions - only home EV chargers	89
5.11	Branches currents magnitudes - min, mean and max over all NUM_SIM simula- tions - home-and-POIs EV chargers	90
5.12	Slack apparent power magnitudes - boxplot over all NUM_SIM simulations - without EV chargers	90
5.13	Slack apparent power magnitudes - boxplot over all NUM_SIM simulations - only home EV chargers	91
5.14	Slack apparent power magnitudes - boxplot over all NUM_SIM simulations - home-and-POIs EV chargers	91
5.15	Probability to violate nodal voltage magnitudes - Only home EV chargers	93
5.16	Probability to violate nodal voltage magnitudes - home-and-POIs EV chargers .	94
5.17	Probability to violate nodal voltage magnitude of the grid bus with highest violations - only home EV chargers	95
5.18	Probability to violate nodal voltage magnitude of the grid bus with highest violations - home-and-POIs EV chargers	96
5.19	Probability to violate nodal voltage magnitude of the grid bus with most viola- tions - only home EV chargers	97
5.20	Probability to violate nodal voltage magnitude of the grid bus with most viola- tions - home-and-POIs EV chargers	98
5.21	Probability to violate branch current magnitudes	99
5.22	Probability to violate branch current magnitude of the grid branch with highest & most violations	99
5.23	Probability to violate slack apparent power magnitude - only home EV charging - 100% EV penetration	100
5.24	Probability to violate slack apparent power magnitude - home-and-POIs EV charging	101
5.25	Rolle Hopital grid - network topology	102
5.26	The EPFL-DESL microgrid EVCS	105
5.27	Results of the load unbalances experiment performed using the Jaguar I-Pace .	108

5.28 Results of the EV controllability experiment: nodal current and power injections profiles	110
6.1 Network graph with resource placement. \mathcal{R} is a resource node. \mathcal{Z} is a zero-injection node. \mathcal{C} is a resource node containing EVCSs.	127
6.2 Aggregated PV (positive) and load (negative) active power profiles for the simulated summer weekday.	127
6.3 Post-MCLFSs results: probabilities to violate static grid operational constraints during the simulated 24 hours	131
6.4 Post-MCLFSs results: probabilities to violate power quality grid operational constraints during the simulated 24 hours	132
6.5 Difference between desired SoC at departure and actual one, for all nodes with EVCSs and for each simulated control algorithm	133
7.1 Schematic overview of the proposed two-stage ADN dispatch	136
7.2 Flowchart of data-agnostic modelling toolbox	139
7.3 Flowchart of the multi-variate GMM approach block	141
7.4 Flowchart of the univariate GMM approach block	142
7.5 Flowchart of the mixed GMM approach block	143
7.6 Flowchart of the mixed GMM approach block	144
7.7 Low-Voltage ADN of the ELL building at the EPFL Lausanne campus.	151
7.8 EVCS1	152
7.9 B1	153
7.10 PCC nodal power injections	158
7.11 UEE time evolution	159
7.12 Power-to-current setpoint lookup tables	168
7.13 Experimental validation: day-ahead UEE time evolution over 24 hours	169
7.14 Experimental validation results - non-slack active power injections: forecast (day-ahead) vs. realization (real-time)	171
7.15 Experimental validation results - slack active power injections: DP (day-ahead) vs. realization (real-time)	172
7.16 Experimental validation results - UEE over experiment horizon: day-ahead vs. real-time	172

List of Tables

2.1	Number of Arithmetic Operations i.e. sums/subtractions (+/−) and multiplications/divisions (\times/\div) to construct \mathbf{A} and $\mathbf{w}(X)$	22
2.2	RMS and max differences between Alg. 1 and first (Jacobian inversion) benchmark	23
3.1	Reconnection steps proposed by the IEEE std. for ADN controllers	28
4.1	Summary of processes and outputs of the <i>Check</i> functions of Alg. 4	59
4.2	4-Node network parameters	69
4.3	Resource parameters (in p.u.) for the IEEE34 <i>Voltage and Current Violation</i> simulation	73
4.4	Initial setpoint (in p.u.) for the IEEE34 Network <i>Voltage and Current Violation</i> simulation, for all nodes $i \in \mathcal{N} \setminus \mathcal{S}$. Zero-injection and generation nodes are highlighted in red and blue, respectively.	75
5.1	Rolle Gare grid - resource nodes with description and peak injections	84
5.2	Rolle Hopital grid - resource nodes with description and peak injections	103
5.3	EPFL-DESL microgrid EVCS technical characteristics	106
5.4	Response times of the on-board controllers of the Jaguar I-Pace and Tesla Models S for setpoint variation starting from 6A – the minimum per-phase setpoint an EV can receive as per the IEC-61851 communication protocol – to a desired setpoint	111
6.1	IEEE-34 branch parameters - Original vs. Used in simulation	126
6.2	Maximum three phase nodal injections and power factor range per non-EV resource.	128
6.3	EV simulated environment	129
7.1	Metrics to compare different approaches and choose the <i>best-fit</i>	143
7.2	Considered non-EV injection scenarios	145
7.3	Considered <i>extra-features</i> to describe an EV user scenario	146
7.4	Cost functions of all considered controllable resources	147
7.5	Constraints of all considered controllable resources	148
7.6	Day-ahead numerical simulation: branch parameters.	154
7.7	Day-ahead numerical simulation: node parameters.	155

List of Tables

7.8 Day-ahead numerical simulation: transformer parameters.	155
7.9 Day-ahead numerical simulation: controllable resource parameters.	155
7.10 Day-ahead numerical simulation: simulation parameters.	156
7.11 Day-ahead numerical simulation: inputted historical data.	156
7.12 Metrics used to quantify the performance of the result of Alg. 7.	159
7.13 Simulation 1 - results	159
7.14 Simulation 2 - results	161
7.15 Simulation 2 - results - continued	162
7.16 Real-time stage objectives and constraints of an EVCS aggregator connected to node $i \in \mathcal{C}$	164
7.17 Experiment: resource parameters	166
7.18 Day-long EV-scenario used for the experiment	167
7.19 Experimental Validation Results: KPI metrics	173

Nomenclature

Exhaustive List of Abbreviations

AC	Alternating Current
ADMM	Alternating Direction Method of Multipliers
ADN	Active-Distribution-Network
ADN-CC	Active Distribution Network Central Controller
AI	Analog Input
AO	Analog Output
ATF	Affine-Transformable-Functions
BESS	Battery Energy Storage System
BLSA	Backtracking Line Search Algorithm
BMS	Battery Management System
CCB	Controllable Circuit Breaker
CCS	Combined Charging System
CMS	Centralised Monitoring System
CP	Charging Profile
CPC	Controllable Power Converters
CS	Charging Station
DC	Direct Current
DER	Distributed Energy Resource
DESL	Distributed Electrical Systems Laboratory
DG	Distributed Generator

Nomenclature

DP	Dispatch Plan
DSO	Distribution System Operator
e-IpDFT	Enhanced-Interpolated Discrete Fourier Transform
EPFL	École Polytechnique Fédérale de Lausanne
ESS	Energy Storage System
EV	Electric Vehicle
EVCS	Electric Vehicle Charging Station
FCL	Frequency Control Law
GHG	Greenhouse Gas
GMM	Gaussian Mixture Model
IpDFT	Interpolated Discrete Fourier Transform
KPI	Key Performance Indicator
LF	Load Flow
LFMCS	Load Flow Monte-Carlo Simulations
LHS	Left-Hand-Side
MAE	Maximum Absolute Error
MPC	Model Predictive Control
MPPT	Maximum Power Point Tracker
MV-LV	Medium Voltage - Low Voltage
NI	National Instruments
NN	Neural Network
NR	Newton-Raphson
OP	Optimization Problem
OPF	Optimal-Power-Flow
P-V	Photo-Voltaic
PCC	Point of Common Coupling
PDF	Probability Density Function

PID	Proportional Integral Derivative
PLCC	Pearson's Linear Correlation Coefficient
PLL	Phasor-Locked-Loop
PMU	Phasor Measurement Units
RMS	Root Mean Square
SB	Synchro-Breaker
SC	(LF) Sensitivity Coefficient
SoC	State of Charge
UEE	Uncovered Energy Error

Main Mathematical Sets

Λ_i^ϕ	Set of couples of constant weights and exponents describing the voltage-dependency of nodal active power injections at node $i \in \mathcal{N}$ and phase $\phi \in \{a, b, c\}$
\mathcal{C}	Subset of PQ-buses containing buses to which EVCSs are connected
\mathcal{K}	Subset of PQ-buses containing buses where CPCs in grid-following mode are connected
\mathcal{L}	Set of all electrical branches in an electrical grid
\mathcal{N}	Set of buses in an electrical-grid
\mathcal{PQ}	Set of PQ-buses in an electrical-grid
\mathcal{PV}	Set of PV-buses in an electrical-grid
\mathcal{R}	Subset of PQ-buses containing buses where resources are connected
\mathcal{S}	Set of slack-buses in an electrical-grid
\mathcal{U}	Set of admissible setpoints
\mathcal{Z}	Subset of PQ-buses containing zero-injection buses
Ω_i^ϕ	Set of couples of constant weights and exponents describing the voltage-dependency of nodal reactive power injections at node $i \in \mathcal{N}$ and phase $\phi \in \{a, b, c\}$

Main Electrical-grid symbols

P	Nodal active power injections
Q	Nodal reactive power injections

Nomenclature

\bar{E}^{seq}	Phase-to-ground nodal voltages in sequence domain
\bar{E}	Phase-to-ground nodal voltages in abc or phasor domain
\bar{I}	Nodal injected currents
\bar{I}_{in}	Branch currents from bus (node) i to n
\bar{S}	Nodal apparent power injections
\bar{Y}	Compound admittance matrix
\bar{Y}_{Lin}	3-phase longitudinal admittance of the branch between nodes i and n
$\bar{Y}_{Tin,i}$	3-phase shunt admittance of the branch between node i and the ground
$P_{0,i}^{\phi}$	Nodal active power injections, at node $i \in \mathcal{N}$ and phase $\phi \in \{a, b, c\}$, at nominal voltage
$Q_{0,i}^{\phi}$	Nodal reactive power injections, at node $i \in \mathcal{N}$ and phase $\phi \in \{a, b, c\}$, at nominal voltage

Miscellaneous symbols

Δt	Control period for proposed algorithms and/or optimization problems
ΔT_h	Prediction horizon for the estimation of the downstream PCC nodal voltage phase-angles
$\tilde{\Pi}_{\Gamma}(\mathbf{x})$	Approximated projection of \mathbf{x} onto the feasible set Γ using the method of alternating projects

Thesis Introduction

The increasing penetration of stochastic renewable distributed generation, ESSs and novel loads (e.g. EVs) in ADNs or microgrids has triggered the need to develop real-time (e.g. minutes to sub-second) control frameworks to avoid grid-operational problems. These can be split in two main categories of active constraints: *static* and *power-quality*. *Static* constraints refer to branches' capacity limitations, nodal voltage magnitudes' security-bounds as well as resources' limitations (e.g. MV-LV substation transformer apparent power limitations, power converters' capability curves and general constraints of the internal states of ESSs). *Power-quality* constraints, instead, refer to the quality-of-service for the end-users that must be guaranteed by the power distribution utility.

Within this context, this thesis focuses on the development of *real-time* ADN controls, in the form of frameworks or control-enabling methodologies, that take into account the above-mentioned power-grid operational constraints while considering grid *uncertainties* and *unbalances*. By grid *uncertainties* we refer to either *natural stochasticities*, i.e. resources whose performance is a function of external factors such as weather or human behaviors, or, *designed uncertainties*, i.e. uncertainties arising from the technical designs of resources (e.g. setpoint implementation inaccuracies). Indeed, within the context of this thesis, we assume that grid models, i.e. network topologies and branch parameters, are fully known and do not present uncertainties. By grid *unbalances* we refer to injections/absorptions that are unbalanced over the phases. Indeed, we do not power-grids with unbalanced grid models.

In terms of literature, the problem of real-time control under grid unbalances and/or uncertainties has been extensively studied. As a result, each contribution of the upcoming chapters is individually positioned w.r.t the state-of-the-art in order to only present relevant works. However, for the interested reader, we advise the reading of recently published survey or review papers that concisely summarise the relevant literature. For instance, [1, 2] thoroughly discuss the problem of stochastic optimization of power-grids by extensively presenting all relevant works on the subject. In [3, 4] authors tackle the problem of ADNs control by reviewing the newest trends in terms of real-time resource management. For completeness, we refer the interested reader to works such as [5] that review the controllability of specific resources (here ESSs) while studying their integration in ADNs.

In terms of contributions, in its first part, the thesis focuses on a general (i.e. resource-

agnostic) methodology to linearize the power-flow equations and showcases its real-time control-enabling advantages through two sub-second control examples. Then, in the second part, a deeper focus is given to the operational challenges raised by the large presence of EVCSs in ADNs. More specifically, here below the contributions of both parts of the thesis are listed with more details.

1. *Part 1 - Efficient methods for the control of multiple unsymmetric and uncertain ADN resources*

- First, an analytical method for computing general-three-phase SCs, considering voltage-dependent nodal power injections, is presented. SCs are the partial derivatives of any electrical quantity w.r.t. control variables (e.g. nodal active power injections and nodal voltage magnitudes at PV-nodes). The proposed method assumes the knowledge of the grid-model and relies on the resolution of unique and full-rank linear systems of equations to compute nodal voltage SCs. Finally, by knowing the nodal voltage SCs and the grid model, one can compute all other desired SCs (e.g. branch current ones).
- Second, an application example of SCs is presented. More specifically, the problem of securely reconnecting unbalanced islanded ADNs to their upstream grids at the PCC is tackled. The process is usually called *resynchronization* and is split into two process: steering the PCC downstream nodal voltages of an isolated ADN towards their upstream counterparts and asserting nodal voltage phasors' alignment on both sides of the PCC to close the PCC-breaker. An algorithm is proposed for each process. The first leverages SCs to approximately solve a three-phase OPF. The second makes use of the enhanced-Interpolated-Discrete-Fourier-Transform (e-IpDFT) to extract and compare the per-phase nodal voltage phasors at both sides of the PCC. Both processes are experimentally validated on a real-scale laboratory microgrid.
- Third, a second application example of SCs is presented. More specifically, a novel technique to render an intractable OPF problem solvable, is presented. The proposed algorithms account for the uncertainties due to set-point implementation by the resources' controllers. The result of the proposed methods is the computation of optimal control setpoints that are admissible i.e. satisfies grid and resource operational constraints for all uncertainties realizations.

2. *Part 2 - Efficient methods for the safe operation of electric-vehicle-charging-stations*

- First, a specific analysis is presented to quantify: (i) how uncontrolled EV charging can affect ADN static operational constraints, (ii) how some EVCS can increase grid-load-unbalances, and (iii) EV on-board controller reaction times. The analysis leverages (i) a Monte-Carlo load-flow framework, and (ii) a small-scale experiment using a non-commercial Type-2 EVCS connected to a real-scale laboratory microgrid.

- Second, a distributed real-time, i.e. seconds to minute scale, control framework for EVCSs is presented. The framework consists in solving a three-phase OPF that is: (i) *augmented*, i.e. accounts for EV user needs, (ii) *approximated*, i.e. leverages SCs to linearize the power-flow equations, and (iii) *distributed*, i.e. its solutions adopts the ADMM algorithm.
- Third, a day-ahead ADN DP generator, extending the work done in [6], is presented. The proposed algorithm accounts for next-day load and generation stochasticity through scenario-based optimization. It further considers that, in both day-ahead and real-time stages both ESSs *and* EVCSs are controllable entities. The generated DP is experimentally validated on a real-scale laboratory microgrid using the real-time distributed controller of [6] augmented by an MPC-based variant of the EVCS aggregator controller developed in the previous contribution.

Finally, in terms of document outline, **Chapter 1** introduces part I of the thesis. **Chapter 2** details the first contribution of part I. **Chapter 3** details the second contribution of part I. **Chapter 4** details the third contribution of part I. **Chapter 5** introduce part II of the thesis and details the first contribution of part II. **Chapter 6** details the second contribution of part II. **Chapter 7** details the third contribution of part II. Finally, the **General Conclusion** chapter, concludes the thesis by summarizing the each chapter's conclusion section and future works.

Efficient methods for the control of multiple unsymmetric and uncertain active distribution network resources

Part I

1 Context

1.1 Introduction & Motivations

This part tackles the problem of controlling ADNs that contain unsymmetric and uncertain resources. Unsymmetric grid resources are grid-connected entities whose absorptions are unbalanced over the phases. The unbalance usually concerns loads that consume electric power over a single-phase, e.g. Type 1 EVs that have on-board single-phase chargers. Uncertain grid resources are grid-connected entities whose injections and/or absorptions are either stochastic by nature or uncertain by design. Natural stochasticity refers to variable processes that are not a result of the performance of a resource but from external factors, e.g. (i) P-V power plants' outputs are directly affected by the movement of the clouds and (ii) residential load demands present a certain periodicity that is correlated to the inhabitants routines and habits. The degree of uncertainty by design, instead, depends on the accuracies and efficiencies of the system that controls a grid-connected resource, e.g. (i) setpoint tracking inaccuracies and (ii) ESS-inverters' output power dependencies on AC and/or DC-side nodal voltages. Accounting for all above-mentioned uncertainties leads to more robust control frameworks.

As previously mentioned, with the penetration of distributed generation and power-demanding load units in electric-power-grids, the need for novel control frameworks is advocated by the power systems technical community. Real-time control of power-grids has emerged as a potential solution to efficiently compute optimal setpoints and thus quickly respond to the potential uncertainties of the different resources. The later control frameworks can be achieved if the resolution of multi-phase robust OPF problems is made computationally efficient. Indeed, multi-phase non-approximated OPFs that include the AC non-linear power-flow equations are known to be hard non-convex problems, which renders them practically impossible to solve in real-time, e.g. at sub-second resolution times. Interestingly, as power-grid states vary slower as the control timestep is reduced, using first-order Taylor linearizations of the power-flow equations to approximate the highly non-convex grid operational constraints – e.g. nodal voltage and branch current magnitudes within safety bounds – renders the security-

constrained-OPF-resolution-times compatible with sub-seconds to seconds scales. Finally, as known, OPs with convex objectives and linear constraints have unique solutions which removes the issues of (i) non-uniqueness and (ii) sensitivity to the initial guess of the resolution algorithms of non-linear problems.

To this end, this thesis's first part focuses on a general (i.e. resource-agnostic) methodology to linearize the power-flow equations and showcases its real-time control-enabling advantages through two sub-second control examples. In the following, the details of the contributions of the next chapters of Part I, are given.

1.2 Contributions of the next chapters of Part I

This part contains three contributions that tackle the above-raised issues. Each contribution constitutes an upcoming chapter. In the following, a summary of the latter is given.

1. **Chapter 2** The first contribution [7] consists in an analytical method to compute the derivatives of power-grid controllable quantities (e.g. nodal voltages at PQ nodes, branch currents, nodal sequence voltages, etc.) with respect to control variables, i.e. nodal active and reactive power injections at PQ¹ nodes, nodal voltage magnitudes and nodal active power injections at PV² nodes and nodal voltage magnitudes and phase-angles at slack nodes. The latter are called SCs and can directly be leveraged to linearize the power-flow equations (c.f. sec. 2). The proposed method (i) assumes the knowledge of the grid model, i.e. branch parameters and grid topology, (ii) utilizes the grid states, i.e. nodal phase-to-ground voltage phasors at all buses, coming, for instance, from a state-estimator, (iii) computes the coefficients for all node-types (i.e. slack, PQ and PV nodes), (iv) can be applied to power-grids with generic number of phases and topologies, and (v) unlike what can be found in the literature, accounts for voltage-dependent nodal power injections. It will become clearer further-on that this contribution is the theoretical basis of all the other developments of this thesis as it enables a tractable inclusion of power-grid operational constraints in optimal ADN management problems and, therefore, answers to the increasing need for real-time control in power-systems.
2. **Chapter 3** The second contribution [8] consists in an application example of the first contribution. More specifically, the problem of the resynchronization of an islanded ADN, in the presence of grid-unbalances, is tackled. Resynchronization is the process of securely reconnecting ADNs – e.g. microgrids – to their upstream grids at the PCC. The latter has to be done with care in order to avoid large transient current flows resulting from differences of nodal voltage phasors at both sides of the PCC. The active resynchronization process can be split into two tasks: the PCC-control and the synchrocheck. The PCC-control refers to the process used to steer the PCC nodal voltage at the ADN's

¹Buses where active and reactive nodal power injections are regulated (traditionally called *load* buses).

²Buses where nodal active power injections and nodal voltage magnitudes are regulated (traditionally called *generator* buses).

side (i.e. downstream) towards the PCC nodal voltage at the upstream-grid's side (i.e. upstream). The synchrocheck refers to the algorithm used to check the synchronization (i.e. phasor alignment within tolerances) of the upstream and downstream PCC nodal voltages. Methods for PCC-control and synchrocheck presented in the literature commonly ignore the ADN's operational constraints and rely on the assumption of a balanced power systems. In this respect, first, an OPF problem is proposed to control ADN's resources in order to rapidly steer their PCC downstream nodal voltages close to their non-controllable upstream counterparts. The proposed OPF is (i) *linearized* using SCs and (ii) is *solved approximately* using a gradient-descent based algorithm to render it compatible with real-time applications. Second, an IpDFT-based synchrocheck method that verifies the alignment of all three-phases of both upstream and downstream nodal voltages at the PCC, is proposed. The proposed algorithms of this second contribution are experimentally validated on the CIGRE-low-voltage-benchmark-microgrid available at the DESL at the EPFL where the results of the developed synchrocheck are further benchmarked against the Schneider Electric's Micom P143 grid relay.

3. **Chapter 4** The third contribution consists in an extension of the previous contribution that further accounts for grid uncertainties. More specifically, as a preamble, the contribution first presents an overview of stochastic grid control problems. In particular, a non-exhaustive list of power-system uncertainties together with their mathematical modeling techniques are presented. Furthermore, a synthesis of the different techniques used in power-grids applications, dealing with the above-mentioned uncertainties, is presented. The main focus of this section is the development of two real-time ad-hoc algorithms that account for state-dependent-control-setpoint-implementations-uncertainties. The first algorithm, denoted as *the admissibility test*, leverages SCs to assert whether or not an optimal-control-setpoint, e.g. coming from any-OPF-based framework, is admissible. Admissibility is guaranteed if the grid and resources' operational constraints are satisfied for all possible-realizations – due to resource controllers implementation inaccuracies – of an optimal control-setpoint. The second algorithm is activated if the admissibility test fails. Its objective is to compute the closest (in terms of Euclidean distance) vector of optimal-control-setpoints w.r.t. the optimal non-admissible vector of optimal-control-setpoints given as its input. To do the latter, the algorithm iteratively approximately solves a linear and tractable OPF problem. Both tractability and linearizations of the OPF are achieved by leveraging SCs which, in turn, renders the proposed method compatible with real-time controls. The algorithms of this chapter, including the presented resource-uncertainty-models, are numerically tested on a MATLAB-simulated-version of the IEEE-34 [9] node test distribution feeder augmented with several controllable-resources.

2 Analytical Computation of Power Grids' Sensitivity Coefficients with Voltage-Dependent Injections

Keywords— Sensitivity coefficients, voltage-dependent nodal power injections, unbalanced power grids.

2.1 Introduction & Literature Review

As power-flow equations are strongly non-linear, their linear approximations are used to create efficiently solvable constraints or objectives for OPF-based control of power grids. In practice, some power-flow linearizations leverage SCs to link control variables (i.e. nodal active and reactive power injections at PQ nodes, nodal voltage magnitudes and nodal active power injections at PV nodes and nodal voltage magnitudes and phase-angles at slack nodes) to controlled variables (e.g. nodal voltage magnitudes at PQ nodes and branch currents). SCs are formally defined as the partial derivatives of controlled variables w.r.t. control variables. In the literature, the different SCs' estimation methods can be clustered in two categories: *model-based* and *model-less*.

Model-based SCs estimation methods rely on the knowledge of the grid model i.e. grid-topology together with the branch parameters and the associated admittance matrix. Historically, the first methods proposed to compute SCs relied on the inversion of the Jacobian matrix of the LF problem (e.g. [10]). For computational efficiency, the latter were replaced by methods that only rely on the knowledge of the grid model and its state. In [11], using a fixed-point approach and under the assumption of constant nodal power injections, the authors were the first to propose a method that does not rely on the Jacobian-matrix inversion to determine nodal voltage SCs for PQ nodes. Then, in [12], authors present a method based on solving linear systems of equations to compute voltage SCs for PQ nodes. They rigorously prove the applicability of the method to unbalanced radial electrical distribution networks in the presence of voltage independent nodal power injections. More recently, in [13], using a decentralised LF expression that assumes a radial network topology and the absence of shunt elements, authors proposed a closed-form expression to compute nodal voltage magnitude SCs for PQ nodes.

Model-less SCs estimation methods rely *only* on measurements and assume no knowledge of the grid model. In [14], authors present a least-squared-based identification method to compute nodal voltage SCs. Their method considers the presence of measurement noise. In [15], compared to [14], authors went a step further by accounting in their regression for cross-correlations between nodal power injections. In [16], the authors rely on a least-squares-based method exploiting the analytical relation

Chapter 2. Analytical Computation of Power Grids' Sensitivity Coefficients with Voltage-Dependent Injections

between nodal active and reactive power injections and the squares of nodal voltage magnitudes. The method neglects shunt elements and is only applicable to radial distribution networks. More recently, in [17], authors present a robust technique leveraging recursive-least-squares to compute nodal voltage SCs. The estimation is done online and is updated as soon as new measurements are available. Finally, it is worth mentioning that the load dependence on voltage fluctuations is inherently taken into account in SC *model-less* estimation techniques unlike in *model-based* SC estimation techniques, where it has to be explicitly included in the problem's equations.

To our knowledge, no *model-based* method that derives *all-node-types* (i.e. PQ, PV and Slack) SCs considering voltage-dependent nodal power injections and three-phase unbalanced networks can be found in the literature. In this respect, we present a *model-based* technique that relies on solving systems of linear equations to compute *all-node-types* voltage SCs and that accounts for generic voltage-dependency of nodal power injections. The method is applicable to polyphase networks with any grid topology (i.e. radial or meshed), allows users to compute SCs w.r.t. to any selection of control variables and relies solely on the knowledge of the grid model and its present state (e.g. can be coupled with a state estimator to feed suitable control applications). Finally, we present an exhaustive list of all SCs, e.g. the magnitude, phase-angle or complex coefficients of branch current, sequence voltages and nodal currents, that can be derived from nodal voltage SCs using the *known* grid model (see Section 2.2.4).

The structure of this chapter is as follows. Section 2.2 introduces the problem formulation. Section 2.3 presents the proposed method to compute all-node-types nodal voltage SCs considering a generic voltage-dependent power injection model. Section 2.4, presents a formal computational analysis of the proposed method. Section 2.5, first presents benchmarking processes to validate the computation of nodal voltage SCs and then, using the latter, shows a numerical validation of the proposed method performed on the IEEE-34 test distribution feeder [9]. Finally, section 2.6 concludes the chapter.

2.2 Problem Formulation

2.2.1 Grid Model

In this chapter³, electrical networks are assumed 3-phase (denoted as a , b and c), with $|\mathcal{N}|$ buses, where \mathcal{N} is the set of bus indexes. $\mathcal{PQ} \subset \mathcal{N}$ is the set of PQ nodes. $\mathcal{PV} \subset \mathcal{N}$ is the set of PV nodes. $\mathcal{S} \subset \mathcal{N}$ is the set of slack nodes. Without loss of generality and assuming that zero-injection nodes can be modelled as PQ nodes, we have $\mathcal{N} = \mathcal{PQ} \cup \mathcal{PV} \cup \mathcal{S}$ and $|\mathcal{PQ}| + |\mathcal{PV}| + |\mathcal{S}| = |\mathcal{N}|$. The network is described by the so-called, assumed to be known⁴, compound admittance matrix [19] given by $\bar{\mathbf{Y}} \in \mathbb{C}^{3|\mathcal{N}| \times 3|\mathcal{N}|} = [\bar{\mathbf{Y}}_{in}^{\phi\phi'}] \forall i, n \in \mathcal{N}$ and $\forall \phi, \phi' \in \{a, b, c\}$.

The relation between phase-to-ground nodal voltages $\bar{\mathbf{E}} = [\bar{E}_1^a, \bar{E}_1^b, \bar{E}_1^c, \dots, \bar{E}_{|\mathcal{N}|}^a, \bar{E}_{|\mathcal{N}|}^b, \bar{E}_{|\mathcal{N}|}^c]$ and, nodal injected currents $\bar{\mathbf{I}} = [\bar{I}_1^a, \bar{I}_1^b, \bar{I}_1^c, \dots, \bar{I}_{|\mathcal{N}|}^a, \bar{I}_{|\mathcal{N}|}^b, \bar{I}_{|\mathcal{N}|}^c]$ is given by, $\bar{\mathbf{I}} = \bar{\mathbf{Y}}\bar{\mathbf{E}}$. By relying on the assumptions of [20], namely that different branches are not electromagnetically coupled and have non-zero-admittances, network branches can be represented by 3-phase Π -circuit equivalents as in Fig. 2.1. Thus,

³In the following, matrices and vectors will be denoted in bold (e.g. \mathbf{M}), complex numbers will be denoted with an upper bar (e.g. $\bar{x} = |\bar{x}| \exp(j\angle(\bar{x})) = \Re\{\bar{x}\} + j\Im\{\bar{x}\}$) and complex conjugates with a bar underneath (e.g. $\bar{x} = \text{conj}(\bar{x}) = |\bar{x}| \exp(-j\angle(\bar{x})) = \Re\{\bar{x}\} - j\Im\{\bar{x}\}$).

⁴The knowledge of the grid-model is an assumption that is recurrent all throughout this thesis. The study of the needed accuracy of the model for the proposed methods to work properly is outside the scope of this thesis. However, for completeness, we refer the interested readers to the work presented in [18] where authors quantify the error propagation of branch parameter uncertainties.

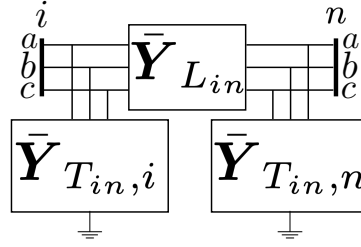


Figure 2.1: Schematic representation of a generic 3-phase network branch

a branch current \bar{I}_{in} can be expressed as follows:

$$\bar{I}_{in} = \begin{pmatrix} \bar{I}_{in}^a \\ \bar{I}_{in}^b \\ \bar{I}_{in}^c \end{pmatrix} = \bar{Y}_{Lin} \left[\begin{pmatrix} \bar{E}_i^a \\ \bar{E}_i^b \\ \bar{E}_i^c \end{pmatrix} - \begin{pmatrix} \bar{E}_n^a \\ \bar{E}_n^b \\ \bar{E}_n^c \end{pmatrix} \right] + \bar{Y}_{Tin,i} \begin{pmatrix} \bar{E}_i^a \\ \bar{E}_i^b \\ \bar{E}_i^c \end{pmatrix}, \quad (2.1)$$

where $\bar{Y}_{Lin} \in \mathbb{C}^{3 \times 3}$ and $\bar{Y}_{Tin,i} \in \mathbb{C}^{3 \times 3}$ are respectively the 3-phase longitudinal admittance between nodes $i \in \mathcal{N}$ and $n \in \mathcal{N}$ and the 3-phase shunt admittance between node $i \in \mathcal{N}$ and the ground. Consequently, the nodal apparent power injections $\bar{S} = [\bar{S}_1^a, \bar{S}_1^b, \bar{S}_1^c, \dots, \bar{S}_{|\mathcal{N}|}^a, \bar{S}_{|\mathcal{N}|}^b, \bar{S}_{|\mathcal{N}|}^c]$, with $\bar{S}_i^\phi = P_i^\phi + jQ_i^\phi$ where P_i^ϕ and Q_i^ϕ are, respectively, the nodal active and reactive power injections for node $i \in \mathcal{N}$ and phase $\phi \in \{a, b, c\}$, can be expressed as,

$$\bar{S}_i^\phi = \bar{E}_i^\phi \sum_{\substack{n \in \mathcal{N}, \\ \phi' \in \{a, b, c\}}} \bar{Y}_{in}^{\phi\phi'} \bar{E}_n^{\phi'}, \quad i \in \mathcal{N}, \phi \in \{a, b, c\}. \quad (2.2)$$

2.2.2 Voltage-Dependent Power Injections Model

A generic nodal power injection model is considered to encapsulate voltage-dependency. It is given by:

$$\begin{cases} P_i^\phi &= P_{0,i}^\phi \sum_{(\alpha, \lambda) \in \Lambda_i^\phi} \alpha |\bar{E}_i^\phi|^\lambda \\ Q_i^\phi &= Q_{0,i}^\phi \sum_{(\beta, \omega) \in \Omega_i^\phi} \beta |\bar{E}_i^\phi|^\omega \end{cases}, \quad (2.3)$$

where $P_{0,i}^\phi$ and $Q_{0,i}^\phi$ are respectively the reference active and reactive nodal power injections, at node $i \in \mathcal{N}$ and phase $\phi \in \{a, b, c\}$, at nominal voltage. Λ_i^ϕ and Ω_i^ϕ are sets containing couples of constant weights and exponents (usually in the range $[0; 3]$ [21]). Note that, the widely-used ZIP and exponent injection models [22] are, with the right constant and exponent sets, instances of (2.3). In this respect, we consider (2.3) as the most general form of voltage-dependent nodal power injections. Finally, for completeness, it is worth mentioning that the estimation of the parameters Λ_i^ϕ and Ω_i^ϕ is considered outside the scope of this thesis⁵. Indeed, the latter are considered given.

⁵We refer the interested reader to [23–25] where online and offline methods for estimating the injection model parameters, are presented.

2.2.3 Voltage SCs for all node types

In control applications, the targeted control variables depend on the type of node. For slack nodes the control variables are the magnitude and phase-angle of the nodal voltages (i.e. $|\bar{E}_k^\Phi|$ and $\angle(\bar{E}_k^\Phi)$, $\forall k \in \mathcal{S}$ and $\forall \Phi \in \{a, b, c\}$). For PQ nodes the control variables are the nodal active and reactive power injections at nominal voltage (i.e. $P_{0,l}^\Phi$ and $Q_{0,l}^\Phi$, $\forall l \in \mathcal{PQ}$ and $\forall \Phi \in \{a, b, c\}$). For PV nodes the control variables are the nodal active power injections at nominal voltage and the magnitude of the nodal voltages (i.e. $P_{0,m}^\Phi$ and $|\bar{E}_m^\Phi|$, $\forall m \in \mathcal{PV}$ and $\forall \Phi \in \{a, b, c\}$).

The method here proposed aims to compute nodal voltage SCs w.r.t. any control variable, i.e. $\frac{\partial \bar{E}_i^\phi}{\partial X}$, with $X \in \{|\bar{E}_k^\Phi|, \angle(\bar{E}_k^\Phi), P_{0,l}^\Phi, Q_{0,l}^\Phi, P_{0,m}^\Phi, |\bar{E}_m^\Phi|\}$ where $i \in \mathcal{N}$, $k \in \mathcal{S}$, $l \in \mathcal{PQ}$, $m \in \mathcal{PV}$ and $\phi, \Phi \in \{a, b, c\}$, as, knowing the grid model, once the nodal voltage SCs are computed, all other control-application-relevant-auxiliary-SCs can be analytically inferred (see Section 2.2.4).

2.2.4 Auxiliary SCs

From the grid model and the nodal voltage SCs one can analytically infer the SCs of any auxiliary electrical quantity (e.g. nodal currents, branch currents, slack powers and sequence voltages/currents). Assuming that $\bar{\mathbf{Y}}$ is invariant to control variables' changes, the nodal current SCs can be computed by taking the partial derivative of $\bar{\mathbf{I}} = \bar{\mathbf{Y}} \bar{\mathbf{E}}$ w.r.t. any control variable. Similarly, the branch current SCs can be computed by differentiating (2.1) and the slack power SCs can be computed by differentiating (2.2) for $i \in \mathcal{S}$. Knowing that the sequence-to-phase transformation matrix $\mathbf{H}^{\text{seq} \rightarrow \text{abc}} = (1, 1, 1; h^2, h, 1; h, h^2, 1)$, where $h = \exp(j2\pi/3)$, and its inverse $\mathbf{H}^{\text{abc} \rightarrow \text{seq}}$ are invariant to control variables' changes [26], any sequence (i.e. positive, negative and zero triplet) quantity can be computed by taking the partial derivative, w.r.t. any control variable, of $\bar{\mathbf{W}}^{\text{seq}} = \mathbf{H}^{\text{abc} \rightarrow \text{seq}} \bar{\mathbf{W}}^{\text{abc}}$, with $\bar{\mathbf{W}}^{\text{abc}}$ being an arbitrary unbalanced three-phase set of phasors (e.g. $(\bar{E}_i^a, \bar{E}_i^b, \bar{E}_i^c)$, $(\bar{I}_i^a, \bar{I}_i^b, \bar{I}_i^c)$ or $\bar{\mathbf{I}}_{in}$, for $i, n \in \mathcal{N}$), and $\bar{\mathbf{W}}^{\text{seq}}$ being the latter's sequence-domain equivalent.

2.2.5 Complex, magnitude and phase-angle SCs

The analytical relationships between complex ($\bar{\bullet}$), magnitude ($|\bar{\bullet}|$) and phase-angle ($\angle(\bar{\bullet})$) SCs are given by (2.4).

$$\begin{aligned} \frac{\partial \bar{\bullet}}{\partial X} &= \bar{\bullet} \left(\frac{1}{|\bar{\bullet}|} \frac{\partial |\bar{\bullet}|}{\partial X} + j \frac{\partial \angle(\bar{\bullet})}{\partial X} \right) \\ \frac{\partial |\bar{\bullet}|}{\partial X} &= \frac{1}{|\bar{\bullet}|} \Re \left\{ \bar{\bullet} \frac{\partial \bar{\bullet}}{\partial X} \right\} \\ \frac{\partial \angle(\bar{\bullet})}{\partial X} &= \frac{1}{|\bar{\bullet}|^2} \Im \left\{ \bar{\bullet} \frac{\partial \bar{\bullet}}{\partial X} \right\} \end{aligned} \tag{2.4}$$

With \bullet being any controlled electrical quantity (e.g. nodal voltages, nodal currents, sequence voltages and currents, branch currents and slack powers) and $X \in \{|\bar{E}_k^\Phi|, \angle(\bar{E}_k^\Phi), P_{0,l}^\Phi, Q_{0,l}^\Phi, P_{0,m}^\Phi, |\bar{E}_m^\Phi|\}$ where $k \in \mathcal{S}$, $l \in \mathcal{PQ}$, $m \in \mathcal{PV}$ and $\phi, \Phi \in \{a, b, c\}$, being any control variable.

2.3 Method

As said, the proposed method aims at computing the nodal voltage SCs w.r.t. any control variable (i.e. $\frac{\partial \bar{E}_i^\phi}{\partial X}$, with $X \in \{|\bar{E}_k^\Phi|, \angle(\bar{E}_k^\Phi), P_{0,l}^\Phi, Q_{0,l}^\Phi, P_{0,m}^\Phi, |\bar{E}_m^\Phi|\}$ where $i \in \mathcal{N}$, $k \in \mathcal{S}$, $l \in \mathcal{PQ}$, $m \in \mathcal{PV}$ and $\phi, \Phi \in \{a, b, c\}$). Assuming that slack nodal voltages are *fixed*⁶, i.e. cannot be influenced by control variables other than their own), the nodal voltage SCs of slack nodes can be directly computed as

$$\frac{\partial \bar{E}_i^\phi}{\partial X} = d(i, \phi, X) = \begin{cases} 0 & \text{if } X \in \{P_{0,l}^\Phi, Q_{0,l}^\Phi, \\ & P_{0,m}^\Phi, |\bar{E}_m^\Phi|\} \\ \mathbb{I}_{i=k, \phi=\Phi} \left\{ \exp(j\angle(\bar{E}_i^\phi)) \right\} & \text{if } X \in \{|\bar{E}_k^\Phi|\} \\ \mathbb{I}_{i=k, \phi=\Phi} \left\{ j\bar{E}_i^\phi \right\} & \text{if } X \in \{\angle(\bar{E}_k^\Phi)\} \end{cases} \quad (2.5)$$

where $i, k \in \mathcal{S}$, $l \in \mathcal{PQ}$, $m \in \mathcal{PV}$, $\phi, \Phi \in \{a, b, c\}$ and $\mathbb{I}_{\diamond \Delta}$ is a function equal to Δ if all boolean conditions \diamond are met or zero otherwise.

For the remaining nodal voltage SCs (i.e. $\frac{\partial \bar{E}_i^\phi}{\partial X}$ with $i \in \mathcal{PV} \cup \mathcal{PQ}$), we propose solving a system of linear equations per control variable (i.e. X). The first step to get the latter is to differentiate (2.2) and (2.3) $\forall i \in \mathcal{PV} \cup \mathcal{PQ}$ and $\forall \phi \in \{a, b, c\}$ w.r.t. a control variable; with some rearranging and using (2.4), this leads to the system of $3|\mathcal{PV}| + 3|\mathcal{PQ}|$ equations given by

$$\begin{aligned} & \left(\frac{\partial P_{0,i}^\phi}{\partial X} \sum_{(\alpha, \lambda) \in \Lambda_i^\phi} \alpha |\bar{E}_i^\phi|^\lambda + P_{0,i}^\phi \sum_{(\alpha, \lambda) \in \Lambda_i^\phi} \alpha \lambda |\bar{E}_i^\phi|^{\lambda-1} \frac{\partial |\bar{E}_i^\phi|}{\partial X} \right) + \\ & j \left(\frac{\partial Q_{0,i}^\phi}{\partial X} \sum_{(\beta, \omega) \in \Omega_i^\phi} \beta |\bar{E}_i^\phi|^\omega + Q_{0,i}^\phi \sum_{(\beta, \omega) \in \Omega_i^\phi} \beta \omega |\bar{E}_i^\phi|^{\omega-1} \frac{\partial |\bar{E}_i^\phi|}{\partial X} \right) = \\ & \sum_{\substack{n \in \mathcal{N} \\ \phi' \in \{a, b, c\}}} \bar{E}_i^\phi Y_{in}^{\phi\phi'} \bar{E}_n^{\phi'} \left[\left(\frac{1}{|\bar{E}_i^\phi|} \frac{\partial |\bar{E}_i^\phi|}{\partial X} + \frac{1}{|\bar{E}_n^{\phi'}|} \frac{\partial |\bar{E}_n^{\phi'}|}{\partial X} \right) + j \left(\frac{\partial \angle(\bar{E}_i^\phi)}{\partial X} - \frac{\partial \angle(\bar{E}_n^{\phi'})}{\partial X} \right) \right] \end{aligned} \quad (2.6)$$

By taking the real and imaginary parts of each equation in (2.6), i.e. $\Re\{(2.6)\}$ and $\Im\{(2.6)\}$ $\forall i \in \mathcal{PV} \cup \mathcal{PQ}$ and $\forall \phi \in \{a, b, c\}$, using (2.4) and (2.5), and, assuming that a control variable cannot be influenced by another control variable [12], i.e.

$$\frac{\partial P_{0,i}^\phi}{\partial X} = f(i, \phi, X) = \begin{cases} \mathbb{I}_{X=P_{0,l}^\Phi, \{1\}} & \text{if } i \in \mathcal{PQ} \\ & i=l, \\ & \phi=\Phi \\ \mathbb{I}_{X=P_{0,m}^\Phi, \{1\}} & \text{if } i \in \mathcal{PV} \\ & i=m, \\ & \phi=\Phi \end{cases} \quad (2.7)$$

⁶This remains applicable in situations with multiple slack nodes as the power distribution ratio between different slack nodes has to be fixed. As a result, their respective nodal voltages can be *fixed*.

$$\frac{\partial Q_{0,i}^\phi}{\partial X} = g(i, \phi, X) = \begin{cases} \mathbb{I}_{X=Q_{0,l}^\phi, \{1\}} & \text{if } i \in \mathcal{PQ} \\ i=l, \\ \phi=\Phi & \\ \frac{\partial Q_{0,i}^\phi}{\partial X} & \text{if } i \in \mathcal{PV} \end{cases}, \quad (2.8)$$

$$\frac{\partial |\bar{E}_i^\phi|}{\partial X} = h(i, \phi, X) = \begin{cases} \frac{\partial |\bar{E}_i^\phi|}{\partial X} & \text{if } i \in \mathcal{PQ} \\ \mathbb{I}_{X=|\bar{E}_m^\phi|, \{1\}} & \text{if } i \in \mathcal{PV} \\ i=m, \\ \phi=\Phi & \end{cases}, \quad (2.9)$$

with $l \in \mathcal{PQ}$, $m \in \mathcal{PV}$ and $k \in \mathcal{S}$, one can obtain the system of equations (2.10).

$$\left\{ \begin{aligned} & \left(f(i, \phi, X) \sum_{(\alpha, \lambda) \in \Lambda_i^\phi} \alpha |\bar{E}_i^\phi|^\lambda + P_{0,i}^\phi \sum_{(\alpha, \lambda) \in \Lambda_i^\phi} \alpha \lambda |\bar{E}_i^\phi|^{\lambda-1} h(i, \phi, X) \right) \\ &= \sum_{\substack{n \in \mathcal{N} \\ \phi' \in \{a, b, c\}}} \frac{\Re \{ \bar{F}_{in}^{\phi\phi'} \}}{|\bar{E}_i^\phi|} h(i, \phi, X) - \Im \{ \bar{F}_{in}^{\phi\phi'} \} \frac{\partial \angle(\bar{E}_i^\phi)}{\partial X} \\ &+ \sum_{\substack{n \in \mathcal{PQ} \cup \mathcal{PV} \\ \phi' \in \{a, b, c\}}} \frac{\Re \{ \bar{F}_{in}^{\phi\phi'} \}}{|\bar{E}_n^{\phi'}|} h(n, \phi', X) + \Im \{ \bar{F}_{in}^{\phi\phi'} \} \frac{\partial \angle(\bar{E}_n^{\phi'})}{\partial X} \\ &+ \sum_{\substack{n \in \mathcal{S} \\ \phi' \in \{a, b, c\}}} \frac{\Re \{ \bar{F}_{in}^{\phi\phi'} \}}{|\bar{E}_n^{\phi'}|^2} \Re \{ r(n, \phi', X) \} + \frac{\Im \{ \bar{F}_{in}^{\phi\phi'} \}}{|\bar{E}_n^{\phi'}|^2} \Im \{ r(n, \phi', X) \} \\ & \left(g(i, \phi, X) \sum_{(\beta, \omega) \in \Omega_i^\phi} \beta |\bar{E}_i^\phi|^\omega + Q_{0,i}^\phi \sum_{(\beta, \omega) \in \Omega_i^\phi} \beta \omega |\bar{E}_i^\phi|^{\omega-1} h(i, \phi, X) \right) \\ &= \sum_{\substack{n \in \mathcal{N} \\ \phi' \in \{a, b, c\}}} \Re \{ \bar{F}_{in}^{\phi\phi'} \} \frac{\partial \angle(\bar{E}_i^\phi)}{\partial X} + \frac{\Im \{ \bar{F}_{in}^{\phi\phi'} \}}{|\bar{E}_i^\phi|} h(i, \phi, X) \\ &- \sum_{\substack{n \in \mathcal{PQ} \cup \mathcal{PV} \\ \phi' \in \{a, b, c\}}} \Re \{ \bar{F}_{in}^{\phi\phi'} \} \frac{\partial \angle(\bar{E}_n^{\phi'})}{\partial X} - \frac{\Im \{ \bar{F}_{in}^{\phi\phi'} \}}{|\bar{E}_n^{\phi'}|} h(n, \phi', X) \\ &- \sum_{\substack{n \in \mathcal{S} \\ \phi' \in \{a, b, c\}}} \frac{\Re \{ \bar{F}_{in}^{\phi\phi'} \}}{|\bar{E}_n^{\phi'}|^2} \Im \{ r(n, \phi', X) \} - \frac{\Im \{ \bar{F}_{in}^{\phi\phi'} \}}{|\bar{E}_n^{\phi'}|^2} \Re \{ r(n, \phi', X) \} \end{aligned} \right\} \quad (2.10)$$

Where $\bar{F}_{in}^{\phi\phi'} = \bar{E}_i^\phi Y_{in}^{\phi\phi'} \bar{E}_n^{\phi'}$ and $r(n, \phi', X) = \bar{E}_n^{\phi'} d(n, \phi', X)$. The system (2.10) contains $2 \times (3|\mathcal{PV}| + 3|\mathcal{PQ}|)$ equations, is linear in terms of the variables $\frac{\partial Q_{0,i}^\phi}{\partial X} \forall i \in \mathcal{PV}$, $\frac{\partial |\bar{E}_i^\phi|}{\partial X} \forall i \in \mathcal{PQ}$ and $\frac{\partial \angle(\bar{E}_i^\phi)}{\partial X} \forall i \in \mathcal{PQ} \cup \mathcal{PV}$, $\forall \phi \in \{a, b, c\}$, and has as many variables as equations. Using the notation $\left[\circ_i^\phi \right] \forall i, \forall \phi$ and

$\left[\circ_{in}^{\phi\phi'}\right] \forall i, \forall n, \forall \phi, \phi'$ to, respectively, denote column vectors composed of the elements \circ_i^ϕ and matrices composed of the elements $\circ_{in}^{\phi\phi'}$, the system (2.10) can be written in the form $\mathbf{A}\mathbf{x}(X) = \mathbf{w}(X)$, where $\mathbf{A} = (\mathbf{A}_{11}, \mathbf{A}_{12}, \mathbf{A}_{13}, \mathbf{A}_{14}; \mathbf{A}_{21}, \mathbf{A}_{22}, \mathbf{A}_{23}, \mathbf{A}_{24}; \mathbf{A}_{31}, \mathbf{A}_{32}, \mathbf{A}_{33}, \mathbf{A}_{34}; \mathbf{A}_{41}, \mathbf{A}_{42}, \mathbf{A}_{43}, \mathbf{A}_{44})$,

with,

$$\begin{aligned}
 \mathbf{A}_{11} &= \mathbb{O}^{|\mathcal{PQ}| \times |\mathcal{PV}|} \\
 \mathbf{A}_{12} &= \left(\left[\frac{\Re\{\bar{F}_{in}^{\phi\phi'}\}}{|\bar{E}_n^{\phi'}|} \right] \forall i \in \mathcal{PQ}, \forall n \in \mathcal{PQ}, \forall \phi, \phi' \in \{a, b, c\} \right) + \\
 &\quad \text{diag} \left(\left[\begin{array}{c} -P_{0,i}^\phi \sum_{(\alpha, \lambda) \in \Lambda_i^\phi} \alpha \lambda |\bar{E}_i^\phi|^{\lambda-1} + \sum_{\substack{n \in \mathcal{N} \\ \phi' \in \{a, b, c\}}} \frac{\Re\{\bar{F}_{in}^{\phi\phi'}\}}{|\bar{E}_i^\phi|} \\ \forall i \in \mathcal{PQ}, \forall \phi \in \{a, b, c\} \end{array} \right] \right) \\
 \mathbf{A}_{13} &= \left(\left[\Im\{\bar{F}_{in}^{\phi\phi'}\} \right] \forall i \in \mathcal{PQ}, \forall n \in \mathcal{PQ}, \forall \phi, \phi' \in \{a, b, c\} \right) + \\
 &\quad \text{diag} \left(\left[- \sum_{\substack{n \in \mathcal{N} \\ \phi' \in \{a, b, c\}}} \Im\{\bar{F}_{in}^{\phi\phi'}\} \right] \forall i \in \mathcal{PQ}, \forall \phi \in \{a, b, c\} \right) \\
 \mathbf{A}_{14} &= \left[\Im\{\bar{F}_{in}^{\phi\phi'}\} \right] \forall i \in \mathcal{PQ}, \forall n \in \mathcal{PV}, \forall \phi, \phi' \in \{a, b, c\} \\
 \mathbf{A}_{21} &= \mathbb{O}^{|\mathcal{PV}| \times |\mathcal{PV}|} \\
 \mathbf{A}_{22} &= \left[\frac{\Re\{\bar{F}_{in}^{\phi\phi'}\}}{|\bar{E}_n^{\phi'}|} \right] \forall i \in \mathcal{PV}, \forall n \in \mathcal{PQ}, \forall \phi, \phi' \in \{a, b, c\} \\
 \mathbf{A}_{23} &= \left[\Im\{\bar{F}_{in}^{\phi\phi'}\} \right] \forall i \in \mathcal{PV}, \forall n \in \mathcal{PQ}, \forall \phi, \phi' \in \{a, b, c\} \\
 \mathbf{A}_{24} &= \left(\left[\Im\{\bar{F}_{in}^{\phi\phi'}\} \right] \forall i \in \mathcal{PV}, \forall n \in \mathcal{PV}, \forall \phi, \phi' \in \{a, b, c\} \right) + \\
 &\quad \text{diag} \left(\left[- \sum_{\substack{n \in \mathcal{N} \\ \phi' \in \{a, b, c\}}} \Im\{\bar{F}_{in}^{\phi\phi'}\} \right] \forall i \in \mathcal{PV}, \forall \phi \in \{a, b, c\} \right) \\
 \mathbf{A}_{31} &= \mathbb{O}^{|\mathcal{PQ}| \times |\mathcal{PV}|} \\
 \mathbf{A}_{32} &= \left(\left[\frac{\Im\{\bar{F}_{in}^{\phi\phi'}\}}{|\bar{E}_n^{\phi'}|} \right] \forall i \in \mathcal{PQ}, \forall n \in \mathcal{PQ}, \forall \phi, \phi' \in \{a, b, c\} \right) + \\
 &\quad \text{diag} \left(\left[\begin{array}{c} -Q_{0,i}^\phi \sum_{(\beta, \omega) \in \Omega_i^\phi} \beta \omega |\bar{E}_i^\phi|^{\omega-1} + \sum_{\substack{n \in \mathcal{N} \\ \phi' \in \{a, b, c\}}} \frac{\Im\{\bar{F}_{in}^{\phi\phi'}\}}{|\bar{E}_i^\phi|} \\ \forall i \in \mathcal{PQ}, \forall \phi \in \{a, b, c\} \end{array} \right] \right) \\
 \mathbf{A}_{33} &= \left(\left[-\Re\{\bar{F}_{in}^{\phi\phi'}\} \right] \forall i \in \mathcal{PQ}, \forall n \in \mathcal{PQ}, \forall \phi, \phi' \in \{a, b, c\} \right) + \\
 &\quad \text{diag} \left(\left[\sum_{\substack{n \in \mathcal{N} \\ \phi' \in \{a, b, c\}}} \Re\{\bar{F}_{in}^{\phi\phi'}\} \right] \forall i \in \mathcal{PQ}, \forall \phi \in \{a, b, c\} \right)
 \end{aligned} \tag{2.11}$$

Chapter 2. Analytical Computation of Power Grids' Sensitivity Coefficients with Voltage-Dependent Injections

$$\begin{aligned}
\mathbf{A}_{34} &= \left[-\Re \left\{ \bar{F}_{in}^{\phi\phi'} \right\} \right] \forall i \in \mathcal{PQ}, \forall n \in \mathcal{PV}, \forall \phi, \phi' \in \{a, b, c\} \\
\mathbf{A}_{41} &= \text{diag} \left(\left[- \sum_{(\beta, \omega) \in \Omega_i^\phi} \beta |\bar{E}_i^\phi|^\omega \right] \forall i \in \mathcal{PV}, \forall \phi \in \{a, b, c\} \right) \\
\mathbf{A}_{42} &= \left[\frac{\Im \left\{ \bar{F}_{in}^{\phi\phi'} \right\}}{|\bar{E}_n^{\phi'}|} \right] \forall i \in \mathcal{PV}, \forall n \in \mathcal{PQ}, \forall \phi, \phi' \in \{a, b, c\} \\
\mathbf{A}_{43} &= \left[-\Re \left\{ \bar{F}_{in}^{\phi\phi'} \right\} \right] \forall i \in \mathcal{PV}, \forall n \in \mathcal{PQ}, \forall \phi, \phi' \in \{a, b, c\} \\
\mathbf{A}_{44} &= \left(\left[-\Re \left\{ \bar{F}_{in}^{\phi\phi'} \right\} \right] \forall i \in \mathcal{PV}, \forall n \in \mathcal{PV}, \forall \phi, \phi' \in \{a, b, c\} \right) + \\
&\quad \text{diag} \left(\left[\sum_{\substack{n \in \mathcal{N} \\ \phi' \in \{a, b, c\}}} \Re \left\{ \bar{F}_{in}^{\phi\phi'} \right\} \right] \forall i \in \mathcal{PV}, \forall \phi \in \{a, b, c\} \right)
\end{aligned}$$

where $\mathbb{O}^{t_1 \times t_2} \subset \mathbb{R}^{t_1 \times t_2}$ is a matrix of zeros and $\text{diag}(\mathbf{v})$ being an operator that creates a diagonal matrix from the vector \mathbf{v} ,

$$\mathbf{x}(X) = \begin{pmatrix} \left[\frac{\partial Q_{0,i}^\phi}{\partial X} \right] \forall i \in \mathcal{PV}, \forall \phi \in \{a, b, c\} \\ \left[\frac{\partial |\bar{E}_i^\phi|}{\partial X} \right] \forall i \in \mathcal{PQ}, \forall \phi \in \{a, b, c\} \\ \left[\frac{\partial \angle(\bar{E}_i^\phi)}{\partial X} \right] \forall i \in \mathcal{PQ}, \forall \phi \in \{a, b, c\} \\ \left[\frac{\partial \angle(\bar{E}_i^\phi)}{\partial X} \right] \forall i \in \mathcal{PV}, \forall \phi \in \{a, b, c\} \end{pmatrix}, \quad (2.12)$$

and, $\mathbf{w}(X) = (\mathbf{w}_1, \mathbf{w}_2; \mathbf{w}_3; \mathbf{w}_4)$, with,

$$\begin{aligned}
\mathbf{w}_1 &= \left[\mathbb{I}_{X=P_{0,l}^\Phi, \{1\}} \sum_{\substack{i=l, \\ \phi=\Phi}} \alpha |\bar{E}_i^\phi|^\lambda - \right. \\
&\quad \sum_{\substack{n \in \mathcal{PV} \\ \phi' \in \{a, b, c\}}} \frac{\Re \left\{ \bar{F}_{in}^{\phi\phi'} \right\}}{|\bar{E}_n^{\phi'}|} \mathbb{I}_{X=|\bar{E}_m^\Phi|, \{1\}} - \\
&\quad \left. \sum_{\substack{n \in \mathcal{P} \\ \phi' \in \{a, b, c\}}} \frac{\Re \left\{ \bar{F}_{in}^{\phi\phi'} \right\}}{|\bar{E}_n^{\phi'}|^2} \Re \{r(n, \phi', X)\} + \frac{\Im \left\{ \bar{F}_{in}^{\phi\phi'} \right\}}{|\bar{E}_n^{\phi'}|^2} \Im \{r(n, \phi', X)\} \right] \\
&\quad \forall i \in \mathcal{PQ}, \forall \phi \in \{a, b, c\}
\end{aligned} \quad (2.13)$$

$$\begin{aligned}
 \mathbf{w}_2 = & \left[\mathbb{I}_{X=P_{0,m}^\Phi, \{1\}} \sum_{\substack{i=m, \\ \phi=\Phi}} \alpha |\bar{E}_i^\phi|^\lambda + \right. \\
 & P_{0,i}^\phi \sum_{(\alpha,\lambda) \in \Lambda_i^\phi} \alpha \lambda |\bar{E}_i^\phi|^{\lambda-1} \mathbb{I}_{X=|\bar{E}_m^\Phi|, \{1\}} - \\
 & \sum_{\substack{n \in \mathcal{N} \\ \phi' \in \{a,b,c\}}} \frac{\Re\{\bar{F}_{in}^{\phi\phi'}\}}{|\bar{E}_i^\phi|} \mathbb{I}_{X=|\bar{E}_m^\Phi|, \{1\}} - \\
 & \sum_{\substack{n \in \mathcal{PV} \\ \phi' \in \{a,b,c\}}} \frac{\Re\{\bar{F}_{in}^{\phi\phi'}\}}{|\bar{E}_n^{\phi'}|} \mathbb{I}_{X=|\bar{E}_m^\Phi|, \{1\}} - \\
 & \left. \sum_{\substack{n \in \mathcal{S} \\ \phi' \in \{a,b,c\}}} \frac{\Re\{\bar{F}_{in}^{\phi\phi'}\}}{|\bar{E}_n^{\phi'}|^2} \Re\{r(n, \phi', X)\} + \frac{\Im\{\bar{F}_{in}^{\phi\phi'}\}}{|\bar{E}_n^{\phi'}|^2} \Im\{r(n, \phi', X)\} \right] \\
 & \forall i \in \mathcal{PV}, \forall \phi \in \{a, b, c\} \\
 \\
 \mathbf{w}_3 = & \left[\mathbb{I}_{X=Q_{0,l'}^\Phi, \{1\}} \sum_{\substack{i=l, \\ \phi=\Phi}} \beta |\bar{E}_i^\phi|^\omega - \right. \\
 & \sum_{\substack{n \in \mathcal{PV} \\ \phi' \in \{a,b,c\}}} \frac{\Im\{\bar{F}_{in}^{\phi\phi'}\}}{|\bar{E}_n^{\phi'}|} \mathbb{I}_{X=|\bar{E}_m^\Phi|, \{1\}} + \\
 & \left. \sum_{\substack{n \in \mathcal{S} \\ \phi' \in \{a,b,c\}}} \frac{\Re\{\bar{F}_{in}^{\phi\phi'}\}}{|\bar{E}_n^{\phi'}|^2} \Im\{r(n, \phi', X)\} - \frac{\Im\{\bar{F}_{in}^{\phi\phi'}\}}{|\bar{E}_n^{\phi'}|^2} \Re\{r(n, \phi', X)\} \right] \\
 & \forall i \in \mathcal{DQ}, \forall \phi \in \{a, b, c\} \\
 \\
 \mathbf{w}_4 = & \left[Q_{0,i}^\phi \sum_{(\beta,\omega) \in \Omega_i^\phi} \beta \omega |\bar{E}_i^\phi|^{\omega-1} \mathbb{I}_{X=|\bar{E}_m^\Phi|, \{1\}} - \right. \\
 & \sum_{\substack{n \in \mathcal{N} \\ \phi' \in \{a,b,c\}}} \frac{\Im\{\bar{F}_{in}^{\phi\phi'}\}}{|\bar{E}_i^\phi|} \mathbb{I}_{X=|\bar{E}_m^\Phi|, \{1\}} - \\
 & \sum_{\substack{n \in \mathcal{PV} \\ \phi' \in \{a,b,c\}}} \frac{\Im\{\bar{F}_{in}^{\phi\phi'}\}}{|\bar{E}_n^{\phi'}|} \mathbb{I}_{X=|\bar{E}_m^\Phi|, \{1\}} + \\
 & \left. \sum_{\substack{n \in \mathcal{S} \\ \phi' \in \{a,b,c\}}} \frac{\Re\{\bar{F}_{in}^{\phi\phi'}\}}{|\bar{E}_n^{\phi'}|^2} \Im\{r(n, \phi', X)\} - \frac{\Im\{\bar{F}_{in}^{\phi\phi'}\}}{|\bar{E}_n^{\phi'}|^2} \Re\{r(n, \phi', X)\} \right] \\
 & \forall i \in \mathcal{PV}, \forall \phi \in \{a, b, c\}
 \end{aligned}$$

Note that \mathbf{A} is independent of the chosen control variable while $\mathbf{w}(X)$, on the other hand, is.

Chapter 2. Analytical Computation of Power Grids' Sensitivity Coefficients with Voltage-Dependent Injections

To summarize, the proposed method consists in numerical evaluations and subsequent solutions of linear systems of equations to compute nodal voltage SCs for all node types. All the needed steps are summarised in Alg. 1. Finally, it is worth noting that the solvability of each linear system of equations $\mathbf{Ax}(X) = \mathbf{w}(X)$ is not studied in this thesis. However, each system has as many equations as it has variables and, through numerical simulations, seems to have a unique solution when the grid state is *meaningful* (i.e. the state exists within solvability bounds of the power-flow equations c.f. [27]).

Algorithm 1 Method to compute nodal voltage SCs

- 1: Get state of the grid, i.e. $\bar{E}_i^\phi \forall i \in \mathcal{N}$ and $\forall \phi \in \{a, b, c\}$
 - 2: Construct \mathbf{A} using (2.11) and the state of the grid;
 - 3: **for all** Desired control variables X **do**
 - 4: i Compute nodal voltage SCs for slack nodes (i.e. $\frac{\partial \bar{E}_i^\phi}{\partial X}, \forall i \in \mathcal{S}, \forall \phi \in \{a, b, c\}$) using (2.5);
 - ii Construct $\mathbf{w}(X)$ using (2.13) and solve the linear system of equations $\mathbf{Ax}(X) = \mathbf{w}(X)$;
 - iii From $\mathbf{x}(X)$, get the nodal voltage SCs for PQ and PV nodes (i.e. $\frac{\partial \bar{E}_i^\phi}{\partial X}, \forall i \in \mathcal{PQ} \cup \mathcal{PV}, \forall \phi \in \{a, b, c\}$) using (2.4);
 - iv *(if needed)* Compute auxiliary SCs using nodal voltage SCs as explained in Section 2.2.4.
 - 5: **end for**
-

2.4 Computational Complexity & Scalability

The computation complexity and scalability of an algorithm can be determined by studying the amount of memory and number of arithmetic operations used until its convergence. When it comes to memory, Alg. 1 requires storage space that is dependent to the number of nodes in the system. As a result, the proposed method's memory usage will scale linearly for vectors and quadratically for matrices, as the network size (i.e. number of nodes) increases. When it comes to arithmetic operations, Alg. 1 requires, for a given state, (i) constructing \mathbf{A} once, (ii) for each control variable, constructing $\mathbf{w}(X)$ and solving $\mathbf{Ax}(X) = \mathbf{w}(X)$. Tables 2.1a-2.1e show the number of arithmetic operations needed to construct, respectively, \mathbf{A} and $\mathbf{w}(X)$. It is clear that the number of operations needed to construct the sub-blocks of \mathbf{A} and $\mathbf{w}(X)$ scale at most quadratically as the network size increases (see Sec. 2.5 for an example of computation times⁷ achieved on the IEEE-34 feeder [9]). The number of arithmetic operations needed to solve each linear system of equations, using for instance Gaussian factorization, is $\mathcal{O}((2(3|\mathcal{PQ}| + 3|\mathcal{PV}|))^3)$. Finally, it is worth nothing that further investigations, e.g. matrix factorization, into the solving of each system was left for future works, however, for the interested reader, we recommend reading [28] to get insights on the newest methods and

⁷We refer the interested reader to [12] – where, as previously stated, a similar method was presented – for other numerical values of computation times.

achievable performances when it comes to solving linear systems of equations.

2.5 Validation

In order to numerically validate the proposed method, two different benchmark processes were used. The first consists in inverting the Jacobian matrix of the power-flow equations obtained by taking the real and imaginary parts of (2.2) where the LHS is replaced by (2.3) and the nodal voltages and elements of the admittance matrix are expressed in polar coordinates. Using (2.4) and the sub-matrices of the inverted Jacobian one can obtain $\frac{\partial \bar{E}_i^\phi}{\partial P_{0,l}^\Phi}$, $\frac{\partial \bar{E}_i^\phi}{\partial Q_{0,l}^\Phi}$ and $\frac{\partial \bar{E}_i^\phi}{\partial P_{0,m}^\Phi}$, $\forall i \in \mathcal{PV} \cup \mathcal{PQ}$, $\forall l \in \mathcal{PQ}$, $\forall m \in \mathcal{PV}$ and $\forall \phi, \Phi \in \{a, b, c\}$. The second benchmark consists in performing subsequent LF computations using the latter voltage-dependent power-flow formulation and its associated Jacobian. In between the subsequent computations, small variations in the remaining targeted control variables are applied, and thus the nodal voltage SCs are approximately computed by taking the ratio of the subsequent nodal voltage (magnitude and phase-angle) variations over the subsequent control variable variations ΔX (see Section II-A in [14]). In order to increase the accuracy of the obtained approximated SCs, each variation of control variables is done separately (i.e. all other control variables remain constant in between subsequent LF computations). Note that, the reason the second benchmark is needed is due to the fact that the inversion of the Jacobian matrix does not make available $\frac{\partial \bar{E}_i^\phi}{\partial |\bar{E}_m^\Phi|}$, $\frac{\partial \bar{E}_i^\phi}{\partial \angle(\bar{E}_k^\Phi)}$ and $\frac{\partial \bar{E}_i^\phi}{\partial \angle(\bar{E}_k^\Phi)}$, $\forall i \in \mathcal{PV} \cup \mathcal{PQ}$, $\forall k \in \mathcal{S}$, $\forall m \in \mathcal{PV}$ and $\forall \phi, \Phi \in \{a, b, c\}$. It is worth underlining that the second benchmark can lead to inaccurate results if the control variable variations are not small enough. Indeed, the smaller the variations, the better the variations ratio approximates the SCs.

The simulations were performed on MATLAB⁸ using the IEEE34 bus feeder without the regulators [9]. The Jacobian and network state were computed using the NR algorithm with a stopping criteria of 10^{-8} p.u. for the NR-intra-iteration residuals of all quantities that need to be imposed (i.e. control variables). For a specific network state, the results of the first and second benchmarks are reported in Tab. 2.2 and Fig. 2.2 respectively. All errors, i.e. absolute differences between the proposed method and benchmarks, are, at most, of the same magnitude set for the tolerance of the NR algorithm. For completeness, in this simulation, step 2 of Alg. 1 took around 1ms and, for each control variable, steps 4.i-4.iii took on average 0.275ms. Finally, all MATLAB scripts (simulation example and sub-functions) can be found open-source at <https://go.epfl.ch/SCs>.

2.6 Conclusion

This chapter illustrated an analytical method to compute all-node type (i.e. PQ, PV and slack) nodal voltage SCs w.r.t. to *all* possible control variables in a power grid (i.e. nodal active

⁸Ran on a Macbook Pro with 3.5 GHz Dual-Core Intel Core i7

Chapter 2. Analytical Computation of Power Grids' Sensitivity Coefficients with Voltage-Dependent Injections

Table 2.1: Number of Arithmetic Operations i.e. sums/subtractions (+/-) and multiplication-
s/divisions (\times/\div) to construct \mathbf{A} and $\mathbf{w}(X)$

(a) \mathbf{A}							
	A_{11}	A_{12}		A_{13}	A_{14}	A_{21}	A_{22}
$+/-$	0	$3 \mathcal{PQ} \left(\Lambda_i^\phi + \mathcal{N} \right)$		$3 \mathcal{PQ} \mathcal{N} $	0	0	0
\times/\div	0	$3 \mathcal{PQ} \left(3 \mathcal{PQ} + \mathcal{N} +2 \Lambda_i^\phi +1\right)$		0	0	0	$9 \mathcal{PQ} \mathcal{PV} $

(b) \mathbf{A} - continued							
	A_{23}	A_{24}	A_{31}	A_{32}		A_{33}	A_{34}
$+/-$	0	$3 \mathcal{PV} \mathcal{N} $	0	$3 \mathcal{PQ} \left(\Omega_i^\phi + \mathcal{N} \right)$		$3 \mathcal{PQ} \mathcal{N} $	0
\times/\div	0	0	0	$3 \mathcal{PQ} \left(3 \mathcal{PQ} + \mathcal{N} +2 \Omega_i^\phi +1\right)$		0	0

(c) \mathbf{A} - continued				
	A_{41}	A_{42}	A_{43}	A_{44}
$+/-$	$3 \mathcal{PV} \left(\Omega_i^\phi -1\right)$	0	0	$3 \mathcal{PV} \mathcal{N} $
\times/\div	$3 \mathcal{PV} \Omega_i^\phi $	$9 \mathcal{PQ} \mathcal{PV} $	0	0

(d) $\mathbf{w}(X)$						
	$ \bar{E}_k^\Phi $		$\angle\left(\bar{E}_k^\Phi\right)$		$P_{0,l}^\Phi$	
	$+/-$	\times/\div	$+/-$	\times/\div	$+/-$	\times/\div
\mathbf{w}_1	$6 \mathcal{PQ} (\mathcal{S} -1)$	$18 \mathcal{PQ} \mathcal{S} $	$6 \mathcal{PQ} (\mathcal{S} -1)$	$18 \mathcal{PQ} \mathcal{S} $	$ \Lambda_i^\phi -1$	$ \Lambda_i^\phi +1$
\mathbf{w}_2	$6 \mathcal{PV} (\mathcal{S} -1)$	$18 \mathcal{PV} \mathcal{S} $	$6 \mathcal{PV} (\mathcal{S} -1)$	$18 \mathcal{PV} \mathcal{S} $	0	0
\mathbf{w}_3	$6 \mathcal{PQ} (\mathcal{S} -1)$	$18 \mathcal{PQ} \mathcal{S} $	$6 \mathcal{PQ} (\mathcal{S} -1)$	$18 \mathcal{PQ} \mathcal{S} $	0	0
\mathbf{w}_4	$6 \mathcal{PV} (\mathcal{S} -1)$	$18 \mathcal{PV} \mathcal{S} $	$6 \mathcal{PV} (\mathcal{S} -1)$	$18 \mathcal{PV} \mathcal{S} $	0	0

(e) $\mathbf{w}(X)$ - continued						
	$Q_{0,l}^\Phi$		$P_{0,m}^\Phi$		$ \bar{E}_m^\Phi $	
	$+/-$	\times/\div	$+/-$	\times/\div	$+/-$	\times/\div
\mathbf{w}_1	0	0	0	0	0	$3 \mathcal{PQ} $
\mathbf{w}_2	0	0	$ \Lambda_i^\phi -1$	$ \Lambda_i^\phi +1$	$ \Lambda_i^\phi +6 \mathcal{PV} $	$3 \Lambda_i^\phi +6 \mathcal{PV} +1$
\mathbf{w}_3	$ \Omega_i^\phi -1$	$ \Omega_i^\phi +1$	0	0	0	$3 \mathcal{PQ} $
\mathbf{w}_4	0	0	0	0	$ \Omega_i^\phi +6 \mathcal{PV} $	$3 \Omega_i^\phi +6 \mathcal{PV} +1$

Table 2.2: RMS and max differences between Alg. 1 and first (Jacobian inversion) benchmark

	$P_{0,l}^\Phi$		$Q_{0,l}^\Phi$		$P_{0,m}^\Phi$	
	RMS	Max	RMS	Max	RMS	Max
$\frac{\partial \bar{E}_i^\Phi }{\partial X}$	10^{-9}	10^{-8}	10^{-10}	10^{-8}	10^{-9}	10^{-8}
$\frac{\partial \angle(\bar{E}_i^\Phi)}{\partial X}$	10^{-8}	10^{-7}	10^{-9}	10^{-8}	10^{-8}	10^{-7}

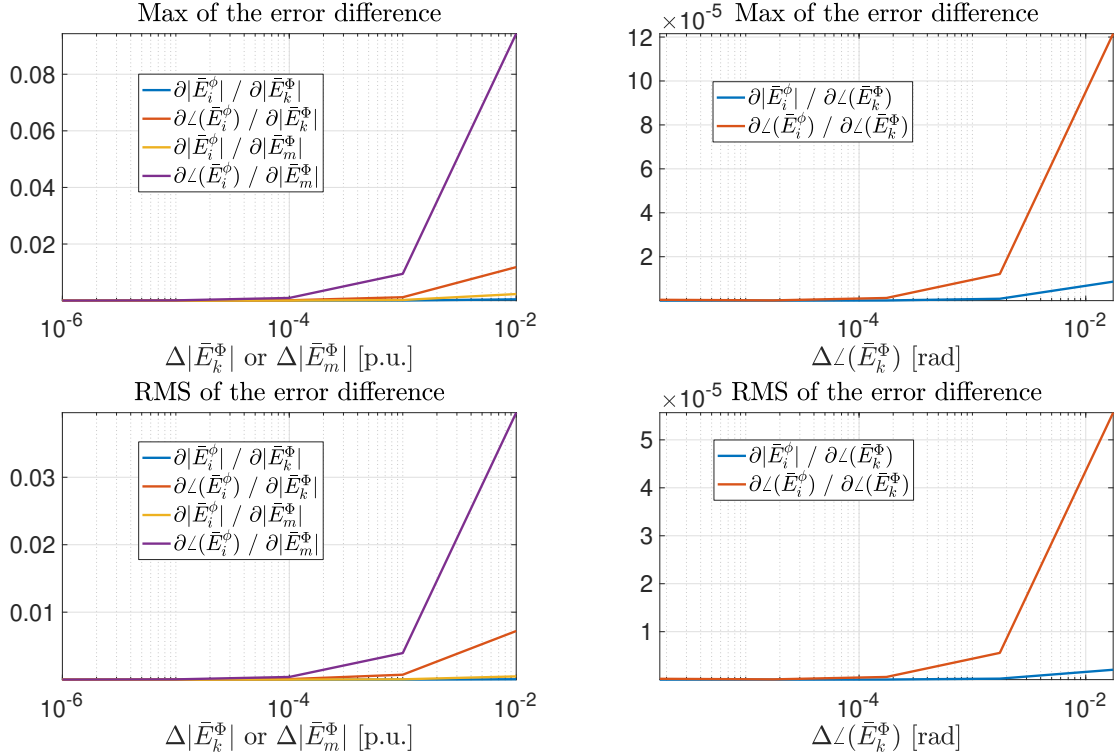


Figure 2.2: RMS and max differences between Alg. 1 and second benchmark

and reactive power injections at PQ nodes, nodal voltage magnitudes and nodal active power injections at PV nodes and nodal voltage magnitudes and phase-angles at slack nodes). The proposed method relies on the knowledge of the grid model and state, algebraic evaluations and the solution of a linear system of equations to determine nodal voltage SCs w.r.t a *user-defined* control variable. In this respect, the user can compute the latter for any selection of control variables. Furthermore, since the grid model is assumed to be known, the user can directly infer other (c.f. section 2.2.4) SCs that can, as previously explained, be used in the context of objective or constraints linearization in power grid control problems (e.g. constrained OPFs). The chapter further includes numerical benchmarks (performed on the IEEE-34 feeder), a complexity analysis and a MATLAB implementation of the proposed method. Results confirmed that the proposed method is accurate, scalable and easy to implement. It is worth noting that further research can be done to investigate the properties of the matrix \mathbf{A} in order to: (i) explore matrix factorization to potentially increase computational speeds, and, (ii)

Chapter 2. Analytical Computation of Power Grids' Sensitivity Coefficients with Voltage-Dependent Injections

find the conditions (if any) that guarantee the uniqueness of the solutions of the linear systems of equations in step 4.ii of Alg. 1 (i.e. conditions that \mathbf{A} is full-rank). Finally, the applicability of the proposed method is showcased in all subsequent contributions of this thesis as all of its OPF linearizations leverage the use of SCs.

3 Resynchronization of Islanded Unbalanced ADNs: Control, Synchrocheck and Experimental Validation

Keywords—Active distribution networks, Island Resynchronization, Synchronism check, Unbalanced Three-Phase Control.

3.1 Introduction & Literature Review

ADNs, e.g. microgrids, are small power grids for electricity distribution hosting dispersed power generation, demand-side management and energy storage devices. ADNs can be controlled and operated in either grid-connected-mode, i.e. connected to an upstream network at the PCC, or islanded-mode, i.e. disconnected from the upstream network. The latter configuration represents a solution to guarantee the continuity of supply when the upstream network is experiencing faults or outages that may propagate downstream [29]. In practice, a reconnection to the upstream-grid is inevitable due to lack of supply and/or sufficient energy storage. The transition between the two modes must be handled carefully. In particular, during a resynchronization process (i.e. islanded to grid-connected), it is important to ensure that the three-phase nodal voltages on both sides (i.e. upstream and downstream) of the PCC are within security bounds in terms of magnitudes, phase-angles and frequencies, before closing the PCC breaker [30]. In other words, ensure nodal voltage phasors synchronisation and alignment needs to be insured before the reconnection actuation. Failing in doing so may provoke large current transients that can damage the ADN's equipment.

As explained in the IEEE std. on distributed resource island systems (e.g. islanded ADNs) [29], the resynchronization process can be done in three ways: *open-transition*, *passive* and *active*. Open-transition resynchronization refers to the complete deenergization of the ADN before reclosing the PCC breaker. Passive resynchronization relies on constantly checking the alignment of the upstream and downstream PCC nodal voltages and only closing the breaker if they are synchronised, without the need to deenergize the local – i.e. downstream – grid. The algorithm used to detect the PCC nodal voltages synchronization is referred to as *synchronism-check* or *synchrocheck* and its function is "*the determination that acceptable voltages exist on the two sides of the circuit breaker, and the phase-angle and frequency difference (slip) between them is within a specified limit for a specified time.*" (c.f. [31] for details on when this functionality is needed and how it is configured). Active resynchronization refers to frameworks with a control mechanism that actively steers the PCC downstream nodal voltages

Chapter 3. Resynchronization of Islanded Unbalanced ADNs: Control, Synchrocheck and Experimental Validation

in order to synchronize them with their upstream counterparts. The latter control mechanism is hereinafter referred to as *PCC-control*. It is interesting to note at this point that, even though *open-transition* resynchronization is the safest option in terms of avoiding current transients, the focus of this thesis and the preferred resynchronization strategy is the *active* method as it guarantees a quick reconnection that, if done properly, does not interrupt the ADN's continuity and deteriorate quality-of-supply.

In the literature, methods tackling the problem of *PCC-control* can be clustered in two categories: *single* and *multiple* device-based frameworks.

Single device methods rely on having a specific device connected in close proximity to the PCC aiming to locally control the downstream PCC nodal voltages. Traditionally that device was a synchronous-generator-based-resource whose speed (i.e. frequency) and nodal voltage magnitudes could be controlled, respectively, through their governor and automatic-voltage-regulators. For instance, in [32], a dedicated DG is proposed to be installed in order to locally align the nodal voltage phase-angles and frequencies at both sides of the PCC. Another example is in [33] where authors propose to control the DG through an adaptive-droop-control-strategy to adjust the frequency, phase-angle and amplitude of the downstream PCC nodal voltages. Alternatively, non-generator-based-dedicated devices used for the resynchronization process were also proposed in the literature. For instance, in [34], authors suggest to connect a controllable capacitor-bank near the PCC in order to locally alter the downstream nodal voltages through reactive-power compensation. Even though such solutions relying on one physical device may work well, the fact that ADNs are not expected to resynchronize frequently, renders this solution costly as *most* dedicated devices may remain idle for long periods where a resynchronization is not needed (e.g. when ADNs are grid-connected).

Multiple device methods rely on controlling one or more resources already present in the ADN in order to steer the PCC downstream nodal voltages. In [35] authors present a PID-based active resynchronization method where a central controller generates set-points for DGs that are assumed to be controlled using their respective droops. In [36] authors present a distributed active synchronization strategy relying on PID-based transfer function control. To ensure better post-resynchronization behavior they consider the ADN's voltage unbalances by extending the typical criteria listed in [30] to include harmonics and nodal voltage negative-sequence limitations. In [37], a distributed PI-controller-based active resynchronization method is proposed where DGs cooperatively communicate with each other to adjust their local droops in order to collectively steer the downstream PCC nodal voltages towards their upstream counterparts. Similarly in [38], authors present a distributed consensus-based phase-angle droop-method for DGs to perform PCC-control. Additionally, it leverages the use of phasor measurement units (PMUs) to get accurate measurements of the phase-angle of different nodal voltages.

In most of the above works the *synchrocheck* functionality is implemented through PLL-based algorithms that measure both nodal voltage phase-angles and frequencies in conjunction with standard nodal voltage magnitude measurements. In the specific literature on *synchrocheck* most works do the same, however, some present alternative methods. For instance, in [39], the authors present a method leveraging low-pass filters, voltage zero-crossing detection coupled with a digitizer to, first, measure nodal voltage magnitudes, phases and frequencies, then, actuate a breaker in case of synchronism. More recently, data driven approaches have been proposed. For instance, in [40], a learning-based classification method is proposed to detect phasor synchronization. Alternatively, in [41], a method is proposed to detect phasor alignment by comparing the correlations of the different analog nodal voltage signals over several periods.

In all the above *PCC-control* frameworks, authors ignore the downstream-ADN's operational, i.e. static and power quality constraints (i.e. branch currents magnitudes, nodal voltages magnitudes, ratios of nodal voltages negative- over positive- sequences and zero- over positive- sequences, all within predefined bounds). Furthermore, even though PMUs are seen to be the future backbone for ADN automation [42], none of these works explicitly use PMU measurements to detect the synchronisation of both upstream and downstream PCC nodal voltage phasors. Indeed, some use PMUs in order to get accurate measurements of nodal voltage phase-angles but it remains unclear whether PMUs are directly used in the *synchronism-check*. As a result, this chapter proposes: (i) a centralised optimal-power-flow (OPF)-based algorithm to control an ADN's resources to steer the PCC downstream nodal voltages towards their upstream non-controllable counterparts, and (ii) an IpDFT-based synchrocheck method that checks the alignment of all three-phases of both upstream and downstream nodal voltages at the PCC. Both contributions are experimentally validated – i.e. an active resynchronization using both contribution was achieved within 1-2 seconds – on the CIGRE low-voltage benchmark microgrid available at the DESL at EPFL, referred to hereinafter as EPFL-DESL microgrid, where the results of the developed synchrocheck are further benchmarked against Schneider Electric's Easergy Micom P143 grid relay [43].

The rest of the chapter is structured as follows. Section 3.2 schematically presents an overview of the chapter's contributions. Section 3.3 contains the details of the proposed PCC-control strategy. Section 3.4 presents the proposed synchrocheck algorithm. Section 3.5 first presents the experimental setup, then, shows the experimental validation results of both proposed contributions. Section 3.6, synthesizes the chapter's findings.

3.2 Schematic Overview

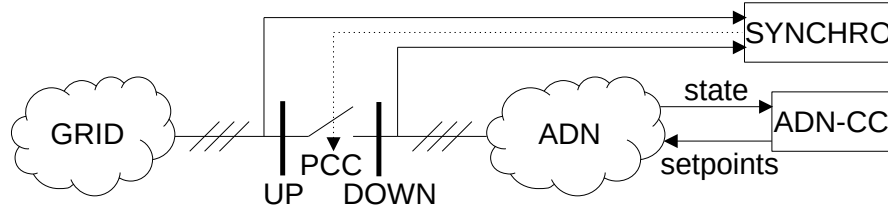


Figure 3.1: Resynchronization schematic overview

As discussed in the IEEE std. for ADN controllers [44], the reconnection of an ADN to its upstream network requires the four steps reported in Tab. 3.1. The proposed active resynchronization framework deals with steps 1 and 2 of Tab. 3.1 while also trying to guarantee smoothness and minimal effort for the fulfilment of steps 3 and 4. Fig. 3.1 schematically demonstrates the contributions of this chapter.

The first contribution is the ADN-CC that aims at steering, over several control timesteps, the downstream nodal voltages at the PCC towards their upstream target counterparts while accounting for the ADN's operational, i.e. static and power-quality, constraints. This entails that the ADN is protected pre- and post-reconnection as invasive actions, e.g. non-essential load-shedding that will need to be restored post-resynchronization, are implicitly minimized. Therefore, the PCC-control algorithm running on the ADN-CC deals with steps 1 & 2 of Table 3.1, but also minimizes said-restorations of step 4. As seen in Fig. 3.1, the ADN-CC needs as an input the ADN's-state, provided, for instance, by a centralised monitoring system (CMS), and, outputs setpoints for the ADN's controllable resources (c.f.

Chapter 3. Resynchronization of Islanded Unbalanced ADNs: Control, Synchrocheck and Experimental Validation

Table 3.1: Reconnection steps proposed by the IEEE std. for ADN controllers

Steps	Action
1 - Initiation	Match PCC nodal voltage phasors within prescribed limits
2 - Returning	Set local controllers and protection devices through appropriate setpoints
3 - Grid-Connected	Close PCC-breaker to reconnect
4 - Normal Operation	Transition to grid-connected control and restore non-critical loads

Sec. 3.3).

The second contribution, denoted as SYNCHRO, consists of a synchrocheck running an IpDFT-based method that extracts the per-phase phase-angle, frequency and magnitude of downstream *and* upstream PCC nodal voltage phasors then compares them, per-phase, vis-a-vis the tolerances presented in [30], to verify and claim synchronization (c.f. Sec. 3.4). As seen in Fig. 3.1, the SYNCHRO block needs as inputs all six nodal voltages at both sides (i.e. DOWN and UP) of the PCC. Its output is a Boolean signal guaranteeing the synchronization of the PCC phasors. The output can be directly coupled with breaker-actuation signals (see Sec. 3.5.2).

3.3 PCC-Control

As previously mentioned, the proposed PCC-control strategy is an OPF that is approximately-solved using a gradient-descent-based algorithm. The idea of the proposed algorithm is to *quickly* and *securely* steer the PCC downstream nodal voltages over several timesteps. In the following, first an overview of the control framework is given, second, the problem formulation is detailed, and, finally the algorithm used to solve the problem is presented.

3.3.1 Control framework: Assumptions and Overview

In this work, we consider that controllable DERs (i.e. loads, sources and storage) in an ADN can be regulated by means of CPCs. Furthermore, we only consider two control-modes for CPCs⁹: i. *grid-forming* mode where the converter's ADN-side-nodal-voltage magnitude and frequency are regulated, and, ii. *grid-following* mode where the converter's ADN-side-nodal-active-and-reactive-power injections are regulated. As a result, no rotating machines are present in the considered ADNs¹⁰. Additionally, in the adopted control framework, as long as the ADN is islanded, only one CPC is assumed to be controlled in grid-forming mode. This entails that the latter plays the role of the slack bus since it sets the voltage at its bus and the frequency of the islanded ADN¹¹. Naturally, this implies that it must be connected to a bidirectional resource able to respond to positive/negative power imbalances

⁹For the interested reader, a thorough definition of the different control-modes of CPCs can be found in [45].

¹⁰The non-presence of rotating-machines in ADNs is becoming more and more common in modern power-grids and, therefore, even though it will become imminently clear that this assumption is not limiting, it remains a practical one.

¹¹We assume that the frequency is the same everywhere in the ADN, which is reasonable given the small size of distribution grids.

and compensate grid-losses (e.g. in general, this device can be an ESS [46]). It is important to note that the unique slack assumption can be relaxed as the proposed PCC-control strategy can easily be extended to multi-slack islanded ADNs by accounting for the slacks grid-forming CPCs' power-sharing-law in the problem constraints (c.f. Sec. 3.3.2 for considered constraints) and by ensuring that the latter all implement the same frequency set-point. At this point, it is important to clarify that, the above-assumptions were set *mostly* to match the experimental setup used throughout this thesis (c.f. section 3.5.1). More specifically, as was explained in the previous chapter, by leveraging SCs, power-flow linearizations can include control variables from any node type. Therefore, even though for the remainder of this chapter the focus is on PQ-nodes and a unique slack node, the reader should put in mind that all node-types and control variables – i.e. nodal active and reactive power injections for PQ-nodes, nodal active power injections and voltage magnitudes for PV-nodes and nodal voltage magnitudes and phase-angles for slack nodes – can, in practice, be directly included in the proposed method.

Next, we assume that the ADN's grid topology, line-parameters and compound admittance matrix are known¹² and that its state (i.e. nodal voltage phasors at every bus), including the upstream¹³ PCC bus, is available in real-time by means of a PMU-aided state-estimation¹⁴ algorithm running on the CMS. The deployed state estimator is assumed to output estimates with better accuracy than those of any *commercial* single measurement device. Furthermore, the use of a state-estimator increases reliability as they are inherently built for redundancy and bad-data rejection, e.g. the state can be accurately estimated even if 20-30% of the input measurements are erroneous (e.g. bad, lost, etc.). The CMS communicates – with a high reporting rate of, e.g., 20 ms – the state to the ADN-CC, which is the device running the PCC-control algorithm that computes explicit set-points to be implemented by the CPCs. If that communication is broken, or if the CMS fails to compute the grid state, the ADN-CC halts its control actions. The control period of the ADN-CC is chosen to be short enough (e.g., 100 ms) such that the downstream nodal voltages at the PCC are steered towards their upstream targets after a few control-steps even if the set-points computed at each control-step are sub-optimal (c.f. Sec. 3.3.3). Note that, the fast reporting rates and control-periods, given as examples above, correspond to the ones of the setup used for the experimental validation (c.f. Sec 3.5.1). However, if these numbers increase due to practical limitations, the proposed methods would still be applicable.

Finally, we consider that each CPC is managed by a dedicated agent (real-time controller) that communicates with the ADN-CC. The ADN-CC sends explicit set-points to be implemented and, oppositely, the CPC's agent advertises the measured active and reactive nodal power injections as well as the updated power limits of the resource it is connected to (e.g. the maximum discharge power of a battery decreases with its SoC). Fig. 3.2 shows an overview of the adopted PCC-control framework, as presented above.

¹²This assumption is only needed for the method used for the considered grid model linearizations (c.f. Sec. 3.3.2). However, as explained in section 2, other *model-less* techniques exist in the literature and can achieve similar linearization performance accuracies without the knowledge of the grid-model.

¹³There are no particular assumptions made on the upstream PCC nodal voltages, however, the state of grounding of both upstream and downstream networks needs to be identical and, naturally, all measurement devices used in the process of inducing the states need to have the same references.

¹⁴This assumption is considered to achieve high-controlling speeds enabled by the accuracy and high-reporting rates of PMUs. However, it is important to note that, other forms of *slower* state-estimators can be used to feed the states to the proposed PCC-control algorithm forcing it to adapt the rapidness of its control decisions but ultimately reach its intended target.

Chapter 3. Resynchronization of Islanded Unbalanced ADNs: Control, Synchrocheck and Experimental Validation

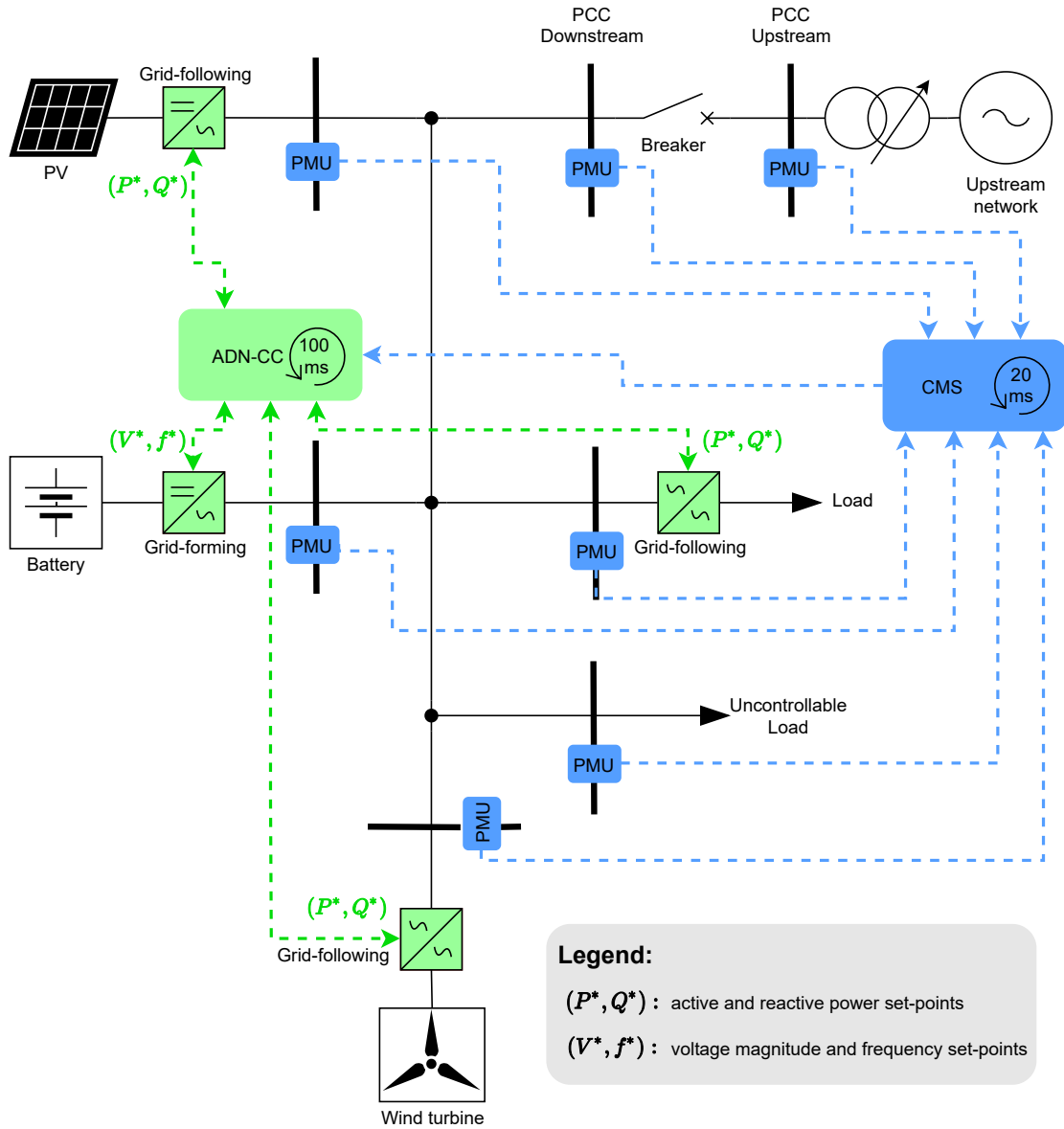


Figure 3.2: Schematic illustration of the proposed PCC-control framework for the resynchronization of islanded ADNs using explicit set-points

3.3.2 Problem formulation

Grid model

As in the previous chapter, we consider three-phase¹⁵ ADN with any grid topologies, i.e. meshed or radial, and $|\mathcal{N}|$ nodes, where \mathcal{N} is the set of all nodes. $\mathcal{Z} \subset \mathcal{PQ}$ is the set of both zero-injection nodes. $\mathcal{R} \subset \mathcal{PQ}$ is the set of nodes where resources are connected. $\mathcal{K} \subset \mathcal{R}$ is the set of PQ-nodes where CPCs in grid-following mode are connected. $\mathcal{S} = \{s\}$ is the set containing the slack node (i.e. the node to which is connected the only considered CPC in grid-forming mode when the ADN is islanded). Without loss of generality¹⁶, we assume that $\mathcal{Z} \cap \mathcal{R} \cap \mathcal{S} = \emptyset$ and $|\mathcal{Z}| + |\mathcal{R}| + |\mathcal{S}| = |\mathcal{N}|$. The set of all electrical branches is denoted by $\mathcal{L} = \{(i, j) \mid i, j \in \mathcal{N}, \tilde{\mathbf{Y}}_{ij} \neq \mathbf{0}\}$, with $\tilde{\mathbf{Y}}_{ij} = \begin{bmatrix} \tilde{\mathbf{Y}}_{ij}^{\phi\psi} \end{bmatrix} \in \mathbb{C}^{3 \times 3}$ being the submatrices composing the compound-block-admittance matrix $\tilde{\mathbf{Y}}$ ([20]).

Even though we are tackling a control problem that involves grid dynamics, we assume that they are *slow enough* to be captured by the time evolution of AC phasors. Therefore, the power equilibrium is still captured by the power flow equations – i.e., the relation between the nodal phase-to-ground voltages $\tilde{\mathbf{E}}_i = [\tilde{E}_i^a, \tilde{E}_i^b, \tilde{E}_i^c]$ and the nodal apparent power injections $\tilde{\mathbf{S}}_i = [\tilde{S}_i^a, \tilde{S}_i^b, \tilde{S}_i^c]$ – given by¹⁷

$$\tilde{\mathbf{S}}_i = \mathbf{P}_i + j\mathbf{Q}_i = \tilde{\mathbf{E}}_i \circ \sum_{j \in \mathcal{N}} \mathbf{Y}_{ij} \tilde{\mathbf{E}}_j \quad \forall i \in \mathcal{N} \quad (3.1)$$

Voltage-dependent loads

Inspired by the previous chapter, the active and reactive nodal power absorptions of voltage-dependent loads are modelled using the generalised model (2.3). For the interested reader, some examples of weights and exponents together with their identification methods can be found in [47].

Note that, as previously mentioned, the control variables of PQ-nodes are the *voltage-independent* active and reactive nodal power injections (i.e. $\mathbf{P}_{0,k}$ and $\mathbf{Q}_{0,k}$, $\forall k \in \mathcal{K}$, meaning the active and reactive nodal power injections at nominal nodal voltages).

Linearization of the LF grid model

In order to achieve a convex OPF that can be solved in real-time, the LF equations are linearized around the estimated states provided by the CMS. The linearization of the power flow equations (3.1) including (2.3), is made possible through the computation of the SCs presented in the last chapter. We recall that SCs are the partial derivatives of electrical quantities (e.g. nodal voltages, branch currents, nodal sequence voltages, slack apparent power) with respect to control variables which are, under the assumptions of this chapter, the active-and-reactive-nodal-power-injection-set-points for grid-following converters and the nodal-voltage-magnitude-and-frequency-set-points for the grid-forming converter. The derivation of the SCs uses the method presented in section 2.3. By leveraging a first-order Taylor expansion, the variations of electrical quantities can be estimated using SCs that are computed using the system's present state (denoted thereafter with the subscript t_0). Note that, even though the

¹⁵Phases are denoted by superscripts a, b and c .

¹⁶*Virtual* branches (i.e. close-to-lossless lines) and buses could be added in case different-mode CPCs or resources share the same node.

¹⁷The operator \circ denotes the Hadamard product and \bar{z} denotes the complex conjugate of the complex number $z = |\bar{z}| \angle (\bar{z})$.

Chapter 3. Resynchronization of Islanded Unbalanced ADNs: Control, Synchrocheck and Experimental Validation

control time-step is short (e.g., 100 ms), the ADN-CC steers the ADN's global state slowly enough such that, as previously explained, the use of phasors and, consequently, SCs are adequate to formulate the constraints of the OP (see Sec. 3.3.2). Finally, since the islanded-ADN's operating frequency is constrained within a tight range (e.g., ± 0.6 Hz) around 50 Hz, we assume that its contribution to the variations of other electrical quantities (e.g. nodal voltage magnitudes) can be neglected without loss of accuracy.

Power converters' dynamics

The implementation of a new control set-point by a CPC is not done instantaneously due to the latter's dynamics. Let us denote by Δx^* the desired variation of the control set-point sent to a CPC at the beginning of the control step, i.e. at $t = t_0$, and by Δx the actual implemented variation at the end of the control step, that is, after the control period Δt . Thus, we can write without loss of generality

$$\Delta x = \beta(t' = \Delta t) \Delta x^* \quad (3.2)$$

where $\beta(t')$ is a function, where $0 \geq t' \leq \Delta t$, that tends to 0 as the control period is shortened and tends to 1 when the latter gets sufficiently long compared to the CPC's time-constant (e.g. slow-rate). The control period being a fixed parameter, we assume that the gain $\beta (= \beta(t' = \Delta t))$ is known a-priori and is, therefore, constant for each control variable.

This is acceptable for all control variables except the frequency as its dynamics are needed for the estimation of the downstream phase-angles at the PCC. Indeed, the latter is based on the integral of the frequency, hence, the function accounting for the frequency evolution during some prediction horizon ΔT_h must be known. In this respect, we model the frequency dynamics, defined over a control period, of the CPC in grid-forming mode as a first-order transfer function, with a step response given by

$$\Delta f(t') = H(t' - L) \left(1 - e^{-r(t' - L)} \right) \Delta f^* \quad (3.3)$$

where $H(t)$ is the Heaviside function, L is the converter's delay and r its slow rate. Consequently, at the end of the prediction horizon, the angle variation due to the frequency evolution ($f(t)$) is:

$$\begin{aligned} \int_{t_0}^{t_0 + \Delta T_h} 2\pi f(t) dt &= \int_{t_0}^{t_0 + \Delta T_h} 2\pi f_{t_0} dt + \int_0^{\Delta T_h} 2\pi \Delta f(t') dt' \\ &= 2\pi f_{t_0} \Delta T_h + \beta_f \Delta f^* \\ \text{with } \beta_f &= 2\pi \left(\Delta T_h - L - \frac{1 - e^{-r(\Delta T_h - L)}}{r} \right) \end{aligned} \quad (3.4)$$

where f_{t_0} is the estimated ADN frequency at the beginning of each control time-step.

Full optimization problem

In this section, we formulate the PCC-control problem in the form of a constrained convex OP. For the sake of readability, we temporarily adopt the notation $|\bar{z}| = z$ where z is the vector of moduli of the complex vector $\bar{z} \in \mathbb{C}^n$, $n \geq 1$. By leveraging on first-order Taylor expansions, we consider implicitly the relation between an approximated quantity $\mathbf{x} \in \mathbb{R}^n$ (or $\bar{\mathbf{x}} \in \mathbb{C}^n$), $n \geq 1$, and its variation $\Delta \mathbf{x}$ ($\Delta \bar{\mathbf{x}}$) from its

initial centroid \mathbf{x}_{t_0} ($\bar{\mathbf{x}}_{t_0}$), that is, $\mathbf{x} = \mathbf{x}_{t_0} + \Delta\mathbf{x}$ ($\bar{\mathbf{x}} = \bar{\mathbf{x}}_{t_0} + \Delta\bar{\mathbf{x}}$). The optimization problem OP1 is given by

$$\begin{aligned} \text{OP1: } \min_{\substack{\Delta\mathbf{P}_{0,k}^*, \Delta\mathbf{Q}_{0,k}^*, \\ \Delta\mathbf{E}_s^*, \Delta f^*}} \quad & \|\mathbf{E}_{down} - \mathbf{E}_{up, t_0}\|^2 + \gamma \|\boldsymbol{\theta}_{down} - \boldsymbol{\theta}_{up}\|^2 \\ \text{subject to} \quad & \end{aligned}$$

$$\mathbf{E}_{i,min} \leq \mathbf{E}_i \leq \mathbf{E}_{i,max} \quad \forall i \in \mathcal{N} \quad (3.5a)$$

$$\mathbf{I}_{ij} \leq \mathbf{I}_{ij,max} \quad \forall (i, j) \in \mathcal{L} \quad (3.5b)$$

$$\mathbf{S}_s \leq \mathbf{S}_{s,max} \quad s \in \mathcal{S} \quad (3.5c)$$

$$\mathbf{P}_{s,min} \leq \mathbf{P}_s \leq \mathbf{P}_{s,max} \quad s \in \mathcal{S} \quad (3.5d)$$

$$\mathbf{Q}_{s,min} \leq \mathbf{Q}_s \leq \mathbf{Q}_{s,max} \quad s \in \mathcal{S} \quad (3.5e)$$

$$\mathbf{E}_i^{zero} \leq \text{tol}_{zero} \mathbf{E}_i^{pos} \quad \forall i \in \mathcal{N} \quad (3.5f)$$

$$\mathbf{E}_i^{neg} \leq \text{tol}_{neg} \mathbf{E}_i^{pos} \quad \forall i \in \mathcal{N} \quad (3.5g)$$

$$\begin{aligned} \left(P_{0,k}^{\phi,*}\right)^2 + \left(Q_{0,k}^{\phi,*}\right)^2 &\leq \left(S_{k,max}^{\phi}\right)^2 \quad \forall k \in \mathcal{K} \\ &\quad \forall \phi \in \{a, b, c\} \end{aligned} \quad (3.6a)$$

$$\mathbf{P}_{k,min} \leq \mathbf{P}_{0,k}^* \leq \mathbf{P}_{k,max} \quad \forall k \in \mathcal{K} \quad (3.6b)$$

$$\mathbf{Q}_{k,min} \leq \mathbf{Q}_{0,k}^* \leq \mathbf{Q}_{k,max} \quad \forall k \in \mathcal{K} \quad (3.6c)$$

$$\mathbf{E}_{s,min} \leq \mathbf{E}_s^* \leq \mathbf{E}_{s,max} \quad s \in \mathcal{S} \quad (3.6d)$$

$$f_{min} \leq f^* \leq f_{max} \quad (3.6e)$$

$$\Delta\mathbf{E}_i = \sum_{k \in \mathcal{K}} \left(\mathbf{C}_{P_{0,k}}^{E_i} \Delta\mathbf{P}_{0,k}^* + \mathbf{C}_{Q_{0,k}}^{E_i} \Delta\mathbf{Q}_{0,k}^* \right) + \mathbf{C}_{E_s}^{E_i} \Delta\mathbf{E}_s^* \quad (3.6f)$$

$$\Delta\mathbf{I}_{ij} = \sum_{k \in \mathcal{K}} \left(\mathbf{C}_{P_{0,k}}^{I_{ij}} \Delta\mathbf{P}_{0,k}^* + \mathbf{C}_{Q_{0,k}}^{I_{ij}} \Delta\mathbf{Q}_{0,k}^* \right) + \mathbf{C}_{E_s}^{I_{ij}} \Delta\mathbf{E}_s^* \quad (3.6g)$$

$$\Delta\mathbf{S}_s = \sum_{k \in \mathcal{K}} \left(\mathbf{C}_{P_{0,k}}^{S_s} \Delta\mathbf{P}_{0,k}^* + \mathbf{C}_{Q_{0,k}}^{S_s} \Delta\mathbf{Q}_{0,k}^* \right) + \mathbf{C}_{E_s}^{S_s} \Delta\mathbf{E}_s^* \quad (3.6h)$$

$$\Delta\bar{\mathbf{S}}_s = \sum_{k \in \mathcal{K}} \left(\bar{\mathbf{C}}_{P_{0,k}}^{\bar{S}_s} \Delta\mathbf{P}_{0,k}^* + \bar{\mathbf{C}}_{Q_{0,k}}^{\bar{S}_s} \Delta\mathbf{Q}_{0,k}^* \right) + \bar{\mathbf{C}}_{E_s}^{\bar{S}_s} \Delta\mathbf{E}_s^* \quad (3.6i)$$

$$\Delta\mathbf{E}_i^{seq} = \sum_{k \in \mathcal{K}} \left(\mathbf{D}_{P_{0,k}}^{E_i} \Delta\mathbf{P}_{0,k}^* + \mathbf{D}_{Q_{0,k}}^{E_i} \Delta\mathbf{Q}_{0,k}^* \right) + \mathbf{D}_{E_s}^{E_i} \Delta\mathbf{E}_s^* \quad (3.6j)$$

$$\Delta\boldsymbol{\varphi} = \sum_{k \in \mathcal{K}} \left(\mathbf{C}_{P_{0,k}}^{\varphi} \Delta\mathbf{P}_{0,k}^* + \mathbf{C}_{Q_{0,k}}^{\varphi} \Delta\mathbf{Q}_{0,k}^* \right) + \mathbf{C}_{E_s}^{\varphi} \Delta\mathbf{E}_s^* \quad (3.6k)$$

$$\Delta\boldsymbol{\theta}_{down} = (2\pi f_{t_0} \Delta T_h + \beta_f \Delta f^*) \mathbf{e} + \Delta\boldsymbol{\varphi} \quad (3.6l)$$

$$\Delta\boldsymbol{\theta}_{up} = (2\pi f_{up, t_0} \Delta T_h) \mathbf{e} \quad (3.6m)$$

The objective function of OP1 is the weighted sum of the ℓ^2 -norms of the deviations between the upstream (\cdot_{up}) and downstream (\cdot_{down}) PCC nodal voltage magnitudes and phase-angles. The tuning parameter $\gamma \in \mathbb{R}$ ensures that both objective terms are comparable (i.e. are of the same nature) enabling it to give more importance either to the nodal voltage magnitude or phase-angle realignment. Note

Chapter 3. Resynchronization of Islanded Unbalanced ADNs: Control, Synchrocheck and Experimental Validation

that, the frequency deviation is not explicitly minimized because it is already accounted for in the phase-angle objective term. Indeed, the phase-angle being the integral of the frequency, if the former is resynchronized continuously for multiple timesteps, then the latter is necessarily resynchronized as well. Therefore, this requires to compute the integrals of the ADN's and upstream frequencies over a prediction horizon that is longer than the control period, i.e. $\Delta T_h > \Delta t$. Additionally, if $\Delta T_h = \Delta t$, OP1 would try to force the PCC nodal-voltage phase-angles to be in sync at the end of the short, e.g. 100 ms, control period. Indeed, this would lead to an aggressive control law with large setpoint oscillations between subsequent control timesteps, which, in turn, would entail (i) LF linearizations inaccuracies, and (ii) faster resource ageing due to over-utilization.

The optimisation variables are the variations of the active and reactive power set-points $\Delta \mathbf{P}_{0,k}^*$, $\Delta \mathbf{Q}_{0,k}^*$ for CPCs in grid-following mode $k \in \mathcal{K}$, and the variations of the voltage magnitude and frequency set-points $\Delta \mathbf{E}_s^*$, Δf^* for the CPC in grid-forming mode.

Constraints (3.5a) to (3.5e) guarantee the static operational constraints of the ADN. Namely, it ensures that the nodal voltage magnitudes $|\bar{\mathbf{E}}_i| = \mathbf{E}_i = [E_i^a, E_i^b, E_i^c]$, $\forall i \in \mathcal{N}$, branch-current magnitudes¹⁸ $|\bar{\mathbf{I}}_{ij}| = \mathbf{I}_{ij} = [I_{ij}^a, I_{ij}^b, I_{ij}^c]$, $\forall (i, j) \in \mathcal{L}$ and slack nodal power injections $\bar{\mathbf{S}}_s = \mathbf{P}_s + j\mathbf{Q}_s = [\bar{S}_s^a, \bar{S}_s^b, \bar{S}_s^c]$ are within bounds as per the instructions of the international standard EN-50160 [48].

Constraints (3.5f) and (3.5g) guarantee the operational power quality constraints by enforcing nodal voltage grid unbalances to be within the bounds stated in [48]¹⁹. Let the vector of voltage sequence components be defined as $\bar{\mathbf{E}}_i^{seq} = [\bar{E}_i^{zero}, \bar{E}_i^{pos}, \bar{E}_i^{neg}]$, $|\bar{E}_i^{zero}| = E_i^{zero}$ denotes the zero-sequence nodal voltage magnitude, $|\bar{E}_i^{pos}| = E_i^{pos}$ the positive-sequence nodal voltage magnitude and $|\bar{E}_i^{neg}| = E_i^{neg}$ the negative-sequence nodal voltage magnitude, of node i . The parameters $tol_{zero}, tol_{neg} \in \mathbb{R}_+$ define, respectively, the maximum acceptable magnitudes of zero- and negative-sequence nodal voltages with respect to the positive-sequence (c.f. [48]).

Constraints (3.6a) to (3.6c) ensure that the active and reactive power setpoints satisfy the power limits – in terms of active, reactive and apparent powers – of all CPCs in grid-following mode. Similarly, constraints (3.6d) and (3.6e) ensure that the voltage magnitude and frequency setpoints given to the CPC in grid-forming mode comply with the converter's and ADN devices' operating limits. Note that, the limits $\mathbf{P}_{k,min}$, $\mathbf{P}_{k,max}$, $\mathbf{Q}_{k,min}$, $\mathbf{Q}_{k,max}$, $\mathbf{E}_{s,min}$ and $\mathbf{E}_{s,max}$ depend on the AC- and DC-side voltages of the CPCs. As a result, as previously explained, these values are updated at every control-step with the values sent by the CPCs to the ADN-CC.

The linearized model of the grid is described by constraints (3.6f) to (3.6k), which are first-order Taylor expansions of grid-quantities around centroids inferred from the states provided by the CMS. As previously explained, the expansions leverage the use of SCs. To simplify notation, the SCs and the dynamics of the power converters (c.f. Sec. 3.3.2) are encapsulated in the matrices $\mathbf{C}_x^y, \mathbf{D}_x^y \in \mathbb{R}^{3 \times 3}$ and

¹⁸For more information about the computation of branch-currents and their associated SCs refer to section 2.2.4

¹⁹Note that, all the above-mentioned ADN operational constraints are listed in the international standard EN-50160 [48] as hard-constraints except the ratio of the zero- over positive-sequence constraint. Indeed, as explained in the standard, verifying the negative- over -positive sequence constraint is enough. However, as known, minimizing the zero-sequence injections leads to lower load unbalances. Therefore, we decided here to add it as a hard constraint, but, in case a user considers this approach as too strict, the hard-constraint can be transformed into a soft one by minimizing the zero-sequence injections in the problem objective.

$\bar{\mathbf{C}}_{\mathbf{x}}^{\bar{\mathbf{y}}} \in \mathbb{C}^{3 \times 3}$. More specifically, the latter are defined as

$$\begin{aligned} \mathbf{C}_{\mathbf{x}}^{\mathbf{y}} &= \left[\frac{\partial y^\phi}{\partial x^\psi} \right]_{t_0} \beta_{k \text{ or } s}^\psi, \mathbf{y} \in \{\mathbf{E}_i, \mathbf{I}_{ij}, \mathbf{S}_s, \boldsymbol{\varphi}\} \\ \bar{\mathbf{C}}_{\mathbf{x}}^{\bar{\mathbf{y}}} &= \left[\frac{\partial \bar{y}^\phi}{\partial x^\psi} \right]_{t_0} \beta_{k \text{ or } s}^\psi, \bar{\mathbf{y}} = \bar{\mathbf{S}}_s \\ \mathbf{D}_{\mathbf{x}}^{\mathbf{y}} &= \left[\frac{\partial y^\sigma}{\partial x^\psi} \right]_{t_0} \beta_{k \text{ or } s}^\psi, \mathbf{y} = \mathbf{E}_i, \forall \sigma \in \{zero, pos, neg\} \end{aligned}$$

where $\phi, \psi \in \{a, b, c\}$, $\mathbf{x} \in \{\mathbf{P}_{0,k}^*, \mathbf{Q}_{0,k}^*, \mathbf{E}_s^*\}$, $k \in \mathcal{K}$, $s \in \mathcal{S}$.

Finally, constraints²⁰ (3.6l) and (3.6m) describe, respectively, the evolution of the phase-angles (i.e. phases a,b & c) at the downstream ($\boldsymbol{\theta}_{dwn}$) and the upstream ($\boldsymbol{\theta}_{up}$) sides of the PCC. The variations of the downstream PCC nodal voltage phase-angles depend on: (i) the integral of the ADN's frequency during the prediction horizon which is given by (3.4) and (ii) control set-points variations other than the frequency (i.e. $\Delta \mathbf{P}_{0,k}^*$, $\Delta \mathbf{Q}_{0,k}^*$, and $\Delta \mathbf{E}_s^*$) which are given by (3.6k) where $\Delta \boldsymbol{\varphi} \in \mathbb{R}^3$. Unlike the downstream case, the model of the upstream grid is assumed to be unknown. As a result, the frequency of the upstream network is considered constant between control timesteps, which means that the variation of the upstream PCC nodal voltage phase-angles $\boldsymbol{\theta}_{up}$ during the prediction horizon (ΔT_h) is computed as the integral of the upstream frequency estimate provided by the CMS.

Decoupling the full optimization problem

Even though OP1 can be solved in real-time, we propose to go one step further by splitting the downstream PCC nodal voltage magnitudes steering and phase-angles/frequency regulation. The reason behind this is that in OP1 the only constraint where the frequency intervenes with other control variables is (3.6l), namely the variation of the downstream PCC nodal voltage phase-angles. In practice, in ADNs with low-power rating devices, a change in frequency will have more effect on nodal voltage phase-angles compared to variations of any other control variables (i.e. nodal active and reactive power injections for PQ-nodes and nodal voltage magnitudes for slack-nodes). Thus, if control setpoints variations other than the frequency do not lead to large downstream-PCC-nodal-voltage-phase-angles' variations, i.e. $\Delta \boldsymbol{\varphi} \ll \beta_f \Delta f^*$, $\forall \phi \in \{a, b, c\}$, OP1 can be reduced to only steer the downstream PCC-nodal-voltage-magnitudes, i.e. all variables and constraints related to the frequency and downstream-PCC-nodal-voltage-phase-angles can be removed from the OP. As a result, the objective is reduced to $\|\mathbf{E}_{POC} - \mathbf{E}_{up,0}\|^2$ and constraints (3.6e), (3.6k), (3.6l) and (3.6m) can be removed. Thus leading to the optimization problem OP2, given by,

$$\text{OP2: } \min_{\substack{\Delta \mathbf{P}_{0,k}^*, \Delta \mathbf{Q}_{0,k}^*, \\ \Delta \mathbf{E}_s^*}} \|\mathbf{E}_{dwn} - \mathbf{E}_{up,0}\|^2$$

subject to

$$\begin{aligned} &(3.5a), (3.5b), (3.5c), (3.5d), (3.5e), (3.5f), (3.5g), (3.6a), \\ &(3.6b), (3.6c), (3.6d), (3.6f), (3.6g), (3.6h), (3.6i), (3.6j) \end{aligned}$$

In parallel to solving OP2, a control law regulating the frequency (FCL2) and, therefore, the nodal voltage phase-angles at the downstream-side of the PCC needs to be derived. We propose an analytical

²⁰The symbol \mathbf{e} denotes the three-dimensional vector of ones, that is, $\mathbf{e} = [1, 1, 1]$.

Chapter 3. Resynchronization of Islanded Unbalanced ADNs: Control, Synchrocheck and Experimental Validation

control-law. More specifically, the idea is to equate the downstream phase-angles with the upstream phase-angles at the end of the prediction horizon (ΔT_h), in other words, the control-law computes the optimal downstream ADN frequency setpoint that would guarantee nodal voltage phase-angles' alignment at both sides of the PCC after the prediction horizon. Thus, starting from

$$\theta_{down,t_0} + \int_{t_0}^{t_0+\Delta T_h} 2\pi f(t) dt = \theta_{up,t_0} + \int_{t_0}^{t_0+\Delta T_h} 2\pi f_{up}(t) dt, \quad (3.8)$$

one can write, using (3.4) and, as previously explained, assuming that the upstream frequency remains constant during the prediction horizon,

$$\theta_{down,t_0} + 2\pi f_{t_0} \Delta T_h + \beta_f \Delta f^* = \theta_{up,t_0} + 2\pi f_{up,t_0} \Delta T_h, \quad (3.9)$$

from which we isolate the frequency set-point variation Δf^* – that will be sent to the CPC in grid-forming mode – leading to (3.10).

$$\Delta f^* = \frac{\theta_{up,t_0} - \theta_{down,t_0} + 2\pi(f_{up,t_0} - f_{t_0})\Delta T_h}{\beta_f} \quad (3.10)$$

Finally, in order to also guarantee constraint (3.6e) for the non-decoupled problem, the proposed decoupled frequency control-law, i.e. FCL2, outputs a coerced set-point f^* . FCL2 is given by (3.11).

$$\text{FCL2: } f^* = \begin{cases} f_{min} & \text{if } f_{t_0} + \Delta f^* < f_{min} \\ f_{max} & \text{if } f_{t_0} + \Delta f^* > f_{max} \\ f_{t_0} + \Delta f^* & \text{otherwise} \end{cases} \quad (3.11)$$

3.3.3 Optimzation problem resolution

As previously explained, thanks to the high update rate of the ADN-CC, computing sub-optimal set-points at each control step is acceptable as it would still succeed at steering, over time, the PCC downstream nodal voltages towards their upstream counterparts (i.e. it does not need to necessarily achieve full-resynchronization in one control step). As a result, solving the convex OP by computing gradient-descent-iterates that converge towards the optimum in a few control timesteps is perfectly fine. In this respect, we propose to solve the OPs (i.e. OP1 and OP2) using a projected-gradient-descent-algorithm coupled with a barrier-method. To illustrate how the gradient descent operates, let us consider the following generic-form-OP:

$$\begin{aligned} \min_{\mathbf{x}} \quad & g_0(\mathbf{x}) \\ \text{s.t.} \quad & g_i(\mathbf{x}) \leq 0, \quad i = 1, \dots, m \\ & \mathbf{Ax} = \mathbf{b} \end{aligned}$$

where, in our case, \mathbf{x} is the vector of control set-points variations (i.e. $[\Delta \mathbf{P}_{0,k}^*, \Delta \mathbf{Q}_{0,k}^*, \Delta \mathbf{E}_s^*, \Delta f^*]$ for OP1 and $[\Delta \mathbf{P}_{0,k}^*, \Delta \mathbf{Q}_{0,k}^*, \Delta \mathbf{E}_s^*]$ for OP2, $\forall k \in \mathcal{K}$ and $s \in \mathcal{S}$), $g_0(\mathbf{x})$ is the objective function, $g_{1\dots m}(\mathbf{x})$ are the inequality constraints (i.e. (3.5a) to (3.6e) for OP1 and (3.5a) to (3.6d) for OP2) and $\mathbf{Ax} = \mathbf{b}$ the linear equality constraints (i.e. (3.6f) to (3.6m) for OP1 and (3.6f) to (3.6j) for OP2). As suggested in [49], to approximately solve the problem, the constrained problem is first relaxed into an unconstrained one. Namely, the inequality constraints ($g_i(\mathbf{x}) \leq 0$) are included in the objective function ($g_0(\mathbf{x})$) by means

of logarithmic barriers $c_i(\mathbf{x}) = -\log(-g_i(\mathbf{x}))$, $\forall i = 1, \dots, m$ and the linear equality constraints ($\mathbf{Ax} = \mathbf{b}$) are injected into $g_0(\mathbf{x})$ and each $c_i(\mathbf{x})$ by means of direct substitution. This leads to,

$$\min_{\mathbf{x}} \quad g_0(\mathbf{x}) + \frac{1}{u} \sum_{i=1}^m c_i(\mathbf{x})$$

where the parameter $u > 0$ tunes the trade-off between optimality and feasibility. The unconstrained OP can be solved using the barrier method as presented in [49]. The barrier method consists in solving a sequence of subproblems, called *centering steps*, while varying u . Each centering step is composed of several gradient steps. For each gradient step, the step-size is chosen by means of backtracking line search²¹. Indeed, each centering step yields a sequence of iterates $\{\mathbf{x}^{(1)}, \mathbf{x}^{(2)}, \dots, \mathbf{x}^{(k)}, \dots\}$ called a *central path*. The last element of every central path is called the *central point*. The subsequent centering step starts at the previous-iteration's central point considering a new objective for the unconstrained OP where u is increased by a factor $\mu > 0$, hence putting more weight on optimality. The first starting point of the first centering and gradient steps is set to $\mathbf{0}$.

In addition to the barrier method, the vector of set-points variations is projected onto the feasible set, $\Gamma = \{\mathbf{x} | g_i(\mathbf{x}) \leq 0, \forall i = 1, \dots, m\}$, at the end of each gradient step. The projection is done to: (i) ensure the *strict* feasibility of each iterate in case some constraints $g_i \leq 0$ are not strictly ensured by the barrier method, and (ii) make sure that the subsequent gradient descent step starts from a feasible point. A Euclidean projection onto the feasible set is computationally as complex as solving the original OPs (i.e. OP1 and OP2). As a result, the Euclidean projection is approximated by the method of alternating projections [50], denoted by $\tilde{\Pi}_{\Gamma}(\mathbf{x})$, that is, the projection of \mathbf{x} onto the feasible set Γ . Note that, each inequality constraint of the optimization problems OP1 and OP2 defines either a half-space or a disc. Hence, the application of the method of alternating projections to both problems only requires the computation of orthogonal projections onto hyperplanes and circles, which can be done analytically.

The proposed method, coupling the barrier method and the method of alternating projections, to solve the generic-form-OP is presented in Alg 2. The parameters n_c and n_g denote the number of centering and gradient steps, respectively. The parameter u_0 is the initial trade-off between optimality and feasibility. We propose to set it to:

$$u_0 = \eta \frac{\|\sum_{i=1}^m \nabla c_i(\mathbf{x}^{(0)})\|}{\|\nabla g_0(\mathbf{x}^{(0)})\|}, \quad 0 < \eta < 1$$

meaning that during the first centering step, feasibility is preferred to optimality, thus steering the first central point near the analytic center of the feasible set.

3.3.4 PCC-Control synthesis and scalability

To summarize, two methods are proposed to steer the downstream-PCC-nodal-voltage phasors towards their upstream counterparts. The first relies on approximately solving OP1 using Alg. 2 and is applicable to ADNs with high-power-rated CPCs in grid-following mode that can induce nodal-voltage-phase-angle variations comparable to ones resulting from frequency variations. The second relies on using FCL2 together with the approximate solving of OP2 using Alg. 2 and is applicable to ADNs where the

²¹ Given the complexity of OP1 and OP2, an exact line-search is not used to compute the optimal step-size for each gradient-step. Indeed, solving an exact line-search would lead to computation times similar to solving the original OPs. For more information about inexact and exact line-search algorithms see [49].

Chapter 3. Resynchronization of Islanded Unbalanced ADNs: Control, Synchrocheck and Experimental Validation

Algorithm 2 Proposed gradient descent method

Inputs: $\mathbf{x}^{(0)} = \mathbf{0}$, g_0 , $c_{1,\dots,m}$, $\Gamma := \bigcap_{i=1}^m g_i$
Parameters: n_c , n_g , $u = u_0$, μ

```

for  $j = 0$  to  $n_c - 1$  do                                     # Loop of centering steps
  for  $k = 0$  to  $n_g - 1$  do                                     # Loop of gradient steps
    Compute  $\nabla g_0(\mathbf{x}^{(k)})$ 
    Compute  $\nabla c_i(\mathbf{x}^{(k)})$ ,  $i = 1, \dots, m$ 
     $\nabla h(\mathbf{x}^{(k)}) \leftarrow \nabla g_0(\mathbf{x}^{(k)}) + \frac{1}{u} \sum_{i=1}^m \nabla c_i(\mathbf{x}^{(k)})$ 
    Compute step size  $\alpha^{(k)}$  using backtracking line search in the direction of  $-\nabla h(\mathbf{x}^{(k)})$ 
     $\mathbf{y}^{(k+1)} \leftarrow \mathbf{x}^{(k)} - \alpha^{(k)} \nabla h(\mathbf{x}^{(k)})$ 
     $\mathbf{x}^{(k+1)} \leftarrow \tilde{\Pi}_{\Gamma}(\mathbf{y}^{(k+1)})$                                # Analytical alternating projs
  end for
   $\mathbf{x}^{(0)} \leftarrow \mathbf{x}^{(n_g)}$ 
   $u \leftarrow \mu u$ 
end for

```

Output: $\mathbf{x}^{(n_g)}$

induced nodal-voltage-phase-angle variations due to set-point-changes at CPCs in grid-following mode are *negligible* compared to ones following frequency changes. Indeed, for a generic ADN, *a-priori* LF computations should be done to determine which method is best-suited. Both proposed methods leverage a security-constrained OPF and the full available resource flexibilities of the islanded ADN. As a result, if said flexibility is enough to steer the downstream PCC nodal voltages, then the *secure* resynchronization of the islanded ADN is guaranteed.

Concerning the scalability of the proposed methods, as the grid size increases – e.g. larger number of power grids’ nodes and more controllable resources – there are three aspects to consider:

1. *Delays in the construction of OP objective and constraints*
2. *Delays in the execution of Alg. 2.*
3. *No delays in the state-estimator and subsequent sending of the state to the ADN-CC:* The state estimator problem remains linear and can be solved efficiently.

The first two aspects might incur some minor delays. However, as long as these delays remain negligible compared to the chosen control timestep the PCC-control will successfully, in time, steer the downstream-PCC-nodal-voltages towards their upstream counterparts.

3.4 Synchrocheck

As previously mentioned, the proposed synchrocheck strategy relies on an IpDFT-based method that extracts the per-phase nodal voltage phasor of both-sides of the PCC then checks whether their differences are within the tolerances given in [30]. If the tolerances are successively respected for a

given amount of time, the phasors are deemed synchronised and the PCC breaker can be closed (i.e. the process of reconnecting the ADN to its upstream-grid is green-lighted). In the following, first the IpDFT-based method for phasor estimation is presented, then, an algorithmic formulation of the full synchrocheck algorithm of the SYNCHRO block (see Fig. 3.1) is presented.

3.4.1 IpDFT-based phasor extraction

The IpDFT-based phasor extraction used in this work is the enhanced-IpDFT (e-IpDFT) method presented in [51]. In the following, we briefly summarize the basics of e-IpDFT. Assuming that an electrical quantity (\hat{l}_p) can be modelled in time by a main tone varying around a rated frequency f_{rate} (i.e. neglecting harmonics, DC offsets and amplitude and/or phase modulations) and is sampled, e.g. by a PMU, with a frequency $f_{sam} = 1/t_{sam}$ over a time window $T_{win} (= D \times t_{sam}$, where D is the number of samples per sampling period t_{sam}) short-enough to assume stationarity, one can write

$$\hat{l}_p(d) = l_p \cos(2d\pi f_p t_{sam} + \phi_p), \quad d \in [0, D-1] \quad (3.12)$$

where l_p , f_p and ϕ_p are, respectively, the amplitude, frequency and phase-angle of the main-tone that will be estimated. Following the assumptions in [51] and assuming the use of the Hanning windowing function with a window sequence $\{w(d)\}$, the DFT of (3.12) can be written as,

$$\hat{\tilde{L}}_p(m) = \frac{1}{W} \sum_{d=0}^{D-1} w(d) \cdot \hat{l}_p(d) \cdot e^{-jm\kappa_d}, \quad m \in [0, D-1] \quad (3.13)$$

where $W = \sum_{d=0}^{D-1} w(d)$ and $\kappa_d = 2\pi d/D$. Following the assumptions in [51], the *true* frequency f_p is situated between two successive DFT bins and can be expressed, as a function of the DFT frequency resolution $1/T_{win}$, as

$$f_p(\delta) = \frac{m_1 + \delta}{T_{win}} \quad (3.14)$$

with $-0.5 < \delta \leq 0.5$ being the deviation of f_p from the frequency with the maximum DFT bin (i.e. $m_1 T_{win}$, where $m_1 \in [0, D-1]$ is the index of the frequency with the largest DFT bin). From there, as explained in [51], with $\psi = \text{sign}(|\hat{\tilde{L}}_p(m_1 + 1)| - |\hat{\tilde{L}}_p(m_1 - 1)|)$, one can directly write,

$$\begin{aligned} l_p(\delta) &= 2|\hat{\tilde{L}}_p(m_1)| \cdot \frac{\pi\delta \cdot (1 - \delta^2)}{\sin(\pi\delta)} \\ \phi_p(\delta) &= \angle(\hat{\tilde{L}}_p(m_1)) - \pi\delta \end{aligned} \quad (3.15)$$

where

$$\delta = \psi \frac{2|\hat{\tilde{L}}_p(m_1 + \psi)| - |\hat{\tilde{L}}_p(m_1)|}{|\hat{\tilde{L}}_p(m_1 + \psi)| + |\hat{\tilde{L}}_p(m_1)|}. \quad (3.16)$$

As explained in [51], from this point, one can go a step further to improve the estimation by trying to remove the spectral interference due to the negative image of the DFT spectrum from the positive

Chapter 3. Resynchronization of Islanded Unbalanced ADNs: Control, Synchrocheck and Experimental Validation

bins-used-in (3.15). To do so, first, the DFT of (3.12) is re-expressed as,

$$\hat{\tilde{L}}_p(m) = \frac{1}{W} [\tilde{V}_p(\delta) \cdot \Upsilon(m - T_{win} f_p(\delta)) + V_p(\delta) \cdot \Upsilon(m + T_{win} f_p(\delta))] \quad (3.17)$$

where $\tilde{V}_p(\delta) = (l_p(\delta)/2j) e^{j\phi_p(\delta)}$, $V_p(\delta)$ its complex conjugate and $\Upsilon(m) = -0.25v(m-1) + 0.5v(m) - 0.25v(m+1)$ being the Fourier transform of the Hanning window, where

$$v(m) = e^{-jm\pi(D-1)/D} \cdot \frac{\sin(m\pi)}{\sin(m\pi/D)}. \quad (3.18)$$

Finally, substituting (3.14) in (3.17) can lead to an improved δ , namely,

$$\tilde{\delta} = \psi \frac{2|\hat{\tilde{L}}_p(m_1 + \psi)| - |\hat{\tilde{L}}_p(m_1)|}{|\hat{\tilde{L}}_p(m_1 + \psi)| + |\hat{\tilde{L}}_p(m_1)|} \quad (3.19)$$

where $\hat{\tilde{L}}_p(m) = \frac{1}{W} \sum_{d=0}^{D-1} w(d) \cdot \hat{l}_p(d) \cdot e^{-jm\pi d} - \frac{1}{W} V_p(\delta) \Upsilon(m + m_1 + \delta)$. Thus, the final-e-IpDFT-estimates for nodal-voltage magnitudes, phase-angle and frequency are respectively given by $l_p(\tilde{\delta})$, $\phi_p(\tilde{\delta})$ and $f_p(\tilde{\delta})$.

Finally, it is worth noting that the process of removing the spectral interference due to the negative image of the DFT formally defined by (3.17)–(3.19), can be performed iteratively to reduce the estimation errors [52]. However, due to timing constraints imposed by the *IEEE std for Synchrophasor Measurements for Power Systems* requirements [53], in this thesis, the process is iterated only once.

3.4.2 Full Synchrocheck algorithm

Alg. 3 summarizes the proposed synchrocheck algorithm running on the SYNCHRO block with the a refresh-period ΔT_{SYN} . Taking as input samples of the three-phase upstream ($\hat{E}_{up}(d)$) and downstream ($\hat{E}_{down}(d)$) PCC nodal voltages, it computes the magnitude, phase-angles and frequencies of all the signals using the e-IpDFT method presented in Sec. 3.4.1 and checks whether, for each phase, the differences between the phasors are within the bounds, i.e. $tol_E = 10\%$, $tol_\phi = 0.34$ rad and $tol_f = 0.3$ Hz, presented in [30]. If all criteria are met, the intra-iteration counter (Count) is updated. If all constraints are satisfied for several *subsequent* timesteps (i.e. Count is larger or equal than an input parameter n_{syn}), the Boolean-flag-output of Alg. 3, i.e. SYNC, is set to 1, otherwise, it is set to 0. Setting SYNC to 1 confirms the synchronization of the inputted three-phase signals which means, in the context of this chapter, that the PCC breaker can be *securely* closed.

3.5 Experimental Validation

3.5.1 Setup

The experimental validation of the proposed PCC-control and synchrocheck algorithms was done on the EPFL-DESL microgrid [54]. Fig. 3.3 shows a schematic depiction of the ADN with its base-values.

Algorithm 3 Proposed synchrocheck

Inputs: Count, $\lambda = 1$, $\hat{E}_{up}(d)$, $\hat{E}_{down}(d)$, $d \in [0, D - 1]$

Parameters: n_{syn} , tol_E , tol_ϕ , tol_f

```

for  $j \in \{a, b, c\}$  do                                     # Loop for each-phase
    Compute  $[E_{up}^j, \phi_{up}^j, f_{up}^j] = \text{eIpDFT}(\hat{E}_{up}^j(d))$ 
    Compute  $[E_{down}^j, \phi_{down}^j, f_{down}^j] = \text{eIpDFT}(\hat{E}_{down}^j(d))$ 
    Compute  $\lambda = \lambda \wedge \left( \left| 1 - \frac{\min\{E_{up}^j, E_{down}^j\}}{\max\{E_{up}^j, E_{down}^j\}} \right| \leq tol_E \right) \wedge$ 
                                      $((|\phi_{up}^j - \phi_{down}^j| \leq tol_\phi)) \wedge$ 
                                      $((|f_{up}^j - f_{down}^j| \leq tol_f))$ 
end for
if  $\lambda == 1$  then Count = Count + 1 else Count = 0 end if
if Count  $\geq n_{syn}$  then SYNC = 1 else SYNC = 0 end if

```

Output: SYNC

The EPFL-DESL microgrid²² is a three-phase replica of the CIGRE benchmark microgrid whose description and branch parameters can be found in [56]. The PMUs of the ADN are all streaming measurements to the phasor-data-concentrator of the CMS (unit that runs the state-estimation-process). The agents in Fig. 3.3 are software-based units that can monitor and explicitly-control the resources they are connected to. Agents also bidirectionally communicate with the ADN-CC through user-datagram-protocol on a wired local-area-network. The SB is composed of a software unit coupled with a CCB – the Compact NSX 250F by Schneider-Electric [57]. The SB runs Alg. 3 and, when it detects that the nodal voltages on both sides of the PCC (i.e. B01 in Fig. 3.3) are synchronised (i.e. SYNC = 1 c.f. Alg. 3), it sends an actuation signal that orders the CCB to close. All software-codes. (i.e. ADN-CC, SYNCHRO, Agents and CMS) were implemented using LabView on CompactRIOs provided by NI²³. Finally, it is worth noting that the communication network of the EPFL-DESL-microgrid is *wired*²⁴, therefore, communication latencies are assumed null²⁵.

3.5.2 Experimental Notes

Due to the relatively low-power rating of the resources in the EPFL-DESL microgrid, the decoupled-gradient-decent method presented in Sec. 3.3.4 is used in this chapter's experimental validation. The later runs in the ADC-CC block. The control-period Δt and the prediction-horizon ΔT_h of the ADN-CC were set to, respectively, 100 ms and 300 ms. The number of centering-steps n_c , number of gradient-steps n_g , the reduction parameter μ and the scaling parameter η of Alg. 2 were set to, respectively, 3, 5, 10 and 0.1. As previously stated, the BLSA used in Alg. 2 is the one presented in [49, pp. 33-35]. The

²²Further details and pictures of the EPFL-DESL microgrid can be found in [55] and Sec. 7.5.

²³More details about the hardware and software infrastructures of the EPFL-DESL microgrid can be found in [54].

²⁴In practice, the resynchronization process requires *wired* communication networks as in any power-systems relaying application. Therefore, the experimental setup is adapted to the tested application (i.e. resynchronization).

²⁵The assumption that communication delays are negligible is recurrent throughout the thesis. In fact, in *wired* networks the communication latencies are usually less than 5 ms while in 4G systems they can go up to 1 s. Therefore, as long as the control periods are sufficiently larger than the latter values the assumption is justified.

Chapter 3. Resynchronization of Islanded Unbalanced ADNs: Control, Synchrocheck and Experimental Validation

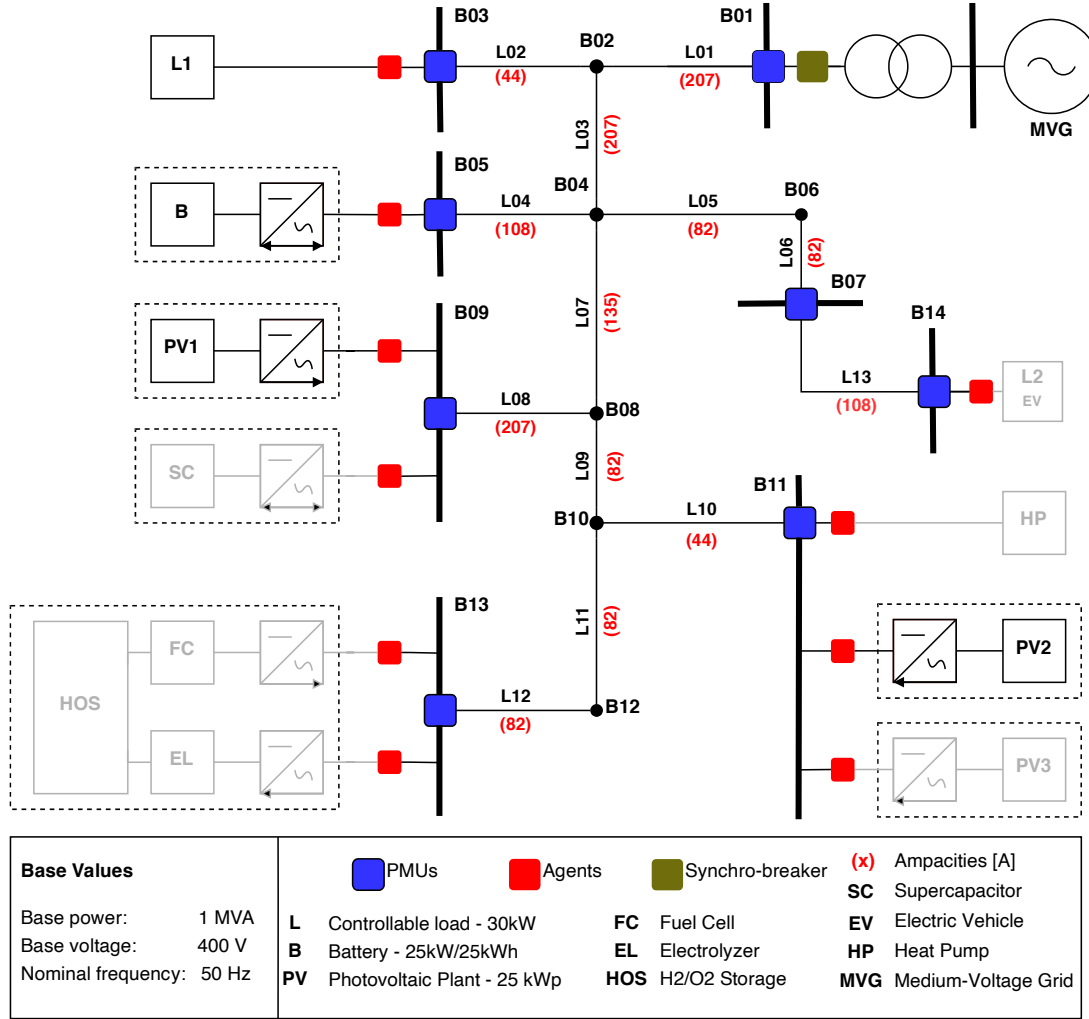


Figure 3.3: EPFL-DESL microgrid schematic diagram. Greyed-out resources were not used in the experiment of Sec. 3.5.3

latter's reduction factor of the step-size, minimum admissible decrease in the objective and maximum number of iterations, are set to, respectively, 0.5, 0.3 and 10. The latter parameters are chosen to ensure that during the BLSA's last iteration the setpoints residues are negligible. Furthermore, in the implemented version of Alg. 2, the alternating-projections method is made more conservative. Indeed, projecting exactly onto a constraint might be problematic since the logarithmic barrier of a binding inequality constraint is undefined. Therefore, numerical issues are avoided by projecting onto constraints with a margin of 1% inwards the feasibility regions of said constraints. Finally, it is worth nothing that due to the ultra-fast internal regulation of the CPCs in the EPFL-DESL microgrid, the converters' output nodal power injections were quasi voltage-independent, i.e. in the model (2.3) one constant is set to 1 while the rest of the constants and exponents are set to 0.

For the SYNCHRO block, a refresh period T_{SYN} of 50 ms is chosen and the number of successive positive tolerances check to declare synchronization n_{syn} is set to 20.

To conclude, in its present form, the EPFL-DESL microgrid is practically a balanced three-phase grid. Indeed, most CPCs are, by design, forced to minimize any injection unbalances through their internal balanced-controllers. As a result, in the ADC-CC block the unbalanced constraints (3.5f)-(3.5g) are always verified. Consequently, in the next section, only the values of nodal-voltages and branch-currents of phase a of the EPFL-DESL microgrid are shown.

3.5.3 Results

The experimental validation performed in this chapters consists in running both the ADN-CC and SYNCHRO blocks on a the EPFL-DESL microgrid depicted in Fig. 3.3. The microgrid²⁶ starts in islanded-mode with a 5kVA/25kWh battery acting as its slack (i.e. CPC in grid-forming-mode), two controllable (i.e. CPCs in grid-following-mode) resources, namely, a balanced-three-phase controllable load (L1) and P-V plant (PV1) with, respectively, 25kW/25kVar and 4kW²⁷/10kVar peak powers, and a non-controllable resource in the form of a P-V plant (PV2) with 3kW²⁷/0kVar peak powers. In order to stress-test the developed PCC-control algorithm, the chosen operational bounds were tighter than the specifications presented in the EN-50160 standard [48]. Namely, $\mathbf{E}_{i,min} = [1, 1, 1]$ p.u., $\mathbf{E}_{i,max} = [1.05, 1.05, 1.05]$ p.u. $\forall i \in \mathcal{N} \setminus \mathcal{S}$ and $\mathbf{I}_{ij,max} = [10, 10, 10]$ A, $\forall (i, j) \in \mathcal{L}$. To further stress-test the proposed algorithms, the initial grid-state is deliberately chosen outside the feasibility set Γ (i.e. violates grid-operational and resource (see *lim* in Figs. 3.4 to 3.6) constraints).

The results of the experiment are shown in Figs. 3.4 to 3.6. At $t = 1$ s the resynchronization process (i.e. ADN-CC) is activated. In a few iterations (~ 300 ms) the grid is forced into the feasibility set as shown in Figs. 3.5 & 3.6. Simultaneously, the realignment of the PCC nodal-voltage phasors is pursued and is achieved at $t = 2.5$ s, i.e. 1.5 s after the beginning of the resynchronization process. The alignment is guaranteed for the rest of the simulation as seen by the green-rectangles in Fig. 3.4. Fig. 3.4 shows that the proposed synchrocheck detects synchronization exactly 1 s after the criteria were met. This is perfectly in-line with our design choice as the SYNCHRO block's refresh period is set to 50 ms and the number of positive-successive-tolerances checks needed for it to detect synchronism is set to 20, i.e. synchronisation should be detected after 1 s of successive tolerance checks. To further benchmark our method, Fig. 3.4 shows that the Micom P143 relay [43] (Schneider SYNCHRO) also detects synchronism at $t = 2.5$ s. It is important to note that, the Micom P143's synchronism check relies on the three-phase balanceness of the upstream-grid and only senses phase-a of the nodal voltage signal of the upstream grid. The developed synchrocheck *does not* rely on such assumption and is therefore more robust against upstream-grid-irregularities (e.g. unbalanceness). Finally, it can be seen that some resource injections (and consequently some branch-currents) keep oscillating after the synchronization (i.e. after the 2.5 s mark), this is due to the gradient-descent-nature of the proposed PCC-control process that is naturally oscillating around a *feasible* equilibrium. Such oscillations can be reduced through the tuning of the parameters of Alg. 2 (e.g. re-tuning the BLSA parameters, the scaling parameter and/or the reduction parameter).

²⁶Note that the resource power limits were reduced on purpose to stress test the proposed PCC-control algorithm.

²⁷The low active peak power of the P-V plants was due to the fact that experiments were held on a cloudy day.

Chapter 3. Resynchronization of Islanded Unbalanced ADNs: Control, Synchrocheck and Experimental Validation

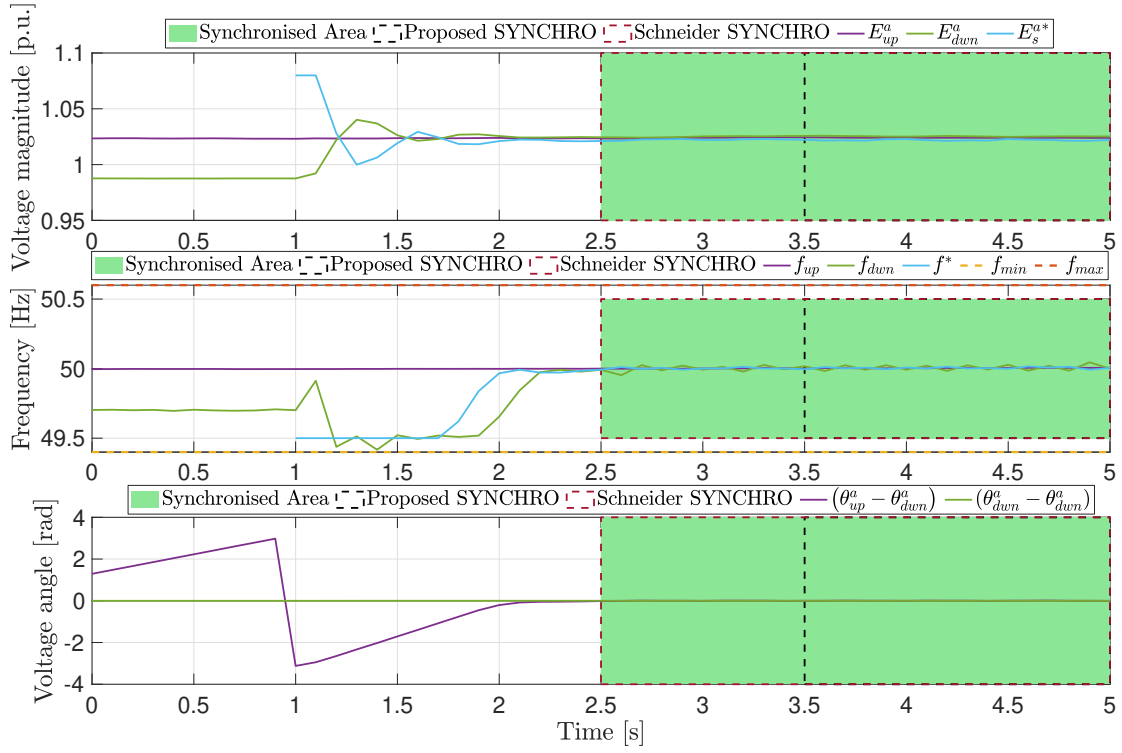


Figure 3.4: PCC voltage magnitudes, phase-angles and frequency

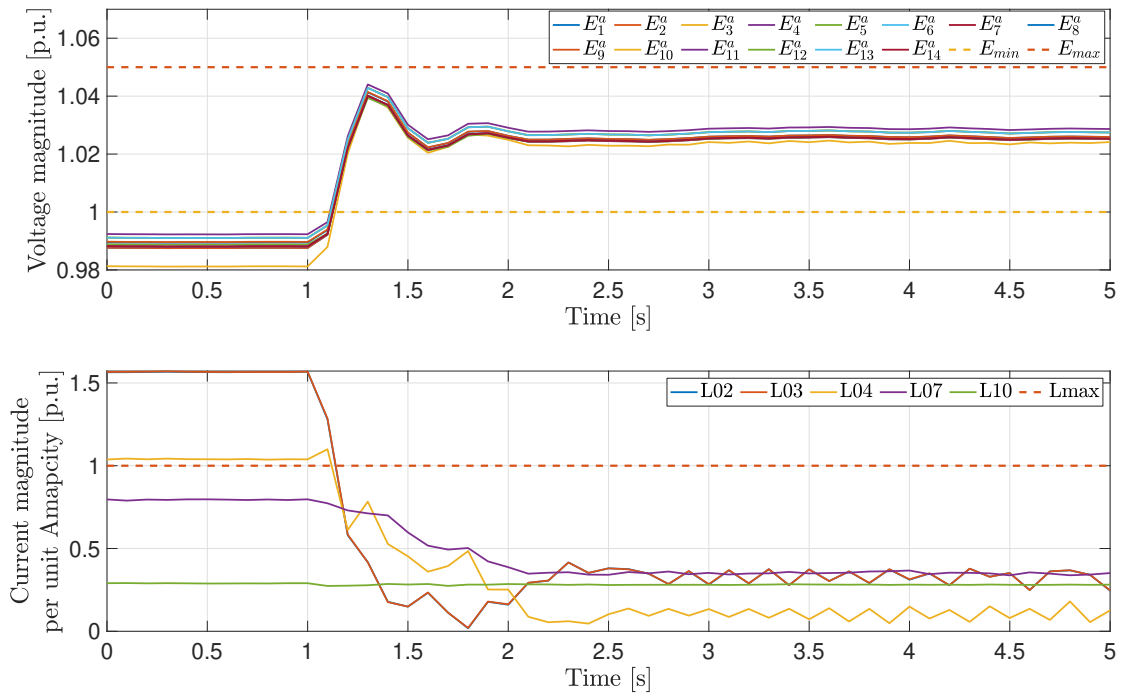


Figure 3.5: Voltage and branch current magnitudes - phase a

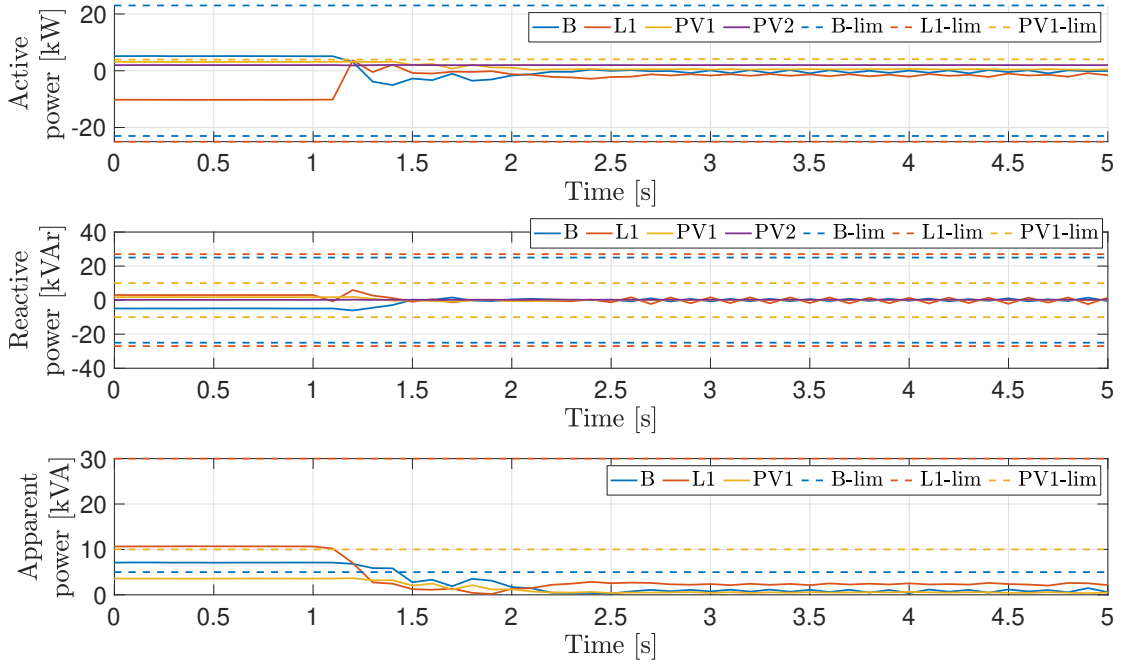


Figure 3.6: Three-phase resources' nodal power injections

3.6 Conclusion

This chapter proposed: (i) a centralised PCC-control in the form of an algorithm that approximately solves a three-phase-unbalanced OPF aiming to steer an ADN's downstream PCC nodal voltages towards their upstream counterparts while guaranteeing ADN and resources' operational constraints, and (ii) a synchrocheck algorithm relying on e-IPDFT phasor extraction to determine whether two three-phase phasors are aligned or not. Both contributions were experimentally validated on the EPFL-DESL microgrid. The proposed synchrocheck was further benchmarked against the Schneider Electric Micom P143 grid-relay with synchronism check [43]. Unlike the proposed methods, the Micom P143 is designed to *only* detect synchronization between the islanded and external grid without any resources' control. Furthermore, it relies on the assumption that the PCC upstream nodal voltages are perfectly balanced. The experimental validation showed that within 1.5 s the resynchronization of PCC nodal-voltages was achieved by the proposed algorithm even if the process was launched when the islanded-microgrid was in an infeasible state. Furthermore, due to its present configuration, the tested microgrid was operating in a balanced three-phase condition, lacking the possibility to showcase the ability of the proposed PCC-control algorithm to deal with unbalances. As a result, following planned three-phase control-enabling-expansions of the EPFL-DESL microgrid, further experimental validations can be carried out to showcase the ability to *securely* resynchronize an ADN to its upstream grid in case both systems operate in unbalanced conditions. Finally, it is worth mentioning that the presented OPF-resolution-algorithm can be used to *efficiently* solve any linearized OPF that has a tractable number of constraints, e.g. After the resynchronization of an ADN, if the objective function of OP1 is modified and the grid-forming CPC is changed to grid-feeding mode, OP1 can be directly used to securely continue controlling the ADN in grid-connected mode. Indeed, this will be shown in the next chapter where it is presented a general ADN control framework that can guarantee robustness w.r.t setpoint implementation uncertainties of heterogeneous resources.

4 Efficient Computation of Admissible Power-Grid-Control-Setpoints for Heterogeneous, Unbalanced, Stochastic & Uncertain Energy Resources

Keywords— Active Distribution Networks, Feasible Network Operation, Power Grid Uncertainties, Resource Uncertainty & Stochasticity, Unbalanced Three-Phase Control, Robust Optimization.

4.1 Preamble on Uncertainty Models & Methods

It is without surprise that, as in many other research domains, decisions to be issued under uncertainties are widely present in the area of power-systems. Uncertainties can (i) arise from multiple factors, (ii) take many forms and (iii) may affect both planning and operational aspects for ADNs and, more in general, for power systems. It is well known that, when considered, uncertainties add computational burden on any control problem when compared to its deterministic counterpart. This entails that, as long as research in optimizing computational efficiencies is advancing, novel and efficient techniques dealing with uncertainties will continue to be developed (e.g. [1, 2]). It is also worth mentioning that in some power-systems control problems, ignoring uncertainties can lead not-only to sub-optimal but also dangerous decisions that could harm the electrical-power-grid. For instance, in minute-scale real-time ADN control problems, if the meteorological-related²⁸ uncertainties are not taken into account through proper forecasting and/or modelling (e.g. [6, 58]) optimal control setpoints may lead to ADN states that violate the grid's operational constraints. In the following, first a non-exhaustive²⁹ list of uncertainty models in power-systems is presented. Then, a recap of different methods, applied in different areas of power-system control, that deal with the latter, is given. Finally, recalling that the focus of this part of the thesis is sub-second control, after the preamble the main contribution of this chapter is presented. The latter consists in algorithms for the real-time control of ADNs accounting for the resources' state-dependent-control-setpoint-implementations-uncertainties.

²⁸Especially in the presence of distributed renewable generating resources.

²⁹For more information, we refer the interested reader to novel survey-reviews that extensively cover the topic of uncertainty in power-grids [1, 2, 59, 60].

4.1.1 Uncertainty Models

As previously mentioned, in power-systems uncertainties can take many forms and can come from multiple sources. In the following we present two families of modeling techniques used in various power-systems problems.

- *Mathematical functional modeling*
 1. *PDFs*. PDFs are widely used to encapsulate uncertain behavior of many quantities in many different domains. In power-systems, time-varying quantities that need probabilistic forecasting, such as meteorological-phenomena (e.g. solar irradiance, temperature, wind profiles etc.), residential active loads, electricity-market-prices and availability of the grid infrastructure, can be modelled with PDFs. Typically, constructing PDFs can be done through clustering and parametric model identification (see, for instance, Sec. 6.2.1 or c.f. [61]) performed on historical data. The complexity of the model depends on the application where it's used.
 2. *Deterministic functions (e.g. set-valued functions)*. Uncertainties can also be encapsulated by mathematical functions. For instance, in many power-systems applications uncertainties are considered to lie within a coverage interval with either parametrized (e.g. [62] or c.f. Sec. 4.3) constant bounds. This, for instance, can lead to the so-called *structured sets* that encapsulate uncertain behaviors of plant-models that were identified with model identification techniques, such as vector-fitting and grey-box identification (e.g. `greyest()` function of MATLAB c.f. [63]). In other applications, uncertainty models can be identified by studying the general physics of the uncertain quantity [64].
- *Data-driven modeling*. These techniques rely on *model-less* parametrized representations of the uncertainty. For instance, historically, ARIMA-based modeling techniques were proposed as a means to forecast residential load punctual values along with their corresponding prediction intervals [65]. The latter techniques work well when trying to forecast injections such as residential loads that present some-kind of repeated, e.g. stationary, behavior. However, with the emergence of novel injections, e.g. EV charging and P-V solar power generation, machine-learning-based modelling techniques emerged as potential solutions to better encapsulate the stochasticity of the latter, e.g. end-users behaviors for EV charging and irradiance evolution for P-V generation, leading to improved uncertainties quantification (e.g. [58]).

4.1.2 How to deal with different uncertainties

In the literature, one can find many works that deal with power-grid uncertainties. The methods used to either (i) directly account for, or (ii) approximate uncertainties depend on the setting of the problems being tackled. In the following, we present three families of control methods that deal with uncertainties in the forms that were previously presented.

Methods relying on chance-constraints

When uncertainty PDFs are known, the use of chance-constrained optimization becomes very relevant. The idea of chance-constrained optimization revolves around solving an uncertain problem by (i) accounting for uncertainties with an average or a conditional-at-risk value of the objective, and (ii)

imposing the satisfaction of the constraints with a given probability (e.g. [2]). Chance-constraints can be analytically reformulated into tractable problems when (i) the constraints or objectives do not contain non-convex functions, and (ii) the uncertainties follow *well-known* PDFs (e.g. uni- or multi-variate normal distributions [66]). In the literature, one can find general techniques to render chance-constrained optimization tractable in case the previous two conditions are not met in the original problem formulation. In the following, a few are presented.

- *Bounds tightening.* For instance, in the scope of transmission grids, in [67] an iterative constraints bound tightening algorithm is proposed to solve the AC OPF problem.
- *Approximate reformulation of the chance-constraints.* In [68], authors assume that uncertainties follow normal distributions to approximately reformulate the AC OPF problem. In [69], authors present a real-time control framework that pre-computes optimal policies accounting for grid uncertainties. In the offline stage, chance constraints are used and approximated using a polynomial chaos expansion to render the problem tractable and solvable.
- *Analytical reformulation of the chance-constraints following a relaxation of non-convex equations, e.g. power-flow equations.* In [70, 71] authors leverage power-flow equations' linearizations and assume that uncertainties follow normal distributions to reformulate the chance-constraints in the proposed OPF problems. In both works the penetration of renewable DGs is accounted for. Unlike in [70], where an iterative procedure is used to solve the problem, in [71] authors further exploit the normality assumption and analytically reformulate the grid operational constraints into tractable linear constraints.

Finally, it is worth noting that many of the presented methods are difficult to apply in real-time control problems, i.e. at sub-second level, due to the complexity of the reformulations or the slow iterative nature of the proposed solution techniques. Furthermore, for the ones that can be applied, usually, the assumptions used to render them tractable are too constraining, i.e. the problem is sometimes over-simplified.

Methods relying on Scenario-based optimization

Scenario-based optimization is a well-known technique that is based on sampling, e.g. from known PDFs, coverage intervals or any parametric data model (e.g. ARIMA or NNs), different *scenarios* of uncertain quantities to transform an intractable problem into a deterministic one. In that respect, if enough scenarios are considered, one could assert that the problem, with a user-defined probability, accounts for the possible realizations of the uncertain quantities within the user-defined coverage. It is clear that, the computational complexity of the considered problem increases with the increase of the number of chosen scenarios. Therefore, scenario-based optimization is non-applicable to problems with sub-second dynamics. However, researchers have extensively explored the topics of (i) the minimum number of scenarios that would adequately account for the uncertainties (e.g. [72]), and (ii) the different sampling techniques to generate scenarios that are rich in information (e.g. [73]), rendering scenario-based optimization applicable in many power-systems problems. In the following, some examples of scenario-based optimization in power-systems are given. They are grouped based on the uncertainty model used to generate the scenarios.

- *Scenarios coming from projected changes in the power-grid.* In the topic of power-system planning, scenario-based optimization is widely used as means to account for potential future

Chapter 4. Efficient Computation of Admissible Power-Grid-Control-Setpoints for Heterogeneous, Unbalanced, Stochastic & Uncertain Energy Resources

realizations and/or configurations of the grid. For instance, in [74], different real-world scenarios are considered to solve an energy-storage planning problem.

- *Scenarios sampled from PDFs.* In the topic of power-system control, scenario-based optimization is used to account for uncontrollable uncertain grid quantities. For instance, in [6] authors experimentally validate a day-ahead optimal DP generator with corrective next-day minute-scale real-time control. In the day-ahead stage, due to the presence of uncontrollable loads and P-V plants in the considered ADN, the proposed OPF leverages scenarios of next-day power injections to render the outputted DP more resilient to next-day unexpected variability. The scenarios are sampled from PDFs that are created from historical nodal power injections data. Another example can be found in [75] where authors solve an uncertain OPF to manage the operation of a microgrid in the presence of renewable generation uncertainty. Each scenario is first generated and given a certain probability. Then, each individual scenario probability and all the joint-probabilities are accounted for in the OPF resolution. Other works, e.g. [76], use scenarios sampled from PDFs in the formulation of power-grid planning problems.
- *Scenarios sampled from coverage intervals.* If a given uncertain quantity is modelled using coverage intervals or set-valued functions, scenarios of the latter can be sampled to transform an intractable problem into a set of deterministic ones.

Finally, it is worth mentioning that scenario-based optimization can *also* be used to render chance-constraints tractable. For instance, in [77], PDF scenario-sampling is used to account for uncertain load injections and render a reserve scheduling problem, formulated using chance-constraints, solvable.

Other Methods

In the power-systems literature, one can find other methods dealing with uncertainties that can be modelled using set-valued functions, e.g. fixed coverage intervals. In the following, two families of methods are presented.

- *Mathematical transformations*, e.g. primal-dual algorithms (c.f. [78]), augment the set of constraints and objective of a given problem. This naturally entails that the problem becomes *computationally complex* due to the increased number of constraints but also the complexity of the added constraints. For instance, if an uncertain quantity lies within an interval where the extremities are affine functions of a certain variable (c.f. Sec. 4.3), using primal-dual transformations would add quadratic constraints to the original problem (e.g. in [79] where the AC OPF problem in transmission grids is tackled). This would drastically increase computation times and render the problem resolution non-compatible with real-time control, e.g. sub-seconds to seconds scale.
- *Online/Offline bound or constraint tightening*, where, as the name suggests, an intractable problem is made tractable by computing tighter constraint bounds that account for the uncertainties (e.g. [80, 81]). The main drawback of such techniques is that the tight-deterministic equivalent of the original problem is usually too conservative with a consequent smaller solution space.

4.2 Introduction

As previously mentioned, with the large-scale integration of DGs, ESSs and novel power-hungry loads in ADNs, many control frameworks tackling the problem of computing, for a given horizon, explicit power setpoints, have been proposed in the literature. As seen, c.f. Sec. 4.1.2, some of the works in the literature go a step further by accounting for grid uncertainties to compute optimal setpoints that are resilient to general stochasticity. There are two aspects to consider when looking into the works that have been already proposed in the literature: *computation speeds* and *uncertainty models*. In terms of computation speeds, other than in [71] where leveraging *simplified* power-flow linearization schemes and assuming normal distributions for the considered uncertainties, most works present in the literature cannot comply with real-time, i.e. sub-seconds to seconds, control timestep resolutions. In terms of uncertainty models, to the best of our knowledge, with the exception of the works presented in [66] and [82], most uncertainty models are not considered functions of the OP's variables.

This raises the question of *how to, in real-time, ensure safe operation, with respect to the operational grid and resource constraints, for all potential realizations of optimally computed setpoints whose implementation-uncertainties are function of the problem variables*. This contribution addresses that question by proposing numerically tractable algorithms. First, the *admissibility test* is proposed. The latter is a computationally-efficient method that asserts whether a collection of precomputed setpoints guarantees the grid and resource operational constraints, and that, due to controller-uncertainty, for all possible implementation-realizations. Indeed, the test accounts for the fact that a resource controller can, in practice, achieve implementation-realizations that are not *exactly* equal to the desired optimal setpoint. To ensure computational efficiency and tractability, the test, respectively, leverages SCs and assumes that all possible implementation-realizations are within a-priori known sets that are function of each setpoint (see Sec. 4.5 for examples). Second, an iterative real-time linearized three-phase-OPF-based algorithm, is proposed. The latter takes as an input a collection of non-admissible setpoints. By leveraging SCs, the second algorithm outputs a collection of admissible setpoints that is closest, in terms of euclidean distance, to its input. Both algorithms are numerically tested on a MATLAB-simulated-version of the IEEE-34 [9] node test distribution feeder augmented with several controllable-resources.

The rest of the chapter is organized as follows. Section 4.3 provides the problem formulation. Section 4.4 presents the two proposed algorithms. Section 4.5 lists different resource models. More specifically, for a few resources, the feasibility regions and uncertainty models are presented. Section 4.6 shows the simulation results of the proposed methods on different networks. Finally, section 4.7 concludes the chapter.

4.3 Problem Formulation

As in the previous chapter, we target three-phase unbalanced power grids whose states are evolving slowly enough such that they can be modelled by phasors. Specifically, we focus on ADNs where the admittance matrix is known and whose power equilibrium is described by the standard AC power-flow equations. Furthermore, we consider that such grids contain controllable resources, usually connected to the grid through *grid-following* CPCs, that can receive active and reactive power setpoints sent from, for instance, a central controller.

Regardless of the control strategy, the main purpose of the proposed algorithms is to ensure that,

Chapter 4. Efficient Computation of Admissible Power-Grid-Control-Setpoints for Heterogeneous, Unbalanced, Stochastic & Uncertain Energy Resources

during a control timestep, the grid state remains *feasible* under all possible setpoint implementation-realizations. In other words, ensure that an optimal vector of issued setpoints would satisfy the grid – static and power-quality, i.e. branch currents magnitudes, nodal voltages magnitudes, ratios of nodal voltages negative and zero over positive sequences, all within predefined bounds – and resources operational constraints for any implementation-realization of a previously computed collection of optimal setpoints. Indeed, the problem becomes non-trivial to solve when, due to uncertainty, unpredictability or implementation inaccuracies of the distributed resources, the actual implementation of the setpoint is different from the requested one. Examples of such uncertainties can be (i) P-V plant converters implementing inaccurate setpoints due to weather-induced variability [58], or, (ii) thermostatically-controlled load controllers' inaccuracies due to restricted ON/OFF operation [83]. Thus, the goal is to ensure, in real-time, that all possible implementation-realizations of the requested setpoints, within a-priori known sets, are feasible, namely the setpoint is *admissible*. More specifically, when an optimal collection of setpoints is computed, the idea is that its admissibility is first verified through the proposed *admissibility test*; if the test fails, the collection is sent to the second contribution of this chapter: an ad-hoc algorithm that finds the closest, in terms of Euclidean-distance, admissible collection of setpoints. A schematic representation of the proposed methods can be found in Fig. 4.1 where both contributions are delimited in the dashed rectangle.

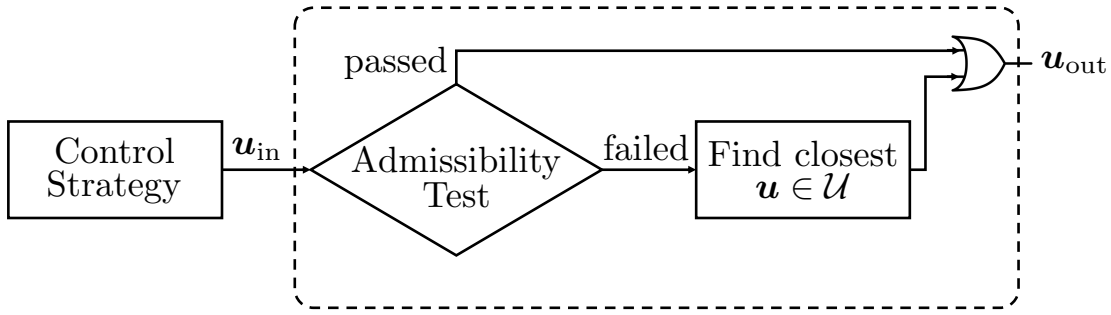


Figure 4.1: Schematic diagram of the problem formulation together with the contributions. \mathbf{u}_{in} and \mathbf{u}_{out} are vectors of setpoints (c.f. (4.1))

As in the previous chapters, we consider grids with $|\mathcal{N}|$ buses. Additionally, we assume (i) to know the grid-model and, (ii) that there's only one slack-node, i.e. $\mathcal{S} = \{s\}$. Furthermore, in this chapter, all nodes where resources are connected are considered as PQ buses³⁰ with interfacing *grid-following* CPCs. As a result, the components of a generic control setpoint $\mathbf{u} = [\mathbf{u}_1, \dots, \mathbf{u}_{|\mathcal{N}|-1}]^T$ are given by (4.1), where $\mathbf{P}_i = [P_i^a, P_i^b, P_i^c]^T$ and $\mathbf{Q}_i = [Q_i^a, Q_i^b, Q_i^c]^T$, are respectively the three-phase³¹ active and reactive power setpoints that are sent to a generic resource $i \in \mathcal{R}$.

$$\mathbf{u}_i = \begin{cases} [u_i^a, u_i^b, u_i^c]^T = [(P_i^a, Q_i^a), (P_i^b, Q_i^b), (P_i^c, Q_i^c)]^T & \forall i \in \mathcal{R} \\ (0, 0) & \text{otherwise, i.e. } \forall i \in \mathcal{I}. \end{cases} \quad (4.1)$$

³⁰As in the previous chapters, these assumptions are not strict as it is straightforward to extend the proposed algorithms to account for either (i) all node-types, or (ii) multi-slack grids (c.f. Sec. 2).

³¹For the sake of notation, all resources are considered controllable on all three phases. However, in case a resource is in practice balanced over the phases, extra constraints are added to guarantee that all per-phase apparent powers are equal. Furthermore, in the remainder of this chapter, nodal power injections' dependency on nodal voltage magnitudes is omitted, without loss of generality (c.f. Sec.2), to alleviate notation.

In practice, a setpoint \mathbf{u}_i can be issued to resource $i \in \mathcal{R}$ only within its available capability set $\mathcal{A}_i = \mathcal{A}_i^a \times \mathcal{A}_i^b \times \mathcal{A}_i^c \subset \mathbb{R}^2 \times \mathbb{R}^2 \times \mathbb{R}^2$, while the resulting deployed, i.e. implemented-realization, power \mathbf{x}_i will lie, for the given short control horizon, with large probability, in the uncertainty set $\mathcal{B}_i(\mathbf{u}_i) = \mathcal{B}_i^a(u_i^a) \times \mathcal{B}_i^b(u_i^b) \times \mathcal{B}_i^c(u_i^c) \subset \mathbb{R}^2 \times \mathbb{R}^2 \times \mathbb{R}^2$ (see 4.5 for examples). In view of (4.1), both sets are regions of the PQ -plane. Zero-injection nodes do not have resources, therefore, neither capability nor uncertainty sets. Finally, the slack node is assumed *uncontrollable* – as it is not a PQ-node – yet, it has a capability set \mathcal{A}_s that encapsulates its physical limits.

In this chapter, capability sets are considered as convex-sets delimited by lines *and/or* semi-circles. The latter polytopes can be expressed as, $\mathcal{A}_m^\phi = \{l \in \mathbb{R}^2 \mid \mathbf{M}_m^\phi l^T \leq \mathbf{b}_m^\phi, \|l\|_2^2 \leq r_m\}$, where the radius r_m , $\mathbf{M}_m^\phi \in \mathbb{M}^{K_m \times 2}$ and $\mathbf{b}_m^\phi \in \mathbb{R}^{K_m}$ describe the set, with $m \in \{\mathcal{R} \cup \mathcal{S}\}$ and $\phi \in \{a, b, c\}$. Furthermore, uncertainty sets $\mathcal{B}_i^\phi(u_i^\phi)$, $i \in \mathcal{R}$ and $\phi \in \{a, b, c\}$, are replaced by their outer rectangular hull $\tilde{\mathcal{B}}_i^\phi(u_i^\phi)$ with, $\tilde{\mathcal{B}}_i^\phi(u_i^\phi) = [P_i^{\phi, \min}(u_i^\phi), P_i^{\phi, \max}(u_i^\phi)] \times [Q_i^{\phi, \min}(u_i^\phi), Q_i^{\phi, \max}(u_i^\phi)]$. Additionally, the functions $P_i^{\phi, \min}(u_i^\phi)$, $P_i^{\phi, \max}(u_i^\phi)$, $Q_i^{\phi, \min}(u_i^\phi)$ and $Q_i^{\phi, \max}(u_i^\phi)$ are assumed to be ATFs. ATFs are functions that can be converted into affine functions in the scope of an OP. Examples of the uncertainty bound functions and ATFs can be found in Sec. 4.5 and Appendix A. Finally, it will become clear that the above approximations are made in order to render the problem solvable in real-time, i.e. sub-second scale (see Sec. 4.4).

We define an admissible control setpoint \mathbf{u} such that, any combination of the resulting implemented powers $\mathbf{x} = [\mathbf{x}_1, \dots, \mathbf{x}_{|\mathcal{N}-1|}]^T$ will guarantee the operational constraints of the power-grid and all the resources. Hence, the *admissible set*, \mathcal{U} , i.e. the set of all admissible setpoints, can be expressed as

$$\mathcal{U} = \left\{ \begin{array}{c} \mathbf{u}, \\ \mathbf{u}_i \in \mathcal{A}_i, i \in \mathcal{R} \end{array} \left| \begin{array}{l} \forall \mathbf{x}: \mathbf{x}_i^\phi \in \tilde{\mathcal{B}}_i^\phi(u_i^\phi), i \in \mathcal{R}, \phi \in \{a, b, c\} \\ \mathbf{x}_i^\phi = (0, 0), i \notin \mathcal{R}, \phi \in \{a, b, c\} \\ \mathbf{x} \in \mathcal{F} \end{array} \right. \right\} \quad (4.2)$$

with,

$$\mathcal{F} = \left\{ \mathbf{x} \left| \begin{array}{ll} \mathbf{E}_i(\mathbf{x}) \leq \mathbf{E}_{i, \max} & \forall i \in \mathcal{N} \\ -\mathbf{E}_i(\mathbf{x}) \leq -\mathbf{E}_{i, \min} & \forall i \in \mathcal{N} \\ \mathbf{I}_{ij}(\mathbf{x}) \leq \mathbf{I}_{ij, \max} & \forall (i, j) \in \mathcal{L} \\ \frac{E_i^{\text{zero}}(\mathbf{x})}{E_i^{\text{pos}}(\mathbf{x})} \leq \text{tol}_{\text{zero}} & \forall i \in \mathcal{N} \\ \frac{E_i^{\text{neg}}(\mathbf{x})}{E_i^{\text{pos}}(\mathbf{x})} \leq \text{tol}_{\text{neg}} & \forall i \in \mathcal{N} \\ \mathbf{S}_s(\mathbf{x}) \leq \mathbf{S}_{s, \max} & \forall s \in \mathcal{S} \\ \mathbf{P}_s(\mathbf{x}) \leq \mathbf{P}_{s, \max} & \forall s \in \mathcal{S} \\ -\mathbf{P}_s(\mathbf{x}) \leq -\mathbf{P}_{s, \min} & \forall s \in \mathcal{S} \\ \mathbf{Q}_s(\mathbf{x}) \leq \mathbf{Q}_{s, \max} & \forall s \in \mathcal{S} \\ -\mathbf{Q}_s(\mathbf{x}) \leq -\mathbf{Q}_{s, \min} & \forall s \in \mathcal{S} \end{array} \right. \right\}$$

Where $\mathbf{E}_i = [E_i^a, E_i^b, E_i^c]$ are the nodal voltage magnitudes of node $i \in \mathcal{N}$, $\mathbf{I}_{ij} = [I_{ij}^a, I_{ij}^b, I_{ij}^c]$ are the branch current magnitudes of branch $(i, j) \in \mathcal{L}$, E_i^{pos} , E_i^{neg} and E_i^{zero} are, respectively, the positive, negative and zero sequence components of the nodal voltage magnitudes of node $i \in \mathcal{N}$ and $\mathbf{S}_s = [S_s^a, S_s^b, S_s^c]$, $\mathbf{P}_s = [P_s^a, P_s^b, P_s^c]$ and $\mathbf{Q}_s = [Q_s^a, Q_s^b, Q_s^c]$, are, respectively, the magnitudes of the nodal apparent, active and reactive power injections at the slack node s . Note that, the definition of \mathcal{F} assumes the solution of a full AC LF and does not explicitly include the solvability of the latter in

Chapter 4. Efficient Computation of Admissible Power-Grid-Control-Setpoints for Heterogeneous, Unbalanced, Stochastic & Uncertain Energy Resources

its definition. Indeed, this is because it is assumed that the grid is in a state that guarantees the solvability of the power-flow equations³². Furthermore, the parenthesis (\mathbf{x}) here means the electrical quantity resulting from the implementation of the vector of power setpoints \mathbf{x} . Hereinafter, \mathbf{x} in (4.2) is parametrized as $\mathbf{x}(\mathbf{t}, \mathbf{u})$ where $\mathbf{t} = \{(a_i^\phi, s_i^\phi)\}, \forall i \in \mathcal{R}$ is a collection of coordinates ($0 \leq a_i^\phi, s_i^\phi \leq 1$) such that,

$$x_i^\phi(t_i^\phi, u_i^\phi) = \begin{cases} \left(a_i^\phi P_i^{\phi, \max}(u_i^\phi) + (1 - a_i^\phi) P_i^{\phi, \min}(u_i^\phi), \right. \\ \left. s_i^\phi Q_i^{\phi, \max}(u_i^\phi) + (1 - s_i^\phi) Q_i^{\phi, \min}(u_i^\phi) \right) & \forall i \in \mathcal{R}, \forall \phi \in \{a, b, c\} \\ (0, 0) & \text{otherwise, i.e. } \forall i \in \mathcal{I}. \end{cases} \quad (4.3)$$

The proposed methods, presented in the next section, make use of the parametrization in (4.3).

Finally, with the definition in (4.2), the problem of computing the closest admissible control setpoint (see Fig. 4.1) can be, formally written as

$$\mathbf{u}_{\text{out}} = \underset{\mathbf{u} \in \mathcal{U}}{\operatorname{argmin}} d(\mathbf{u}, \mathbf{u}_{\text{in}}), \quad (4.4)$$

with $d(\cdot)$ being a measure of distance, e.g. the Euclidean one.

4.4 Method

The definition of \mathcal{U} in (4.2) implies infinite *non-linear* constraints due to power-flow equations and the uncountable nature of some of the uncertainty sets $\mathcal{B}_i^\phi(u_i^\phi)$ (see 4.5 for examples) leading to an intractable problem. In the following, the proposed methods deal exactly with that by rendering the problem tractable and efficiently solvable.

4.4.1 Admissibility Test

Alg. 4 is proposed to check the admissibility of a setpoint \mathbf{u} . The latter asserts whether or not *all* possible implementation-realizations of an inputted setpoint, if deployed, would satisfy the grid operational constraints. More specifically, first, the function $\mathbf{T} = \text{computeCoordinates}(\tilde{\mathbf{Y}}, \mathbf{u}, \mathcal{R})$ aims at finding, for each LHS quantity of the inequalities defining \mathcal{F} , an implementation power that, if deployed, will result in the largest value of the LHS quantity. As previously explained, implementation-realizations lie within pre-defined set-valued functions that depend on the setpoint. Formally, $\text{computeCoordinates}$ aims at finding $\mathbf{x}(\hat{\mathbf{t}}(\mathbf{u}), \mathbf{u})$, such that

$$\hat{\Gamma}(\mathbf{u}) = \Gamma\left(\mathbf{x}\left(\hat{\mathbf{t}}(\mathbf{u}), \mathbf{u}\right)\right) = \max_{\mathbf{x} \in \prod_{\substack{m \in \mathcal{R} \\ \phi \in \{a, b, c\}}} \mathcal{B}_m^\phi(u_m^\phi)} \Gamma(\mathbf{x}) \quad (4.5)$$

³²This justification is similar to the one in the concluding arguments of Sec. 2.3.

Algorithm 4 Admissibility Test, i.e. $\mathbf{u} \in \mathcal{U}$?**Inputs:** $\mathbf{u}, \mathcal{N}, \mathcal{S}, \mathcal{L}, \mathcal{R}$ **Parameters:** $\tilde{\mathbf{Y}}, E_{i,max}, E_{i,min}, I_{ij,max}, S_{s,max}, P_{s,max}, Q_{s,max}, P_{s,min}, Q_{s,min}, tol_{zero} \& tol_{neg}$

ADM = 1;

 $T = \text{computeCoordinates}(\tilde{\mathbf{Y}}, \mathbf{u}, \mathcal{R});$ **for** $i \in \mathcal{N}$ **do**

Loop over all nodes

ADM = ADM & CheckVoltUp($\tilde{\mathbf{Y}}, \mathbf{u}, T, i, E_{i,max}$);ADM = ADM & CheckVoltLow($\tilde{\mathbf{Y}}, \mathbf{u}, T, i, E_{i,min}$);ADM = ADM & CheckVoltZero($\tilde{\mathbf{Y}}, \mathbf{u}, T, i, tol_{zero}$);ADM = ADM & CheckVoltNeg($\tilde{\mathbf{Y}}, \mathbf{u}, T, i, tol_{neg}$);**end for****for** $s \in \mathcal{S}$ **do**

Loop over all slack nodes

ADM = ADM & CheckSlackS($\tilde{\mathbf{Y}}, \mathbf{u}, T, s, S_{s,max}$);ADM = ADM & CheckSlackPUp($\tilde{\mathbf{Y}}, \mathbf{u}, T, s, P_{s,max}$);ADM = ADM & CheckSlackPLow($\tilde{\mathbf{Y}}, \mathbf{u}, T, s, P_{s,min}$);ADM = ADM & CheckSlackQUp($\tilde{\mathbf{Y}}, \mathbf{u}, T, s, Q_{s,max}$);ADM = ADM & CheckSlackQLow($\tilde{\mathbf{Y}}, \mathbf{u}, T, s, Q_{s,min}$);**end for****for** $(i, j) \in \mathcal{L}$ **do**

Loop over all branches

ADM = ADM & CheckCurrentUp($\tilde{\mathbf{Y}}, \mathbf{u}, T, (i, j), I_{ij}^{max}$);**end for****Output:** ADM

where $\Gamma \in \{ "E_i^\phi", "-E_i^\phi", "I_{ij}^\phi", "\frac{E_i^{\phi,zero}}{E_i^{\phi,pos}}", "\frac{E_i^{\phi,neg}}{E_i^{\phi,pos}}", "S_s^\phi", "P_s^\phi", "-P_s^\phi", "Q_s^\phi", "-Q_s^\phi" \}$.

In that way, the definition of \mathcal{U} in (4.2) becomes tractable, as, for instance, verifying

$$\hat{E}_i^\phi(\mathbf{u}) = \max_{\substack{\mathbf{x} \in \prod_{m \in \mathcal{R}} \tilde{\mathcal{B}}_m^\phi(u_m^\phi) \\ \phi \in \{a,b,c\}}} E_i^\phi(\mathbf{x}) \leq E_{i,max}^\phi, \quad (4.6)$$

where $\Gamma = "E_i^\phi"$ (c.f. (4.5)), entails that \mathbf{u} is admissible with respect to the upper-bound-nodal-voltage-magnitude operational constraint at node i and phase ϕ .

The output of `computeCoordinates` is, therefore, a collection of coordinates $\{t^{\hat{\Gamma}}(\mathbf{u})\}$ stored in \mathbf{T} . The latter are computed leveraging the SCs of the LHS quantities of \mathcal{F} w.r.t the chosen control variables, i.e. nodal active and reactive power injections at resource nodes. As previously defined, SCs are partial derivatives that, for a given known state and using the grid-model, can be analytically computed (c.f. Sec. 2.3). Hereinafter, SCs will be denoted by $K_\Psi^\Gamma(\mathbf{x})$, reading the partial derivative of Γ w.r.t. $\Psi = \{ "P_m^\phi", "Q_m^\phi" \}$ – i.e. nodal active and reactive power injections at node $m \in \mathcal{R}$ and phase $\phi \in \{a,b,c\}$ – computed using the state resulting from the deployment of \mathbf{x} .

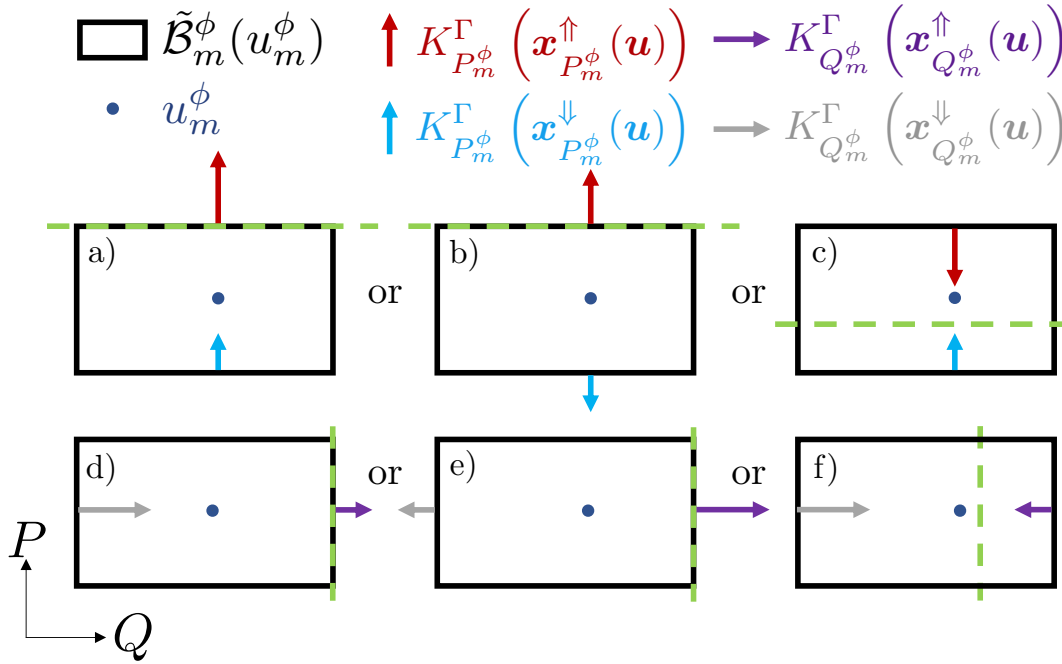


Figure 4.2: Illustration of all possible cases for $t_m^{\phi, \hat{\Gamma}}(\mathbf{u})$ for a resource $m \in \mathcal{R}$ and a given phase $\phi \in \{a, b, c\}$ when the control setpoint is \mathbf{u} . The green dashed line represent the active (top) or reactive (bottom) power levels at which the resulting Γ will be the highest.

The idea behind the computation of each $t^{\hat{\Gamma}}(\mathbf{u})$ is illustrated in Fig. 4.2. The computation is done coordinate-by-coordinate, i.e. active and reactive nodal power injections in the PQ-plane. Namely, to compute $t_m^{\phi, \hat{\Gamma}}(\mathbf{u}) = (a_m^{\phi, \hat{\Gamma}}(\mathbf{u}), s_m^{\phi, \hat{\Gamma}}(\mathbf{u}))$ $m \in \mathcal{R}$ (see ((4.3)), we propose two steps.

1. First, for a given quantity Γ , the SCs at the edges of the uncertainty sets $\tilde{\mathcal{B}}_m^\phi(u_m^\phi)$, $\forall m \in \mathcal{R}$ and $\phi \in$

$\{a, b, c\}$ are derived. Indeed, for a given uncertainty set, four, i.e. two upper $K_{\Psi}^{\Gamma}(\mathbf{x}_{\Psi}^{\uparrow}(\mathbf{u}))$ and two lower $K_{\Psi}^{\Gamma}(\mathbf{x}_{\Psi}^{\downarrow}(\mathbf{u}))$ derivatives, are computed by varying only *one* component, i.e. P (c.f. Fig. 4.2 a)-c)) or Q (c.f. Fig. 4.2 d)-f)), at a time. In other words, the latter SCs are computed at the state resulting from the deployment of a vector of nodal power injections $-\mathbf{x}_{\Psi}^{\uparrow}(\mathbf{u})$ with $\uparrow \in \{\uparrow, \downarrow\}$ – that is equal to the inputted \mathbf{u} except at resource m and phase ϕ . This can formally be expressed as

$$x_{i,\Psi}^{\phi,\uparrow}(\mathbf{u}) = \begin{cases} u_i^{\phi} & \forall i \neq m \\ \Lambda(u_i^{\phi}, \Psi, \uparrow) & i = m \end{cases}, \quad (4.7)$$

with

$$\Lambda(u_i^{\phi}, \Psi, \uparrow) = \begin{cases} (P_i^{\phi, \min}(u_i^{\phi}), Q_i^{\phi}) & \Psi = P_m^{\phi} \text{ \& } \uparrow = \downarrow \\ (P_i^{\phi, \max}(u_i^{\phi}), Q_i^{\phi}) & \Psi = P_m^{\phi} \text{ \& } \uparrow = \uparrow \\ (P_i^{\phi}, Q_i^{\phi, \min}(u_i^{\phi})) & \Psi = Q_m^{\phi} \text{ \& } \uparrow = \downarrow \\ (P_i^{\phi}, Q_i^{\phi, \max}(u_i^{\phi})) & \Psi = Q_m^{\phi} \text{ \& } \uparrow = \uparrow \end{cases} \quad (4.8)$$

2. Second, each $a_m^{\phi, \hat{\Gamma}}(\mathbf{u})$ is obtained by comparing the two SCs w.r.t active power (i.e. $K_{\Psi}^{\Gamma}(\mathbf{x}_{P_m^{\phi}}^{\uparrow}(\mathbf{u}))$) and, similarly, the two SCs w.r.t. reactive power (i.e. $K_{\Psi}^{\Gamma}(\mathbf{x}_{Q_m^{\phi}}^{\uparrow}(\mathbf{u}))$) are compared to obtain $s_m^{\phi, \hat{\Gamma}}(\mathbf{u})$. This is done for all resources $m \in \mathcal{R}$, over all phases $\phi \in \{a, b, c\}$ and for all quantities Γ , i.e. " E_i^{ϕ} ", " $-E_i^{\phi}$ ", " I_{ij}^{ϕ} ", " $\frac{E_i^{\phi, zero}}{E_i^{\phi, pos}}$ ", " $\frac{E_i^{\phi, neg}}{E_i^{\phi, pos}}$ ", " S_s^{ϕ} ", " P_s^{ϕ} ", " $-P_s^{\phi}$ ", " Q_s^{ϕ} ", " $-Q_s^{\phi}$ ".

In the following, for all the scenarios i.e. all the cases illustrated in Fig. 4.2, the computation of the coordinates $t_m^{\phi, \hat{\Gamma}}(\mathbf{u}) = (a_m^{\phi, \hat{\Gamma}}(\mathbf{u}), s_m^{\phi, \hat{\Gamma}}(\mathbf{u}))$ are presented.

- *Case a)*, both derivatives with respect to P_m^{ϕ} have the same sign. Therefore, assuming that they will not change signs inside the uncertainty set (c.f. Remark 1) along the P axis, i.e. $Q = Q_m^{\phi}$, the direction of the SC in the P coordinate will lead to $\hat{\Gamma}(\mathbf{u})$. The lowest magnitude will arise following the opposite direction. Consequently, $a_m^{\phi, \hat{\Gamma}}(\mathbf{u}) = 1$. Equivalently, if both derivatives point in the decreasing direction, $a_m^{\phi, \hat{\Gamma}}(\mathbf{u}) = 0$.
- *Case b)*, the derivatives with respect to P_m^{ϕ} have opposite signs. As illustrated in Fig. 4.2, the minimizer of Γ will be achieved if the active power is between the active power limits of the uncertainty set. Namely, assuming that there is only one local minimum along the $Q = Q_m^{\phi}$ axis, it is reasonable to assume that it is closer to the lower active power limit seeing that $|K_{P_m^{\phi}}^{\Gamma}(\mathbf{x}_{P_m^{\phi}}^{\downarrow}(\mathbf{u}))| < |K_{P_m^{\phi}}^{\Gamma}(\mathbf{x}_{P_m^{\phi}}^{\uparrow}(\mathbf{u}))|$.

For the maximizer, which is the quantity of interest, as in case a), $\hat{\Gamma}(\mathbf{u})$ will be achieved if the implementation follows the direction of the SCs. Since the SCs are of opposite signs, the active power can be set to either the maximum or minimum uncertainty set limit. To deal with this, we propose to set the active power to the limit with the highest product of active power and SC. Namely,

$$a_m^{\phi, \hat{\Gamma}}(\mathbf{u}) = \begin{cases} 1 & \text{if } \begin{matrix} P_m^{\phi, \max}(u_m^{\phi})|K_{P_m^{\phi}}^{\Gamma}(\mathbf{x}_{P_m^{\phi}}^{\uparrow}(\mathbf{u}))| \geq \\ P_m^{\phi, \min}(u_m^{\phi})|K_{P_m^{\phi}}^{\Gamma}(\mathbf{x}_{P_m^{\phi}}^{\downarrow}(\mathbf{u}))| \end{matrix} \\ 0 & \text{otherwise.} \end{cases} \quad (4.9)$$

- *Case c)*, in this case the logic is inverted compared to case b). Meaning, the minimizer will be achieved at one of the uncertainty set limits while the maximizer will lie somewhere in

Chapter 4. Efficient Computation of Admissible Power-Grid-Control-Setpoints for Heterogeneous, Unbalanced, Stochastic & Uncertain Energy Resources

between the active power uncertainty limits along the along the $Q = Q_m^\phi$. Consequently, we propose to set the coordinate using ratios of the SCs. Specifically, in view of the definition of the coordinates in (4.3), taking the ratio of the lower-bound SC over the sum of the two others will lead to the desired effect. Formally, this leads to,

$$a_m^{\phi, \hat{\Gamma}}(\mathbf{u}) = \frac{|K_{P_m^\phi}^\Gamma(\mathbf{x}_{P_m^\phi}^\downarrow(\mathbf{u}))|}{|K_{P_m^\phi}^\Gamma(\mathbf{x}_{P_m^\phi}^\downarrow(\mathbf{u}))| + |K_{P_m^\phi}^\Gamma(\mathbf{x}_{P_m^\phi}^\uparrow(\mathbf{u}))|}. \quad (4.10)$$

It can be seen in (4.10) that if $|K_{P_m^\phi}^\Gamma(\mathbf{x}_{P_m^\phi}^\downarrow(\mathbf{u}))| < |K_{P_m^\phi}^\Gamma(\mathbf{x}_{P_m^\phi}^\uparrow(\mathbf{u}))|$ the computed coordinate will be closer to the lower-bound of the uncertainty set, while, if $|K_{P_m^\phi}^\Gamma(\mathbf{x}_{P_m^\phi}^\downarrow(\mathbf{u}))| > |K_{P_m^\phi}^\Gamma(\mathbf{x}_{P_m^\phi}^\uparrow(\mathbf{u}))|$, the coordinate will be closer to the upper-bound.

- Cases d), e) & f), follow respectively the same logic as for cases a), b) & c), but this time referring to the nodal reactive power injections (i.e. the horizontal axis in Fig. 4.2). All the equations used to set $s_m^{\phi, \hat{\Gamma}}(\mathbf{u})$ are the same as the ones used for $a_m^{\phi, \hat{\Gamma}}(\mathbf{u})$ with the except that all P_m^ϕ are replaced by Q_m^ϕ .

Remark 1. The solutions proposed to deal with the cases presented in Fig. 4.2 leveraged one main assumption. Indeed, what was presented assumes, indirectly, the monotonicity of the SCs. In other words, it assumes a continuous behavior with, at most, one local extreme within the uncertainty set. This assumption is, in general, true as long as the uncertainty sets are not too large, which is what was assumed in this chapter to remove the need of explicitly adding the solvability of the power-flow equations in \mathcal{F} (see Sec. 4.3).

Furthermore, as explained in [82], under the same assumptions of this chapter, the maximizers of most of the LHS quantities of the inequalities of \mathcal{F} are achieved at the edges of the power uncertainty sets when rectangular sets are considered. This means that, with a large probability, cases a) and d) of Fig. 4.2 will be predominant. The analysis done in [82] assumes single-phase grids, however, when looking at the formal proofs and intuitions given in the paper, one can easily conclude that the results are extendable to three-phase grids, particularly to the power-quality constraints. The latter was extensively verified through numerical simulations.

Alg. 4 then loops around all the nodes and branches of the grid to assert admissibility. More specifically, each `Check` function first uses the corresponding maximizer coordinates ($\mathbf{t}^{\hat{\Gamma}}(\mathbf{u})$) stored in \mathbf{T} and the admittance matrix to compute the maximum value, i.e. $\hat{\Gamma}(\mathbf{u})$ (see (4.5), of each constraint defining \mathcal{F} . Then, using the inputted tolerances, each function outputs a Boolean asserting whether or not the maximizer violates the constraint. Tab. 4.1 summarises the processes and outputs of each function. Finally, through the Boolean AND operator (&), Alg. 4 ensures that only if *all* constraints are within bounds, then $\text{ADM} = \text{TRUE}$ (or $\mathbf{u} \in \mathcal{U}$).

4.4.2 Computation of the closest admissible setpoint

Optimization Problem

Alg. 5 is proposed to solve (4.4). The latter iteratively and *approximately* solves quadratic OPs with *linear* constraints and outputs the closest, in terms of Euclidean distance, admissible setpoint to its input \mathbf{u}_{in} .

Table 4.1: Summary of processes and outputs of the Check functions of Alg. 4

Function	Processes	Output
CheckVoltUp	i. Infer $\mathbf{x} \left(\mathbf{t}^{\hat{E}_i^\phi}(\mathbf{u}), \mathbf{u} \right)$ using $\mathbf{t}^{\hat{E}_i^\phi}(\mathbf{u}) \in T$; ii. Perform LF computations to get $\hat{E}_i^\phi(\mathbf{u})$; iii. Compute $\hat{E}_i^\phi(\mathbf{u}) \leq E_{i,max}^\phi$.	TRUE, if $\hat{E}_i^\phi(\mathbf{u}) \leq E_{i,max}^\phi$ FALSE, otherwise
CheckVoltLow	i. Infer $\mathbf{x} \left(\mathbf{t}^{-\hat{E}_i^\phi}(\mathbf{u}), \mathbf{u} \right)$ using $\mathbf{t}^{-\hat{E}_i^\phi}(\mathbf{u}) \in T$; ii. Perform LF computations to get $-\hat{E}_i^\phi(\mathbf{u})$; iii. Compute $-\hat{E}_i^\phi(\mathbf{u}) \leq -E_{i,min}^\phi$.	TRUE, if $-\hat{E}_i^\phi(\mathbf{u}) \leq -E_{i,min}^\phi$ FALSE, otherwise
CheckVoltZero	i. Infer $\mathbf{x} \left(\mathbf{t}^{\frac{E_i^{\hat{zero}}}{E_i^{pos}}}(\mathbf{u}), \mathbf{u} \right)$ using $\mathbf{t}^{\frac{E_i^{\hat{zero}}}{E_i^{pos}}}(\mathbf{u}) \in T$; ii. Perform LF computations to get $\frac{E_i^{\hat{zero}}}{E_i^{pos}}$; iii. Compute $\frac{E_i^{\hat{zero}}}{E_i^{pos}} \leq tol_{zero}$.	TRUE, if $\frac{E_i^{\hat{zero}}}{E_i^{pos}} \leq tol_{zero}$ FALSE, otherwise
CheckVoltNeg	i. Infer $\mathbf{x} \left(\mathbf{t}^{\frac{E_i^{\hat{neg}}}{E_i^{pos}}}(\mathbf{u}), \mathbf{u} \right)$ using $\mathbf{t}^{\frac{E_i^{\hat{neg}}}{E_i^{pos}}}(\mathbf{u}) \in T$; ii. Perform LF computations to get $\frac{E_i^{\hat{neg}}}{E_i^{pos}}$; iii. Compute $\frac{E_i^{\hat{neg}}}{E_i^{pos}} \leq tol_{neg}$.	TRUE, if $\frac{E_i^{\hat{neg}}}{E_i^{pos}} \leq tol_{neg}$ FALSE, otherwise
CheckSlackS	i. Infer $\mathbf{x} \left(\mathbf{t}^{\hat{S}_s^\phi}(\mathbf{u}), \mathbf{u} \right)$ using $\mathbf{t}^{\hat{S}_s^\phi}(\mathbf{u}) \in T$; ii. Perform LF computations to get $\hat{S}_s^\phi(\mathbf{u})$; iii. Compute $\hat{S}_s^\phi(\mathbf{u}) \leq S_{s,max}^\phi$.	TRUE, if $\hat{S}_s^\phi(\mathbf{u}) \leq S_{s,max}^\phi$ FALSE, otherwise
CheckSlackPUp	i. Infer $\mathbf{x} \left(\mathbf{t}^{\hat{P}_s^\phi}(\mathbf{u}), \mathbf{u} \right)$ using $\mathbf{t}^{\hat{P}_s^\phi}(\mathbf{u}) \in T$; ii. Perform LF computations to get $\hat{P}_s^\phi(\mathbf{u})$; iii. Compute $\hat{P}_s^\phi(\mathbf{u}) \leq P_{s,max}^\phi$.	TRUE, if $\hat{P}_s^\phi(\mathbf{u}) \leq P_{s,max}^\phi$ FALSE, otherwise
CheckSlackPLow	i. Infer $\mathbf{x} \left(\mathbf{t}^{-\hat{P}_s^\phi}(\mathbf{u}), \mathbf{u} \right)$ using $\mathbf{t}^{-\hat{P}_s^\phi}(\mathbf{u}) \in T$; ii. Perform LF computations to get $-\hat{P}_s^\phi(\mathbf{u})$; iii. Compute $-\hat{P}_s^\phi(\mathbf{u}) \leq -P_{s,min}^\phi$.	TRUE, if $-\hat{P}_s^\phi(\mathbf{u}) \leq -P_{s,min}^\phi$ FALSE, otherwise
CheckSlackQUp	i. Infer $\mathbf{x} \left(\mathbf{t}^{\hat{Q}_s^\phi}(\mathbf{u}), \mathbf{u} \right)$ using $\mathbf{t}^{\hat{Q}_s^\phi}(\mathbf{u}) \in T$; ii. Perform LF computations to get $\hat{Q}_s^\phi(\mathbf{u})$; iii. Compute $\hat{Q}_s^\phi(\mathbf{u}) \leq Q_{s,max}^\phi$.	TRUE, if $\hat{Q}_s^\phi(\mathbf{u}) \leq Q_{s,max}^\phi$ FALSE, otherwise
CheckSlackQLow	i. Infer $\mathbf{x} \left(\mathbf{t}^{-\hat{Q}_s^\phi}(\mathbf{u}), \mathbf{u} \right)$ using $\mathbf{t}^{-\hat{Q}_s^\phi}(\mathbf{u}) \in T$; ii. Perform LF computations to get $-\hat{Q}_s^\phi(\mathbf{u})$; iii. Compute $-\hat{Q}_s^\phi(\mathbf{u}) \leq -Q_{s,min}^\phi$.	TRUE, if $-\hat{Q}_s^\phi(\mathbf{u}) \leq -Q_{s,min}^\phi$ FALSE, otherwise
CheckCurrentUp	i. Infer $\mathbf{x} \left(\mathbf{t}^{\hat{I}_{ij}^\phi}(\mathbf{u}), \mathbf{u} \right)$ using $\mathbf{t}^{\hat{I}_{ij}^\phi}(\mathbf{u}) \in T$; ii. Perform LF computations to get $\hat{I}_{ij}^\phi(\mathbf{u})$; iii. Compute $\hat{I}_{ij}^\phi(\mathbf{u}) \leq I_{ij,max}^\phi$.	TRUE, if $\hat{I}_{ij}^\phi(\mathbf{u}) \leq I_{ij,max}^\phi$ FALSE, otherwise

Chapter 4. Efficient Computation of Admissible Power-Grid-Control-Setpoints for Heterogeneous, Unbalanced, Stochastic & Uncertain Energy Resources

Algorithm 5 Find the closest admissible setpoint to \mathbf{u}_{in}

```

1: Inputs:  $\bar{\mathbf{Y}}, \mathbf{u}_{\text{in}}, \mathcal{N}, \mathcal{S}, \mathcal{L}, \mathcal{R}, [\mathcal{A}_m^\phi]_{\forall m \in \mathcal{R}, \forall \phi \in \{a,b,c\}}$  and  $[\tilde{\mathcal{B}}_m^\phi]_{\forall m \in \mathcal{R}, \forall \phi \in \{a,b,c\}}$ 
2: Parameters:  $\bar{\mathbf{Y}}, E_{i,\max}, E_{i,\min}, I_{ij,\max}, S_{s,\max}, P_{s,\max}, Q_{s,\max}, P_{s,\min}, Q_{s,\min},$ 
3:  $tol_{\text{zero}}, \& tol_{\text{neg}}$ 
4: Variable:  $\mathbf{u}$ 

5: repeat
6:    $\mathbf{T}_{\text{in}} = \text{computeCoordinates}(\mathbf{u}_{\text{in}}, \mathcal{R});$ 
7:   for  $i \in \mathcal{N}$  do                                     # Loop over all nodes
8:      $\text{OP.CreateVoltUpConstraint}(\bar{\mathbf{Y}}, \mathbf{u}, \mathbf{T}_{\text{in}}, i, \mathbf{u}_{\text{in}}, [\tilde{\mathcal{B}}_m^\phi]_{\forall m \in \mathcal{R}, \forall \phi \in \{a,b,c\}}, E_{i,\max});$ 
9:      $\text{OP.CreateVoltLowConstraint}(\bar{\mathbf{Y}}, \mathbf{u}, \mathbf{T}_{\text{in}}, i, \mathbf{u}_{\text{in}}, [\tilde{\mathcal{B}}_m^\phi]_{\forall m \in \mathcal{R}, \forall \phi \in \{a,b,c\}}, E_{i,\min});$ 
10:     $\text{OP.CreateVoltZeroConstraint}(\bar{\mathbf{Y}}, \mathbf{u}, \mathbf{T}_{\text{in}}, i, \mathbf{u}_{\text{in}}, [\tilde{\mathcal{B}}_m^\phi]_{\forall m \in \mathcal{R}, \forall \phi \in \{a,b,c\}}, tol_{\text{zero}});$ 
11:     $\text{OP.CreateVoltNegConstraint}(\bar{\mathbf{Y}}, \mathbf{u}, \mathbf{T}_{\text{in}}, i, \mathbf{u}_{\text{in}}, [\tilde{\mathcal{B}}_m^\phi]_{\forall m \in \mathcal{R}, \forall \phi \in \{a,b,c\}}, tol_{\text{neg}});$ 
12:   end for
13:   for  $s \in \mathcal{S}$  do                                     # Loop over all slack nodes
14:      $\text{OP.CreateSlackSConstraint}(\bar{\mathbf{Y}}, \mathbf{u}, \mathbf{T}_{\text{in}}, \mathbf{u}_{\text{in}}, s, [\tilde{\mathcal{B}}_m^\phi]_{\forall m \in \mathcal{R}, \forall \phi \in \{a,b,c\}}, S_{s,\max});$ 
15:      $\text{OP.CreateSlackPUpConstraint}(\bar{\mathbf{Y}}, \mathbf{u}, \mathbf{T}_{\text{in}}, \mathbf{u}_{\text{in}}, s, [\tilde{\mathcal{B}}_m^\phi]_{\forall m \in \mathcal{R}, \forall \phi \in \{a,b,c\}}, P_{s,\max});$ 
16:      $\text{OP.CreateSlackPLowConstraint}(\bar{\mathbf{Y}}, \mathbf{u}, \mathbf{T}_{\text{in}}, \mathbf{u}_{\text{in}}, s, [\tilde{\mathcal{B}}_m^\phi]_{\forall m \in \mathcal{R}, \forall \phi \in \{a,b,c\}}, P_{s,\min});$ 
17:      $\text{OP.CreateSlackQUpConstraint}(\bar{\mathbf{Y}}, \mathbf{u}, \mathbf{T}_{\text{in}}, \mathbf{u}_{\text{in}}, s, [\tilde{\mathcal{B}}_m^\phi]_{\forall m \in \mathcal{R}, \forall \phi \in \{a,b,c\}}, Q_{s,\max});$ 
18:      $\text{OP.CreateSlackQLowConstraint}(\bar{\mathbf{Y}}, \mathbf{u}, \mathbf{T}_{\text{in}}, \mathbf{u}_{\text{in}}, s, [\tilde{\mathcal{B}}_m^\phi]_{\forall m \in \mathcal{R}, \forall \phi \in \{a,b,c\}}, Q_{s,\min});$ 
19:   end for
20:   for  $(i, j) \in \mathcal{L}$  do                                     # Loop over all branches
21:      $\text{CreateCurrentUpConstraint}(\bar{\mathbf{Y}}, \mathbf{u}, \mathbf{T}_{\text{in}}, \mathbf{u}_{\text{in}}, (i, j), [\tilde{\mathcal{B}}_m^\phi]_{\forall m \in \mathcal{R}, \forall \phi \in \{a,b,c\}}, I_{ij}^{\max});$ 
22:   end for
23:    $\text{OP.CreateDeployConstraints}(\mathbf{u}, \mathcal{R}, [\mathcal{A}_m^\phi]_{\forall m \in \mathcal{R}, \forall \phi \in \{a,b,c\}})$ 
24:    $\text{OP.CreateObjective}(\mathbf{u}, \mathbf{u}_{\text{in}});$ 
25:    $\mathbf{u}_{\text{out}} = \text{OP.solve}(\mathbf{u});$ 
26:    $\mathbf{u}_{\text{in}} = \mathbf{u}_{\text{out}};$ 
27: until  $\mathbf{u}_{\text{out}} \in \mathcal{U}$  using Alg. 4

28: Output:  $\mathbf{u}_{\text{out}}$ 

```

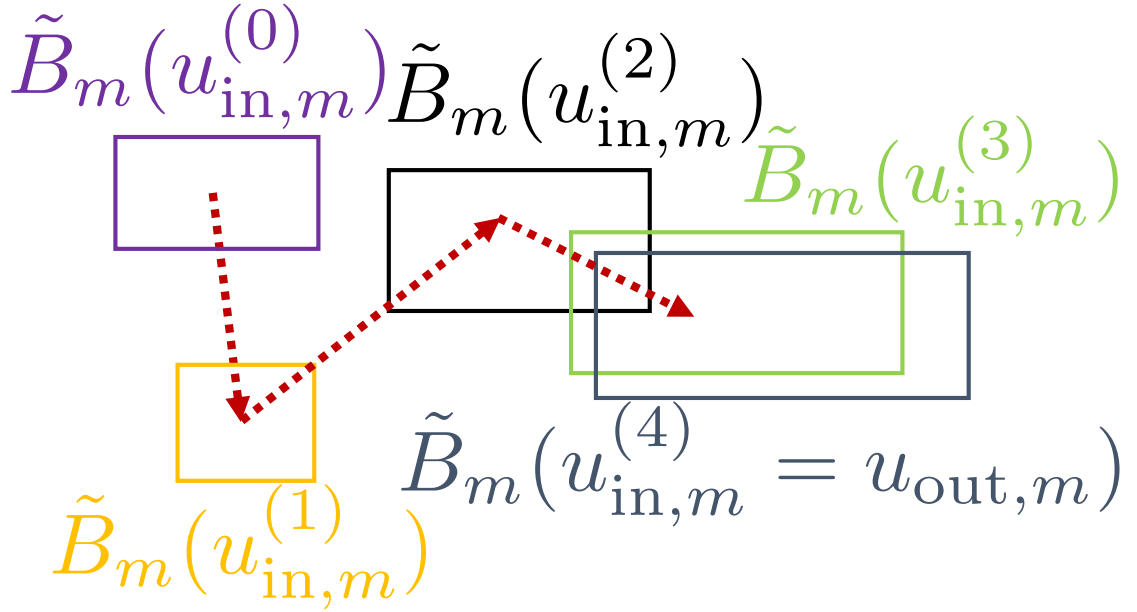


Figure 4.3: Qualitative illustration of convergence of Alg. 5 for a generic resource m and phase ϕ (superscript omitted to alleviate notation).

As in Alg. 4, in each iteration, to enable the creation of the constraints, first, `computeCoordinates` is called. Using the loop's inputted setpoint \mathbf{u}_{in} , the latter computes the maximizer coordinates and stores them in \mathbf{T}_{in} . Note that, since at this point of each iteration, i.e. before solving the OP, the algorithm does not have access to \mathbf{u}_{out} and its corresponding SCs, it is assumed that $\mathbf{t}^{\hat{\Gamma}}(\mathbf{u}_{in}) \cong \mathbf{t}^{\hat{\Gamma}}(\mathbf{u})$, where \mathbf{u} is the OP variable. This is a reasonable assumption because as the iterations progress, by construction, \mathbf{u}_{out} will get closer to the updated \mathbf{u}_{in} . As a result, the variable and inputted setpoints will tend to have similar SCs (see Fig. 4.3 for illustration). This intuition is numerically verified in the simulations section.

In every iteration, after `computeCoordinates` is called, several functions are called to create the OP constraints and objective. First, `CreateVoltUpConstraint` adds the constraint that guarantees that $E_i^\phi(\mathbf{x}(\mathbf{t}, \mathbf{u})) \leq E_{i,max}^\phi$ for all the deployable powers $\mathbf{x}(\mathbf{t}, \mathbf{u})$ in (4.2). As explained in Section 4.4.1, this function uses $\mathbf{t}^{\hat{E}_i^\phi}(\mathbf{u}_{in})$, to create only one constraint per nodal voltage at node $i \in \mathcal{N}$ and phase $\phi \in \{a, b, c\}$. As explained in Sec. 1.1, we target the real-time control of ADNs. As a result, the OP constraints encapsulating the grid operational constraints are *linearized* by leveraging first-order Taylor approximations similar to ones used in Sec. 3.3.2. More specifically, `CreateVoltUpConstraint` expresses each nodal voltage $\hat{E}_i^\phi(\mathbf{u})$ as a linear function of $\hat{E}_i^\phi(\mathbf{u}_{in})$ ³³, the power injections $\mathbf{x}(\mathbf{t}^{\hat{E}_i^\phi}(\mathbf{u}_{in}), \mathbf{u}_{in})$ and the unknown power injections $\mathbf{x}(\mathbf{t}^{\hat{E}_i^\phi}(\mathbf{u}_{in}), \mathbf{u})$, as shown in (4.11).

³³Recall that these are the result of a LF calculation with the known power injections $\mathbf{x}(\mathbf{t}^{\hat{E}_i^\phi}(\mathbf{u}_{in}), \mathbf{u}_{in})$.

$$\begin{aligned}
 \hat{E}_i^\phi(\mathbf{u}) &\approx \hat{E}_i^\phi(\mathbf{u}_{\text{in}}) + \sum_{\substack{m \in \mathcal{R} \\ \phi' \in \{a,b,c\}}} K_{P_m^{\phi'}}^{E_i^\phi} \left(\mathbf{x} \left(\mathbf{t}^{\hat{E}_i^\phi}(\mathbf{u}_{\text{in}}), \mathbf{u}_{\text{in}} \right) \right) \\
 &\left[\left(a_m^{\phi', \hat{E}_i^\phi}(\mathbf{u}_{\text{in}}) P_m^{\phi', \max}(\mathbf{u}_m^{\phi'}) + (1 - a_m^{\phi', \hat{E}_i^\phi}(\mathbf{u}_{\text{in}})) P_m^{\phi', \min}(\mathbf{u}_m^{\phi'}) \right) - \right. \\
 &\quad \left. \left(a_m^{\phi', \hat{E}_i^\phi}(\mathbf{u}_{\text{in}}) P_m^{\phi', \max}(\mathbf{u}_{\text{in}, m}^{\phi'}) + (1 - a_m^{\phi', \hat{E}_i^\phi}(\mathbf{u}_{\text{in}})) P_m^{\phi', \min}(\mathbf{u}_{\text{in}, m}^{\phi'}) \right) \right] \\
 &+ \sum_{\substack{m \in \mathcal{R} \\ \phi' \in \{a,b,c\}}} K_{Q_m^{\phi'}}^{E_i^\phi} \left(\mathbf{x} \left(\mathbf{t}^{\hat{E}_i^\phi}(\mathbf{u}_{\text{in}}), \mathbf{u}_{\text{in}} \right) \right) \\
 &\left[\left(s_m^{\phi', \hat{E}_i^\phi}(\mathbf{u}_{\text{in}}) Q_m^{\phi', \max}(\mathbf{u}_m^{\phi'}) + (1 - s_m^{\phi', \hat{E}_i^\phi}(\mathbf{u}_{\text{in}})) Q_m^{\phi', \min}(\mathbf{u}_m^{\phi'}) \right) - \right. \\
 &\quad \left. \left(s_m^{\phi', \hat{E}_i^\phi}(\mathbf{u}_{\text{in}}) Q_m^{\phi', \max}(\mathbf{u}_{\text{in}, m}^{\phi'}) + (1 - s_m^{\phi', \hat{E}_i^\phi}(\mathbf{u}_{\text{in}})) Q_m^{\phi', \min}(\mathbf{u}_{\text{in}, m}^{\phi'}) \right) \right]
 \end{aligned} \tag{4.11}$$

The Taylor expansion in (4.11) is done in the neighbourhood of $\mathbf{x}(\mathbf{t}^{\hat{E}_i^\phi}(\mathbf{u}_{\text{in}}), \mathbf{u}_{\text{in}})$ as, again, with the progress of the algorithm, \mathbf{u}_{out} will get closer to the updated \mathbf{u}_{in} , which would mean that the uncertainty sets would practically be the same (See Fig. 4.3). Here, it becomes clear that if the uncertainty sets were not described by linearized equations, the Taylor expansion would not be linear. In other words, if the functions $P_i^{\phi, \min}(\mathbf{u}_i^\phi)$, $P_i^{\phi, \max}(\mathbf{u}_i^\phi)$, $Q_i^{\phi, \min}(\mathbf{u}_i^\phi)$ and $Q_i^{\phi, \max}(\mathbf{u}_i^\phi)$ were non-linear, (4.11) would become non-linear even by leveraging SCs. Indeed, in that case, c.f. to Remark 2, the *real-time* aspect of Alg. 5 would not be guaranteed. Finally, the added constraint is, therefore, $(4.11) \leq E_{i, \max}^\phi$.

Then, similarly, `CreateVoltLowConstraint` adds the constraint that guarantees that $-E_i^\phi(\mathbf{x}(\mathbf{t}, \mathbf{u})) \leq -E_{i, \min}^\phi$ for all the deployable powers $\mathbf{x}(\mathbf{t}, \mathbf{u})$ in (4.2). Following the same logic and methodology as `CreateVoltUpConstraint` and substituting \hat{E}_i^ϕ by $-\hat{E}_i^\phi$, the added constraint is therefore

$$\left[(4.11) \right]_{\hat{E}_i^\phi \rightarrow -\hat{E}_i^\phi} \leq -E_{i, \min}^\phi.$$

Then, similarly, `CreateVoltZeroConstraint` adds the constraint that guarantees that $\frac{E_i^{\text{zero}}}{E_i^{\text{pos}}}(\mathbf{x}(\mathbf{t}, \mathbf{u})) \leq \text{tol}_{\text{zero}}$ for all the deployable powers $\mathbf{x}(\mathbf{t}, \mathbf{u})$ in (4.2). Following the same logic and methodology as `CreateVoltUpConstraint` and substituting \hat{E}_i^ϕ by $\frac{E_i^{\text{zero}}}{E_i^{\text{pos}}}$, the added constraint is therefore

$$\left[(4.11) \right]_{\hat{E}_i^\phi \rightarrow \frac{E_i^{\text{zero}}}{E_i^{\text{pos}}}} \leq \text{tol}_{\text{zero}}.$$

Then, similarly, `CreateVoltNegConstraint` adds the constraint that guarantees that $\frac{E_i^{\text{neg}}}{E_i^{\text{pos}}}(\mathbf{x}(\mathbf{t}, \mathbf{u})) \leq \text{tol}_{\text{neg}}$ for all the deployable powers $\mathbf{x}(\mathbf{t}, \mathbf{u})$ in (4.2). Following the same logic and methodology as `CreateVoltUpConstraint` and substituting \hat{E}_i^ϕ by $\frac{E_i^{\text{neg}}}{E_i^{\text{pos}}}$, the added constraint is therefore

$$\left[(4.11) \right]_{\hat{E}_i^\phi \rightarrow \frac{E_i^{\text{neg}}}{E_i^{\text{pos}}}} \leq \text{tol}_{\text{neg}}.$$

Then, similarly, `CreateSlackSConstraint` adds the constraint that guarantees that $S_s^\phi(\mathbf{x}(\mathbf{t}, \mathbf{u})) \leq S_{s,max}^\phi$ for all the deployable powers $\mathbf{x}(\mathbf{t}, \mathbf{u})$ in (4.2). Following the same logic and methodology as `CreateVoltUpConstraint` and substituting \hat{E}_i^ϕ by S_s^ϕ , the added constraint is therefore

$$\left[(4.11) \left| \hat{E}_i^\phi \rightarrow S_s^\phi \right. \right] \leq S_{s,max}^\phi.$$

Then, similarly, `CreateSlackPUpConstraint` adds the constraint that guarantees that $P_s^\phi(\mathbf{x}(\mathbf{t}, \mathbf{u})) \leq P_{s,max}^\phi$ for all the deployable powers $\mathbf{x}(\mathbf{t}, \mathbf{u})$ in (4.2). Following the same logic and methodology as `CreateVoltUpConstraint` and substituting \hat{E}_i^ϕ by P_s^ϕ , the added constraint is therefore

$$\left[(4.11) \left| \hat{E}_i^\phi \rightarrow P_s^\phi \right. \right] \leq P_{s,max}^\phi.$$

Then, similarly, `CreateSlackPLowConstraint` adds the constraint that guarantees that $-P_s^\phi(\mathbf{x}(\mathbf{t}, \mathbf{u})) \leq -P_{s,min}^\phi$ for all the deployable powers $\mathbf{x}(\mathbf{t}, \mathbf{u})$ in (4.2). Following the same logic and methodology as `CreateVoltUpConstraint` and substituting \hat{E}_i^ϕ by $-P_s^\phi$, the added constraint is therefore

$$\left[(4.11) \left| \hat{E}_i^\phi \rightarrow -P_s^\phi \right. \right] \leq -P_{s,min}^\phi.$$

Then, similarly, `CreateSlackQUpConstraint` adds the constraint that guarantees that $Q_s^\phi(\mathbf{x}(\mathbf{t}, \mathbf{u})) \leq Q_{s,max}^\phi$ for all the deployable powers $\mathbf{x}(\mathbf{t}, \mathbf{u})$ in (4.2). Following the same logic and methodology as `CreateVoltUpConstraint` and substituting \hat{E}_i^ϕ by Q_s^ϕ , the added constraint is therefore

$$\left[(4.11) \left| \hat{E}_i^\phi \rightarrow Q_s^\phi \right. \right] \leq Q_{s,max}^\phi.$$

Then, similarly, `CreateSlackQLowConstraint` adds the constraint that guarantees that $-Q_s^\phi(\mathbf{x}(\mathbf{t}, \mathbf{u})) \leq -Q_{s,min}^\phi$ for all the deployable powers $\mathbf{x}(\mathbf{t}, \mathbf{u})$ in (4.2). Following the same logic and methodology as `CreateVoltUpConstraint` and substituting \hat{E}_i^ϕ by $-Q_s^\phi$, the added constraint is therefore

$$\left[(4.11) \left| \hat{E}_i^\phi \rightarrow -Q_s^\phi \right. \right] \leq -Q_{s,min}^\phi.$$

Then, similarly, `CreateCurrentUpConstraint` adds the constraint that guarantees that $I_{ij}^\phi(\mathbf{x}(\mathbf{t}, \mathbf{u})) \leq I_{ij,max}^\phi$ for all the deployable powers $\mathbf{x}(\mathbf{t}, \mathbf{u})$ in (4.2). Following the same logic and methodology as `CreateVoltUpConstraint` and substituting \hat{E}_i^ϕ by I_{ij}^ϕ , the added constraint is therefore

$$\left[(4.11) \left| \hat{E}_i^\phi \rightarrow I_{ij}^\phi \right. \right] \leq I_{ij,max}^\phi.$$

Then, `CreateDeployConstraints` adds the constraints that guarantee that $u_m^\phi \in \mathcal{A}_m^\phi$, $\forall m \in \mathcal{R}$ and $\forall \phi \in \{a, b, c\}$. The added constraints are $\mathbf{M}_m^\phi u_m^{\phi T} - \mathbf{b}_m^\phi \leq 0$, $\forall m \in \mathcal{R}$ and $\forall \phi \in \{a, b, c\}$.

Then, `CreateObjective` creates the OP objective as $\|\mathbf{u} - \mathbf{u}_{in}\|_2$. Where, $\|\cdot\|_2$ is the ℓ_2 -norm.

Finally, `solve` solves the OP. The OP is solved using Alg. 2 presented in Sec. 3.3.3. As before, the reason why the OP is not given to a solver is to gain in computation times (c.f. Remark 2). At the end of every iteration, the approximate solution to the OP, \mathbf{u}_{out} , is tested for admissibility using Alg. 4. If it

Chapter 4. Efficient Computation of Admissible Power-Grid-Control-Setpoints for Heterogeneous, Unbalanced, Stochastic & Uncertain Energy Resources

is admissible, the main loop is stopped, otherwise, Alg. 5 loops again using \mathbf{u}_{out} as input to the next iteration. The iterative process is needed due to: (i) the approximation of the LF equations through SC, (ii) the approximate resolution method, and, more importantly, (iii) to circumvent the chicken-and-egg problem associated to the construction of the constraints, i.e. the non-availability of \mathbf{u}_{out} during the loop to correctly compute the SCs at the edges of the uncertainty sets. As a final note, by construction, the OP is convex and will, therefore, converge [49] towards the direction of an admissible setpoint at each iteration, if the latter exists.

Remark 2. *As explained in the preamble, the problem in (4.4) can be resolved by means of robust-optimization techniques leveraging dual-primal OP transformations. However, these methods are usually computationally heavy and would not be adequate for sub-second real-time control. More specifically, under all the assumptions considered in this chapter, e.g. the dependence of the bounds of the uncertainty sets on the control variable, a dual-primal transformation of the linear grid operational constraints would lead to quadratic constraints, proving again the non-applicability of such well-studied methods for sub-second control.*

Furthermore, the ATF assumption for the bounds of the uncertainty sets could be extended to quadratic functions. More specifically, they could be extended to functions that would define n -spheres for the grid operational constraints. This extension is made possible from the usage of Alg. 2 to solve the OP. However, the bounds were restricted to ATFs as there were no need to go further (see Sec. 4.5).

Finally, since all constraints, under the assumptions of this chapter, are either linear (affine) or spherical, the approximate resolution technique presented in Alg. 2 is fully-applicable. Indeed, this enabled the resolution times of the proposed method to be within the sub-second range.

4.5 Resource Models

By making reference to different resources, in this section we practically show how to express capability (\mathcal{A}_i^ϕ) and uncertainty ($\tilde{\mathcal{B}}_i^\phi$) sets³⁴.

4.5.1 Slack Nodes

For simplicity, in this thesis, slack nodes (SL) are modelled as *sink* nodes whose capability is defined by a rated apparent power $S_{s,\max}$ and maximum/minimum active ($P_{s,\max}/P_{s,\min}$) and reactive ($Q_{s,\max}/Q_{s,\min}$) powers. This leads to,

$$\mathcal{A}_s^\phi \mid \left\{ (P, Q) \in \mathbb{R}^2 : P_{s,\min}^\phi \leq P \leq P_{s,\max}^\phi, Q_{s,\min}^\phi \leq Q \leq Q_{s,\max}^\phi, P^2 + Q^2 \leq (S_{s,\max}^\phi)^2 \right\}$$

4.5.2 Resource Nodes

The considered resources in the scope of this chapter, can be divided into three categories:

- *Energy Storage*, in the form of batteries (B) or supercapacitors (SC);

³⁴We refer the interested reader to [55] for more details concerning resources' modelling.

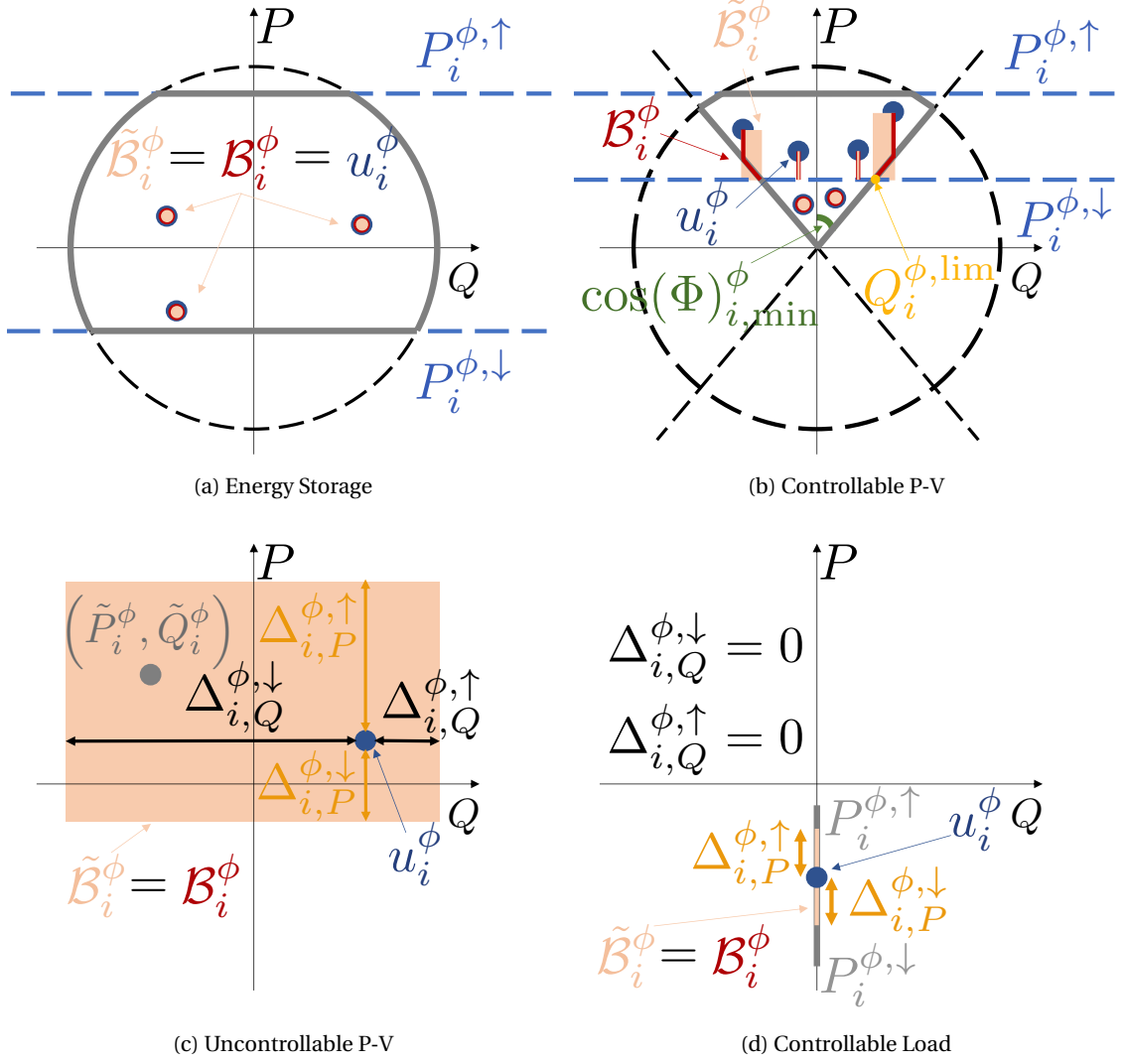


Figure 4.4: Schematic illustration of different capacity and uncertainty sets for a resource connected to node $i \in \mathcal{R}$ on phase $\phi \in \{a, b, c\}$. \mathcal{A}_i^ϕ are the regions delimited by grey lines. \mathcal{B}_i^ϕ are either the red lines, areas or dots. $\tilde{\mathcal{B}}_i^\phi$ are either the pink lines, areas or dots. Different setpoints u_i^ϕ are shown as blue dots.

Chapter 4. Efficient Computation of Admissible Power-Grid-Control-Setpoints for Heterogeneous, Unbalanced, Stochastic & Uncertain Energy Resources

- *Electric Loads*, that can be controllable or uncontrollable (respectively CL and UL);
- *Power Generators*, in the form of controllable and uncontrollable P-V plants (respectively CPV and UPV).

In the following, the modelling details – i.e. capability and uncertainty sets – concerning these resources are presented.

4.5.3 Energy Storage

Storage devices, such as batteries and supercapacitors, are DC resources requiring four-quadrant-inverters to be connected to AC grids. Power converters, connected to node $i \in \mathcal{K} \subset \mathcal{R}$ and phase $\phi \in \{a, b, c\}$ are generally constrained by a maximum apparent power, $S_i^{\phi, \max}$. As DC sources, they also have *internal active-power bounds*. Namely, they have maximum (P_{\max}^{DC}) and minimum (P_{\min}^{DC}) DC power limits that depend on their SoC. DC power limits can be converted to AC maximum ($P_i^{\phi, \uparrow}$) and minimum ($P_i^{\phi, \downarrow}$) power limits. The transformation can be done in a number of ways; here the converter's efficiency is used. Hence, the capability regions of energy storage devices, on their AC-side, can be generally quantified by the intersection of the power-converter limits and the device's converted internal DC power limits. Finally, since these devices are highly controllable, it is expected that their implemented power is equal to the requested setpoint. Fig. 4.4a illustrates the modelling of an energy storage device. Formally, one can express the sets as,

$$\begin{array}{c} \mathcal{A}_i^{\phi} \\ \tilde{\mathcal{B}}_i^{\phi}(u_i^{\phi}) \end{array} \left| \begin{array}{l} \{(P, Q) \in \mathbb{R}^2 : P_i^{\phi, \downarrow} \leq P \leq P_i^{\phi, \uparrow}, P^2 + Q^2 \leq (S_i^{\phi, \max})^2\} \\ \{u_i^{\phi}\} \end{array} \right.$$

4.5.4 Electric Loads

Controllable Loads

Controllable loads are usually three-phase and are directly connected to the grid. They are controllable in the sense that they can implement, with some uncertainty, the control setpoints they receive as long as they are inside their upper and lower active/reactive power limits (respectively $P_i^{\phi, \uparrow}/Q_i^{\phi, \uparrow}$ and $P_i^{\phi, \downarrow}/Q_i^{\phi, \downarrow}$ for a load connected to node $i \in \mathcal{R}$ on phase $\phi \in \{a, b, c\}$). The uncertainty on implementing a setpoint can be modelled with a rectangle around it representing the setpoint tracking inaccuracies. The uncertainty rectangle for a controllable load connected to node $i \in \mathcal{R}$ on phase $\phi \in \{a, b, c\}$ is defined by the parameters $\Delta_{i,P}^{\phi, \uparrow}$, $\Delta_{i,P}^{\phi, \downarrow}$, $\Delta_{i,Q}^{\phi, \uparrow}$ and $\Delta_{i,Q}^{\phi, \downarrow}$. Fig. 4.4d illustrates the modelling of an energy storage device. Finally, formally, one can express the sets as,

$$\begin{array}{c} \mathcal{A}_i^{\phi} \\ \tilde{\mathcal{B}}_i^{\phi}(u_i^{\phi}) \end{array} \left| \begin{array}{l} [P_i^{\phi, \downarrow}, P_i^{\phi, \uparrow}] \times [Q_i^{\phi, \downarrow}, Q_i^{\phi, \uparrow}] \\ [P_i^{\phi} - \Delta_{i,P}^{\phi, \downarrow}, P_i^{\phi} + \Delta_{i,P}^{\phi, \uparrow}] \times [Q_i^{\phi} - \Delta_{i,Q}^{\phi, \downarrow}, Q_i^{\phi} + \Delta_{i,Q}^{\phi, \uparrow}] \end{array} \right.$$

Uncontrollable Loads

Uncontrollable loads are usually three-phase loads that are directly connected to the grid. They are uncontrollable in the sense that they do not accept setpoints. Therefore, their capability region is

defined by their measured powers (\tilde{P}_i^ϕ and \tilde{Q}_i^ϕ for a load connected to node $i \in \mathcal{R}$ on phase $\phi \in \{a, b, c\}$). As before, the uncertainty on implementing a setpoint can be modelled with a rectangle around it. However, in this case, the rectangles represent a next-tim-step forecast of the load. The uncertainty rectangle for an uncontrollable load connected to node $i \in \mathcal{R}$ on phase $\phi \in \{a, b, c\}$ is defined by the parameters $\Delta_{i,P}^{\phi,\uparrow}$, $\Delta_{i,P}^{\phi,\downarrow}$, $\Delta_{i,Q}^{\phi,\uparrow}$ and $\Delta_{i,Q}^{\phi,\downarrow}$. Fig. 4.4c illustrates the modelling of an energy storage device. Finally, formally, one can express the sets as,

$$\mathcal{A}_i^\phi \mid \{(\tilde{P}_i^\phi, \tilde{Q}_i^\phi)\} \\ \tilde{\mathcal{B}}_i^\phi(u_i^\phi) \mid \left[P_i^\phi - \Delta_{i,P}^{\phi,\downarrow}, P_i^\phi + \Delta_{i,P}^{\phi,\uparrow} \right] \times \left[Q_i^\phi - \Delta_{i,Q}^{\phi,\downarrow}, Q_i^\phi + \Delta_{i,Q}^{\phi,\uparrow} \right]$$

4.5.5 Power Generators

Uncontrollable Photo-Voltaic plants

Uncontrollable P-V plans are modelled as uncontrollable loads. They usually produce as much power as possible using, for instance, the MPPT algorithm. As a result, their capability and uncertainty sets are modelled as the ones of uncontrollable loads (see Sec. 4.5.4).

Controllable Photo-Voltaic plants

Controllable PV plants have constraints on reactive power (controlled by a minimum power factor, $\cos(\phi)_{\min}$) and are interfaced to the grid through two-quadrant – i.e. only absorptions – inverters. Hence, a controllable PV plant connected to $i \in \mathcal{K} \subset \mathcal{R}$ on phase $\phi \in \{a, b, c\}$ has, respectively, a minimum power factor ($\cos(\Phi)_{i,\min}^\phi$) and a maximum apparent power rating ($S_i^{\phi,max}$). Furthermore, through the use of forecasting tools [58], their irradiance fluctuation can be modelled in the form of maximum ($P_i^{\phi,\uparrow}$) and minimum ($P_i^{\phi,\downarrow}$) active-power bounds. Their uncertainty sets are defined in a way to account for the next-timestep irradiance uncertainty. As explained in [58], the sets are, in practice, segments that go from the requested setpoint to $P_i^{\phi,\downarrow}$ while respecting the limits of \mathcal{A}_i^ϕ . In summary,

$$\mathcal{A}_i^\phi \mid \left\{ (P, Q) \in \mathbb{R}^2 : 0 \leq P \leq P_i^{\phi,\uparrow}, P^2 + Q^2 \leq (S_i^{\phi,max})^2, \arctan(P/Q) \leq \arccos(\cos(\Phi)_{i,\min}^\phi) \right\} \\ \tilde{\mathcal{B}}_i^\phi(u_i^\phi) \mid \left\{ (P, Q) \in \mathbb{R}^2 : \min\{P_i^\phi, P_i^{\phi,\downarrow}\} \leq P \leq P_i^\phi, \min\{Q_i^\phi, Q_i^{\phi,\lim}\} \leq Q \leq \max\{Q_i^\phi, -Q_i^{\phi,\lim}\} \right\}$$

with $Q_i^{\phi,\lim}$ being the positive reactive power at the intersection of the line $P = P_i^{\phi,\downarrow}$ and the $\cos(\Phi)_{i,\min}^\phi$ constraint line, for a resource connected to $i \in \mathcal{K} \subset \mathcal{R}$ on phase $\phi \in \{a, b, c\}$. An illustrative example is given in Fig. 4.4b.

4.6 Numerical Simulations

In this section, the performance of the proposed algorithms is numerically tested using (i) a simple 4-node network (see Fig. 4.5 and (ii) the IEEE 34 bus feeder [9]. All simulations assume balanced three-phase network operation. As a result, hereinafter, only the grids' single-phase equivalents were considered and the phase-angle superscript is omitted. However, since all grid operational constraints were treated in the same way in the proposed algorithms, this simplification does not affect the

Chapter 4. Efficient Computation of Admissible Power-Grid-Control-Setpoints for Heterogeneous, Unbalanced, Stochastic & Uncertain Energy Resources

applicability of the methods to unbalanced three-phase ADNs. Finally, even though this simplification entails ignoring the nodal voltage sequence SCs, the performance of the latter are still showcased in a further contribution of this thesis (c.f. Sec. 6).

All simulations were performed using MATLAB on a MacBook Pro with a 3.5 GHz i7 processor. Different KPIs, such as number of iterations, convergence, validity of assumptions and computational times, are considered to evaluate the effectiveness of the proposed algorithms. Note that, the computational times were evaluated on a C++ implementation of the same MATLAB code. Both implementations had the same outputs, however, the computational times were drastically decreased when using C++. Finally, it is worth mentioning that both implementations did not include any code optimization (e.g. [84]) which was left for future works.

In the simulations, in both implementations, each resource is encapsulated into a class. Each class has attributes to describe the resource's capability and uncertainty sets. Namely, each class has attributes and built-in functions with particular definitions to match the sets presented in section 4.5.2. As a final note, it is worth recalling that, for the CPV resources, the *min* and *max* functions defining their uncertainty set bounds are ATFs. Therefore, by using the techniques presented in Appendix A, the grid operational constraints remain linear.

Finally, as in the previous chapter, compared to the operational constraints requirements listed in the EN-50160 standard [48], tighter nodal voltage magnitude bounds were chosen to stress-test the proposed method. The chosen maximum and minimum bounds were, respectively, set to $E_{i,min} = 0.95$ p.u and $E_{i,max} = 1.05$ p.u (see Secs. 4.6.1&4.6.2 for the base values of each simulated grid).

4.6.1 4-Node Network

The network topology is shown in Fig. 4.5, when a generic implementation setpoint \mathbf{x} is deployed. The grid is composed of 4 nodes and 3 identical branches. The base voltage is 24.9 kV and the base power is 5 MVA. The grid model and resources' parameters are summarized in Table 4.2. In the following, three simulations performed on the 4-node network are presented.

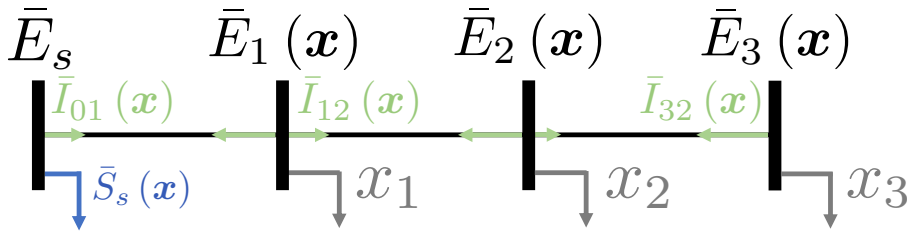


Figure 4.5: 4-Node network topology

Approximation Check

A first simulation was performed to verify the validity of the proposed approximate SC-based method to solve (4.5). In other words, the simulation verified whether the computed quantities $\Gamma(\hat{\mathbf{u}})$ were indeed the constraints' maximizers. To do so, the simulation consists in solving the non-approximated problem in (4.5) for all values of Γ (i.e. " E_i ", " $-E_i$ ", " I_{ij} ", " S_s ", " P_s ", " $-P_s$ ", " Q_s ", " $-Q_s$ "). This is

Table 4.2: 4-Node network parameters

(a) Line parameters				
R [Ω/km]	L [mH/km]	C [μF/km]	length [km]	Ampacity [A]
0.193	0.38	0.24	1	76.21

(b) Resource parameters (in p.u.) for *Branch Current Constraint Violation* simulation

Node	Type	Parameters
0 (s)	SL	$S_{s,max} = 0.5, P_{s,max} = Q_{s,max} = 1, P_{s,min} = Q_{s,min} = -1$
1	CPV	$P_1^\uparrow = 0.6, P_1^\downarrow = 0.38, S_1^{max} = 1, \cos(\Phi)_{1,min} = 0.5$
2	UL	$\Delta_{2,P}^\uparrow = \Delta_{2,P}^\downarrow = 0.2, \Delta_{2,Q}^\uparrow = \Delta_{2,Q}^\downarrow = 0$
3	B	$P_3^\uparrow = 0.2, P_3^\downarrow = -0.5, S_3^{max} = 1$

(c) Resource parameters (in p.u.) for the *Approximation Check & Branch Current, Nodal Voltage and Slack Constraints Violations* simulations

Node	Type	Parameters
0 (s)	SL	$S_{s,max} = 0.3, P_{s,max} = Q_{s,max} = 1, P_{s,min} = Q_{s,min} = -1$
1	UL	$\Delta_{1,P}^\uparrow = \Delta_{1,P}^\downarrow = \Delta_{1,Q}^\uparrow = \Delta_{1,Q}^\downarrow = 0.1$
2	CPV	$P_2^\uparrow = 0.6, P_2^\downarrow = 0.38, S_2^{max} = 1, \cos(\Phi)_{2,min} = 0.5$
3	B	$P_3^\uparrow = 0.2, P_3^\downarrow = -0.5, S_3^{max} = 1$

Chapter 4. Efficient Computation of Admissible Power-Grid-Control-Setpoints for Heterogeneous, Unbalanced, Stochastic & Uncertain Energy Resources

done using MATLAB's `fmincon`, the resource parameters in Tab. 4.2(c) and for several collections of setpoints \mathbf{u} . The resulting maximum error between the non-linear solution and the proposed method, for all constraints, is in the order of $1e-6$ p.u. . These first promising results confirmed the intuition presented in Remark 1.

Branch Current Constraint Violation

In this second simulation, a control setpoint that caused non-admissibility for some branch currents was synthesized and inputted to Alg. 5. More specifically, the initial setpoint is feasible, i.e. $\mathbf{u}_{\text{in}} \in \mathcal{F}$, yet, due to the uncertain behaviour of the UL and the CPV, the latter is not admissible, i.e. $\mathbf{u}_{\text{in}} \notin \mathcal{U}$. Namely, even though its implementation-realization may cause grid operational constraint violations, this setpoint would be normally sent to resources as in itself it does not violate the latter.

The resources parameters used for this simulation are summarized in Tab. 4.2(b). Fig. 4.6a and Fig. 4.6b shows the evolution of $\hat{I}_{ij}(\mathbf{u}_{\text{out}})$, $\hat{E}_i(\mathbf{u}_{\text{out}})$ and $-\hat{E}_i(\mathbf{u}_{\text{out}})$ together with their respective bounds. They also show the evolution of the updated \mathbf{u}_{in} and the evolution of $T_{\%}$. $T_{\%}$ is an introduced KPI representing the accuracy, in percentage, of $T_{\text{in}} = T_{\text{out}}$ with T_{out} being the output of `computeCoordinates`($\bar{\mathbf{Y}}, \mathbf{u}_{\text{out}}, \mathcal{R}$). As algorithm 5 converges, it pushes all violating currents to their ampacity limit, and only stops when the *worst* violation hit the limit, i.e. is projected onto the \mathcal{F} . Furthermore, it can be observed that $T_{\%}$ increases at every iteration. This further validates the assumption $\mathbf{t}^{\Gamma^{\pm}}(\mathbf{u}_{\text{in}}) \cong \mathbf{t}^{\Gamma^{\pm}}(\mathbf{u})$, that done at every OP iteration to create the constraints. Finally, on average the OP approximate-solving time was less than $\sim 5 - 8$ ms, the average time to perform the admissibility test was similar and the total time for the full convergence of the algorithm was less than ~ 20 ms.

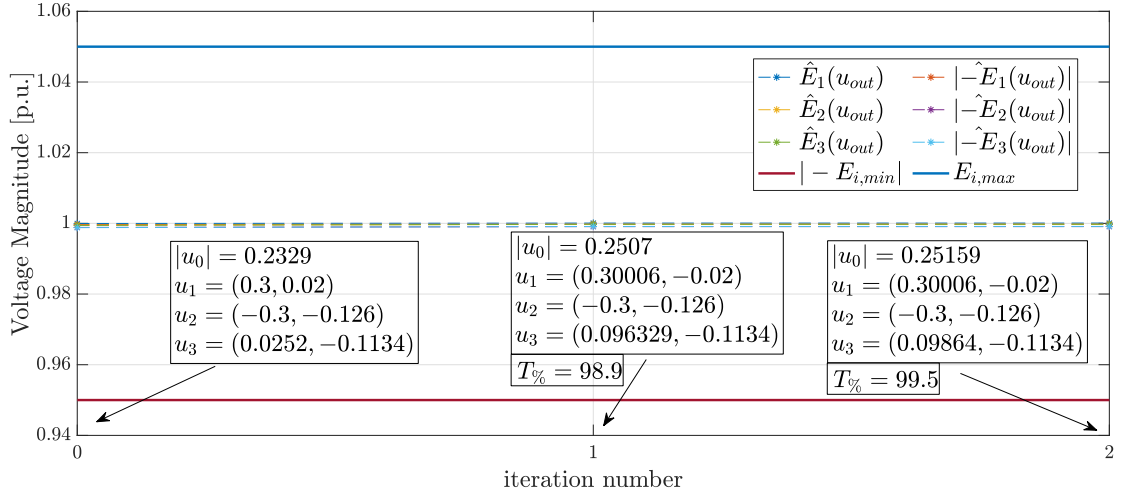
Branch Current, Nodal Voltage and Slack Constraints Violations

In this third simulation, a control setpoint that caused non-admissibility for some branch currents, nodal voltages and slack apparent power constraints, was synthesized and inputted to Alg. 5. Unlike the previous simulation, the initial setpoint is not feasible, i.e. $\mathbf{u}_{\text{in}} \notin \mathcal{F}$. The resources parameters used for this simulation are summarized in Tab. 4.2(c). The line parameters are the same as in the previous simulations except for the lengths that are artificially increased for branches (0,1), (1,2) and (2,3) to, respectively, the extremely large values of 25, 25 and 50 km. This was done to force overvoltages. Fig. 4.7 shows the evolution of $\hat{I}_{ij}(\mathbf{u}_{\text{out}})$, $\hat{E}_i(\mathbf{u}_{\text{out}})$, $-\hat{E}_i(\mathbf{u}_{\text{out}})$ and $\hat{S}_s(\mathbf{u}_{\text{out}})$ together with their respective bounds. Unlike in the previous simulation, since the inputted setpoint was non-admissible in terms of slack apparent power magnitude constraints, Fig. 4.7c shows the evolution of the maximizer of the latter together with its capability set \mathcal{A}_s . The obtained conclusions, i.e. convergence, KPIs and computation times, are similar to the ones of the previous simulation.

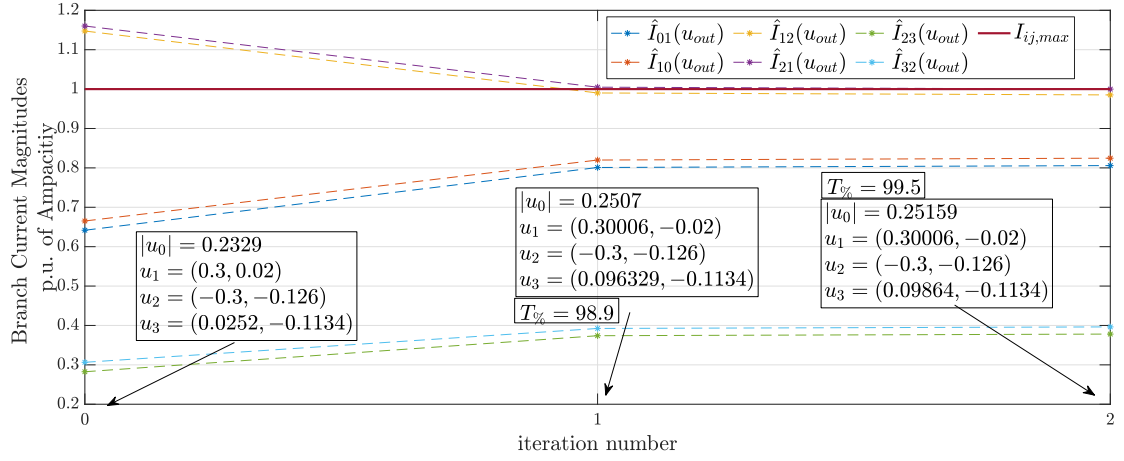
4.6.2 IEEE 34 Test Distribution Feeder

The grid is based on the IEEE 34 test distribution feeder. All the branch parameters can be found in [9]. The base voltage is 24.9 kV and the base power is set to 25 kVA. In this simulation, a control setpoint that caused non-admissibility for some branch currents and nodal voltages magnitude constraints, was synthesized and inputted to Alg. 5. The initial setpoint is not feasible, i.e. $\mathbf{u}_{\text{in}} \notin \mathcal{F}$ (See Fig. 4.8a). The resource allocation can be found in Tab. 4.3. It is based on the *suggested* load profile in [9]. Loads are placed in the same nodes as in [9], and are represented by either controllable and uncontrollable

4.6 Numerical Simulations



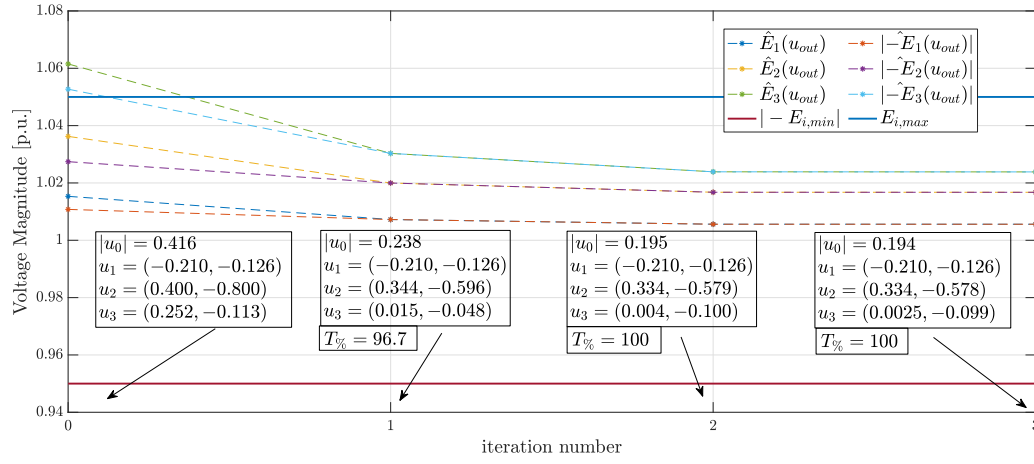
(a) Evolution of nodal voltage magnitude maximizers during one full-run of Alg. 5



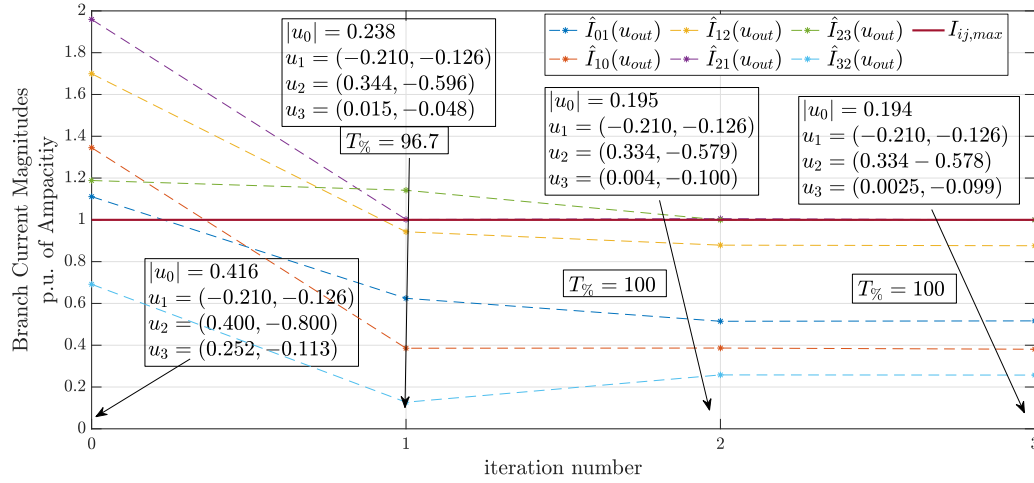
(b) Evolution of branch current magnitude maximizers during one full-run of Alg. 5

Figure 4.6: 4-node network: *Branch Current Constraint Violation* simulation

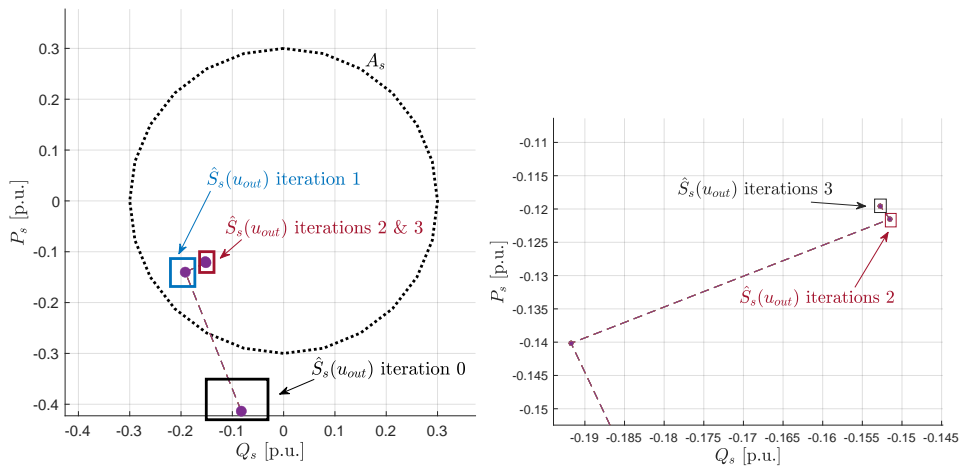
Chapter 4. Efficient Computation of Admissible Power-Grid-Control-Setpoints for Heterogeneous, Unbalanced, Stochastic & Uncertain Energy Resources



(a) Evolution of nodal voltage magnitude maximizers during one full-run of Alg. 5



(b) Evolution of branch current magnitude maximizers during one full-run of Alg. 5



(c) Evolution of slack apparent power magnitude maximizers during one full-run of Alg. 5

Figure 4.7: 4-node network: Branch Current, Nodal Voltage and Slack Constraints Violations simulation

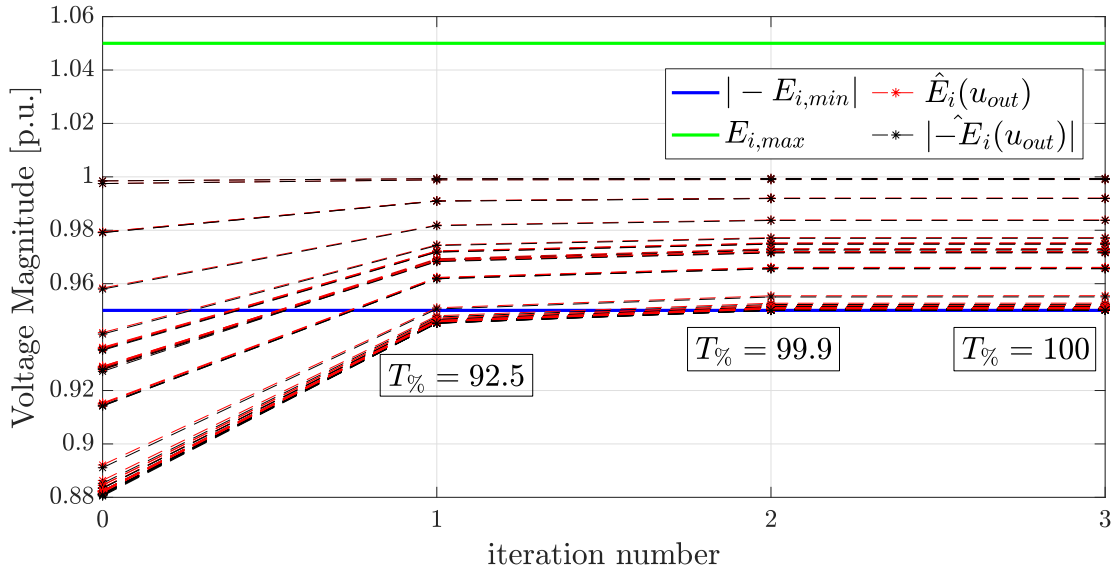
loads or batteries. The grid is augmented with five generation nodes, two of which are in the form of uncontrollable P-V plants while the rest are controllable P-V plants. Fig. 4.8 shows the results of a simulation where the load profile was scaled by a factor of 3 in order to create an undervoltage in the grid. Furthermore, compared to the values in [9], the branch ampacity limits were downscaled to create branch current magnitude violations. The obtained conclusions, i.e. convergence and KPIs, are similar to the ones of the previous simulations. Finally, in terms of computation times the seem to scale linearly with the grid size and number of connected resources. Indeed, on average, the OP solving time was $\sim 100 - 150$ ms, the average time to perform the admissibility tests were similar and the total time for the full convergence of the algorithm was around ~ 500 ms.

Table 4.3: Resource parameters (in p.u.) for the IEEE34 *Voltage and Current Violation* simulation

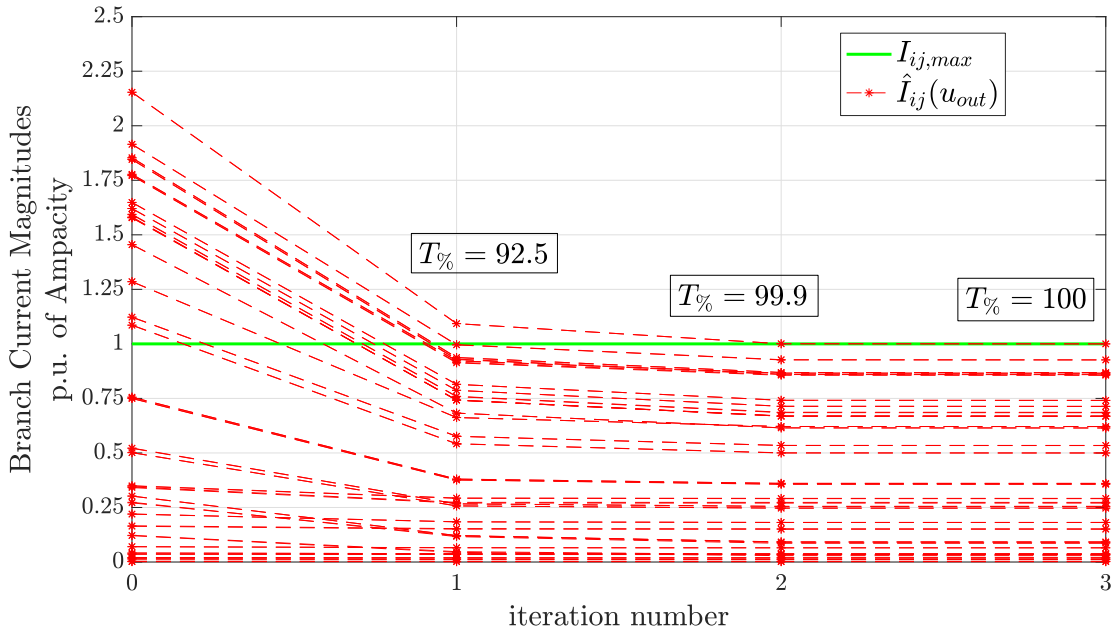
Node	Type	Parameters
0 (s)	SL	$S_{s,max} = 100, P_{s,max} = Q_{s,max} = 100, P_{s,min} = Q_{s,min} = -100$
4	B	$P_4^\downarrow = 1.2, P_4^\uparrow = -1.2, S_4^{max} = 2$
7	CPV	$P_7^\downarrow = 8, P_7^\uparrow = 7.4, S_7^{max} = 10, \cos(\Phi)_{2,min} = 0.3$
9	CL	$P_9^\downarrow = -0.8, \Delta_{9,P}^\uparrow = \Delta_{9,P}^\downarrow = 0.02, P_9^\uparrow = Q_9^\uparrow = Q_9^\downarrow = \Delta_{9,Q}^\uparrow = \Delta_{9,Q}^\downarrow = 0$
10	CL	$P_{10}^\downarrow = -2.8, \Delta_{10,P}^\uparrow = \Delta_{10,P}^\downarrow = P_{10}^\uparrow = Q_{10}^\uparrow = Q_{10}^\downarrow = \Delta_{10,Q}^\uparrow = \Delta_{10,Q}^\downarrow = 0$
11	B	$P_{11}^\downarrow = 2, P_{11}^\uparrow = -2, S_{11}^{max} = 2.4$
15	B	$P_{15}^\downarrow = 2, P_{15}^\uparrow = -2, S_{15}^{max} = 2.4$
18	UPV	$\Delta_{18,P}^\uparrow = \Delta_{18,P}^\downarrow = \Delta_{18,Q}^\uparrow = \Delta_{18,Q}^\downarrow = 0$
20	UPV	$\Delta_{20,P}^\uparrow = \Delta_{20,P}^\downarrow = \Delta_{20,Q}^\uparrow = \Delta_{20,Q}^\downarrow = 0$
21	CL	$P_{21}^\downarrow = -10, \Delta_{10,P}^\uparrow = \Delta_{10,P}^\downarrow = P_{10}^\uparrow = Q_{10}^\uparrow = Q_{10}^\downarrow = \Delta_{10,Q}^\uparrow = \Delta_{10,Q}^\downarrow = 0.001$
24	B	$P_{24}^\downarrow = 2, P_{24}^\uparrow = -2, S_{24}^{max} = 2.4$
26	CL	$P_{26}^\downarrow = -8, \Delta_{26,P}^\uparrow = \Delta_{26,P}^\downarrow = 0.1, P_{26}^\uparrow = Q_{26}^\uparrow = Q_{26}^\downarrow = \Delta_{26,Q}^\uparrow = \Delta_{26,Q}^\downarrow = 0$
27	CPV	$P_{27}^\downarrow = 2.4, P_{27}^\uparrow = 2, S_{27}^{max} = 3, \cos(\Phi)_{2,min} = 0.3$
28	B	$P_{28}^\downarrow = 8, P_{28}^\uparrow = -10, S_{28}^{max} = 12$
30	CPV	$P_{30}^\downarrow = 4, P_{27}^\uparrow = 3.6, S_{27}^{max} = 6, \cos(\Phi)_{2,min} = 0.1$

4.7 Conclusion

In this chapter, methods accounting for the uncertainty of the implementation of setpoints at resource controllers have been proposed. First, a tractable *admissibility test* checking whether a control setpoint is admissible or not, was developed. Second, an iterative algorithm was presented with the following features: (i) it accounts for the grid and resource operational constraints, (ii) it leverages SCs to linearize the power-flow equations, and (iii) it is capable to determine the closest admissible control setpoint to its input. At each algorithm iteration, an admissibility test is performed to verify the validity of the OP's output and, ergo, the validity of the approximations used to linearize the constraints of the OP. The performed simulations show that the algorithms: (i) converge, (ii) satisfy the validity of the posed assumptions and, (iii) are compliant with real-time, i.e. sub-second, control. Note that, even though the performed simulations assumed balanced three-phase operation, the method is capable to control grids operating in generic unbalanced conditions as all grid operational constraints are dealt with



(a) Evolution of nodal voltage magnitude maximizers during one full-run of Alg. 5



(b) Evolution of branch current magnitude maximizers during one full-run of Alg. 5

Figure 4.8: IEEE-34 network: *Nodal Voltage and Branch Current Constraint Violations* simulation

Table 4.4: Initial setpoint (in p.u.) for the IEEE34 Network *Voltage and Current Violation* simulation, for all nodes $i \in \mathcal{N} \setminus \mathcal{S}$. Zero-injection and generation nodes are highlighted in red and blue, respectively.

i	P_i	Q_i	i	P_i	Q_i	i	P_i	Q_i
1	-1.1	-0.19	2	-1.1	-0.19	3	-0.3	-0.05
4	-0.3	-0.05	5	0	0	6	0	0
7	4	-4	8	-0.1	-0.01	9	-0.68	-0.11
10	-3.38	-5.8	11	-2.7	-0.47	12	-0.98	-0.16
13	-0.8	-0.13	14	-0.22	-0.03	15	-1.94	-0.29
16	-0.08	-0.01	17	-0.08	-0.01	18	0.2	4
19	-0.3	-0.05	20	0.2	-4	21	-18	-3
22	-0.98	-0.17	23	-0.04	0.01	24	-3.56	-0.6
25	-0.18	-0.03	26	-17.28	-0.39	27	2.2	4
28	-2.86	5.29	29	-6.96	-1.41	30	2.4	-4
31	-1.88	-0.41	32	-0.56	-0.09	33	-0.56	-0.09

in the same manner. Furthermore, the performance and validity of the nodal sequence voltage SCs is numerically validated further-on in this thesis when it tackles the subject of EVCS integration in ADNs (c.f. Sec.6). Finally, as previously mentioned, no code optimization was performed at this point. Therefore, future works are planned to: (i) optimize the code implementation and, (ii) perform an experimental validation on the EPFL-DESL microgrid by integrating the developed algorithms into a real-time control framework (e.g. COMMELEC [54]).

Efficient methods for the safe operation of electric-vehicle-charging-stations

Part II

5 Context & Motivations

5.1 Introduction

The electrification of the mobility sector has been proposed as a main pathway to reduce GHG emissions of the latter in order to reach the climate targets set by European commission for 2030 and 2050 [85]. Indeed, the mobility sector is among the largest sectors contributing the most ($\sim 16\%$ [86]) to GHG emissions. Furthermore, in Switzerland, even though little legislative advantages are given to private households to buy EVs (hybrid or plug-in), the market share of EVs is steadily increasing: *The public-private initiative [87] aims to increase the share of electric models among new registrations to 50% by 2025. At present, around 25.5% of newly registered vehicles are electric rechargeable models [88].* As a result, the number of EVCSs being connected at different levels of the power-grid is steadily increasing: *The consortium [i.e. the public-private initiative [87]] has also pledged to rapidly increase the number of public charging stations from 7,150 to 20,000 in the next three years. [88].* Indeed, the penetration of (i) low-power (usually between 1.6-10kW per charger) Type-1 (AC-single-phase) & Type-2 (AC-three-phase) chargers in low voltage networks, and (ii) high-power (usually between 10-200kW per charger) CHAdeMO³⁵ & Combined Charging System³⁵ (CCS) charger in medium-to-low voltage networks, is steadily increasing. In fact, aggregated high-power EVCSs may reach peak consumptions of several MWs per feeder in a situation where they are simultaneously used at full-capacity. To this end, in this second part, a deeper look is given to the impact of EVCSs on ADNs. In the following, first, two motivating simulations and experiments are presented. The first set of simulations quantifies the risks that uncontrolled EV charging presents for ADNs' static operational constraints in case of a full electrification scenario of private mobility. The second set of experiments showcases (i) the controllability of EVCSs, i.e. the on-board response times to setpoint variations, and (ii) the effects of unbalanced operation due to single-phase EVCSs. Altogether, the later showcase the importance of the development of methods and algorithms that guarantee the safe operation of EVCSs. Finally, to conclude this context & motivations chapter, a summary of the upcoming chapters of this part is given.

³⁵These types of chargers are usually DC, i.e. the inverter interfacing the EV's battery and the grid if off-board and is balanced. Therefore, the charging of the EV batteries is done directly using DC currents.

5.2 Two Motivating Simulations & Experiments

5.2.1 Macro-effects of electric-vehicle charging on low-voltage power grids

In this subsection we tackle the problem of EVCSS' penetration in low-voltage power grids. For this analysis power-grids are assumed balanced three-phase with a *known* grid model – i.e. network topology and branch parameters – and are, therefore, modelled by their single-phase direct-sequence equivalent. We present a Monte-Carlo-based method that statistically quantifies the effects of EV charging on grids' operational constraints security. The method is illustrated on two real low-voltage networks situated in the western part of Switzerland.

Concept

LFMCSs consist in carrying out a sufficiently large number of load-flow computations with nodal active and reactive power injections randomly sampled from their respective PDFs or CDFs to output CDFs of network states³⁶. In contrast to a traditional LF computation that takes as input a deterministic vector of nodal power injections and outputs one vector of network states (i.e. complex nodal voltages in all nodes of the electrical grid), the aim of LFMCSs is to output as many network states as the number of LF computations performed. The result is then used to create empirical CDFs of the network states along with all other auxiliary electrical quantities that can be derived from the states. Results of LFMCSs statistically quantifies the behaviour of the electric grid quantities while taking into account the stochasticity of the nodal power injections (i.e. stochastic renewable generation, EV and residential loads).

Method

Due to data scarcity, the developed method performs LFMCSs for every hour of a *representative* day. Representative days pertain to a specific season (i.e. winter, spring, summer and autumn) and day-type (i.e. workday or weekend/holidays).

To create the input PDFs/CDFs for the LFMCSs, the method needs hourly nodal injection profiles for every injection (i.e. active or reactive power injection) in the considered grid. Each hourly profile is first clustered into 4 seasons (i.e. $s \in \{\text{winter, spring, summer and autumn}\}$), sub-clustered into day-type (i.e. $w \in \{\text{working days, weekend or vacation days}\}$) then is sub-sub-clustered into hours of the day (i.e. $h \in \{1, \dots, 24\}$).

After the clustering, the idea is to identify a PDF/CDF for each hour of every day-type and season for ever non-zero injection profile. Two options were considered to create the needed PDFs/CDFs.

1. Option 1 is based on non-parametric probability distribution identification. The empirical cumulative distribution function of the data of each sub-sub-cluster s_{w_h} is computed, and thus the needed CDFs are directly available.
2. Option 2 tries to quantify temporal correlations of the data by fitting a multi-variable distribution function over the 24 hours data contained in a sub-cluster s_w . Each random variable is, therefore,

³⁶We only mention power injections as we focus on low-voltage distribution grids where all non-zero injection nodes are modelled as PQ-nodes.

an hour of a sub-cluster. The fitting is repeated for every sub-cluster of every considered injection. The used PDF fitting method outputs a Gaussian Mixture Model (GMM). A GMM is a sum of multivariate Gaussian normal distributions [89]. The number of Gaussian normal distributions is named as the *order* of the GMM. On MATLAB, the function `fitgmdist` fits a GMM model to the inputted data. Seeing that `fitgmdist` has many input parameters, we implemented a *try-catch* function that tries to fit different GMM models with different orders and identification options until the *best-fit* – i.e. the one where the MATLAB algorithm converges with the least inferred probability error – is found. As an example, we considered the *shared covariance* identification option in our *try-catch* function. The *shared covariance* option, if set to TRUE, enforces that the same multivariate covariance matrix should be used for all the Gaussian distributions of the GMM. The implemented *try-catch* iterates over many options until convergence. The final output is the parametric expression of the multivariate PDF (and thus CDF) of a sub-cluster s_w belonging to an injection.

The choice between the two options is purely based on the input datasets. The MATLAB function identifying the GMM models works well if the input data is large enough, i.e. the number of measurements per random variable (here hour) is larger than the total number of random variables (here 24). Thus a simple verification is done before the identification to be sure that there's enough data for the *try-catch* function to converge.

The clustering and distribution identification process is repeated for all the profiles (i.e. all types (generation or load) of active and reactive power injections for all non-slack and non-zero injection nodes). It is worth noting that hourly profiles should have *enough* (i.e. around one year hourly profiles) data for the clustering to be able to lead to meaningful distributions. The method to create the input PDFs/CDFs is schematically shown in Fig. 5.1.

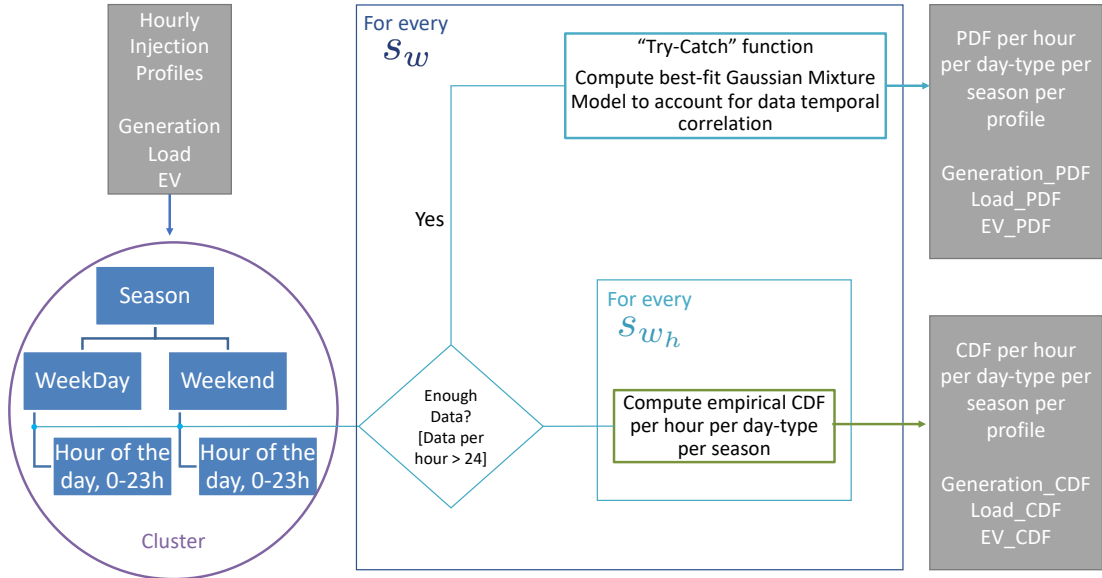


Figure 5.1: Schematic representation of the creation of the input CDFs

With the created distributions, LFMCSs are performed. Namely, for each hour of every day-type pertaining to a specific season, a large number of LF computations, using the NR algorithm, is performed

with injections that are randomly sampled from the created/inputted PDFs/CDFs. The method to set the number of LF computations – a.k.a. Monte-Carlo instances – in order to obtain statistically meaningful results is explained in Remark 3. After sampling all the PDFs/CDFs of all the injections of all nodes for a specific hour, day-type and season, a LF computation can be performed. As previously mentioned, this is done a sufficiently and adequate number of times for every hour of every day-type and every season (in what follow the number of Monte-Carlo instances is called NUM_SIM). Using the outputted states of all the loadflow computations (i.e. $|s| (= 4) \times |w| (= 2) \times |h| (= 24) \times \text{NUM_SIM}$), we create CDFs of all the network states and auxiliary variables (e.g. branch currents and slack apparent power magnitudes) for every hour, day-type and season. The pseudo-code of the main algorithm used to perform the LFMCSs is shown in Fig. 5.2.

Remark 3. *As explained in [90], Monte-Carlo simulations should be designed in a way to achieve a certain performance that has statistical guarantees. Indeed, depending on the problem size the computation times can be drastically increased if an arbitrarily large number of simulations per Monte-Carlo run (NUM_SIM) is chosen. Furthermore, choosing arbitrarily the latter goes against the fundamentals of Monte-Carlo simulations as no quantifiable statistical guarantees can be explicitly given with the results of the simulations. As a result, one needs to choose NUM_SIM depending on certain criteria. Indeed, as explained in [90], the idea is to choose NUM_SIM in order to achieve statistical guarantees in terms of confidence intervals³⁷ on the results given a certain level of precision³⁷. Following the well-known Central Limit Theorem, the formula one can use to determine NUM_SIM is given by*

$$\text{NUM_SIM} \geq \left(\frac{\hat{s} \times z}{p} \right)^2 \quad (5.1)$$

where \hat{s} is the true standard deviation of the output population that, in practice, is replaced by an estimation of the latter; z is the z-statistic associated to the user-desired confidence level and p is the level of desired level of precision.

In the case of our LFMCSs, we focused on designing the simulations to achieve statistical guarantees w.r.t. the nodal voltage magnitudes (i.e. the outputted state of the grid). Indeed, we used the following steps to determine NUM_SIM.

1. Set the confidence level to 97.5%;
2. Set the level of precision to 0.0015 p.u. which translates, with a base voltage of 240V, to 0.36V;
3. Run LFMCSs by setting NUM_SIM to 100;
4. Compute the maximum estimated output standard deviation over all nodal voltage magnitudes, seasons, day-types and hours;
5. Set NUM_SIM using (5.1) and the result of step 4;
6. Re-run the LFMCSs with the updated NUM_SIM;
7. Compute the new maximum estimated output standard deviation over all nodal voltage magnitudes, seasons, day-types and hours;
8. Verify that (5.1) is verified with the updated NUM_SIM. If it is then there's nothing to do as the desired statistical performance is obtained, otherwise, increase NUM_SIM based on the new results obtained in step 7 and repeat steps 6-8.

In our simulations, the latter lead to NUM_SIM= 350.

```

For s = {Winter; Summer; Spring; Fall}
  For d = {Weekday; Weekend/Holiday}
    For h = {0,...,23}
      For r = 1,...,#ofRandomRealizations (=500)
        0. Initialize nodal injection vector
          P = zeros(n,1); where n is network size (multiplied by #of phases)
          Q = zeros(n,1); where n is network size (multiplied by #of phases)
        1. Generation,
          For n = nodes
            if n is Generation node
              Randomly sample Generation_CDF_P{s}{d}{h}{n} or Generation_PDF_P{s}{d}{h}{n} to get nodal active power injection,  $P_{gen,n}$ 
              P(n) = P(n) +  $P_{gen,n}$ 
              Randomly sample Generation_CDF_Q{s}{d}{h}{n} or Generation_PDF_Q{s}{d}{h}{n} to get nodal reactive power injection,  $Q_{gen,n}$ 
              Q(n) = Q(n) +  $Q_{gen,n}$ 
            end
          end
        2. Loads. Do as Generation but with Loads_CDF_P and Loads_CDF_Q to respectively sample  $P_{load,n}$  and  $Q_{load,n}$  and add them respectively to P(n) and Q(n)
        3. EV Loads Charging. Do as Generation but with EV_CDF_P and EV_CDF_Q to respectively c  $P_{EV,n}$  and  $Q_{EV,n}$  and add them respectively to P(n) and Q(n)
        4. Perform Load-Flow computation using P and Q. Store all nodal voltages and branch currents with same clustering as Input Data.
      end
    end
  end
end

```

Figure 5.2: Pseudo-code for the LFMCSs algorithm

Results

In order to illustrate the method, we show the simulation results of LFMCSs performed on two real low-voltage grids situated in the western part of Switzerland (Rolle VD). Both grids do not have EVCSs. However, for the purpose of the simulations we artificially added EVCSs in nodes corresponding to real establishments (e.g. a company, a hospital, a residential building, etc.). Furthermore, the simulation includes EV CPs that were synthesized by taking into account the real characteristics of each establishment (e.g. number of residents in a residential apartment etc.), all while accounting for the behaviour of EV users. The method used to create the latter is detailed in [91]. For both grids, LFMCSs are performed without and with different penetration-percentages of EVCSs in order to showcase the influence of full, partial and null electrification of private transportation on the grids' operational constraints.

Rolle - Gare The network map, topology and real resource location are shown in Figs. 5.3a-5.3b and Tab. 5.1. We recall that the EVCSs were added artificially as they do not exist in the real network.

The yearly power profiles of every node, used to create the input CDFs needed for the LFMCSs are shown in Fig. 5.4. The active generation profile (see Fig. 5.4a) corresponds to real measurements of aggregated PV injections measured at the region of Rolle, VD from 01.01.2014 to 27.07.2016³⁸. The data was not measured *exactly* at the Gare network, however, with the known real maximum power ratings of each installed P-V plant in the Gare network, we were able to disaggregate the profile and get the

³⁷As defined in [90], we recall that (i) Confidence intervals are *characterized by two parameters: confidence level and its associated -statistic*. For instance, a *confidence interval of an estimated population mean* is often presented in terms of a percentage, such as 95%. The *z -statistic* is the standard deviation from the mean. The interpretation of this confidence interval is: we are 95% sure the confidence interval contains the true population mean, which is the subject of estimation, and (ii) Levels of precision are *The maximum degree the true population mean can deviate from the sample mean estimation, subject to a given confidence level*. By the symmetric construction of confidence interval, it is the width of a confidence interval.

³⁸The data for reactive power injections for PV installations were not available and therefore assumed to be null since these installations are required to operate at unitary power factor.

Table 5.1: Rolle Gare grid - resource nodes with description and peak injections

Node	Type	Load-Peak [kW]	Generation-Peak [kW]
6	Residential Home	4	0
7	Residential Home	4	0
13	Company	20	100
15	Train Station	6	0
22	Residential Home	12	0
26	Residential Home	1	0
30	Residential Home	10	0
37	Residential Home	5	0
38	Residential Home	20	16.34
40	Residential Home	1	0
43	Residential Home	6	0
44	Residential Home	3	0
49	Residential Home	4	0
51	Residential Home	2	0
52	Residential Home	1	0
53	Residential Home	4	0
54	Residential Home	7	0
56	Residential Home	1	0
59	Residential Home	2	0
63	Residential Home	1	0
67	Residential Home	1	0
68	Residential Home	2	0
69	Residential Home	2	0
70	Residential Home	2	0
71	Residential Home	1	0
72	Residential Home	2	0
74	Residential Home	4	0

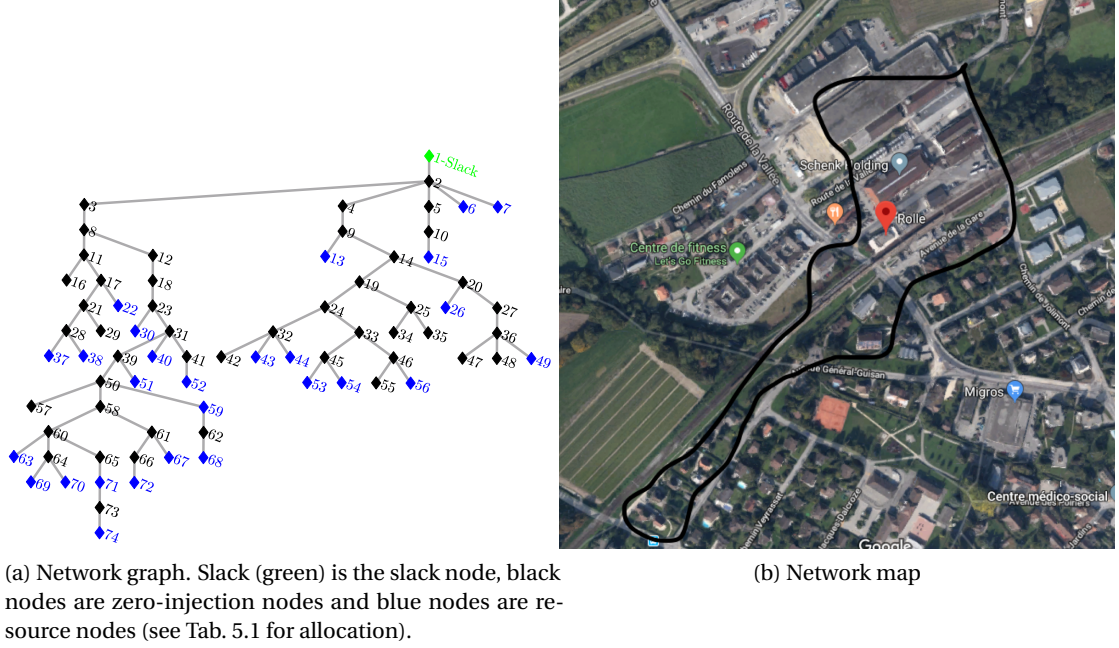


Figure 5.3: Rolle Gare grid - network topology

active power injection profile for each node with a P-V installation. This is fair as the network extension is small enough that P-V profiles of each node have most probably unitary space/time correlation. The active and reactive non-EV load profiles are shown in Fig. 5.4b. The trends come from real data measurements. The measurements come from three different locations: (i) USA (more information and description can be found in [92]), (ii) Italy (more information and description can be found in [93]) and (iii) Germany (more information and description can be found in [94]). The profiles used from the latter datasets were all scaled using the real *known*, per node, peak active/reactive power load of the Rolle-Gare grid. As a result, each non-EV load injection encapsulates the behaviour of the node (i.e. restaurant, train-station, house-hold, etc.) and is scaled properly to have the correct order of magnitudes. Two sets of absorption/CPs of EV CSs (see Fig. 5.5) were synthesized³⁹ for this grid: the first (see Fig. 5.5a) assumes that EV chargers can be placed everywhere (i.e. residential and point-of-interest chargers), and, the second (see Fig. 5.5b) assumes that EV chargers can be placed only at home (i.e. only residential charging). To synthesize them, 100% electrification of private vehicles was assumed. Home chargers were assumed to be rated at 2.3kW while all other chargers were rated at 3.7kW. All EVs were assumed to have batteries with 80kWh of nominal capacity. Each profile was synthesized while taking into account the specific characteristics of each node it is connected to. More specifically, in Fig. 5.5,

- EV-Home corresponds to the aggregated CP of all residential buildings of the grid. That profile was then disaggregated on the different real residential nodes proportionally to the number of inhabitants per node,
- EV-Work corresponds to the aggregated CP of Schenk SA Warehouse. To create the profile it was

³⁹ Provided by Giacomo Pareschi, Aerothermochemistry and Combustion Systems Laboratory, ETH Zurich, Switzerland, pareschi@lav.mavt.ethz.ch.

Chapter 5. Context & Motivations

estimated that about 126 employees worked there,

- EV-Station corresponds to the CP of the potential commuters passing by the Rolle train-station.

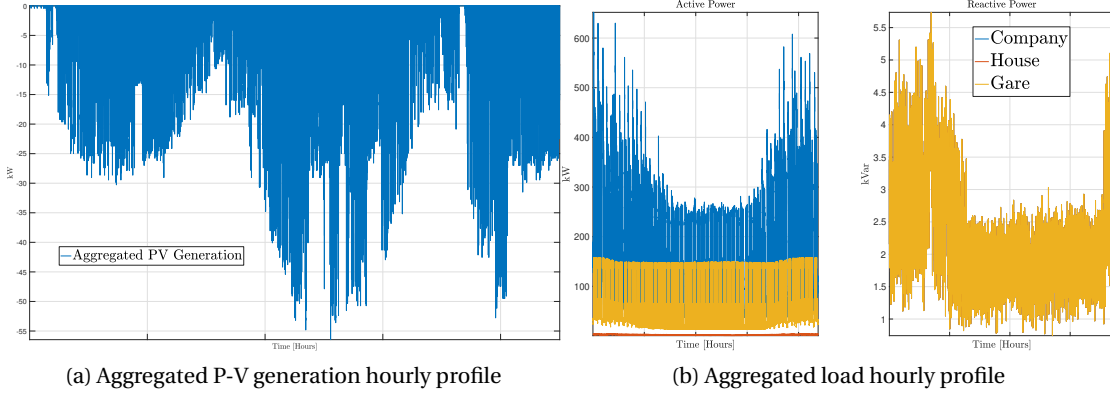


Figure 5.4: Inputted non-EV active and reactive nodal injection profiles

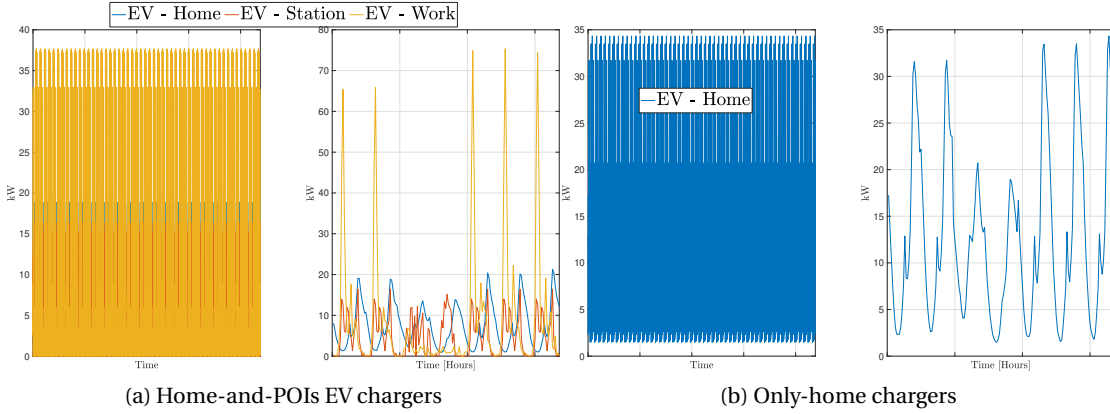


Figure 5.5: Inputted EV active (charging) nodal injection profiles

The post-LFMCSs results can be found in Figs. 5.6-5.24. In agreement with the international standard EN-50160 [48], all LFMCSs results are compared to a voltage variation around nominal voltage of 10% (i.e. $E_{i,min} = 0.9\text{p.u.}$ and $E_{i,max} = 1.1\text{p.u.}$) and also w.r.t. the real ampacity limits of the branches. Figs. 5.6-5.11 show the maximum, minimum and mean values computed from all the LF simulations, of the voltage and branch current magnitudes for all seasons, day-types and hours, for three different EV injection scenarios: no EV injection, 100% electrification with only home chargers and 100% electrification with home-and-point-of-interests (POIs) chargers. Figs. 5.12-5.14 show the boxplot representation of the apparent power for the slack node (see Fig. 5.3a) over the NUM_SIM LF simulations for all seasons, day-types and hours, for all three EV injection scenarios. Unless explicitly specified otherwise, the scales and axis (color axis) are all in per unit with a base voltage of 240V and a base power of 130kVA. It is clear from these figures that the Rolle-Gare grid: (i) *without EV injections* does not exhibit violations of the grid operational constraints, (ii) *with only home charging*, it suffers from voltages, branches currents and slack apparent power constraints violations, and (iii) *with home-and-POIs charging*, it suffers from voltages and slack apparent power constraints violations. This can be explained by the fact that, when more charging points are available, a smoothing effect of the peak-EV loads happens as all

5.2 Two Motivating Simulations & Experiments

generated EV CPs, independently of *only-home* vs. *home-and-POI* charger location hypothesis, satisfy the practically similar EV-user energy needs. Finally, it is important to note that in Figs. 5.9, 5.10 & 5.11 in subplots *Spring - Weekend - MAX* and *Spring - WeekDay - MAX*, there seems to be a few a branches currents magnitudes violations, however, after further investigation, we realised that this happened for only 1 out of the NUM_SIM simulations (c.f. Figs. 5.21a - 5.22)).

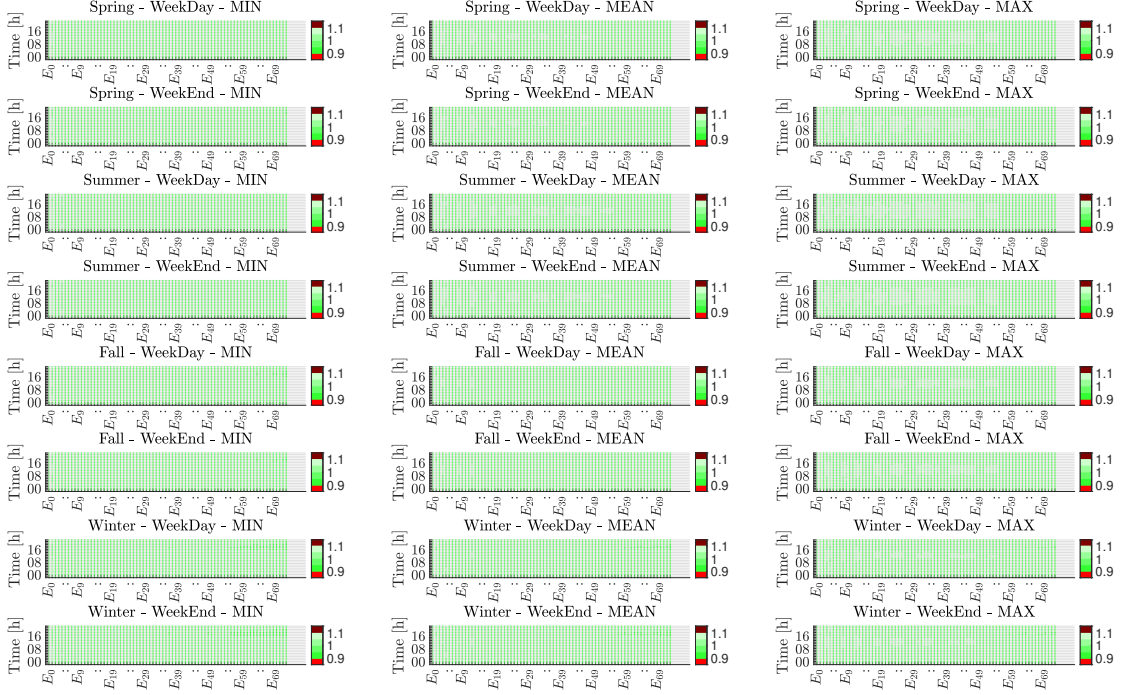


Figure 5.6: Nodal voltage magnitudes - min, mean and max over all NUM_SIM simulations - without EV chargers

To go a step further, and to show the sensitivity analysis vis-a-vis the percentage of the users fleet car electrification, Figs. 5.15-5.24 show the probabilities – computed directly from the obtained CDFs of the states and auxiliary variables of the Rolle-Gare grid – to violate the grid operational constraints. In principle, each figure should contain five sub-figures encapsulating respectively, 0%, 25%, 50%, 75% and 100% of private transport electrification (i.e. EV penetration). However, some graphs have been omitted when there were no statistically significant grid constraints violations (i.e. a violation probability equal to 0 for all seasons, day-types and hours). One can conclude from the figures that:

- Without EV charging there are no violations of the grid security constraints.
- With *only* home charging, at 25% EV penetration there are no grid constraints violations, while at 50% and 75%, there are nodal voltage magnitude constraints violations and at 100% all grid constraints are at risk to be violated (see Figs.5.15, 5.21a & 5.23).
- With home and POI charging, at 25% and 50% EV penetration there are no grid constraints violations, while at 75% and 100% there are nodal voltage magnitude and apparent slack power magnitude violations (see Figs.5.16 & 5.24).
- The more EV injections the more likely (i.e. higher probability) the constraints can be violated.

Chapter 5. Context & Motivations

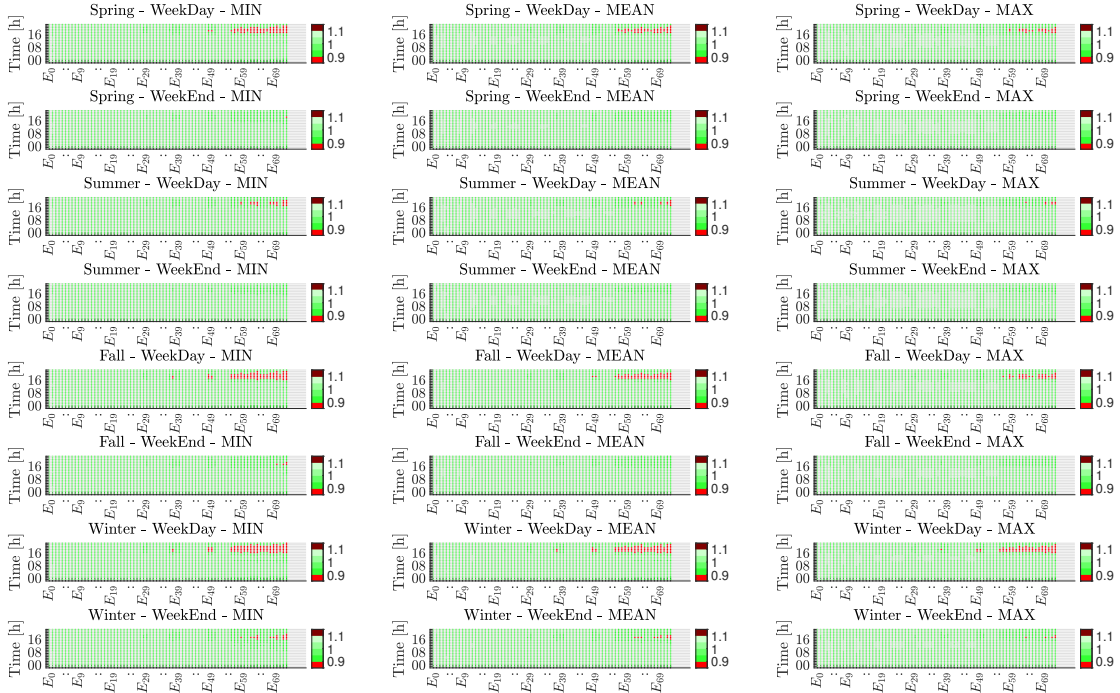


Figure 5.7: Nodal voltage magnitudes - min, mean and max over all NUM_SIM simulations - only home EV chargers

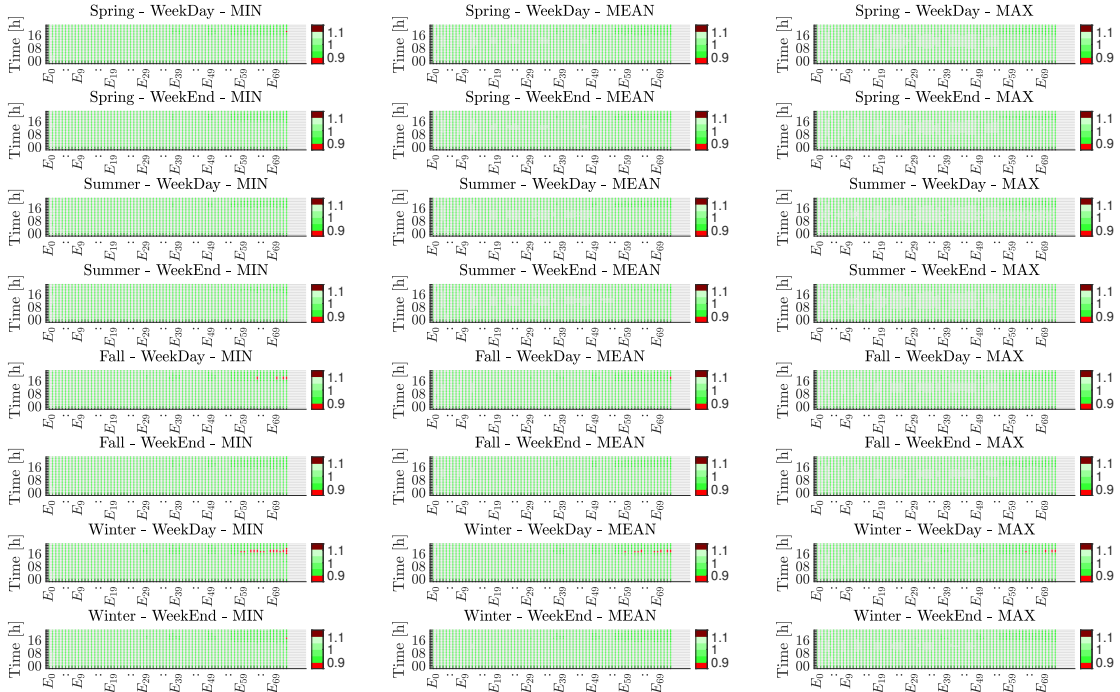


Figure 5.8: Nodal voltage magnitudes - min, mean and max over all NUM_SIM simulations - home-and-POIs EV chargers

5.2 Two Motivating Simulations & Experiments

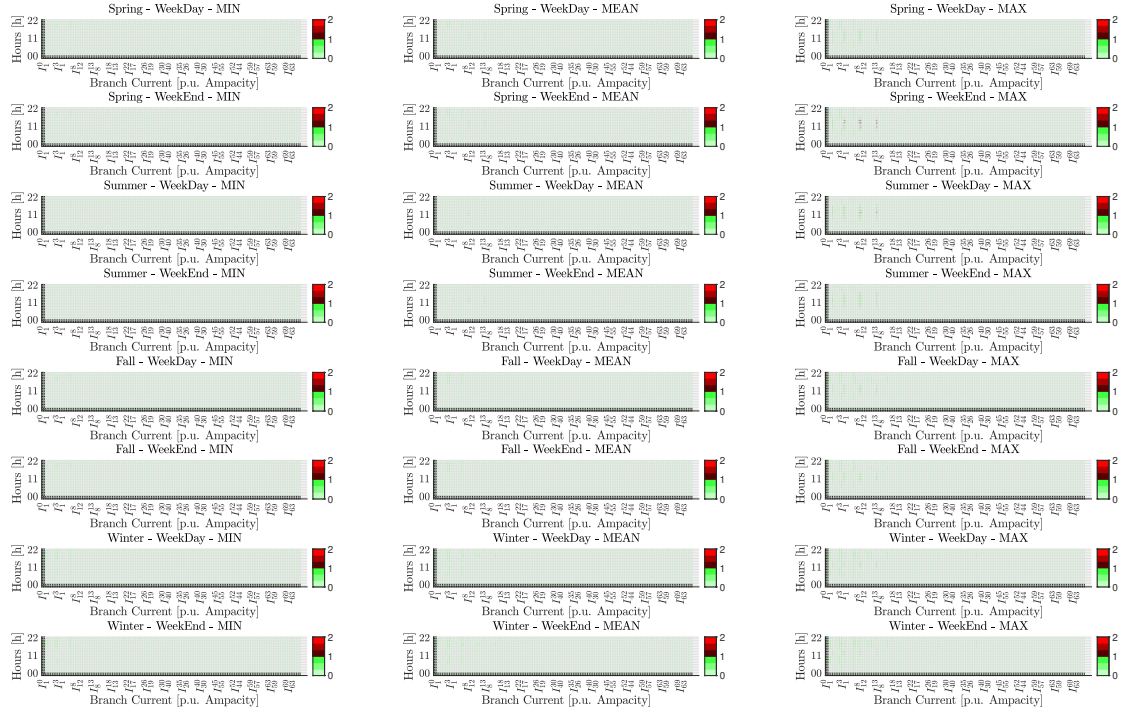


Figure 5.9: Branches currents magnitudes - min, mean and max over all NUM_SIM simulations - without EV chargers

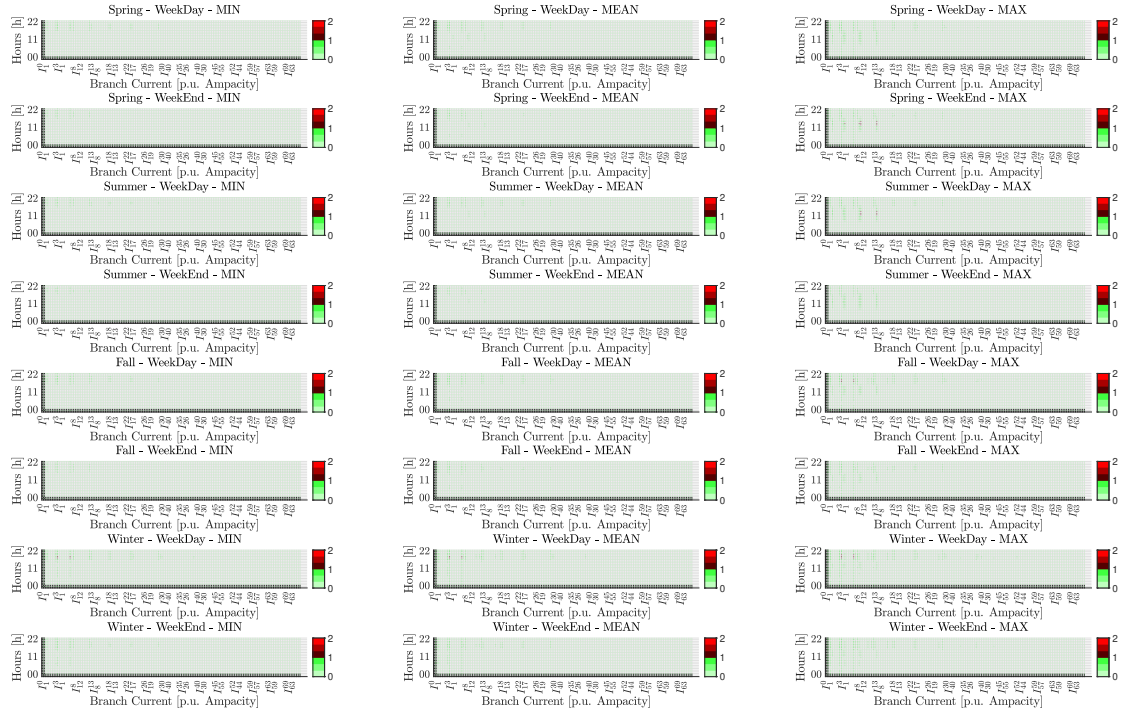


Figure 5.10: Branches currents magnitudes - min, mean and max over all NUM_SIM simulations - only home EV chargers

Chapter 5. Context & Motivations



Figure 5.11: Branches currents magnitudes - min, mean and max over all NUM_SIM simulations - home-and-POIs EV chargers

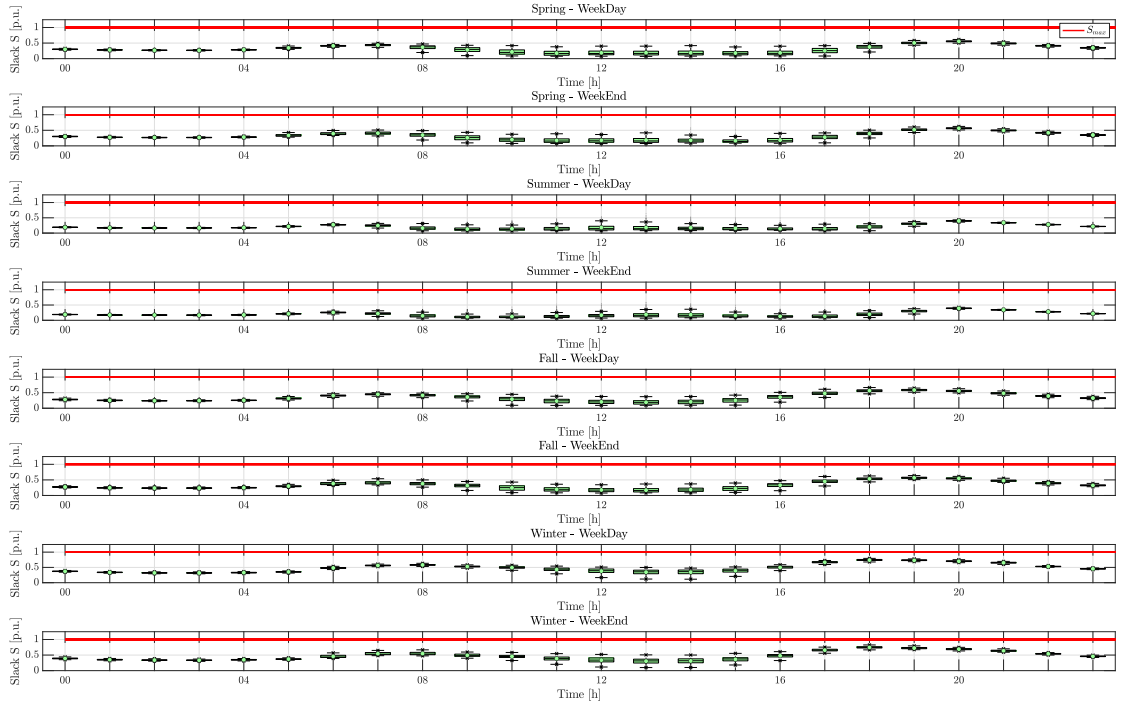


Figure 5.12: Slack apparent power magnitudes - boxplot over all NUM_SIM simulations - without EV chargers

5.2 Two Motivating Simulations & Experiments

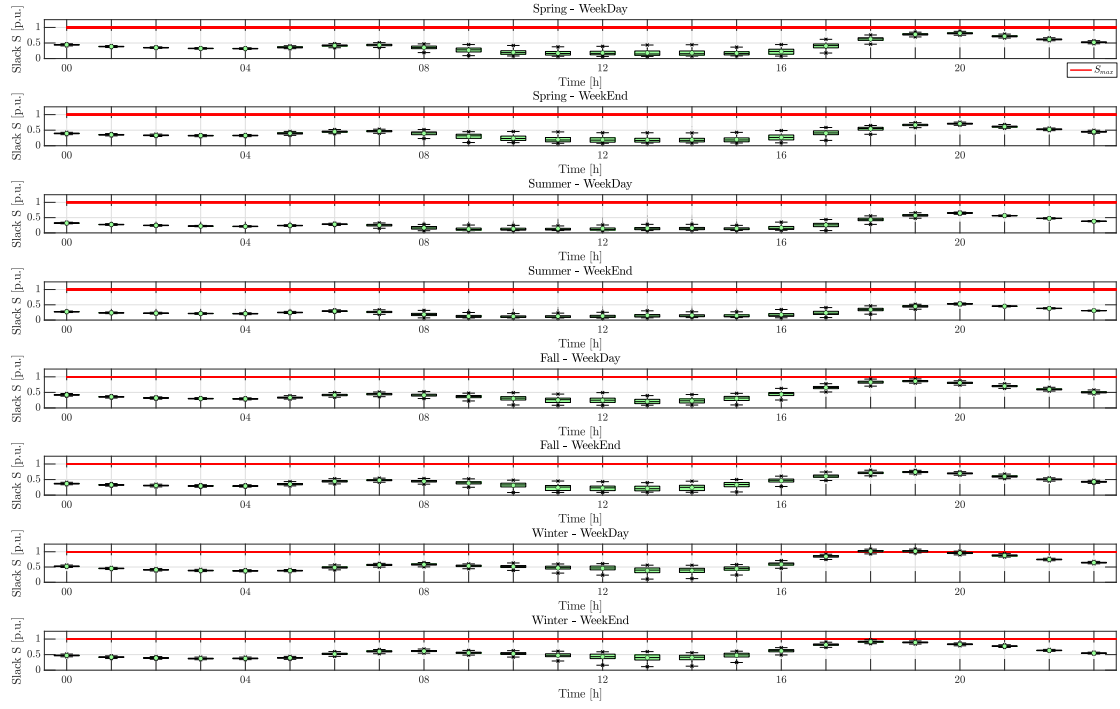


Figure 5.13: Slack apparent power magnitudes - boxplot over all NUM_SIM simulations - only home EV chargers

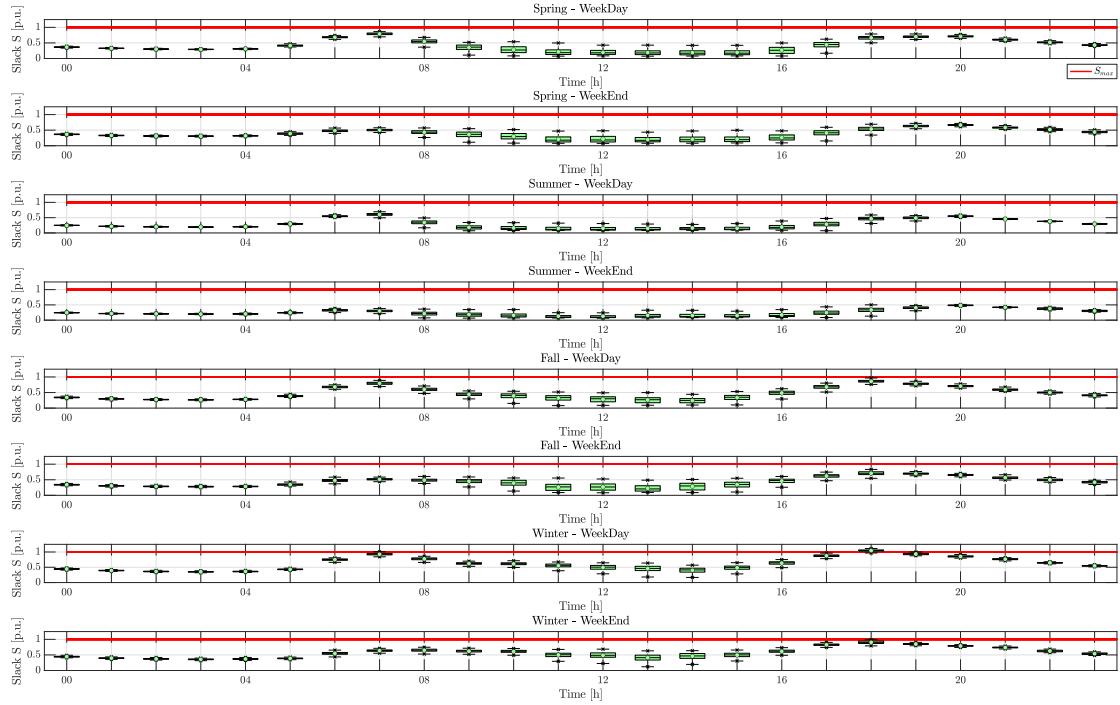
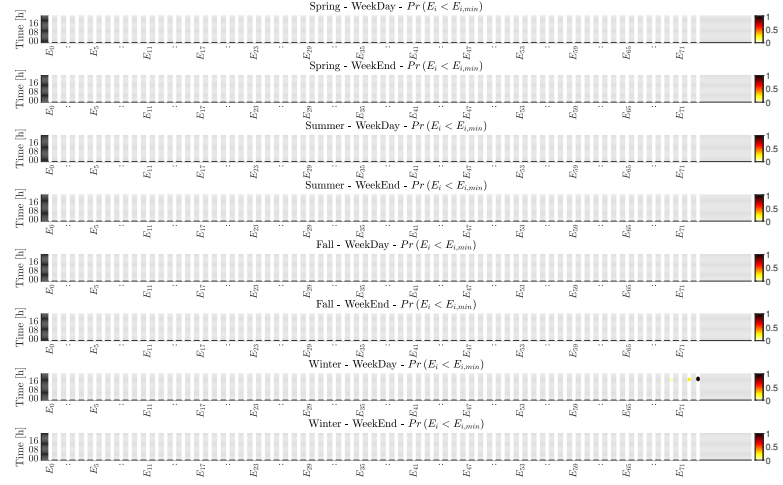


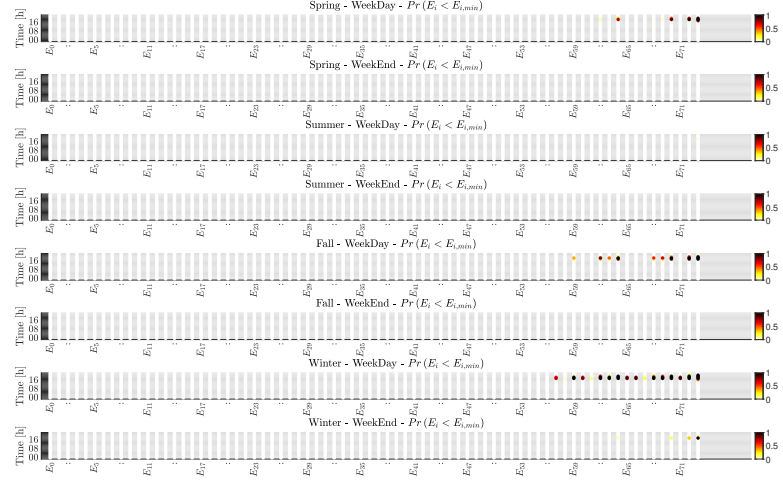
Figure 5.14: Slack apparent power magnitudes - boxplot over all NUM_SIM simulations - home-and-POIs EV chargers

- Voltage magnitude constraint violations occur mostly at night when there is no P-V. Indeed, the violations are more likely to happen in the winter when heating electricity demands are increased compared to the summer. The nodes at the end of the feeder are more likely to experience violations compared to the ones next to slack node. This is in accordance with the radiality of the network topology, the principle of voltage drops along electrical branches and EV load placement. More than one node suffers from potential voltage magnitude constraint violations.
- With the exception of the branch connecting nodes 2 and 7, the capacity limits of the Rolle-Gare grid branches are high enough to sustain the extra EV loads. However, it is clear from Fig. 5.22a that, during winter nights, there's a 80-90% chance that the branch connecting nodes 2 to 7 experiences branch current violations. This suggests that in grids such as this one, even though uncontrolled night charging at home is acceptable most of the year, in the winter it can have severe consequences that call for dedicated controlled charging strategies or grid reinforcements.

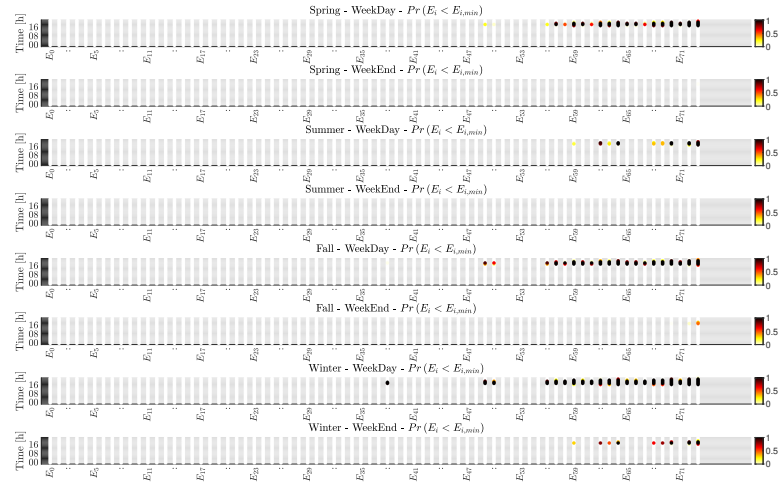
5.2 Two Motivating Simulations & Experiments



(a) 50% EV penetration



(b) 75% EV penetration



(c) 100% EV penetration

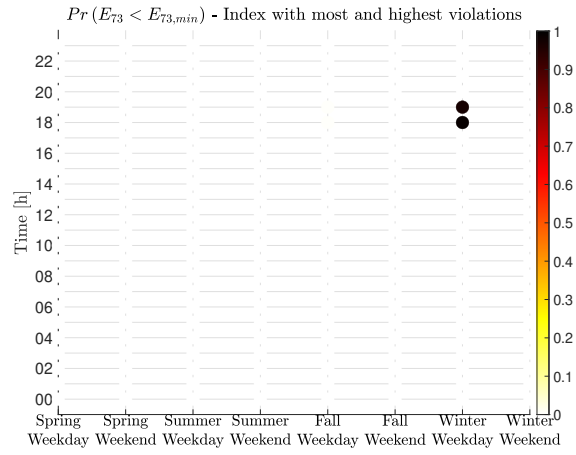
Figure 5.15: Probability to violate nodal voltage magnitudes - Only home EV chargers

Chapter 5. Context & Motivations

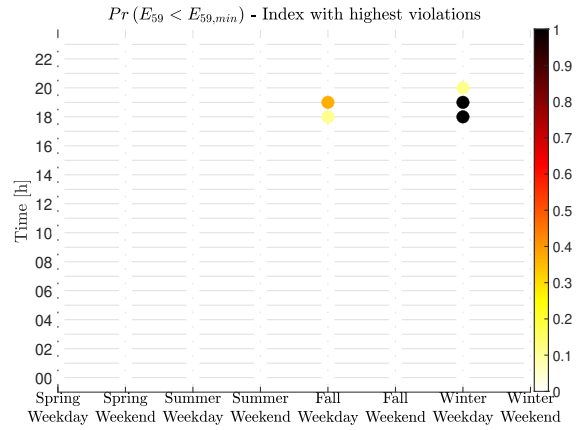


Figure 5.16: Probability to violate nodal voltage magnitudes - home-and-POIs EV chargers

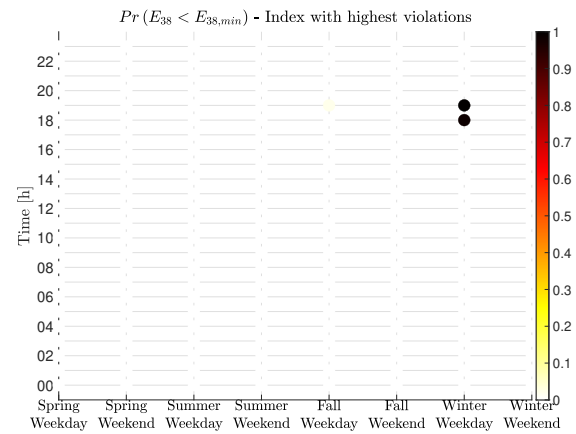
5.2 Two Motivating Simulations & Experiments



(a) 50% EV penetration

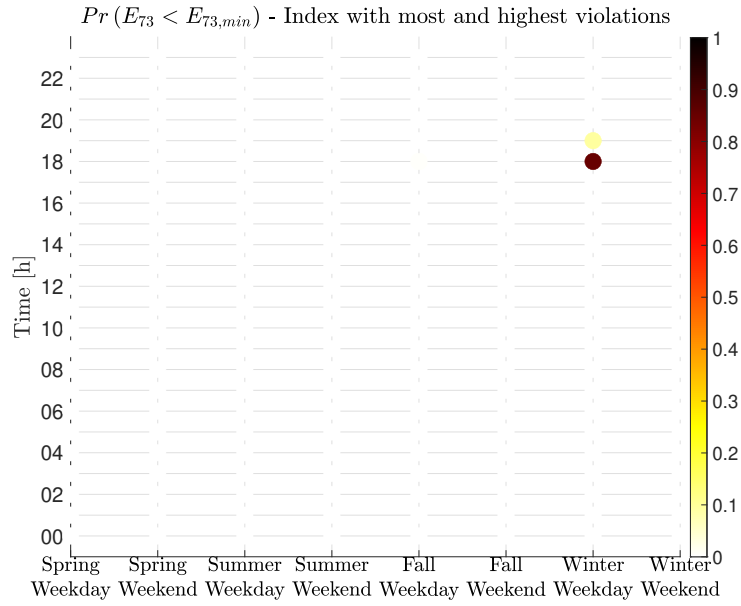


(b) 75% EV penetration

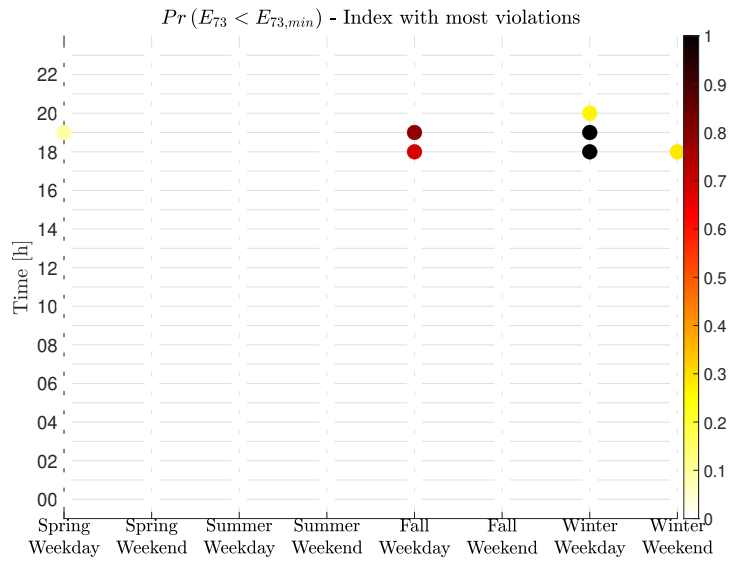


(c) 100% EV penetration

Figure 5.17: Probability to violate nodal voltage magnitude of the grid bus with highest violations - only home EV chargers



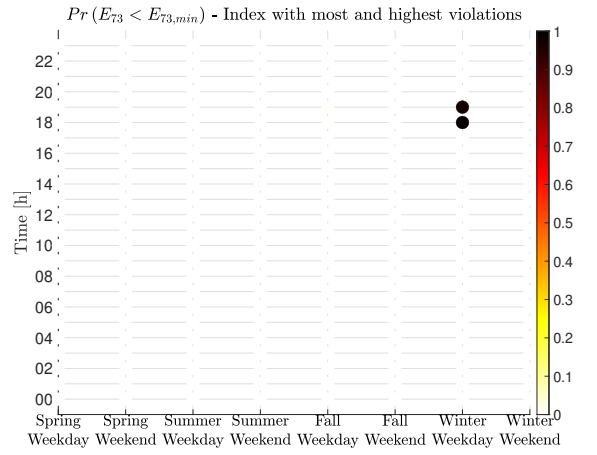
(a) 75% EV penetration



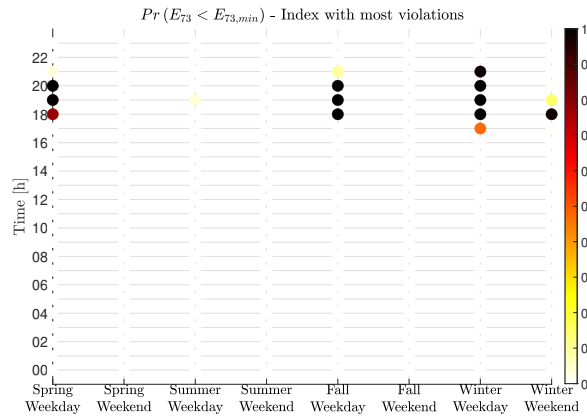
(b) 100% EV penetration

Figure 5.18: Probability to violate nodal voltage magnitude of the grid bus with highest violations - home-and-POIs EV chargers

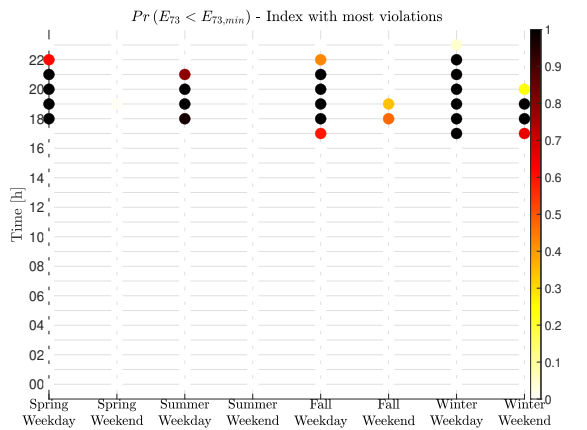
5.2 Two Motivating Simulations & Experiments



(a) 50% EV penetration

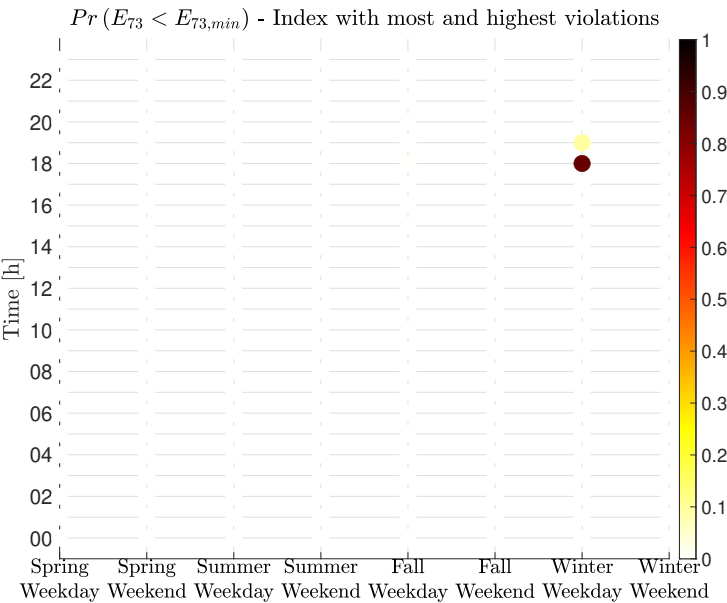


(b) 75% EV penetration

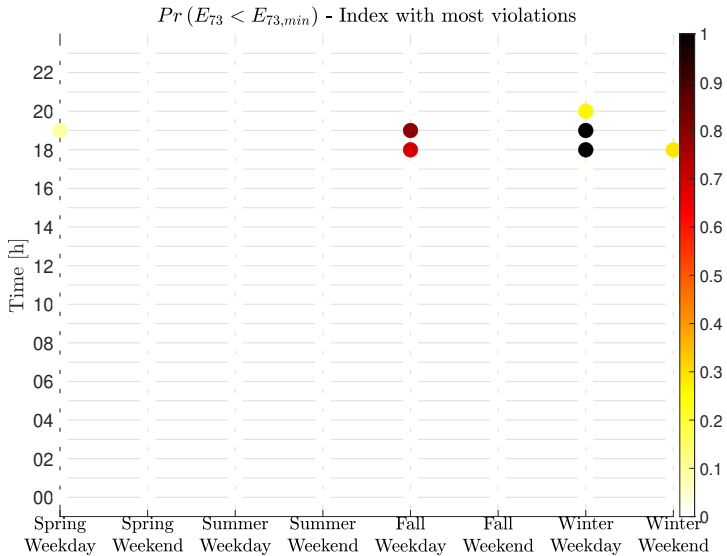


(c) 100% EV penetration

Figure 5.19: Probability to violate nodal voltage magnitude of the grid bus with most violations - only home EV chargers



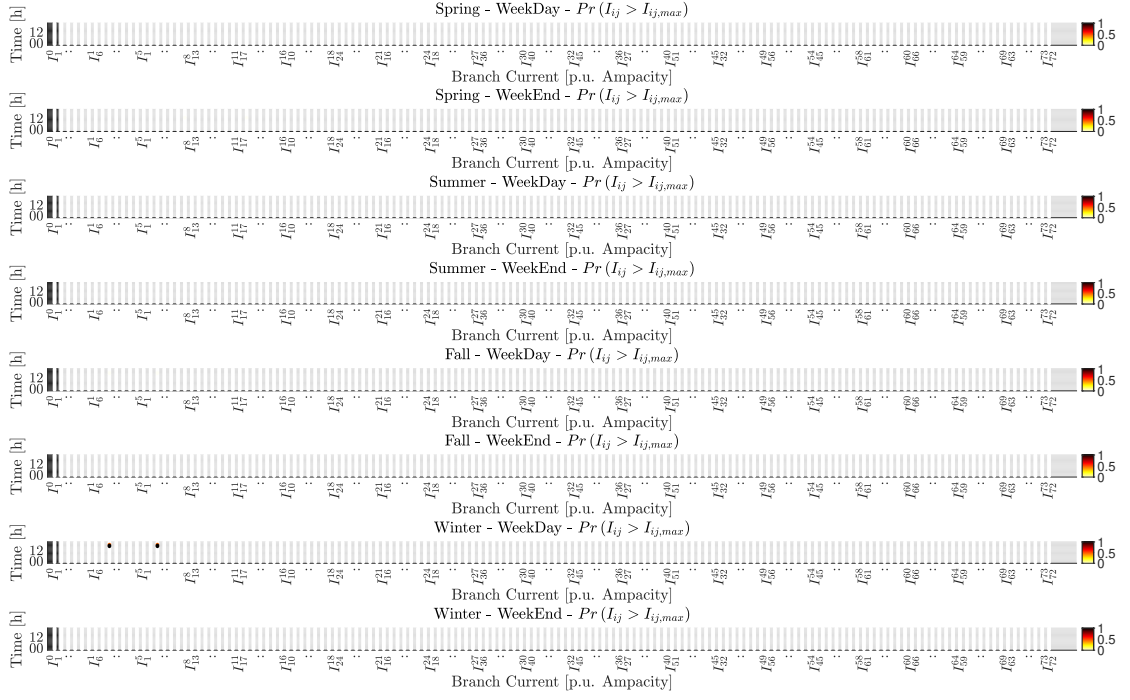
(a) 75% EV penetration



(b) 100% EV penetration

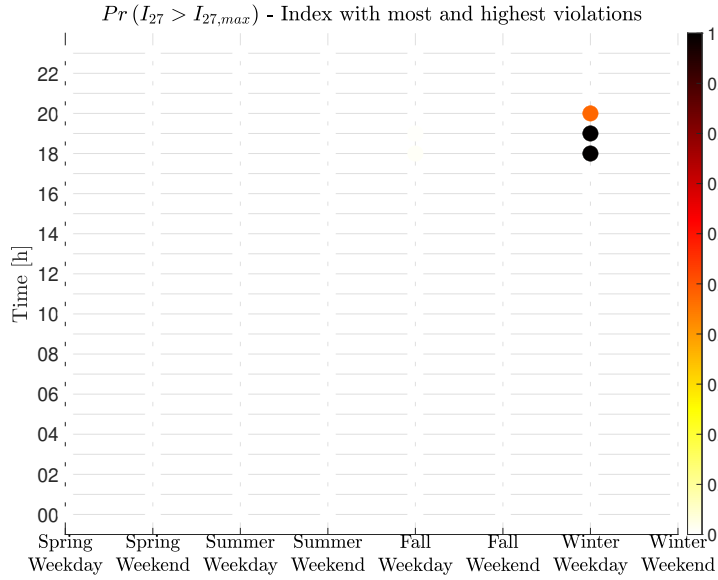
Figure 5.20: Probability to violate nodal voltage magnitude of the grid bus with most violations - home-and-POIs EV chargers

5.2 Two Motivating Simulations & Experiments



(a) Only home EV charging - 100% EV penetration

Figure 5.21: Probability to violate branch current magnitudes



(a) Only home EV charging - 100% EV penetration

Figure 5.22: Probability to violate branch current magnitude of the grid branch with highest & most violations

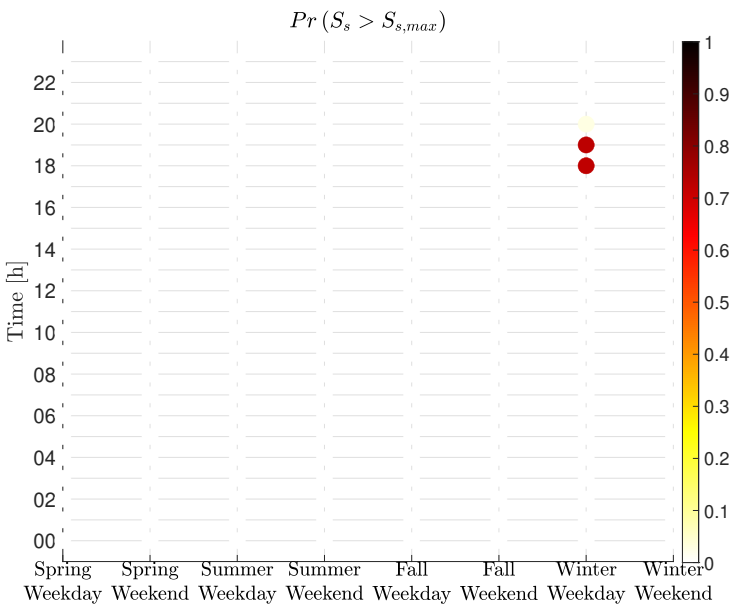
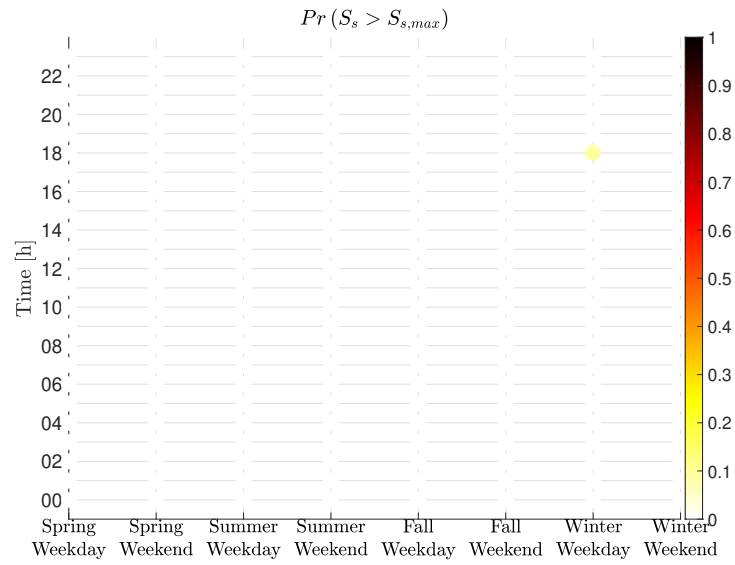
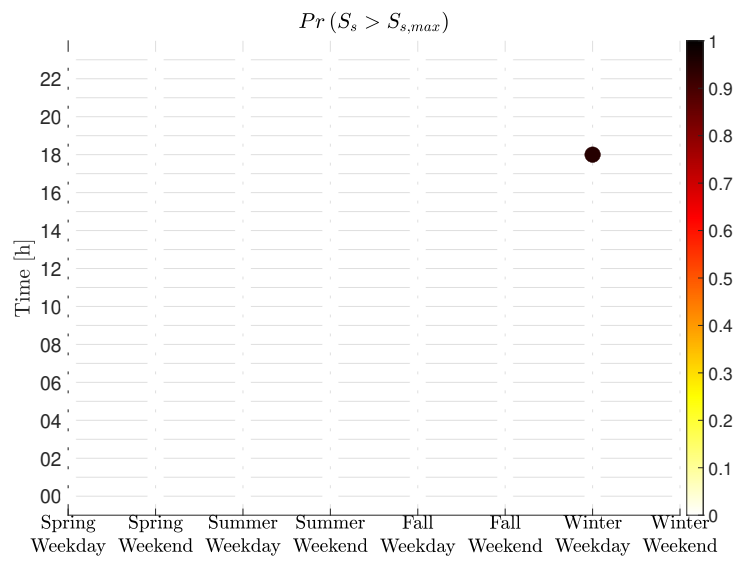


Figure 5.23: Probability to violate slack apparent power magnitude - only home EV charging - 100% EV penetration

5.2 Two Motivating Simulations & Experiments



(a) 75% EV penetration



(b) 100% EV penetration

Figure 5.24: Probability to violate slack apparent power magnitude - home-and-POIs EV charging

Rolle - Hopital The network map, topology and real resource location are shown in Figs. 5.25a-5.25b and Tab. 5.2. We recall that the EVCSs were added artificially as a controlled numerical simulation.

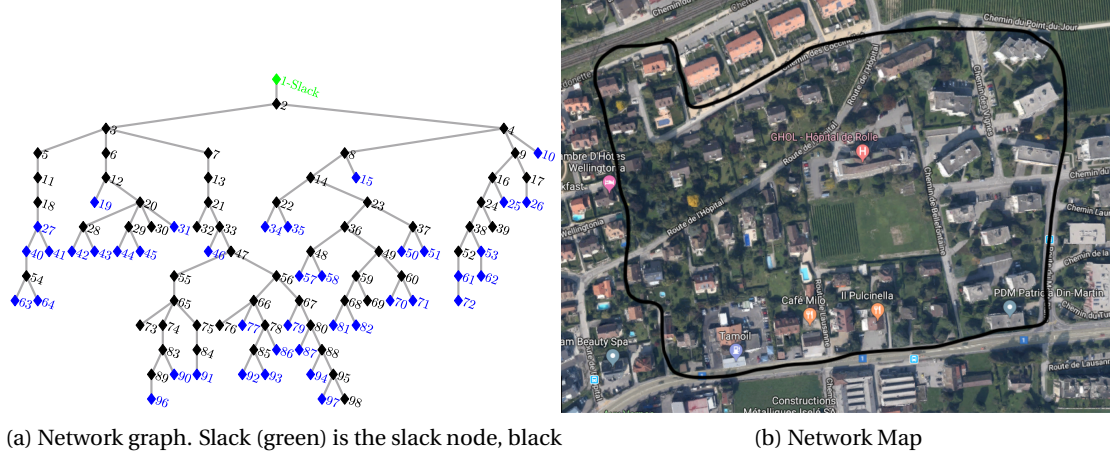


Figure 5.25: Rolle Hopital grid - network topology

The simulation setup, i.e. input data, data synthesis and general assumptions, is similar as the one of the previous simulation. For the sake of space, only the qualitative results are listed hereinafter for this grid⁴⁰. Indeed, unlike the previous grid, without EV injections the Rolle-Hopital grid suffers from minor nodal voltage magnitude constraints violations. Furthermore, with only home and home-and-POIs charging, the grid suffers from voltage, branch current and slack apparent power constraints violations. After analysing all the results, including the sensitivity analysis vis-a-vis the percentage of the users fleet car electrification, one can conclude that:

- Without EV charging there are minor nodal voltage magnitude constraints violations.
- With *only* home charging, at 100%, 75% and 50% EV penetration all grid operational constraints are violated. However, at 25% EV penetration there are no branch current magnitudes violations and only minor slack apparent power constraints violations.
- With home and POI charging, at 100%, 75% and 50% EV penetration all grid operational constraints are violated. However, at 25% EV penetration there are no slack apparent power constraints violations and only minor branch current magnitudes violations.
- As in the other considered grid, the more EV injections the more likely (i.e. higher probability) the grid operational constraints are to be violated.
- Compared to the previous grid, there are more risks of violating voltage magnitude security constraints during more seasons and hours of the day.

⁴⁰The interested reader is referred to [95], where the graphical results can be found in Sec. 6.3.2 of the collaborative report entitled *Electricity-based Mobility: Analysis of greenhouse gas emissions in the context of an evolving energy system*. Note that, the access to the report is restricted, however, contact details can be found on the web-page.

5.2 Two Motivating Simulations & Experiments

Table 5.2: Rolle Hopital grid - resource nodes with description and peak injections

Node	Type	Load-Peak [kW]	Generation-Peak [kW]
10	Residential Home	0.8	0
15	Residential Home	1.6	0
19	Residential Home	14.4	0
25	Company	7.2	0
26	Residential Home	2.4	0
27	Residential Home	2.4	0
31	Residential Home	4	0
34	Residential Home	4.8	0
35	Residential Home	3.2	0
40	Residential Home	2.4	0
41	Residential Home	0.8	0
42	Residential Home	8	0
43	Residential Home	9.6	0
44	Restaurant	11.2	0
45	Restaurant	12	0
46	Gas Station	2.4	0
50	Residential Home	2.4	10.98
51	Residential Home	4.8	10.98
53	Residential Home	4	3.66
57	Residential Home	4	0
58	Residential Home	6.4	0
61	Residential Home	0.8	0
62	Residential Home	4.8	0
63	Residential Home	3.2	0
64	Residential Home	2.4	0
70	Residential Home	4	7.32
71	Residential Home	5.6	0
72	Residential Home	4	0
77	Residential Home	2.4	0
79	Residential Home	0.8	0
81	Residential Home	4.8	0
82	Residential Home	5.6	10.98
86	Hospital	27.2	0
87	Residential Home	0.8	0
90	Residential Home	4	0
91	Residential Home	2.4	0
92	Residential Home	1.6	0
93	Residential Home	0.8	0
94	Residential Home	0.8	0
96	Residential Home	14.4	0
97	Residential Home	1.6	0

Chapter 5. Context & Motivations

- Similarly to the previous grid, the risk of incurring grid operational constraints violations is at its highest during winter nights. However, in this grid, it is clear that the problem occurs also during other seasons and during other periods of the day.
- This grid is *weaker* compared to the previous one and it is evident that, satisfying EV user needs without a dedicated control infrastructure or major grid reinforcements, is quasi-impossible.

Summary

Both simulations revealed that tools like the LFMCSs should be used to quantify the impact of EVCSs on distribution power-grids. Indeed, both simulations showed that EV loads put at risk the grid operational security. Even though the Rolle-Gare network had less issues than the Rolle-Hopital network, both simulations showcased that non-negligible *control* actions are needed if a full electrification of private transport is reached. In the first analysed LV grid (i.e. Rolle-Gare) only minor branch ampacity issues and mostly under-voltages have been quantified. Therefore, one can conclude that minor grid reinforcement, coupled with suitable voltage regulation, are enough to handle the private mobility full electrification in that grid. On the other hand, the Rolle-Hopital network presented major branch ampacity violations, under-voltages and transformer overloads (i.e. slack apparent power larger than 1 p.u.), thus, needed grid reinforcements might implicate major economical expenses. Therefore, in such cases, a smart charging algorithm can be used to satisfy EV user needs while steering the electrical grid to operate in a safe state (c.f. Sec.6). As a final note, it is clear that every grid will behave differently and simulations using the presented tool can give insights on the strategy to be adopted in order to prepare the grid for 100% electrification of private transport.

5.2.2 A deeper look into EVs: Controllability and Local effects on the grid

In this subsection two sets of experiments are performed to showcase the controllability of an EV and its local loading effects on low-voltage grids. In the following, first, the experimental setup is described, then, the results are shown.

Experimental Setup

The experiments were performed on the EPFL-DESL microgrid described in Sec. 3.5.1. The main hardware used for the experiments is the *L2 EV* block shown in Fig. 3.3 connected to bus 14. All other resources were disconnected from the microgrid. The *L2 EV* resource consists in an EVCS with 3 plugs (see Fig. 5.26). More specifically, it consists in two *non-commercial* unidirectional Type-2 plugs and one *commercial* bidirectional CHAdeMO plug. The plugs' technical characteristics are in Tab. 5.3. Finally, it is worth noting that each plug is monitored – in terms of three-phase voltage and current phasor measurements – leveraging sensors that feed a NI cRIO-9068 [96] – equipped with NI 9215 AI Modules – that runs the phasor-extraction algorithm presented in Sec. 3.4.2.

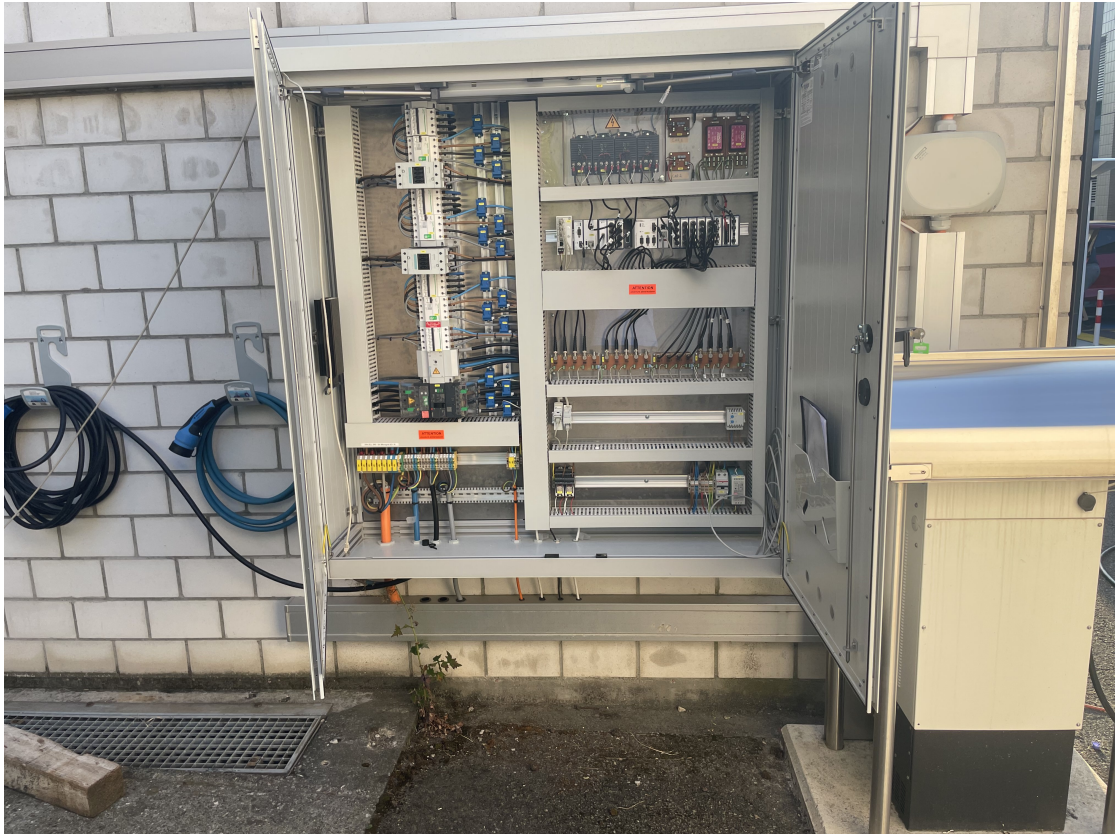


Figure 5.26: The EPFL-DESL microgrid EVCS

Table 5.3: EPFL-DESL microgrid EVCS technical characteristics

	Plug 1 - Type-2	Plug 2 - Type-2	Plug 3 - CHAdEMO
Protocol	IEC-61851 [97]	IEC-61851 [97]	DCMS - proprietary protocol of EvTec [98]
Protocol Notes	<ul style="list-style-type: none"> Based on an analog pulsed <i>control pilot</i> signal Logic implemented using NI CompactRio and AI/AO Modules The maximum per-phase current that the car can consume is set by modulating the control pilot's duty cycle 	<ul style="list-style-type: none"> Based on an analog pulsed <i>control pilot</i> signal Logic implemented using NI CompactRio and AI/AO Modules The maximum per-phase current that the car can consume is set by modulating the control pilot's duty cycle 	<ul style="list-style-type: none"> Based on a TCP/IP-based websockets communication Explicit active power setpoint control
Protection	<ul style="list-style-type: none"> Circuit breaker - A9F84432 - 32A [99] Differential breaker with earth-leakage Type B protection - A9Z61440 [100] 	<ul style="list-style-type: none"> Circuit breaker - A9F84432 - 32A [99] Differential breaker with earth-leakage Type B protection - A9Z61440 [100] 	<ul style="list-style-type: none"> Circuit breaker - A9F84432 - 32A [99] Differential breaker with earth-leakage Type B protection - A9Z61440 [100]
Rating	<ul style="list-style-type: none"> IEC-61851 protocol limited 80A per phase EPFL-DESL Microgrid branch amapcity is 82A A9F84432 circuit breaker trips at 32A 	<ul style="list-style-type: none"> IEC-61851 protocol limited 80A per phase EPFL-DESL Microgrid branch amapcity is 82A A9F84432 circuit breaker trips at 32A 	10kVA

Experimental Results

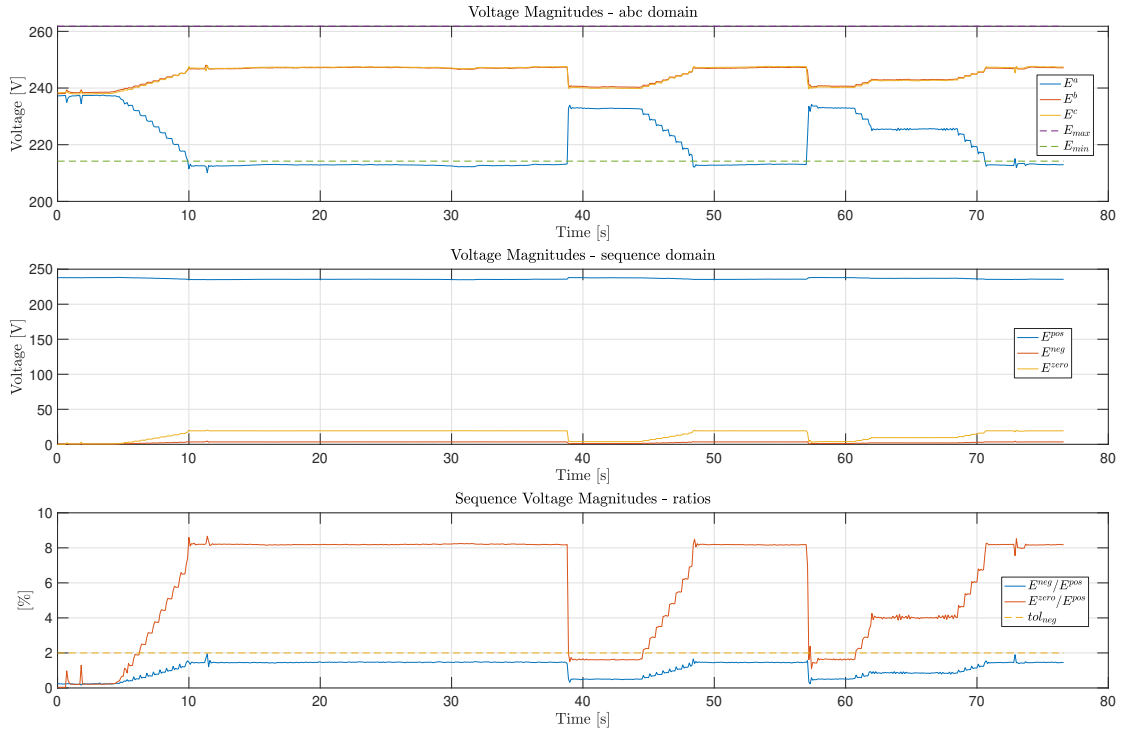
Load unbalances resulting from single-phase charging This experiment was performed on a Jaguar I-Pace. The peculiarity of this EV is that it has a Type-2 plug, i.e. an AC three-phase connector, yet, its on-board charger is a single-phase device (the rated power of the on-board charger is 7kW). The goal of the experiment was to send the EV time varying setpoints – in the form of maximum allowable per-phase charging current – and monitor the behavior of the nodal voltages at the EVCS. More specifically, as we want to showcase the *worst-case* unbalances, we perform two minimum to maximum charging current step-responses where the second-one is done in two-stages. Note that, as per the IEC-81851 protocol [97] the lowest setpoint that could be sent to an EV is 6A. The results are shown in Fig. 5.27. The figures show that, when the car is at full-power consumption, i.e. 32A on phase a, the load unbalance pushes the grid operational constraints to their limits. Indeed, one can see in Fig. 5.27a that (i) the nodal voltage magnitude constraint is violated in the form of an undervoltage, and (ii) the negative- over positive- sequence nodal voltage magnitudes ratio is close to the limit set by the EN-50160 standard [48]. Furthermore, one can see an oscillatory *ladder* behavior together with a ramping effect when the setpoint is increased. The latter is further investigated in the next set of experiments. Finally, it is worth noting that after the first few seconds – $\sim 10s$ – needed by the EV's on-board controller to initialising the charge, the power factor remains unitary practically over the whole charging session despite the little bursts of reactive power injections.

EV on-board controller response times This set of experiments was performed on both a Jaguar I-Pace and a Tesla Model S 90D. The Model S has a Type-2 plug, i.e. an AC three-phase connector, with an on-board three-phase charger (the rated power of the on-board charger is 16.6kW). The goal of the experiment was to send the EVs time varying setpoints – in the form of maximum allowable per-phase charging current – and, this time, monitor the reactivity of the on-board controller to alter the EV's charging power. More specifically, the experiments consists in subsequent pulses from the minimum setpoint of 6A to a user-defined setpoint then back to 6A. The pulses' duration are long enough for the on-board controllers to stably reach the desired setpoint. Between each subsequent pulse, the desired setpoint is increase by 1A. The experiment ends when the last pulse reaches the maximum allowable per-phase charging current of the tested EV (32A for the Jaguar I-Pace and 24A for the Tesla Model S).

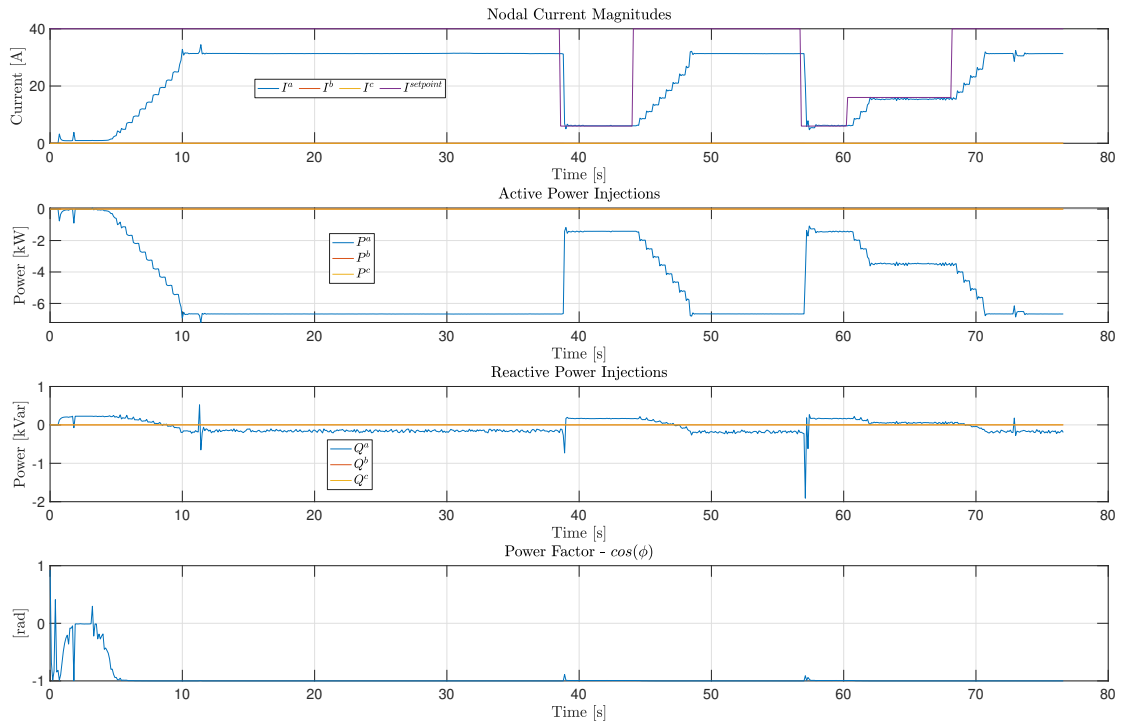
The results are shown in Fig. 5.28. The figures show that, as observed in the previous experiment, the on-board controllers exhibit ramping effects when trying to increase their consumption following a setpoint increase. Furthermore, Fig. 5.28b shows that the on-board Tesla Model S controller has a couple of behaviors that the on-board Jaguar I-Pace controller does not have. More specifically, first, as seen in Fig. 5.28b, the Tesla's controller exhibits a constant deadband of 2.5seconds. Indeed, as soon as the setpoint changes the controller increases its consumption by about 1A then pauses for 2.5seconds before starting the setpoint ramp. Second, as seen in Fig. 5.28b, sometimes the current consumption exhibits an oscillatory behavior before reaching its final intended target setpoint. This can be explained by a potential second-order response that the on-board controller on the Tesla Model S exhibits as a function of its battery DC-voltage dynamics.

The response times for both experiments are reported in Tab. 5.4. Response times are defined as the time-differences between setpoint changes and when the consumed currents start to stabilise. The reporting time, i.e. time-resolution accuracy, of the experiments was set to 100ms. As the communication and sensing infrastructures are either wired or based on analog signals, the latter response times are dominated by the EVs' on-board controllers' reaction times and logic (i.e. communication delays

Chapter 5. Context & Motivations



(a) Nodal voltage profiles



(b) Nodal current and power injections profiles

Figure 5.27: Results of the load unbalances experiment performed using the Jaguar I-Pace

are quasi-nonexistent). From Tab. 5.4 it seems that with the increase of the user-defined setpoint, the response-times of both EVs' on-board chargers linearly increase. This linear trend is very evident in the case of the Jaguar I-Pace while, for the Tesla Model S, the trend is sometimes disrupted by the sporadic second order oscillations that were previously evoked. Oppositely, as in the previous experiment, all setpoint decreases lead to quasi-instantaneous consumption decreases with no ramp limitations. Indeed, independently of user-defined setpoint, the Jaguar I-pace and Tesla Models S's on-board controllers take less than 400 milliseconds to decrease their consumption to 6A per-phase.

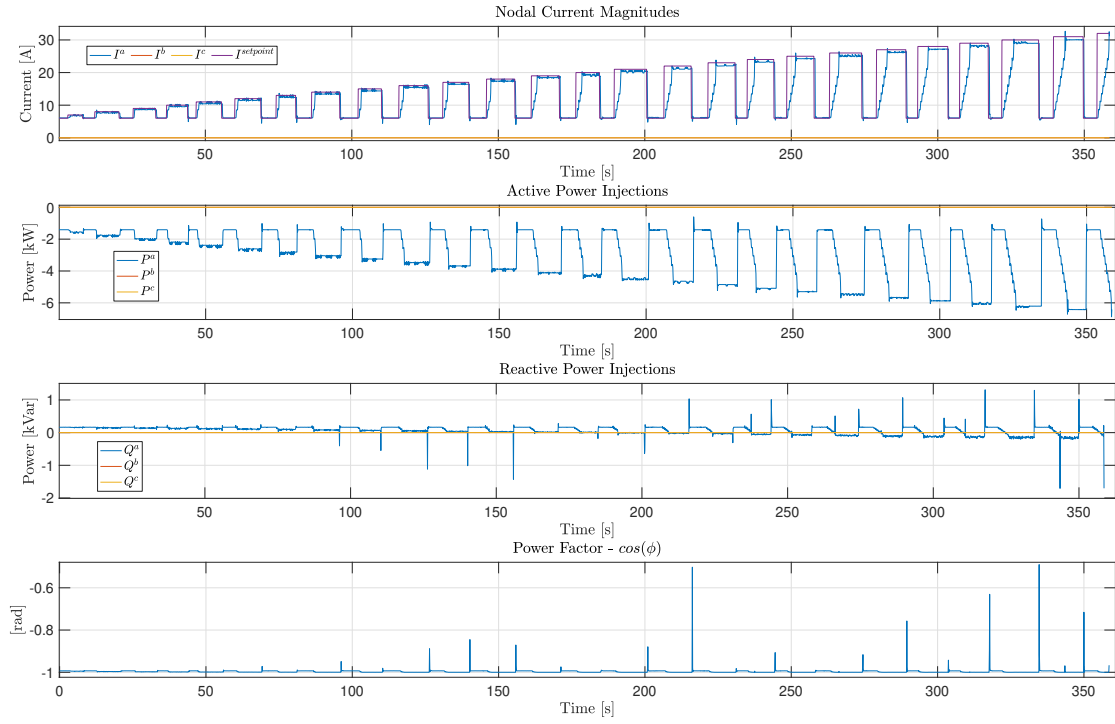
Finally, it is worth mentioning that, the Jaguar's on-board controller seems to perfectly reach the desired setpoint while the Tesla's controller exhibits a behavior where the absorbed phase current is around 1A less than the setpoint. This behavior was well documented in the literature [101]⁴¹ and explains why, for the Tesla Model S, the desired setpoint in Tab. 5.4 goes up to 25A even though its maximum allowable per-phase charging current is 24A.

Summary

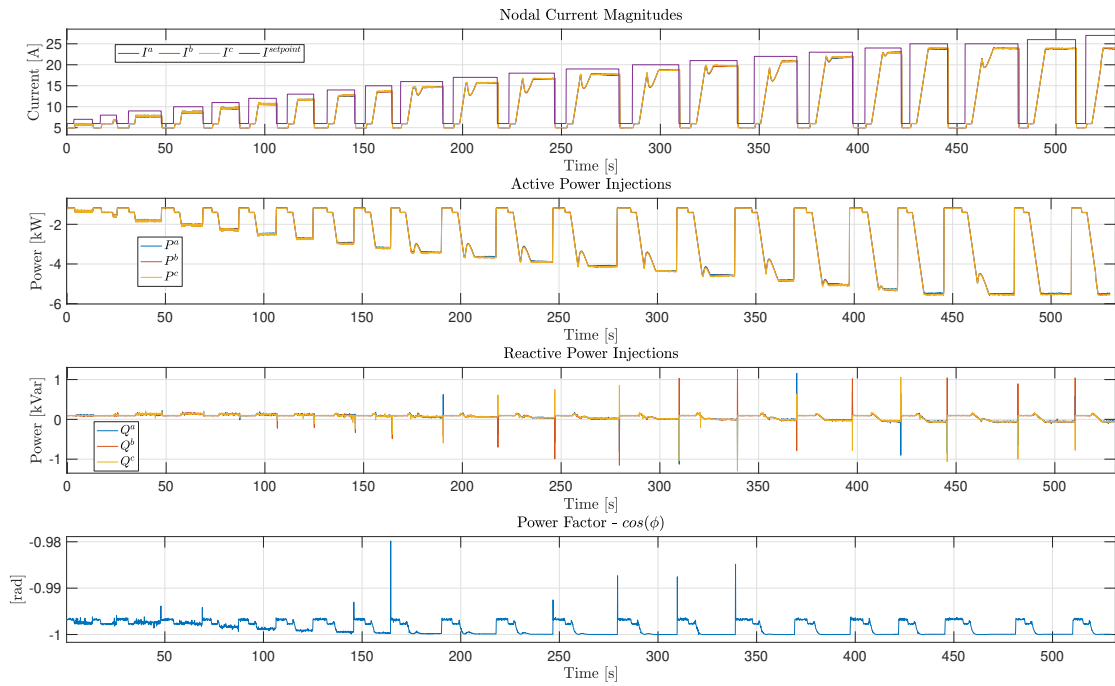
Both sets of experiments revealed that (i) EVs have non-negligible local effects on distribution grids' operational constraints, and (ii) EVs' on-board chargers cannot be controlled in sub-second time-scales. More specifically, even though an individual single-phase charging EV does not heavily violate the local power-quality grid operational constraints, as soon as a few EVs simultaneously charge at full-power on the same grid node, the EN-50160 [48] negative sequence constraint would not be satisfied. Furthermore, by combining the results of both experiments and the LFMCSs, a distribution grid's voltage magnitude constraints are also at risk when single-phase EVs charge simultaneously. Generally speaking, it seems that each car manufacturer designs its EV to safely charge in case it is the only grid-connected resource. However, since in practice multiple other resources and EVs are simultaneously grid-connected, their real impact on grid operational constraints is expected to be way higher. In terms of controllability, the experiments revealed that: (i) not all cars behave exactly the same way when it comes to setpoint tracking, and (ii) independently of the EV, on-board chargers have response-times in the order of seconds or tens of seconds. Therefore, as in the previous section, it is clear that there is a need for different real-time (i.e. seconds-to-minutes scales) smart charging control frameworks if EVs will be used in time-deterministic real-time controls (e.g. frequency containment reserve or local grid voltage/line congestion controls).

⁴¹For the interested reader, we refer to [102] where authors dealt with the phenomena by pre-computing power-to-current look-up tables in order to explicitly control Type-2 EVs in terms of active power consumption (c.f. Sec.7.5.2).

Chapter 5. Context & Motivations



(a) Jaguar I-Pace



(b) Tesla Model S

Figure 5.28: Results of the EV controllability experiment: nodal current and power injections profiles

5.2 Two Motivating Simulations & Experiments

Table 5.4: Response times of the on-board controllers of the Jaguar I-Pace and Tesla Models S for setpoint variation starting from 6A – the minimum per-phase setpoint an EV can receive as per the IEC-61851 communication protocol – to a desired setpoint

Desired Setpoint [A]	Setpoint Variation [A]	Jaguar I-Pace [s]	Tesla Model S [s]
7	1	0.9	0.6
8	2	0.8	4.5
9	3	0.8	3.7
10	4	0.9	4.3
11	5	0.8	4.5
12	6	1.1	4.9
13	7	1.1	5.2
14	8	1.3	5.7
15	9	1.3	6
16	10	1.7	11.1
17	11	1.8	11.9
18	12	1.8	12.3
19	13	2.1	12.7
20	14	2.2	13.2
21	15	2.4	11.9
22	16	2.8	14.1
23	17	2.8	11.4
24	18	2.6	11.4
25	19	2.6	10.4
26	20	3.3	N/A
27	21	3.8	N/A
28	22	3.8	N/A
29	23	3.9	N/A
30	24	4.2	N/A
31	25	4.2	N/A
32	26	4.2	N/A

5.3 Contributions of the next chapters of Part II

The second part of this thesis contains two original contributions addressing the *main* observations of the previous motivational section namely: (i) uncontrolled EV charging could lead to (local) grid operational constraints violations, (ii) simultaneous single-phase EV charging could lead to non-negligible load unbalances that could violate the power quality operational constraints, and (iii) EVs on-board controllers respond within seconds to setpoint variations. Each contribution constitutes an upcoming chapter. In the following, a summary of the latter is given.

1. **Chapter 6** As previously mentioned, the penetration of EVCSs, along with the progressive connection of stochastic distributed generation, is increasing the probability of violating the power distribution grid operational constraints and deteriorate the quality of power supply. To this end, the first contribution [103] consists in a real-time control scheme for allocating power set-points to EVCSs while accounting for the grid operational requirements. In the proposed problem formulation the grid and the power injections are modelled accounting for their unbalanced 3-phase nature, thus enabling to formulate the problem objective and its constraints adopting the sequence decomposition. The EVs' users need, along with the stochastic nature of other uncontrollable injections (e.g. loads and generation from P-V generation units), are also taken into account. A distributed control scheme, with a minute-scale control horizon, is proposed where local controllers, operating at EV aggregation level, compute EV battery-secure power set-points. These controllers send their set-points to a central controller operating at the grid aggregation level. The central controller solves a scenario-based linearized OPF that, by leveraging SCs (c.f. Sec.2.3), accounts for grid operational (i.e. static and power quality) constraints. Then, it sends back its solution to the respective local controllers. The obtained iterative algorithm is efficiently solved until convergence. We analyse the performance of the proposed control scheme via a simulation ran on the IEEE-34 test distribution feeder augmented with EVCSs. Comparisons with two other control algorithms, a grid-unaware local controller and a myopic maximum power controller, are included to benchmark the proposed control scheme.
2. **Chapter 7** The second contribution consists in an extension to the work presented in [6]. Indeed, since the power consumed by EVs adds extra uncertainties on aggregate load/generation imbalances at the PCC of an ADN, this contribution extends the grid-aware algorithms presented in [6] by accounting for EVCSs power and energy demands in the day-ahead planning stage and, by leveraging the other contribution of this part, considers EVs as controllable resources in the real-time control stage. More specifically, in the day-ahead stage, forecasted EV-user behaviours and needs are included in the computation of a grid-aware DP. In the real-time stage, as done for other resources in [6], a modified version of the grid-unaware local controller, presented in the previous contribution, is included in the problem statement in order satisfy inputted EV user needs within user-defined constraints. EVCSs of all types are considered in the context of this contribution, i.e. uni- or bi-directional AC or DC charging. The proposed algorithm is first simulated on MATLAB on a benchmark distribution grid to showcase the advantages of considering EVCSs as controllable entities in the day-ahead stage. Then, an experiment is performed on the EPFL-DESL microgrid, showcasing the ability of the real-time controller to follow the day-ahead EV-aware optimally computed DP.

6 Grid-aware Distributed Control of Electric Vehicle Charging Stations in Active Distribution Grids

Keywords— Electric Vehicles Charging Stations, Real-Time, i.e. seconds-to-minute scale, Distributed Control, Grid Operational Constraints and Power Quality.

6.1 Introduction & Literature Review

As previously mentioned, the electrification of the private transportation sector, along with a move towards distributed renewable generation, are being proposed as early solutions to reduce CO₂ emissions. Due to their high-power demand, the deployment of EVCSs is increasing the probability of violating static distribution grid operational constraints (i.e., exceeding branch ampacity limits, nodal under/over-voltages and substation transformers overloads) [104]. Furthermore, with the increased penetration of single-phase EV chargers, the risk of voltage unbalances, and consequently the deterioration of ADNs' power quality, is high. The complexity behind developing control schemes that deal with the latter originates from several factors: (i) the stochastic behaviour of EV users, (ii) the high EV power demand, (iii) the stochasticity of renewable DG that might not coincide with EV peak load demands, and (iv) the scalability of centralized charge management control frameworks. In this regard, this chapter proposes a real-time, i.e. seconds to minutes scale, *distributed* EV power allocation algorithm that takes into account (i) EV users' needs, (ii) ADNs' operational constraints, and (iii) the stochastic nature of *non-controllable* power generation units and loads that need to be forecasted.

Centralised and distributed *real-time* algorithms for EV scheduling and optimal charging that account for grid constraints has been the object of comprehensive literature. In, [105], a distributed locally optimal scheduling algorithm for EVCSs that determines optimal charging/discharging powers is proposed. The local algorithms take into account EV user needs, battery lifetime and local energy balances using grid forecasts sent by a centralized grid observer. In [106] and [107], two centralised grid-aware EV power allocation algorithms are developed. In [106], authors develop an iterative algorithm that first computes EV power allocations that satisfy user demands based on priority schemes. Then, it verifies through LF calculus whether the allocations satisfy the static grid voltage constraints; in case they do not, charging is postponed to the next time-step. In [107], the proposed algorithm assumes that grids are balanced three-phase, linearizes the power-flow equations and accounts for substation transformer maximum power capacity and voltage magnitude violations at nodes where EVCSs are connected. In [108] and [109], two decentralised grid-aware EV power allocation algorithms are developed. In [108], assuming that the grid is radial and balanced, a lossless LinDistFlow power-flow

Chapter 6. Grid-aware Distributed Control of Electric Vehicle Charging Stations in Active Distribution Grids

linearization is used to develop a decentralised EV charging control scheme that maximizes (i) EV energy demands, and (ii) peak-load shaving. In [109], assuming that grids are radial, "roughly balanced" and that losses are "relatively small", a three-phase power-flow linearization using the branch-flow model is used to develop a decentralised EV charging protocol. Both algorithms in [108] and [109] incorporate EV user needs, however, although battery degradation is considered in [108], they both do not consider non-EV load and generation stochasticity. With the exception of [109], all these works assume balanced three-phase grids thus neglecting the impact that single-phase EV charging may have on voltage unbalance.

Unlike all the presented works, we propose a real-time decentralised control scheme to allocate active (charging) and reactive power setpoints to EVCSs. We directly account in the problem for the ADN's static and power-quality operational constraints without specific assumptions on grid-radiality and losses. To do so, we use a three-phase OPF modelled by power-flow linearization leveraging SCs (c.f. Sec. 2.2). Furthermore, uncontrollable and stochastic loads and generation are taken into account by leveraging scenario-based optimisation (c.f. Sec. 4.1.2). Additionally, (i) EV user needs, i.e. reaching target SoCs at specified departure times, (ii) EV battery wearing, and (iii) EV charging modes, i.e. three-phase, single-phase and DC charging, are all considered and/or accounted for in the problem formulation. Finally, to guarantee scalability, the problem is formulated in a separable form enabling the use of the ADMM to decompose and solve the problem in a distributed manner. ADMM guarantees to converge to the solution of the non-distributed version of the proposed problem as power-flow equations are linearized and the centralised OPF objective is convex. As known, the ADMM splits the non-distributed problem into local problems and a central aggregator problem. In the proposed method, local problems satisfy EV user needs and are solved at the level of EV aggregators of nodes where there are EVCSs. As a result, they do not require any knowledge of the grid model. The central aggregator problem is solved at the level of a grid aggregator, e.g. a DSO. In practice, the goal of the grid aggregator is to coordinate with all EV aggregators to guarantee the satisfaction of grid operational constraints under injection uncertainty while accounting for EV user needs. It is therefore assumed that the developed method is aimed to be used by DSOs to ensure secure EV charging within their ADN.

In summary, the main contributions of this chapter are: i) a formulation of a real-time control scheme that accounts for grid static and power-quality operational constraints ii) a formulation of a generalized control scheme addressing the unbalanced nature of EV chargers, iii) to propose a separable formulation of the problem that decouples the grid and EVCSs aggregators' objectives and constraints, thus, enabling a distributed scalable formulation of the proposed control scheme, and iv) numerically benchmark the proposed method against two controllers that do not account for the grid constraints: (a) grid-unaware local controller (GULC) that only does local EV charge management at the EV aggregator level, and (b) myopic maximum power controller (MMPC) that performs maximum-power EV charging. The numerical simulations are performed on MATLAB using a modified IEEE-34 test distribution feeder [9].

The rest of the chapter is organised as follows. In Sec. 6.2, we first recall the nomenclature and grid modelling, then, we present the mathematical formulation of the problem. In Sec. 6.3 the ADMM technique used to distribute the problem is briefly recalled with respect to its application to the proposed control framework. In Sec. 6.4, numerical simulation results are shown. Finally, Sec. 6.5 concludes the chapter.

6.2 Problem Formulation

As previously, in this chapter, we consider generic 3-phase distribution networks with either *meshed* or *radial* topologies, where the neutral is available and distributed⁴². Similarly, they contain $|\mathcal{N}|$ buses, where \mathcal{N} is the set of bus indexes, and $|\mathcal{L}|$ branches, with \mathcal{L} being the set of network branches. $\mathcal{R} \subset \mathcal{PD}$ is the set of resource nodes. $\mathcal{C} \subset \mathcal{R}$ is the set of nodes to which EVCSs are connected. $\mathcal{Z} \subset \mathcal{PD} \setminus \mathcal{R}$ is the set of zero-injection nodes. All resources (i.e. generation, loads and zero-injection nodes) are modelled as PQ nodes⁴³. $\{s\} \subset \mathcal{S}$ is the slack node⁴³. As in the previous chapters, network branches are represented by 3-phase Π -circuit equivalents with known parameters that already embed the neutral conductor [110]. Thus, the network is described by the so-called compound admittance matrix [19] denoted by $\bar{\mathbf{Y}} = [\bar{Y}_{ij}^{\phi_1\phi_2}]$, with $i, j \in \mathcal{N}$ and $\phi_1, \phi_2 \in \{a, b, c\}$. The phase-to-neutral nodal voltages and nodal injected currents are respectively denoted by $\bar{\mathbf{E}}_t = [\bar{E}_{i,t}^\phi]$ and $\bar{\mathbf{I}}_t = [\bar{I}_{i,t}^\phi]$, with t being the time-step, $i \in \mathcal{N}$ and $\phi \in \{a, b, c\}$. The phase-to-neutral nodal positive-, negative- and zero- sequence voltages are denoted by $\bar{\mathbf{E}}_t^{\text{seq}} = [\bar{E}_{i,t}^{\text{seq}}]$, with $i \in \mathcal{N}$ and $\text{seq} \in \{\text{pos}, \text{neg}, \text{zero}\}$. As previously explained (c.f. Sec. 2.2.4) sequence voltages can be directly computed by multiplying the phase-to-ground nodal voltages with the transformation matrix $\mathbf{H}^{\text{abc} \rightarrow \text{seq}} = \text{diag}(\mathbf{H}_i^{\text{abc} \rightarrow \text{seq}})$, where $\mathbf{H}_i^{\text{abc} \rightarrow \text{seq}} = \frac{1}{3} [1, 1, \alpha; 1, h^2, h; 1, h, h^2]$, with $h = e^{j2\pi/3}$. The branch currents are denoted by $\bar{\mathbf{I}}_{ij,t} = [\bar{I}_{ij,t}^\phi]$, with $(i, j) \in \mathcal{L}$. The apparent power injections are denoted by $\bar{\mathbf{S}}_t = \mathbf{P}_t + j\mathbf{Q}_t = [\bar{S}_{i,t}^\phi] = \bar{\mathbf{s}}_t + \bar{\mathbf{s}}_{t,\text{EV}}$, with $\bar{\mathbf{s}}_t = [\mathbb{1}_{i \in \mathcal{R}} \{\bar{s}_{i,t}^\phi\}]$ being the nodal injections of all resources, $\bar{\mathbf{s}}_{t,\text{EV}} = [\mathbb{1}_{i \in \mathcal{C}} \{\bar{s}_{i,\text{EV},t}^\phi\}]$ being the nodal aggregate injections of all EVCSs. The apparent power injections at the slack node (s) are denoted by $\bar{\mathbf{S}}_{s,t} = [\bar{S}_{s,t}^\phi] = [\bar{E}_{s,t}^\phi \bar{I}_{s,t}^\phi]$ with $\phi \in \{a, b, c\}$. Furthermore, as in the previous chapters, we adopt the convention where negative nodal injections are absorptions while positive injections are actual injections into the grid. Note that aggregate active nodal power injections of EVCSs, $\mathbf{p}_{t,\text{EV}} = \Re\{\bar{\mathbf{s}}_{t,\text{EV}}\}$, are non-positive as we only consider EV charging in the scope of this contribution. However, the aggregate reactive nodal power injections of EVCSs, $\mathbf{q}_{t,\text{EV}} = \Im\{\bar{\mathbf{s}}_{t,\text{EV}}\}$, are considered bi-directional when one or more EVCSs connected to a node $i \in \mathcal{C}$ support bi-directional reactive power-flows (e.g. mode 4 - DC chargers).

The goal of the proposed method is to solve an OP, at every time-step t , that determines $\bar{\mathbf{s}}_{t,\text{EV}}$. The OP objectives and constraints can be grouped into two sub-problems. The first, referred to as *grid sub-problem*, guarantees the safe operation of the grid by solving an OPF that considers the stochastic nature of non-EV nodal injections (c.f. 6.2.1) while accounting for grid operational constraints. The second, referred to as *EV sub-problem*, satisfies EV user requirements while minimizing EV-battery wearing (c.f. 6.2.2). In the following we present the objectives and constraints of each of the sub-problems separately.

6.2.1 Grid sub-problem

The grid sub-problem is a real-time, i.e. seconds-to-minute scale, stochastic security-constrained OPF. As previously explained, OPF problems are non-convex due to the nature of the power-flow equations. Thus, to make it tractable and efficiently solvable, we linearize the power flow equations to

⁴²This assumption is needed as the developed algorithms account for the presence of single-phase EV chargers.

⁴³As in the previous chapters, these assumptions are not strict as it is straightforward to extend the proposed algorithms to account for either (i) all node-types, or (ii) multi-slack grids (c.f. Sec. 2).

Chapter 6. Grid-aware Distributed Control of Electric Vehicle Charging Stations in Active Distribution Grids

express the grid operational constraints⁴⁴ (see Sec. 6.2.1). The control time-step is chosen to be in the seconds-to-minutes scale to match the EV controllability results presented in Sec. 5.2.2. Therefore, to deal with the stochasticity of non-EV injections during minute-scale periods, we use scenario-based optimization (c.f. Sec. 4.1.2). Note that, even though we linearize the power-flow equations, we did not use chance-constrained optimization since our linearization model is dependent on the (stochastic) state of the grid and is not static (see [71] and c.f. Sec. 4.1.2). Each scenario contains a collection of nodal power injections for resource nodes sampled from pre-computed PDFs (c.f. Sec. 5.2.1). In the following, we first recall the method to create the latter PDFs. Then, we explain the formulation of the security constraints and, finally, present the grid sub-problem objective.

Constructing PDFs for resources' nodal power injections

As explained in Sec. 5.2.1, the PDFs are created using historical data in the form of active and reactive nodal injection profiles for every resource connected to a given node. Each of these profiles is first clustered into 4 seasons (i.e. winter, spring, summer and autumn), then, sub-clustered into day-type (i.e. working days, weekend or vacation days), then, finally sub-sub-clustered into the *fixed* time resolution of the control algorithm. For every sub-cluster, a Gaussian mixture model (i.e. a sum of multivariate Gaussian normal distributions) is fitted to the data using MATLAB's function `fitgmdist`. This is done to account for the time correlation between the different time-steps for each specific sub-clusters. At the end, we obtain multivariate (the random variables here are all the time-steps of a given day) PDFs for each nodal injection pertaining to a season and day-type.

Constraints

They are the static operational constraints of an ADN, i.e., the branch currents magnitudes, the nodal voltages magnitudes, the ratios of nodal voltages negative- over positive- sequences and zero- over positive- sequences, and the substation apparent power magnitudes, should all be within predefined bounds. The negative- and zero- sequence voltage bounds are added to abide with the EN-50160 std. [48]⁴⁵ and to mitigate the voltage unbalances created by single-phase EV chargers. As before, each of the latter electrical quantities is linearized and expressed using their partial derivatives with respect to active and reactive nodal injections, i.e., SCs computed using the approach presented in Sec. 2.3. As we consider scenario-based optimization, each grid operational constraint needs to be verified for all scenarios $d = 1, \dots, D$. Recall that a scenario represents random realizations of resource injections that assume the absence of EVCSSs. The constraints are given by,

⁴⁴We refer the interested reader to the work presented in [111] for details on the achievable performances one can expect when linearizing the power-flow equations in security-constrained OPFs.

⁴⁵We recall that, as in the first part of this thesis, all the above-mentioned ADN operational constraints are listed in the international standard EN-50160 [48] as hard-constraints except the ratio of the zero- over positive-sequence constraint. Indeed, as explained in the standard, verifying the negative- over -positive sequence constraint is enough. However, as known, minimizing the zero-sequence injections leads to lower load unbalances. Therefore, we decided here to add it as a hard constraint, but, in case a user considers this approach as too strict, the hard-constraint can be transformed into a soft one by minimizing the zero-sequence injections in the problem objective.

$$\begin{aligned} |\bar{\mathbf{E}}_t|^d &\in [E_{min}, E_{max}], |\bar{\mathbf{I}}_{ij,t}|^d \leq \mathbf{I}_{ij,max}, |\bar{\mathbf{S}}_{s,t}|^d \leq \mathbf{S}_{s,max} \\ |\bar{\mathbf{E}}_t^{neg}|^d &\leq tol_{neg} |\bar{\mathbf{E}}_t^{pos}|^d, |\bar{\mathbf{E}}_t^{zero}|^d \leq tol_{zero} |\bar{\mathbf{E}}_t^{pos}|^d \end{aligned} \quad (6.1)$$

where, E_{min} and E_{max} are, again, the allowed extremes of the nodal voltage magnitudes, tol_{neg} and tol_{zero} are, respectively, tolerances for the magnitudes of the negative- and zero- sequence nodal voltages, $\bar{\mathbf{I}}_{ij,max}$, is the vector of branch ampacity limits, $\bar{\mathbf{S}}_{s,max} = [\bar{S}_{s,max}^\phi]$ is the vector of per phase substation transformer apparent power limits and a superscript d refers to a scenario. $|\bar{\mathbf{E}}_t|$, $|\bar{\mathbf{I}}_{ij,t}|$, $|\bar{\mathbf{S}}_{s,t}|$, $|\bar{\mathbf{E}}_t^{neg}|$, $|\bar{\mathbf{E}}_t^{zero}|$ and $|\bar{\mathbf{E}}_t^{pos}|$ are generically linearly approximated by,

$$\begin{aligned} \Gamma_t^d &\approx \tilde{\Gamma}_t^d(\tilde{\mathbf{S}}_t^d) + \frac{\partial \Gamma_t}{\partial \mathbf{P}_t} \bigg|_{\tilde{\mathbf{S}}_t^d} (\mathbf{p}_{t,EV} - \mathbf{p}_{t-1,EV}) \\ &\quad + \frac{\partial \Gamma_t}{\partial \mathbf{Q}_t} \bigg|_{\tilde{\mathbf{S}}_t^d} (\mathbf{q}_{t,EV} - \mathbf{q}_{t-1,EV}) \end{aligned} \quad (6.2)$$

where, $\Gamma \in \{|\bar{\mathbf{E}}_t|, |\bar{\mathbf{I}}_{ij,t}|, |\bar{\mathbf{S}}_{s,t}|, |\bar{\mathbf{E}}_t^{neg}|, |\bar{\mathbf{E}}_t^{zero}|, |\bar{\mathbf{E}}_t^{pos}|\}$, $\tilde{\Gamma}_t^d(\tilde{\mathbf{S}}_t^d)$ is the electrical quantity resulting from the system-state obtained from a LF computation with nodal injections $\tilde{\mathbf{S}}_t^d = \tilde{\mathbf{s}}_t^d + \bar{\mathbf{s}}_{t-1,EV}$, where $\tilde{\mathbf{s}}_t^d$ are the sampled scenarios and $\bar{\mathbf{s}}_{t-1,EV}$ the optimal EV injections of the previous control timestep. Recall that the SCs $\partial \Gamma_t / \partial \mathbf{P}_t|_{\tilde{\mathbf{S}}_t^d}$ and $\partial \Gamma_t / \partial \mathbf{Q}_t|_{\tilde{\mathbf{S}}_t^d}$ are, respectively, the partial derivatives of the electrical quantity Γ with respect to nodal active and reactive power injections, computed with the injections $\tilde{\mathbf{S}}_t^d$ using the method of Sec. 2.3. We recall that assuming that $\bar{\mathbf{Y}}$ is invariant to nodal injections, all other auxiliary SCs can be directly computed using (6.3).

$$\begin{aligned} \frac{\partial \bar{S}_{s,t}^\phi}{\partial \{\mathbf{P} \text{ or } \mathbf{Q}\}_t} \bigg|_{\tilde{\mathbf{S}}_t^d} &= \frac{\partial \bar{E}_{s,t}^\phi}{\partial \{\mathbf{P} \text{ or } \mathbf{Q}\}_t} \bigg|_{\tilde{\mathbf{S}}_t^d} \bar{I}_{s,t}^\phi + \bar{E}_{s,t}^\phi \frac{\partial \bar{I}_{s,t}^\phi}{\partial \{\mathbf{P} \text{ or } \mathbf{Q}\}_t} \bigg|_{\tilde{\mathbf{S}}_t^d} \\ \frac{\partial [\bar{E}_{i,t}^{zero}, \bar{E}_{i,t}^{pos}, \bar{E}_{i,t}^{neg}]^T}{\partial \{\mathbf{P} \text{ or } \mathbf{Q}\}_t} \bigg|_{\tilde{\mathbf{S}}_t^d} &= \mathbf{H}_i^{abc \rightarrow seq} \frac{\partial [\bar{E}_{i,t}^a, \bar{E}_{i,t}^b, \bar{E}_{i,t}^c]^T}{\partial \{\mathbf{P} \text{ or } \mathbf{Q}\}_t} \bigg|_{\tilde{\mathbf{S}}_t^d} \end{aligned} \quad (6.3)$$

Finally, note that the *only* variables in (6.2) for a control timestep t , i.e., $\mathbf{p}_{t,EV}$ and $\mathbf{q}_{t,EV}$, do *not* have a superscript d as we want these variables to satisfy the constraints for *all* scenarios, rendering the optimal output robust to nodal injections stochasticity as D increases (c.f. Rem. 3 and [72] for information about choosing an adequate number of scenarios).

Objective

From the grid operator perspective, since all the security constraints were added as hard constraints, the objective is, *in theory*, free to be defined by the modeller. In practice, having branch currents close to their ampacity limits can affect the cables' lifetimes and increase network losses, thus, the simplest

considered objective is to minimize

$$\langle \mathbf{1}, \left(\frac{\partial |\bar{\mathbf{I}}_{ij,t}|}{\partial \mathbf{Q}_t} \Big|_{\tilde{\mathbf{s}}_t^d} (\mathbf{q}_{t,\text{EV}} - \mathbf{q}_{t-1,\text{EV}}) \right) \oslash |\bar{\mathbf{I}}_{ij,t}| \rangle, \quad (6.4)$$

where $\mathbf{1}$ is a vector of ones, \oslash is the Hadamard division (i.e. element-wise vector division) and the \langle, \rangle is the standard dot product. The latter objective minimises the per-unit-ampacity branch-current-magnitudes by only exploiting EVCSs reactive power injections. Indeed, this allows the active power to be fully optimised for the EV sub-problem objectives (see section 6.2.2), and, in case EVCSs have unused apparent power, e.g. due to the absence of plugged EVs, a useful utilization of the remaining flexibility.

6.2.2 EV sub-problem

An EVCS sub-problem aims, for every time-step, to compute the power allocations given to the different EVs connected to the different EVCSs k , with $k = 1, \dots, K_i$, where K_i is the total number of EVCSs connected to node $i \in \mathcal{C}$. Indeed, we assume that at every node $i \in \mathcal{C}$, there is an *aggregator* that can send active and reactive power setpoints to all EVCSs (or EV plugs) $k = 1, \dots, K_i$. For simplicity, and without loss of generality, each EVCS is assumed to have a fixed charging mode, i.e. three-phase (3ph), single-phase (1ph) or direct current charging (DC). Furthermore, we assume that (i) three-phase chargers are balanced, (ii) DC chargers are connected to all three phases through a balanced inverter (i.e. balanced in active and reactive powers), and (iii) single-phase chargers can be connected to any phase. Additionally, only EVCSs with DC charging are assumed to have controllable bidirectional reactive power flow as this is the situation in practice⁴⁶. However, in the future, if other charger types start supporting bidirectional power flow, little change needs to be done to the problem formulation as it remains fundamentally the same⁴⁷.

To formulate the problem, we assume that every time an EV is plugged to a CS, the user will input five quantities: (i) the initial SoC of the vehicle in percentage ($\text{SoC}_{t_{0,k,i},k,i}$, with $t_{0,k,i}$ being the arrival time of the car at the k -th CS of node i), (ii) the estimated departure time ($t_{f,k,i}$), (iii) the desired SoC at departure ($\text{SoC}_{t_{f,k,i},k,i}$), (iv) the car model, and, (v) whether or not the user would like the k -th CS to continue providing charging power if the time t exceeds $t_{f,k,i}$ ($\tau_{t,k,i}^+ \in \{0, 1\}$). Note that, in practice, the departure time can be chosen by the user if they actually have a time-constraint, otherwise, the charging duration can be translated to the user as an equivalent charging price. Finally, it is worth mentioning that the car model provides crucial information on the EV, namely (i) the maximum charging powers ($P_{k,i}^{\max} > 0$), (ii) the battery capacity ($E_{k,i}^{\max}$), (iii) the charging efficiency⁴⁸ ($\eta_{k,i}$) and (iv) whether or not the SoC is measured and sent by the vehicle to the CS. In the following we will present the constraints

⁴⁶Indeed, for the moment, the ISO-15118 [112] communication standard for DC chargers is the only EV communication standard that accepts reactive power setpoints. However, it is worth mentioning that, in its present form, the protocol only accepts unidirectional reactive power injections. This was ignored in the scope of this contribution as it is only natural that in the future expansions of the standards will accommodate bidirectional reactive power injection setpoints.

⁴⁷Extending the method to support vehicle-to-grid functionality, i.e. EV discharging, is straight-forward using the techniques presented in [61] (c.f. Sec. 7.3.2).

⁴⁸This thesis assumes that charging efficiencies are inputted constants that do not depend the internal variables of the plugged EV (e.g. SoC). In practice, charging and discharging efficiencies can be modelled in multiple fashions (e.g. [113]). If known, convex-versions of the latter models can be incorporated in the problem formulation.

and objectives pertaining to the EVCSs sub-problem.

Constraints

The constraints of each EV aggregator of node $i \in \mathcal{C}$ ensure three aspects: (i) the SoC of each EV connected to the k -th CS of node i will remain below the target SoC; (ii) the *per-phase* nodal injections correspond to the charging mode of each connected EV, and, (iii) charging powers are all within EV inverter limitations. The constraints are described here below.

SoC lower than target after application of optimal EV power setpoint

$$\text{SoC}_{t,k,i} - \frac{\eta_{k,i} P_{t,k,i} \Delta t}{E_{k,i}^{\max}} \leq \text{SoC}_{t_f,k,i,k,i} \quad (6.5)$$

EV power setpoint limitations

$$(P_{t,k,i}, Q_{t,k,i}) \in \begin{cases} \left\{ (P, Q) \mid P^2 + Q^2 < (S_{k,i}^{\max})^2, P \geq -P_{k,i}^{\max} \right\} & \omega_{t,k,i} = 1 \\ \{(0, 0)\} & \omega_{t,k,i} = 0 \end{cases} \quad (6.6)$$

Translation of EV power setpoint to phase powers

$$\begin{aligned} P_{t,k,i} &= \begin{cases} P_{t,k,i}^a + P_{t,k,i}^b + P_{t,k,i}^c & k \in 3\text{ph or DC} \\ P_{t,k,i}^\phi & k \in 1\text{ph}, \phi \in \{a, b, c\} \end{cases} \\ Q_{t,k,i} &= \begin{cases} Q_{t,k,i}^a + Q_{t,k,i}^b + Q_{t,k,i}^c & k \in \text{DC} \\ 0 & k \in 1\text{ph or 3ph} \end{cases} \\ P_{t,k,i}^a &= P_{t,k,i}^b = P_{t,k,i}^c = P_{t,k,i}^a, P_{t,k,i}^a \leq 0 & k \in 3\text{ph or DC} \\ Q_{t,k,i}^a &= Q_{t,k,i}^b = Q_{t,k,i}^c & k \in \text{DC} \\ P_{t,k,i}^b &= P_{t,k,i}^c = 0, P_{t,k,i}^a \leq 0 & k \in 1\text{ph} \end{aligned} \quad (6.7)$$

Link to Grid sub-problem Variables

$$\bar{s}_{i,\text{EV},t}^\phi = \sum_{k=1}^{K_i} P_{t,k,i}^\phi + j Q_{t,k,i}^\phi, \forall \phi \in \{a, b, c\} \quad (6.8)$$

where, Δt is the fixed control time-step resolution. A subscript t represents time-step t . $P_{t,k,i}$ and $Q_{t,k,i}$ are *variables* representing respectively the active and reactive total power at the k -th CS. $P_{t,k,i}^a$, $P_{t,k,i}^b$, $P_{t,k,i}^c$, $Q_{t,k,i}^a$, $Q_{t,k,i}^b$ and $Q_{t,k,i}^c$ are *variables* representing the active and reactive per phase nodal injections at the k -th CS. $\omega_{t,k,i} \in \{0, 1\}$ is a Boolean constant equal to 1 if an EV is plugged at time-step t to the k -th CS of node $i \in \mathcal{C}$. Indeed, the latter Boolean is known at every time-step. This simplifies the problem as it does not introduce the non-convexity usually associated with integer variables representing EV arrival and departure times. $S_{k,i}^{\max}$ is the maximum supported apparent power of the k -th CS of node i that is here assumed to be independent of the AC and DC-side voltages of each CS. Furthermore, for simplicity, the maximum charging power $P_{k,i}^{\max}$ per EV and associated efficiency are assumed independent of the SoC which, in practice, may not be true as some EVs reduce their charging powers when their SoC gets close to 1. However, if known, these dependencies can easily be added to

Chapter 6. Grid-aware Distributed Control of Electric Vehicle Charging Stations in Active Distribution Grids

the problem formation.

Finally, if the SoC of the present time-step t ($\text{SoC}_{t,k,i}$) is measured then we directly have access to it, otherwise, it is estimated as:

$$\text{SoC}_{t,k,i} = \text{SoC}_{t-1,k,i} - \frac{\omega_{t,k,i} \eta_{k,i} P_{t-1,k,i} \Delta t}{E_{k,i}^{\max}}$$

Objective

The objective of the EV sub-problem is twofold.

The first objective aims to *fairly*⁴⁹ achieve the target SoC for every connected EV in the shortest amount of time possible. This is given by,

$$\sum_{k=1}^{K_i} \kappa_{t,k,i} \left(\text{SoC}_{t_f,k,i} - \text{SoC}_{t,k,i} + \frac{\eta_{k,i} P_{t,k,i} \Delta t}{E_{k,i}^{\max}} \right) \quad (6.9)$$

where $\kappa_{t,k,i}$ is given by

$$\kappa_{t,k,i} = \begin{cases} \mu_{t,k,i} & \tau_{t,k,i} = 0, \omega_{t,k,i} = 1 \\ 0.1 v_{t,k,i} \min_{k' | \tau_{t,k',i} = 0} \mu_{t,k',i} & \tau_{t,k,i} = \tau_{t,k,i}^+ = \omega_{t,k,i} = 1 \\ 0 & \tau_{t,k,i} = \omega_{t,k,i} = 1, \tau_{t,k,i}^+ = 0 \\ 0 & \omega_{t,k,i} = 0 \end{cases}, \quad (6.10)$$

where $\tau_{t,k,i}$ is a Boolean constant that is true if the present time-step t exceeds the k^{th} EV's scheduled-inputted-departure time ($t_{f,k,i}$), $\mu_{t,k,i} \in [0, 1]$ is given by,

$$\mu_{t,k,i} = \frac{\min_{k' | \tau_{t,k',i} = 0} \{t_{f,k',i} - t\}}{t_{f,k,i} - t} \frac{|\text{SoC}_{t_f,k,i} - \text{SoC}_{t,k,i}|}{\max_{k' | \tau_{t,k',i} = 0} \{\text{SoC}_{t_f,k',i} - \text{SoC}_{t,k',i}\}} \quad (6.11)$$

and $v_{t,k,i} \in [0, 1]$ is given by,

⁴⁹In the scope of this thesis, fairness in terms of available grid capacity is omitted. In other words, we do not treat differently an EVCSs connected to the end of a feeder compared to one connected close to the PCC. This was done as we believe that this type of fairness should be accounted for in the planning phase when EVCSs are placed. However, as presented in [114], by leveraging SCs for instance, one can account for this type of fairness in the grid subproblem objective using multi-objective weight tuning.

$$v_{t,k,i} = \frac{\left| \text{SoC}_{t_f,k,i} - \text{SoC}_{t,k,i} \right|}{\max_{k' | \tau_{t,k',i}=1} \left\{ \text{SoC}_{t_f,k',i} - \text{SoC}_{t,k',i} \right\}}. \quad (6.12)$$

The weighting factor $\kappa_{t,k,i}$ gives: (i) more weight to plugged EVs with SoCs that are far from their target SoCs ($\text{SoC}_{t_f,k,i}$) and with little remaining time before their specified departure times ($t_{f,k,i}$) [$\mu_{t,k,i}$], (ii) ten times less weight than the least weighted plugged EV that has not surpassed its $t_{f,k,i}$, to plugged EVs that have surpassed their $t_{f,k,i}$ [$0.1 \min_{k | \tau_{t,k,i}=0} \mu_{t,k,i}$], and (iii) more weight, within plugged EVs that have surpassed their $t_{f,k,i}$, to plugged EVs with SoCs that are far from their target SoC ($\text{SoC}_{t_f,k,i}$) [$v_{t,k,i}$].

The second objective is to minimize EV battery wearing. As suggested in [115], the latter can be achieved by avoiding frequent variations in EV charging power. This is given by,

$$\sum_{k=1}^{K_i} \lambda_{t,k,i} \kappa_{t,k,i} \left| P_{t,k,i} - P_{t-1,k,i} \right| \frac{\Delta t}{E_{k,i}^{\max}}, \quad (6.13)$$

where the scaling factor $\lambda_{t,k,i} \in [0, 0.5]$, given by,

$$\lambda_{t,k,i} = \frac{1}{2} \frac{\sum_{t'=t_{0,k,i}+1}^{t-1} \left| P_{t',k,i} - P_{t'-1,k,i} \right|}{\sum_{t'=t_{0,k,i}+1}^{t-1} P_{k,i}^{\max}} \quad (6.14)$$

gives more weight to, i.e. penalizes more, EVs whose charging powers have changed several times since being plugged. In the worst case where the charging power varies between each consecutive time-steps between 0 and $P_{k,i}^{\max}$ since the EV was plugged, $\lambda_{t,k,i}$ will be equal to 0.5.

As a final note, observe that both (6.9) and (6.13) are of the same nature, i.e. they are all in percentages, and, are scaled by $\kappa_{t,k,i}$. This is done to ensure that for any EV, its battery ageing objective can be weighted, thanks to $\lambda_{t,k,i}$, from zero to half its SoC objective.

6.2.3 Centralised Full Optimization Problem

The centralised full OP is given by,

$$\begin{aligned}
 & \min_{\mathbf{p}_{t,\text{EV}}, \mathbf{q}_{t,\text{EV}}} \sigma_{\text{grid}} ((6.4)) + \sigma_{\text{EV}} \sum_{i \in \mathcal{C}} ((6.9) + (6.13)) \\
 & \text{s.t.} \\
 & (6.1), \quad \forall d = 1, \dots, D \\
 & (6.5) - (6.7), \quad \forall k = 1, \dots, K_i, \forall i \in \mathcal{C} \\
 & (6.8), \quad \forall \phi \in \{a, b, c\}, \forall i \in \mathcal{C}
 \end{aligned} \tag{6.15}$$

where σ_{grid} and σ_{EV} are weights. Note that, minimizing (6.13) smooths the EV active power CPs but also renders the constraints (6.1) less prone to approximation errors. This is because the less nodal injection changes there are between successive iterations, the more the linearizations in (6.1) are accurate.

6.3 Distributed Optimization

Solving the centralized problem (6.15) requires user information from local EV aggregators, which might not be easily accessible due to privacy and security concerns among the EV owners. Also, the centralized approach might not be easily scalable, i.e. solvable in seconds-to-minute scales, with respect to the increase of number of grid-connected EVCSs. Thus, following the approach in [116], we reformulate the centralized OP (6.15) by introducing a set of auxiliary variables $\tilde{s}_{i,\text{EV},t}^{\phi}$, $\forall \phi \in \{a, b, c\}$, $\forall i \in \mathcal{C}$, which mimic the behaviour of original variables $\tilde{s}_{i,\text{EV},t}^{\phi}$, $\forall \phi \in \{a, b, c\}$, $\forall i \in \mathcal{C}$. The augmented problem is given by,

$$\begin{aligned}
 & \min_{\mathbf{p}_{t,\text{EV}}, \mathbf{q}_{t,\text{EV}}, \mathbf{p}'_{t,\text{EV}}, \mathbf{q}'_{t,\text{EV}}} \sigma_{\text{grid}} ((6.4)) + \sigma_{\text{EV}} \sum_{i \in \mathcal{C}} ((6.9) + (6.13)) \\
 & \text{s.t.} \\
 & (6.1), \quad \forall d = 1, \dots, D \\
 & (6.5) - (6.7), \quad \forall k = 1, \dots, K_i, \forall i \in \mathcal{C} \\
 & \tilde{s}_{i,\text{EV},t}^{\phi} = \sum_{k=1}^{K_i} P_{t,k,i}^{\phi} + jQ_{t,k,i}^{\phi}, \quad \forall \phi \in \{a, b, c\}, \forall i \in \mathcal{C} \\
 & \tilde{\mathbf{s}}_{t,\text{EV}} = \tilde{\mathbf{s}}'_{t,\text{EV}}
 \end{aligned} \tag{6.16}$$

The problem in (6.16) is a standard sharing problem that is separable in each component $\tilde{s}_{i,\text{EV},t}^{\phi}$, $\forall \phi \in \{a, b, c\}$, $\forall i \in \mathcal{C}$. Using a sequence of Lagrangian multipliers \mathbf{y}_t and the scaled Lagrangian multipliers $\mathbf{u}_t = \mathbf{y}_t / \rho$, the last constraint of (6.16) can be moved into the objective and the reformulated problem can be solved using Algorithm 6 that exploits the iterative scaled-ADMM sharing problem [117].

Algorithm 6 is iterative, with each iteration ν composed of three steps. First, each EV aggregator associated to node $i \in \mathcal{C}$ solves, separately and in parallel, (6.17), then sends its solutions to the grid aggregator. Once the grid aggregator receives the solutions of all EV aggregators, it solves (6.18) and updates the dual variables with (6.19). Finally, the grid aggregator sends back to the distributed EV aggregators the corresponding dual variables and its optimal solution (i.e. $\tilde{s}_{i,\text{EV},t}^{\phi,\nu}$, $\forall \phi \in \{a, b, c\}$ where the superscript ν entails a value at the ν -th iteration). The procedure is repeated until the convergence criteria are met, i.e. the primal ((6.20)) and dual ((6.21)) residual norms are below, respective, tolerance limits ϵ^{pri} and ϵ^{dual} . Additionally, the tuning parameter ρ^ν is adaptively updated using the

Algorithm 6 ADMM to solve (6.16)

STOP = 0, $v = 1$, $\bar{\mathbf{s}}_{t,\text{EV}}^0 = \bar{\mathbf{s}}_{t,\text{EV}}'^0 = \mathbf{u}^0 = \mathbf{0}$

while ~STOP **do**

1. Solve EV Aggregator Problems (i.e. for each $i \in \mathcal{C}$)

$$\bar{\mathbf{s}}_{i,\text{EV},t}'^{\phi,v} = \underset{\substack{\bar{\mathbf{s}}_{i,\text{EV},t}'^{\phi} \\ \forall \phi \in \{a,b,c\}}}{\text{argmin}} \left\{ \begin{array}{l} \sigma_{\text{EV}}((6.9) + (6.13)) + \\ \frac{\rho^v}{2} \left\| \bar{\mathbf{s}}_{i,\text{EV},t}'^{\phi} - \bar{\mathbf{s}}_{i,\text{EV},t}^{\phi,v-1} + \mathbf{u}_i^{\phi,v-1} \right\|_2^2 \end{array} \right.$$

(6.17)

s.t.

$$\begin{aligned} & (6.5) - (6.7) \quad \forall k = 1, \dots, K_i \\ & \bar{\mathbf{s}}_{i,\text{EV},t}'^{\phi} = \sum_{k=1}^{K_i} P_{t,k,i}^{\phi} + jQ_{t,k,i}^{\phi} \end{aligned}$$

2. Send all $\bar{\mathbf{s}}_{i,\text{EV},t}'^{\phi,v}$ to Grid Aggregator

3. Solve Grid Aggregator Problem

$$\bar{\mathbf{s}}_{t,\text{EV}}^v = \underset{\bar{\mathbf{s}}_{t,\text{EV}}}{\text{argmin}} \left\{ \begin{array}{l} \sigma_{\text{grid}}((6.4)) + \\ \frac{\rho^v}{2} \left\| \bar{\mathbf{s}}_{t,\text{EV}}'^v - \bar{\mathbf{s}}_{t,\text{EV}}^v + \mathbf{u}^{v-1} \right\|_2^2 \end{array} \right.$$

(6.18)

s.t.

$$(6.1) \quad \forall d = 1, \dots, D$$

4. Update Dual Variable \mathbf{u}^v

$$\mathbf{u}^v = \mathbf{u}^{v-1} + \bar{\mathbf{s}}_{t,\text{EV}}'^v - \bar{\mathbf{s}}_{t,\text{EV}}^v \quad (6.19)$$

5. Check Convergence

$$\text{STOP} = \left\{ \left\| \bar{\mathbf{s}}_{t,\text{EV}}'^v - \bar{\mathbf{s}}_{t,\text{EV}}^v \right\|_2 \leq \epsilon^{\text{pri}} \right\} \quad (6.20)$$

$$\text{STOP} = \text{STOP} \text{ and } \left\{ \left\| \bar{\mathbf{s}}_{t,\text{EV}}^v - \bar{\mathbf{s}}_{t,\text{EV}}^{v-1} \right\|_2 \leq \epsilon^{\text{dual}} \right\} \quad (6.21)$$

6. Send back $\bar{\mathbf{s}}_{i,\text{EV},t}^{\phi,v}$ to EV Aggregators

7. Update ρ^{v+1} and $v \leftarrow v + 1$

end while

return $\bar{\mathbf{s}}_{t,\text{EV}}^v$

Chapter 6. Grid-aware Distributed Control of Electric Vehicle Charging Stations in Active Distribution Grids

technique presented in chapters 3.3-3.4 in [117]. Finally, as (6.16) is *linear*, Algorithm 6 is guaranteed, in principle, to converge to the optimal solution of (6.16) [117].

6.4 Comparative Simulation

In order to illustrate the proposed method, a performance comparison between three distributed control algorithms is done. The first controller is the grid-aware distributed controller (GADC) that uses all the steps of Algorithm 6 with $\sigma_{\text{grid}} = 0.1$ and $\sigma_{\text{EV}} = 10$. The second is a grid-unaware local controller (GULC) that *only* solves the EV aggregator local control problems (EV sub-problem) developed in this contribution, i.e. for each EV aggregator, $\forall i \in \mathcal{C}$, (6.17) is *solved* locally without the augmented Lagrangian term in the objective (i.e. with objectives (6.9) + (6.13) subject to the same constraints). The third is a myopic maximum power controller (MMPC) that simply charges any plugged EVs at maximum power until they reach their target SoCs. Note that both grid-unaware controllers only find nodal active power EV injections and set reactive power EV injections to zero as they do not have any incentive to inject/absorb reactive power. The performance comparison consists in finding first the *optimal* EV injections computed by each controller. Then, post-OPF Monte-Carlo simulations (c.f. Sec. 5.2.1 and Remark 3 for more information) using the latter optimal injections and scenarios generated from the non-EV injections CDFs (c.f. Sec. 6.2.1), are performed for each controller separately. This is done to statistically quantify the output performance of each controller by computing the probabilities to violate grid operational constraints with the optimally computed EVCSs injections. More specifically, the simulation consists in performing a 24 hour (from 8:00AM to 7:55AM the next day) control run with a 5 minute control resolution (i.e. $\Delta t = 5$ mins) for a *summer weekday*⁵⁰. At every time-step, the three controllers first solve their EV power allocation problems (i.e. find $\bar{\mathbf{s}}_{t,\text{EV}}$) using the same inputs, i.e. initial EV SoC, arrival/departure times and car model for all three controllers, and non-EV nodal power injections scenarios for the GADC controller). Then, for the same time-step, for each controller, LFMCSs are performed with EV injections fixed to the controller optimum. All three LFMCSs pertaining to the same time-step use the same newly (i.e. different than the *input* scenarios used to solve the GADC problem of the same time-step) randomly sampled scenarios for non-EV nodal power injections. Recall that, MCLFS consists in carrying out a large number of LF computations with different nodal power injections and outputs CDFs of the grid state variables. The number of LFMCSs scenarios was set using the method presented in Remark 3. To recap: the output of the simulation for each controller is, therefore, the optimal EV power allocations for all EV aggregators along with their performances vis-a-vis (i) grid operational static and power quality constraints violations under stochastic non-EV injections, and (ii) meeting EV user needs (i.e. reaching target SoC at EV unplugging).

6.4.1 Grid model and data used in the simulation

The simulation is done on the IEEE34 feeder [9], where (i) the voltage regulators are omitted in order to worsen voltage control problems, and (ii) the single-phase branches, i.e. the two-conductor configurations 302, 303 and 304 in [9], were replaced by four-conductor three-phase-equivalent configurations (see Tab. 6.1). The line geometries, remaining branch parameters and per-configuration-neutral-statuses can be found in [9]. Fig. 6.1 shows the network topology and resource allocation. It is worth mentioning that in this simulation 50%, 25% and 25% of single-phase EV chargers are respectively connected to phases a,b and c of the electrical grid. The base voltage and power are respectively set to 24.9kV and 1 MVA. The grid security bounds are set to $E_{\min} = 0.95$ p.u., $E_{\max} = 1.05$ p.u., $\delta_{\text{inv}} = 0.5\%$, $\delta_{\text{hom}} = 0.75\%$, $S_0^{\max} = 1.5$ p.u. and the amapacity limits found in [9] scaled by a factor of 6. Note that,

⁵⁰The choice of the season and day-type was not random. Firstly, as the summer season is less cloudy than the others, it was chosen to minimize the risk of uncertainty modeling errors that could lead to extreme P-V generation scenarios. Secondly, as people's habits present more routine-like behavior during weekdays, it was chosen to accurately and comprehensively synthesize EV user charging needs.

Chapter 6. Grid-aware Distributed Control of Electric Vehicle Charging Stations in Active Distribution Grids

as in the previous part of this thesis, the latter security bounds are all set to stricter bounds than the ones found in the EN-50160 standard [48] as the idea of this simulation is to stress-test the proposed algorithms. Fig. 6.2 shows all the aggregated (i.e. summed over all nodes and phases) non-EV load (negative) and generation (in the form of positive P-V injections) daily active power profiles already sub-clustered for a summer weekday. Each aggregated profile is first disaggregated to different nodes by scaling the profiles in Fig. 6.2 using the maximum active nodal power injection limits shown in Tab. 6.2. With all the disaggregated profiles, for every node, for every time-step, a multivariate PDF is computed using the technique explained in 6.2.1. These PDFs are used to generate the non-EV active power injection scenarios for the GADC controller *and* the post-OPF LFMCSs. Indeed, using the scenario-reduction technique presented in [72], the number of scenarios D used by the GADC controller at every time-step is set to 75. The number of LF computations used in each post-OPF LFMCSs is set to 350 as per the design choices explained in Remark 3. Note that, reactive power injection scenarios are inferred from the active power injection scenarios using power factors randomly sampled from the *typical* ranges ($[\cos(\phi)_{\min}, \cos(\phi)_{\max}]$) given in Tab. 6.2. Furthermore, to get the injections per phase, the total three phase nodal sampled active and inferred reactive injection scenarios are split pseudo-equally with an intra-phase unbalance randomly chosen between 0 and 20%. This is done since, as previously explained, ADNs usually are in unbalanced states due to load unbalances. Finally, note that the values in Tab. 6.2 were chosen in a way to create *no* grid operational constraint violations when EV injections are *null*.

Table 6.1: IEEE-34 branch parameters - Original vs. Used in simulation

Configuration	Longitudinal Impedance [Ω per mile]		Shunt Admittance [μS per mile]	
	Original	Used	Original	Used
302	$\text{diag} \left(\begin{bmatrix} 2.80 + j1.49 \\ 0 \\ 0 \end{bmatrix} \right)$	$\text{diag} \left(\begin{bmatrix} 2.80 + j1.49 \\ 2.80 + j1.49 \\ 2.80 + j1.49 \end{bmatrix} \right)$	$\text{diag} \left(\begin{bmatrix} 4.23 \\ 0 \\ 0 \end{bmatrix} \right)$	$\text{diag} \left(\begin{bmatrix} 4.23 \\ 4.23 \\ 4.23 \end{bmatrix} \right)$
303	$\text{diag} \left(\begin{bmatrix} 0 \\ 2.80 + j1.49 \\ 0 \end{bmatrix} \right)$	$\text{diag} \left(\begin{bmatrix} 2.80 + j1.49 \\ 2.80 + j1.49 \\ 2.80 + j1.49 \end{bmatrix} \right)$	$\text{diag} \left(\begin{bmatrix} 0 \\ 4.23 \\ 0 \end{bmatrix} \right)$	$\text{diag} \left(\begin{bmatrix} 4.23 \\ 4.23 \\ 4.23 \end{bmatrix} \right)$
304	$\text{diag} \left(\begin{bmatrix} 0 \\ 1.92 + j1.42 \\ 0 \end{bmatrix} \right)$	$\text{diag} \left(\begin{bmatrix} 1.92 + j1.42 \\ 1.92 + j1.42 \\ 1.92 + j1.42 \end{bmatrix} \right)$	$\text{diag} \left(\begin{bmatrix} 0 \\ 4.36 \\ 0 \end{bmatrix} \right)$	$\text{diag} \left(\begin{bmatrix} 4.36 \\ 4.36 \\ 4.36 \end{bmatrix} \right)$

6.4.2 EV users model and data used in the simulation

Even though the method is built to accommodate *any* random EV user behaviours (i.e. random arrival/departure time, target SoC and car model), in this simulation, they are synthesized to stress test the algorithm. Building on that, we categorize all EVCSs connected to a node $i \in \mathcal{C}$ into three groups: home, work and roadside. Home chargers are considered as EVCSs placed in residential buildings/areas that only support AC charging (i.e. three-phase (AC 3ph) and/or single-phase (1ph)). Work chargers are considered as EVCSs placed in industrial buildings/areas that, also, only support AC charging. Roadside chargers, however, are considered to only support DC charging. We assume that, all vehicles connected to single-phase AC chargers are Jaguar i-Pace, all vehicles connected to three-phase AC chargers are Tesla Model S, and, all vehicles connected to DC chargers are Nissan Leaf Plus. This is done to include *real* EV charging efficiencies, maximum powers and battery energy capacities in the simulation (see Tab. 6.3a for values). Depending on the group, the synthesized EV user behaviours are different. Namely,

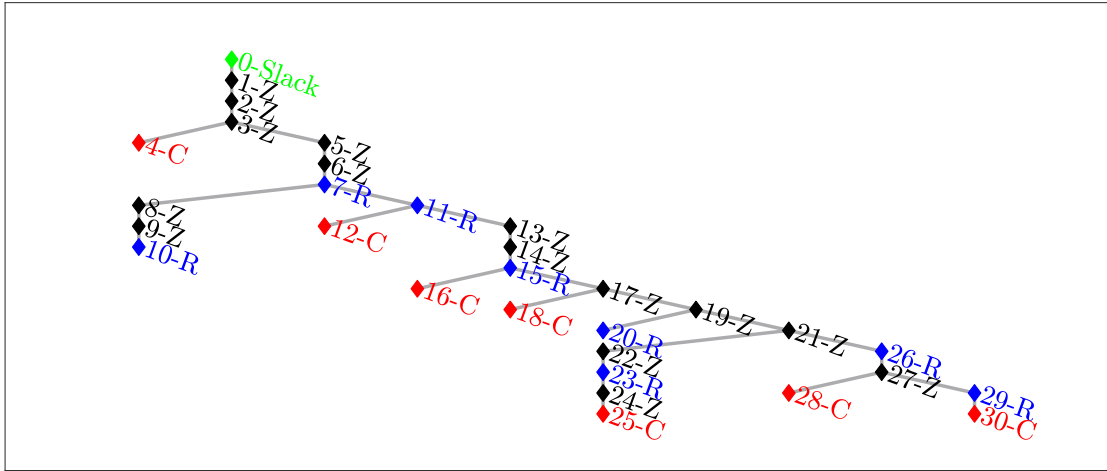


Figure 6.1: Network graph with resource placement. \mathcal{R} is a resource node. \mathcal{Z} is a zero-injection node. \mathcal{C} is a resource node containing EVCSs.

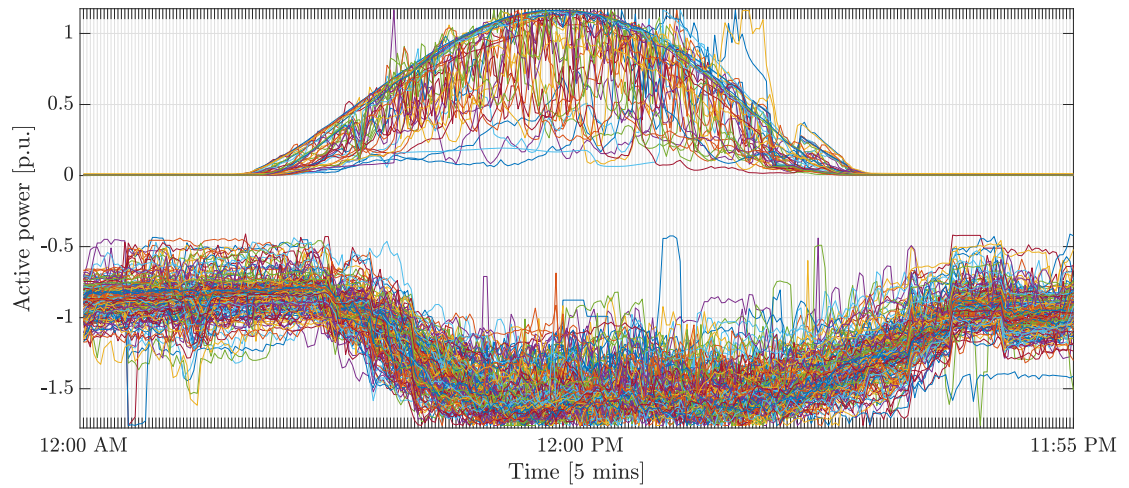


Figure 6.2: Aggregated PV (positive) and load (negative) active power profiles for the simulated summer weekday.

Chapter 6. Grid-aware Distributed Control of Electric Vehicle Charging Stations in Active Distribution Grids

Table 6.2: Maximum three phase nodal injections and power factor range per non-EV resource.

(a) PV Generation Nodes			
Node	Max [kW]	$\cos(\phi)_{\min}$	$\cos(\phi)_{\max}$
7	112.500	± 0.800	± 0.867
15	262.500	± 0.800	± 0.867
18	337.500	± 0.800	± 0.867
23	262.500	± 0.800	± 0.867
25	187.500	± 0.800	± 0.867

(b) Load Nodes			
Node	Max [kW]	$\cos(\phi)_{\min}$	$\cos(\phi)_{\max}$
10	157.500	0.930	1.000
11	315.000	0.930	1.000
20	472.500	0.930	1.000
26	525.000	0.930	1.000
29	288.750	0.930	1.000

we assume that (i) home chargers are only active at night from 5:00PM to 7:55AM the next day, (ii) a quarter of the work chargers are active from 8:30AM to 7:00PM as they are considered reserved for company employees while the rest are active from 9:00AM to 5:30PM as they are considered reserved for visitors, and (iii) roadside chargers have two charging sessions, respectively, from 8:00AM to 10:00AM (i.e. fast charging before arriving at work) and 12:00PM to 7:00PM (i.e. afternoon fast charging). The number of EVCs per node, the charging modes, the *exact* arrival and departure EV times and, the initial and target EV battery SoCs are all randomly sampled from the ranges given in Tabs. 6.3b-6.3d. In Tabs. 6.3c-6.3d we distinguish between *planned* departure time ($t_{f,k,i}$) and actual departure time to account for users that keep their EVs plugged after their announced departure times; we assume that this behaviour is only present for work and roadside chargers as users charging at home usually leave punctually to go to work every morning during a weekday.

6.4.3 Results of the simulation

From the grid perspective

Figs. 6.3 and 6.4 show the post-LFMCSs probabilities to violate, respectively, the grid operational static and power quality constraints for all time steps and control algorithms used in the simulation. It can be observed that the GADC algorithm guarantees close-to-no violations. Indeed, minor violations arise as power-flow equations are linearized which entails discrepancies between the linearized state and the real one. On the other hand, the GULC and MMPC optimal EV nodal power injections create several grid constraints violations. When it comes to grid static operational constraints, Fig. 6.3a, Fig. 6.3b and Fig. 6.3c show that, respectively, nodal voltage magnitudes, branches currents magnitudes and slack node apparent powers violations are practically guaranteed for both grid-unaware controllers during night-time home charging. When it comes to power quality, for both grid-unaware controllers, the negative- and zero-sequence components constraints are also violated mostly at night. This is explained by the presence of a large number of users that plug their single-phase EVs into the grid and

Table 6.3: EV simulated environment

(a) EV considered car models

Charging Mode	Car Model	$P_{k,i}^{\max}$ [kW]	$E_{k,i}^{\max}$ [kWh]	$\eta_{k,i}$
AC 1ph	Jaguar iPace	7.4	84.7	0.92
AC 3ph	Tesla Model S	17	100	0.85
DC	Nissan Leaf Plus	50	64	0.95

(b) EV user synthesized behaviour

Nodes	Category	Charging Mode	$S_{k,i}^{\max}$ [kVA]	K_i
{30, 28, 25}	Home	AC 1ph or AC 3ph	3.3 or 7.4	[60; 120]
{16, 12}	RoadSide	DC	50	[40; 60]
{4, 18}	Work	AC 1ph or AC 3ph	7.4 or 17	[50; 100]

(c) EV user synthesized behaviour - continued

Nodes	$t_{0,k,i}$	$t_{f,k,i}$
{30, 28, 25}	[5:00PM; 11:00PM]	[6:00AM; 7:55AM]
{16, 12}	Session 1 - [8:05AM; 10:00AM]	[8:35AM; 11:00AM]
	Session 2 - [12:00PM; 7:00PM]	[12:35PM; 8:00PM]
{4, 18}	Visitors— [9:00AM; 5:30PM]	$t_{0,k,i} + [30-90]$ mins
	Employees— [8:30AM; 11:00AM]	[5:00PM; 7:00PM]

(d) EV user synthesized behaviour - continued

Nodes	Actual Departure Time	$SOC_{t_{0,k,i},k,i}$	$SOC_{t_{f,k,i},k,i}$
{30, 28, 25}	$t_{f,k,i}$	[0.15; 0.45]	[0.95; 1.00]
{16, 12}	$t_{f,k,i} + [0-20]$ mins	[0.15; 0.35]	[0.60; 0.80]
		[0.10; 0.35]	
{4, 18}	$t_{f,k,i} + [0-30]$ mins	[0.15; 0.50]	[0.25; 0.80]
		[0.30; 0.55]	

Chapter 6. Grid-aware Distributed Control of Electric Vehicle Charging Stations in Active Distribution Grids

thus creating high voltage unbalances. Even though it still performs badly, it can be observed that the GULC controller sometimes incurs lower constraint violation probabilities compared to the MMPC controller. This can be explained by the *smoothing* effect of EV charging that arises due to the GULC's objectives. In summary, from Figs. 6.3 and 6.4, it is safe to conclude that, as was seen in Sec.5.2.1, grid-unaware EV charging largely jeopardizes the safe operation of the grid.

From the EV users perspective

Fig. 6.5 shows, using boxplot representations, the difference between all target SoCs and the actual ones at time of departure. Fig. 6.5a represents a base-case as the MMPC algorithm charges EVs at full power. The reason why there are some unachieved charging targets is due to the fact that initial and desired SoCs are randomly sampled. Thus, sometimes it is simply not possible to achieve the desired SoC during the time window where the EV is plugged. Fig. 6.5b shows that the GULC controller behaves similarly to the *ideal* MMPC control from the EV user perspective. However, their optimal EV injections were different which explains why they incurred different grid constraint violations. This entails that the GULC controller smooths the charging process while still achieving close-to-ideal outcomes for EV users. Fig. 6.5c, however, shows that the GADC does not give the same guarantees. This is especially true for home chargers that on average provide EVs 10% to 20% less energy. This behaviour is in accordance to the grid-constraints-probability-violations shown in Figs. 6.3-6.4 where it is clear that the GADC had to decrease the EV charging powers to guarantee the grid's safety around night-time. Furthermore, the latter behavior can be physically explained by two factors: (i) the high-loading conditions that happen at night-time when the simulated grid has no generating units, and (ii) the fact that in this simulation EV node placement and maximum number of connected EVs per node were chosen at random. This sheds light on the sub-optimal performance of the GADC controller from the EV user's perspective. Indeed, the grid is simply not designed for such simulated high power unbalanced EV load demand. Therefore, as a final note, we believe that with proper CS placement planning together with the deployment of our proposed method (i.e. the GADC controller), the network will remain safe and the EV user needs would be better fulfilled.

6.5 Conclusion

This chapter proposed a grid-aware distributed controller (GADC) for EVCSs connected to electrical grids of generic topologies. It uses the ADMM to distribute a separably formulated OPF problem into local ones. The latter are solved at the EV aggregators level while a central grid aggregator problem ensures the non-violation of the grid operational constraints while taking into account all the solutions coming from the EV aggregators'. The grid aggregator problem takes into account the stochastic nature of various resources by means of scenarios, it relies on a linearization of the power-flow equations and is formulated for generic three phase ADNs. Therefore, it also takes into account voltage unbalances and guarantees proper power quality subject to the EN-50160 std. bounds [48]. Furthermore, as previously explained, as the control time-step is chosen to be in the seconds-to-minutes scale to match the results presented in Sec. 5.2.2, scenario-based optimization was crucial to render the optimally computed setpoints robust against the stochasticity of non-EV nodal power injections. The performance of the method is numerically quantified on the IEEE-34 feeder by comparing it with two grid-unaware controllers. It is shown that the grid-unaware controllers may provide a better service to EV users in terms of matching the desired battery SoC levels. However, this is at the expense of severely violating the grid's static and power quality constraints. From the grid perspective, the proposed GADC kept

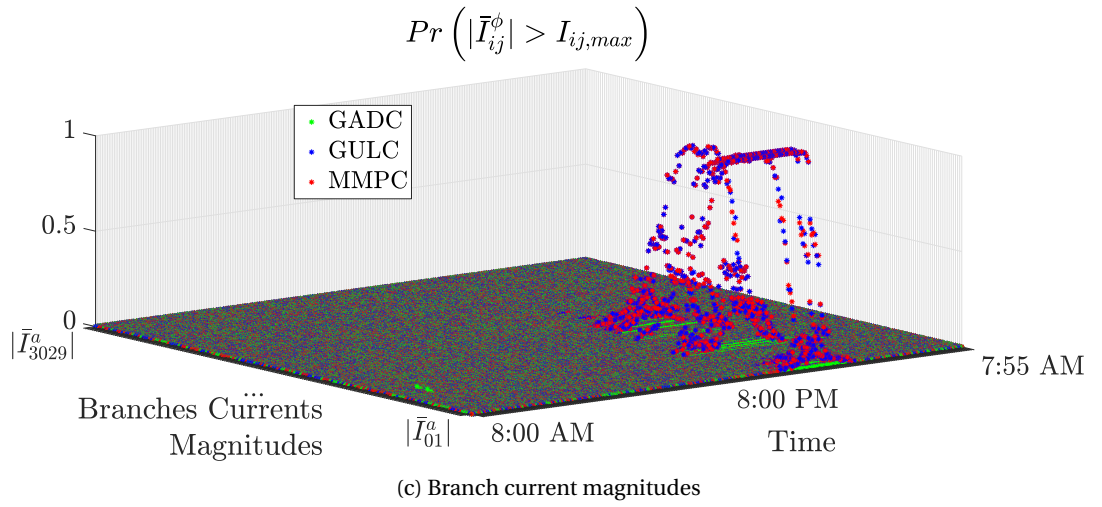
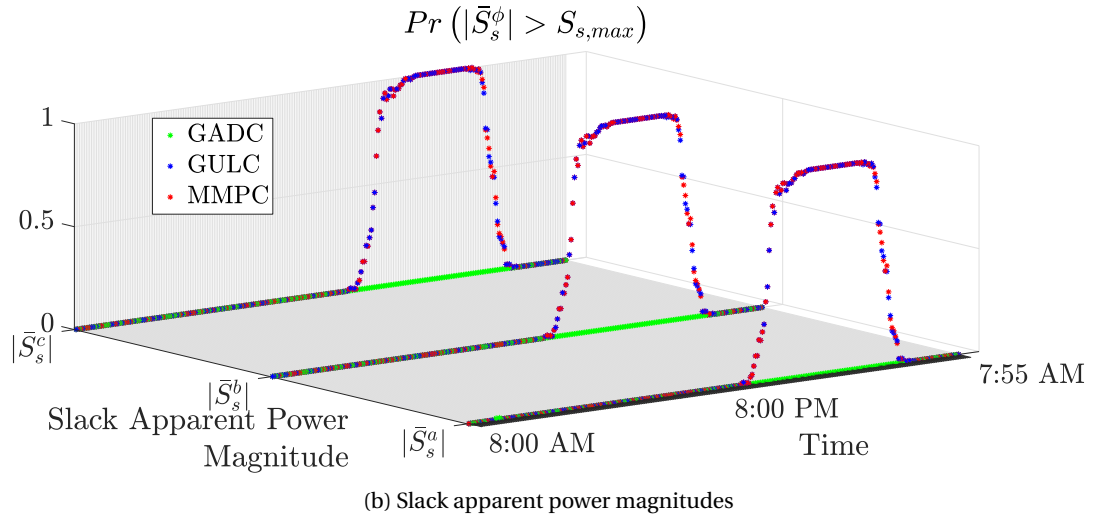
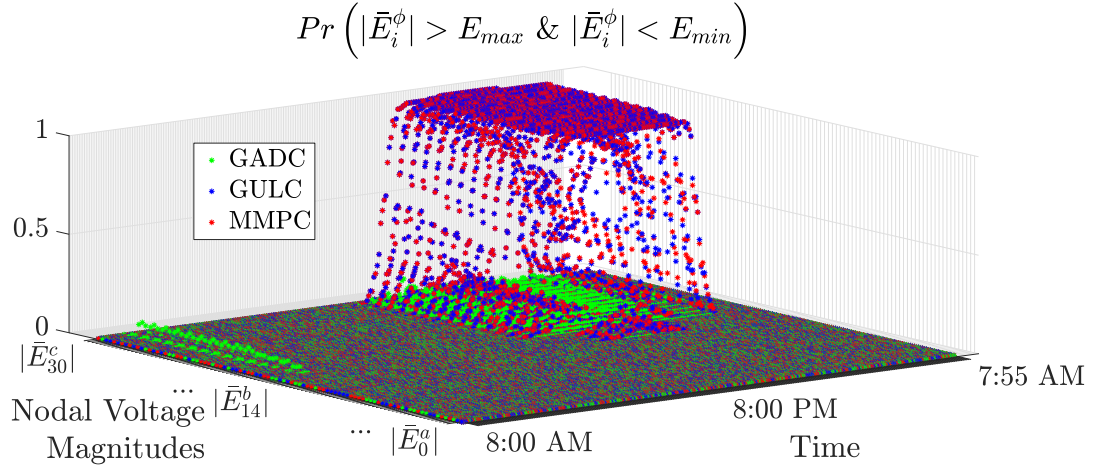
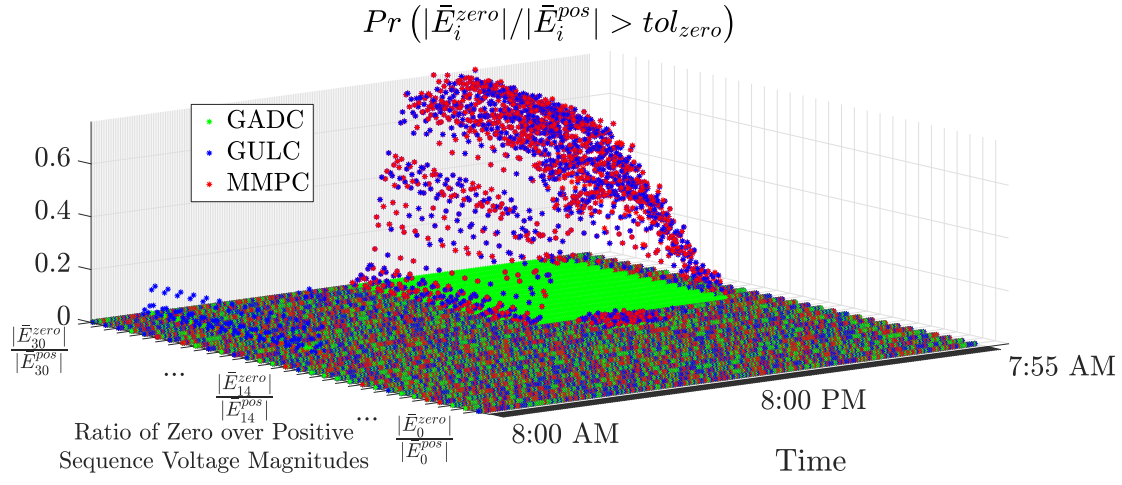
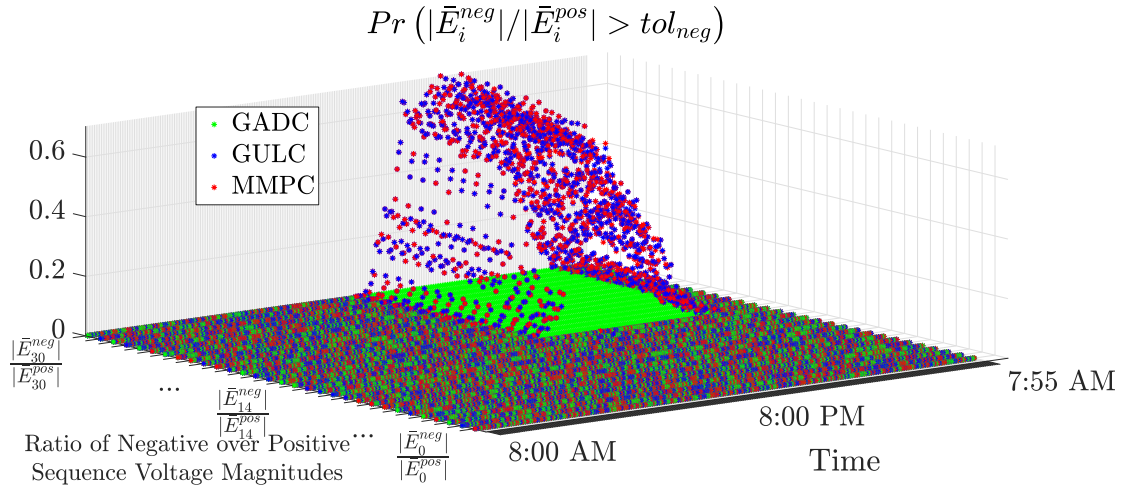


Figure 6.3: Post-MCLFSs results: probabilities to violate static grid operational constraints during the simulated 24 hours



(a) Ratio of zero- and positive- sequence nodal voltage magnitudes



(b) Ratio of negative- and positive- sequence nodal voltage magnitudes

Figure 6.4: Post-MCLFSs results: probabilities to violate power quality grid operational constraints during the simulated 24 hours

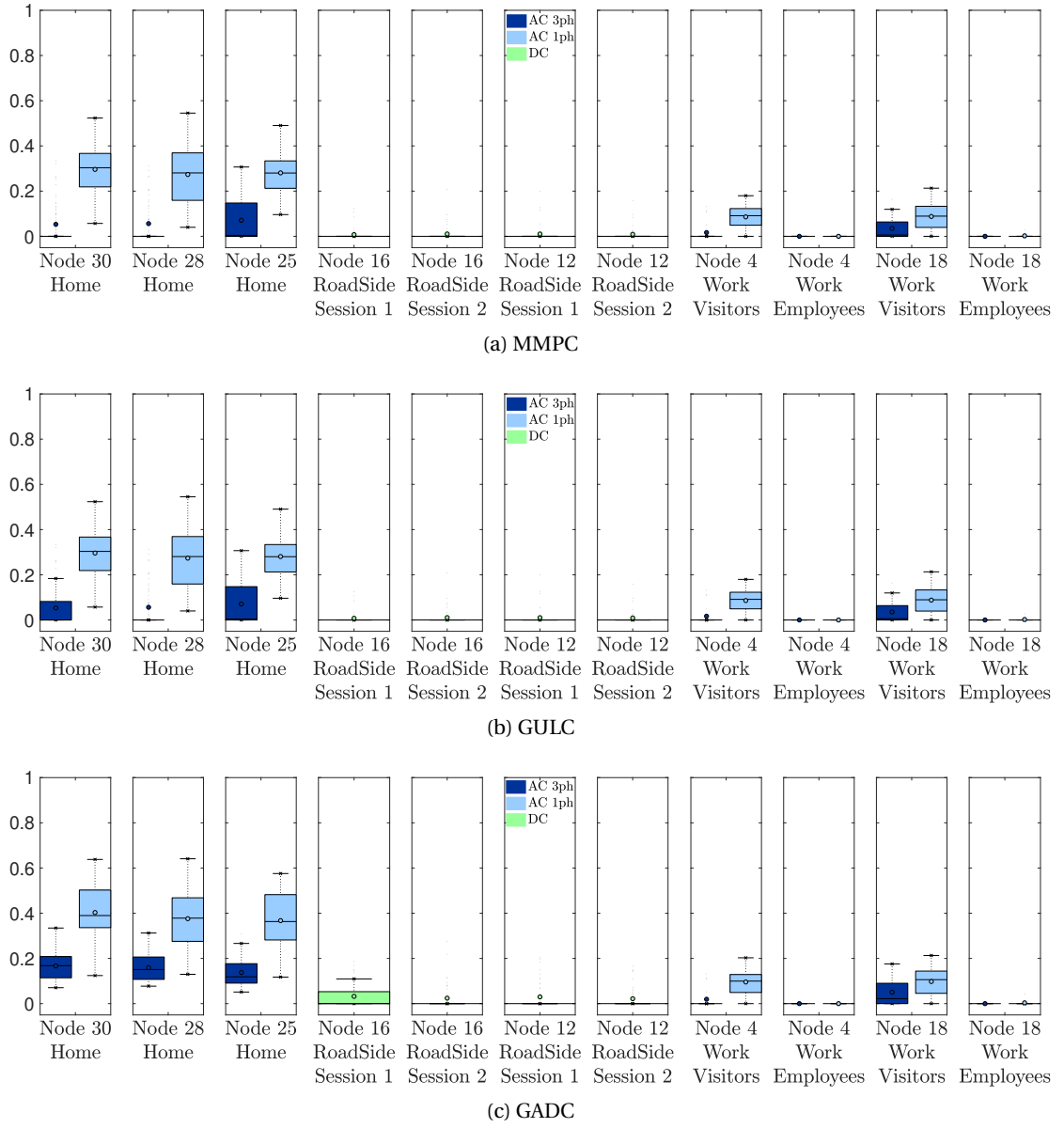


Figure 6.5: Difference between desired SoC at departure and actual one, for all nodes with EVCSs and for each simulated control algorithm

Chapter 6. Grid-aware Distributed Control of Electric Vehicle Charging Stations in Active Distribution Grids

the power grid within safe operational bounds and, in most cases, was capable to satisfy the needs of EV users. It is clear that the developed method can help grid operators to manage *weak* grids that accommodate heavy EV loads. In the next chapter, an MPC-augmented version of the GADC is developed and used to experimentally validate an EV- and grid-aware day-ahead control algorithm aiming at computing an optimal day-ahead DP.

7 EV-aware Day-Ahead Power-Grid-Dispatch: Theory and Experimental Validation

Keywords—ADN Dispatch, Real-Time, i.e. seconds-to-minute scale, Distributed Control, Grid Operational Constraints and Power Quality, Electric Vehicle Charging Stations.

7.1 Introduction

As explained in [6]: "*Day-ahead and intra-day scheduling of heterogeneous DERs has been advocated in the literature as a way to minimize the effect of uncertainties. It consists in determining an average power trajectory (dispatch plan (DP)) at a certain resolution before operations that is then followed during real-time operation.*". Even though the presented algorithms in [6] are aimed to work for heterogeneous resources, EVCSs' power and energy demands were not explicitly accounted for in the proposed problem formulation, and, as hinted at in Sec. 5.2, with adequate control, EVCS can be turned from given boundary conditions (i.e. demand satisfaction) to controllable assets for the control of ADNs.

As a result, this contribution extends the work in [6] by accounting for EVCSs' power and energy demand flexibilities in both day-ahead and real-time stages. More specifically, in the scheduling phase on the day before operations, the stochastic OP computing an aggregated DP at the PCC is extended to account for EVCSs as controllable entities. We recall that the proposed day-ahead OP in [6], accounts for (i) demand/generation forecasting errors using scenarios, (ii) resource constraints, and (iii) grid operational constraints by leveraging SCs. In the real-time phase, the grid-aware MPC-based distributed control algorithm proposed in [6] is extended with an MPC-augmented-version of the EV-subproblem model presented in Sec. 6.2.2. We recall that the distributed real-time OP of [6] aims to *securely* – i.e. while accounting for resource and grid operational constraints – compute active and reactive power set-points for heterogeneous resources so that their aggregated contributions track the day-ahead optimally computed DP. The distributed formulation leverages an ADMM algorithm similar to the one presented in Sec. 6.3.

In summary, the main contributions of this chapter are: i) extending the day-ahead OP of [6] to account for EVCSs as controllable entities by leveraging a developed EV user behavior forecasting tool, ii) extending the distributed real-time control-algorithm of [6] with a MPC-augmented version of the EVCS GULC of Sec. 6.2.2, iii) numerically illustrating the merits of considering EVCSs as controllable entities in the day-ahead DP generation stage, and iv) experimentally validating on the EPFL-DESL

microgrid the proposed real-time extension by safely tracking an optimally generated DP.

The rest of the chapter is organised as follows. In Sec. 7.2 the general assumptions, e.g. grid modelling, and problem formulation are presented. In Sec. 7.3 the day-ahead problem extension is presented. The latter also includes details on the developed EV user behavior forecasting tool and illustrative numerical simulations to showcase the advantages of controlling EVCSs in the day-ahead stage. In Sec. 7.4 the real-time problem extension is presented. In Sec. 7.5 an experimental validation, performed on the EPFL-DESL microgrid, of all contributions of this chapter is shown. Finally, Sec. 7.6 concludes the chapter.

7.2 Problem Statement & Overview

As in previous chapters, we target power grids whose states are evolving slowly enough such that they can be modelled by phasors. Specifically, we focus on ADNs where the admittance matrix is known and whose power equilibrium is described by the standard AC power-flow equations. Furthermore, we consider that such grids contain uncontrollable and controllable resources. Hereinafter, controllable resources are considered to be interfaced through *grid-following* CPCs, that can receive active and reactive power setpoints⁵¹. In this chapter, we focus on dispatching ADNs at their PCC according to an optimally computed DP. To do so the process is split into two-stages as shown in Fig. 7.1.

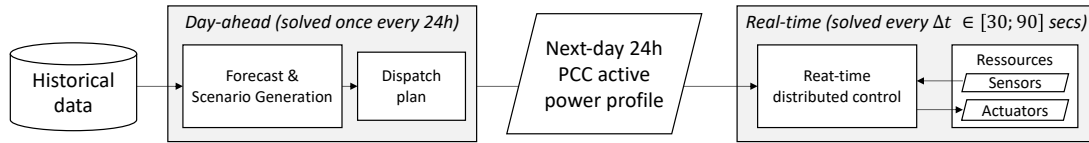


Figure 7.1: Schematic overview of the proposed two-stage ADN dispatch

1. **Day-ahead stage**, in this stage the operator computes a DP in the form of an active power profile to be followed at the PCC during next-day operation. The DP is generated by accounting for ADNs and controllable resources operational constraints by leveraging proper forecasting of next-day grid status (i.e. injections of uncontrollable resources and EV user behaviors). As a result, this stage is split into two processes, depicted as *forecasting* and *dispatch plan* in Fig. 7.1. During the *forecasting* process, historical data is inputted to statistical engines that output parametric probabilistic models (see Sec. 7.3.1). During the *dispatch plan* process, a security-constrained scenario-based OP, leveraging the models created in the last process, is solved to generate a 24h active power DP (see Sec. 7.3.2). Typically, the generated DPs are injection profiles with time-resolutions of 30-600 seconds. The DP enters into effect at 00:00 of the next-day.
2. **Real-time stage**, as explained in [6], in this stage the ADN resources are controlled in real-time to compensate for power mismatches at the PCC between the optimal DP and actual realization. As in the day-ahead stage, the control problem accounts for ADNs and controllable resources operational constraints. Unlike the day-ahead stage, the resources' states are assumed to be known through proper sensing. The problem is expressed by leveraging a distributed MPC

⁵¹As in the previous chapters, these assumptions are not strict as it is straightforward to extend the proposed algorithms to account for either (i) all node-types, or (ii) multi-slack grids (c.f. Sec. 2).

formulation to (i) render the problem resolution efficient and scalable, and (ii) account for potential uncertainties along the optimization horizon. Similarly to what was presented in Sec. 6.3, the distributed formulation leverages the ADMM to decouple the ADN and resources operational problems (see Sec. 7.4). This stage's control algorithm starts and ends at, respectively, 00:00 and 23:59 of the day of operation.

As a final note, it is important to remind that, in view of the large uncertainties accompanying forecasting next-day grid statuses, the day-ahead stage considers ADNs to be balanced and, as a result, only the single-phase direct sequence equivalent of the ADN is considered. Hence, hereinafter, the phase superscript is omitted in the symbols of this chapter.

7.3 Day-ahead stage

As previously mentioned, the main goal of the day-ahead stage is to compute a DP. Indeed, when proper forecasting tools are used, building a 24h active power profile at the PCC for the next-day-real-time controller to track promotes optimal next-day usage of controllable resources. For instance, as the OP leverages a full-day MPC formulation, with proper next-day solar-irradiance forecasting, the controller can anticipate the charge/discharge of a controllable BESS. Furthermore, as explained in [6], the grid operator can practically assume knowledge of the next-day PCC active power consumption since (i) the DP is generated through stochastic scenario-based security-constrained optimization and, (ii) the real-time controller steers the controllable resources to guarantee that the PCC injection realization matches the DP. As a result, the grid operator will have less potential risks of operation and financial costs related to real-time balancing or reserve activation needs [118].

As previously explained, the contribution of this chapter extends the developed algorithms in [6] by accounting for EV user needs and considering EVCSs as controllable resources in both day-ahead and real-time stages. As EV user behaviours (e.g. arrival/departure times and energy needs), and associated CPs, exhibit high stochasticity, including EVCSs in the problem formulation increases the prediction and control complexities of the day-ahead stage. However, by adequately anticipating the latter, the whole bulk power-grid would need less secondary and tertiary power reserves.

In summary, the DP is the optimal result of a stochastic MPC-based OP. As in [6], the OP (i) accounts for next day-stochasticity of non-EV injections through scenarios (see Sec. 7.3.1), (ii) accounts for grid operational constraints by leveraging SCs (see Sec. 7.3.2) and (iii) accounts for controllable resources' operational constraints (e.g. PQ capability and state-of-energy constraints). Unlike in [6], the OP (i) further accounts for next day-stochasticity of EV user behaviour through scenarios (see Sec. 7.3.1), and (ii) is solved iteratively⁵² in order to alleviate the inaccuracies introduced by the linearizations of the power-flow equations (see Sec. 7.3.3). In the following, first the details of the forecasting block of Fig. 7.1 – i.e. the scenario generation block – are given, then the OP objective, constraints and solution algorithm are presented. Finally, the advantages of considering EVCSs as controllable resources in the day-ahead stage are showcased through numerical simulations.

⁵²Similar to the technique adopted in Alg. 5 to deal with linearization inaccuracies.

7.3.1 Scenario Generation

Since the day-ahead OP is solved before the realizations of the next-day, proper forecasting is needed to predict different next-day quantities. The idea of the forecasting tool is to generate scenarios that can be used to formulate the OP of the day-ahead stage. In the following, we first describe the techniques used to create probabilistic models for different stochastic quantities. Then, we present how those models were combined to generate scenarios.

Non-EV injection models

For non-EV injections, as previously explained, a model can be in the form of a PDF created from historical data. Specifically, as detailed in Sec. 5.2.1, the PDFs are created using historical data in the form of active and reactive nodal injection profiles for every resource connected to a given node. For load resources, each of these profiles is first clustered into 4 seasons (i.e. winter, spring, summer and autumn), then, sub-clustered into day-type (i.e. working days, weekend or vacation days), then, finally sub-sub-clustered into the fixed time resolution of the control algorithm. For generation resources, assumed to be in the form of P-V plants, each of these profiles is first clustered into 4 seasons (i.e. winter, spring, summer and autumn), then, sub-clustered into sky-clearness (i.e. sunny, cloudy and overcast), then, finally sub-sub-clustered into the fixed time resolution of the control algorithm. In both cases, for every sub-cluster, a Gaussian mixture model (i.e. a sum of multivariate Gaussian normal distributions) is fitted to the data using MATLAB's function `fitgmdist`. This is done to account for the time correlation between the different time-steps for each specific sub-clusters. At the end, we obtain multivariate (the random variables here are all the time-steps of a given day) PDFs for each nodal injection (i.e. uncontrollable generation or load) pertaining to a season and day-type or sky-clearness. From those models, daily injection profiles can be inferred based on the features – i.e. season and day-type for loads and season and sky-clearness for generation – of the day we wish to forecast.

EV user model

Since EVCSs are considered as controllable entities, i.e. the active and reactive power injections of EVCSs are variables of the problem, the models developed here need to forecast EV user behaviour rather than injections. By EV user behaviour, for a given EVCS, we refer to: (i) the number of EV charging sessions per day, (ii) the EVs' arrival and departure times, (iii) the initial and final, i.e. target, SoCs of EVs' batteries, (iv) the EVs' battery capacities, and (v) the minimum and maximum active power injections (defined as, respectively, the maximum and minimum imposed by either the EVCSs' converters limits or the EV on-board controller).

In view of the large number of quantities that define EV user behaviour, we developed a data-agnostic tool that uses any amount of data with as many features as an input, and, outputs the *best* PDF (or PDFs) that would model the data. As the input data is multi-variate, the output PDFs can be anything from several univariate distributions to a full GMM⁵³ that models all input variables (or features) simultaneously. The algorithm's idea is to fit the data with different functions then output the best-performing-probabilistic-model. The flowchart of the developed toolbox is depicted in Fig. 7.2. As can be seen, the input data is first filtered then fitted to: (i) one multi-variate GMM (Multivariate GMM-approach, see Fig. 7.2), (ii) N univariate GMMs (Univariate GMM-approach, see Fig. 7.2), with N being

⁵³The choice of GMMs as the baseline function for the data-agnostic forecasting tool lies behind its proven performance to adequately model random/stochastic trends [89].

the number of input features, and (iii) a mix of multi- and uni-variate GMMs (Mixed GMM-approach, see Fig. 7.2). Once all three fittings converge, they are compared using accuracy, bias and correlation metrics. Finally, the fitting with the overall best metrics is selected as the best-performing-probabilistic-model, where from the latter, EV user behaviors can be inferred based on the features – i.e. season and day-type – of the day we wish to forecast.

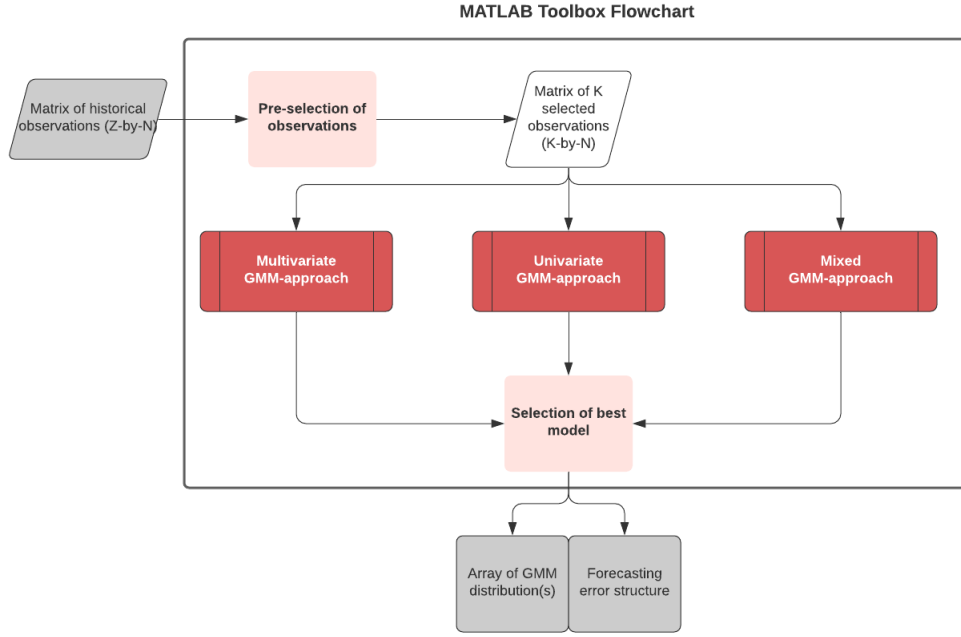


Figure 7.2: Flowchart of data-agnostic modelling toolbox

In the following, each sub-block of the flowchart in Fig. 7.2 is explained.

1. *Pre-selection of observations.* The $Z \times N$ – where Z is the number of measurements and N is the number of features or variables – input matrix of measurement is automatically filtered based on a set of control parameters specified by the user. Namely the user chooses the season and the day-type (i.e. weekend or weekday). Indeed, this enables the user to create EV user behaviour models that pertain to a specific season and day-type. The tool will automatically provide the best model that statistically represents a subset of the historical data where only the desired season and day-type are included. The block outputs a reduced measurement matrix with a dimension of $K \times N$, where K_{meas} is the number of selected measurements.
2. *Multi-variate GMM approach.* In this block, the built-in MATLAB function `fitgmdist` is used together with K-fold cross-validation [119] to compute an optimal GMM model considering all filtered inputted variables simultaneously. As previously explained in Sec. 5.2.1, the `fitgmdist` function has many parameters that can alter the outputted model. Therefore, in the proposed method, we loop over the number of components of the outputted GMM (from one to a user-defined maximum GMM order). For each GMM order, cross-validation is used to avoid over-fitting in cases where the GMM order gets too high (see Fig. 7.6). Namely, for each GMM order, first, the filtered dataset is randomly divided into T groups (or folds) of the same size. Then, for each fold, the training and testing process is repeated T times. The training and testing

process consists in fitting a GMM to the training data using the order of the current iteration, then, regenerate data using the GMM model and compute the mean absolute error between the newly generated data and the test set. Every fitted GMM-distribution is saved during the iterations. The model with the lowest mean absolute error at the loop exit is chosen. The general scheme and details of the proposed method are shown in, respectively, Figs. 7.3 & 7.6.

3. *Uni-variate GMM approach.* In this block, in contrast to the *Multi-variate GMM approach* that implicitly considers the input dataset variables or features to be correlated, the input data is modelled separately, i.e. each variable (column of the filtered data matrix) is considered independent of the others and, therefore, is fitted with its own GMM. Hence, the output of this block is a set of N GMMs. A schematic diagram of the block is shown in Fig. 7.4.
4. *Mixed GMM approach.* This block, combines the functionalities of the two previous blocks. Indeed, if the variables of the input dataset are split into correlated and uncorrelated subset datasets, it is optimal to fit the correlated variables with the multivariate-GMM approach, while, in contrast, the uncorrelated variables would be fit separately using the univariate-GMM approach (see Fig. 7.5). In this approach, the correlation analysis block uses PLCC⁵⁴. The correlation tolerance is user-configurable, with a default value set at 0.5⁵⁵.
5. *Select best GMM approach.* A set of metric is used to select the *best-fitted* models between the three approaches. The metrics aim to evaluate each approach based on (i) *accuracy* (A), i.e. the average discrepancy between individual pairs of observation and forecast, (ii) *bias* (B), i.e. the mean deviation from average observation and average forecast, (iii) *correlation* (R), i.e. PLCC correlation of observation and forecast vectors, and (iv) *goodness-of-fit*, i.e. the result of a P-value (Two-sample Kolmogorov-Smirnow) test on the null hypothesis of having the same underlying distribution for the observation and forecast datasets. Tab. 7.1 enumerates all the metrics used to quantify *accuracy* (Tab. 7.1a) and *bias* (Tab. 7.1b), where $\epsilon_k = y_k - x_k$ is the forecast error and $Q_k = \frac{y_k}{x_k}$, with x and y being, respectively, the K -dimensional observation and forecast vectors. The final selection relies on the global forecasting error defined as a weighted sum of all the metrics. Formally, the forecasting error (FE) is defined as $FE = w_1 A + w_2 B + w_3 R$, where w_1 , w_2 , & w_3 are user-defined weights, and, A , B and R are given by,

$$\begin{aligned}
 A &= \frac{1}{N} \sum_{n=1}^N \frac{|MAPE_n| + |sMAPE_n| + |MSA_n|}{3} \\
 B &= \frac{1}{N} \sum_{n=1}^N \frac{|MPE_n| + |SSPB_n|}{2}, \\
 R &= \frac{1}{N} \sum_{n=1}^N |100(1 - R_n)|
 \end{aligned} \tag{7.1}$$

where each R_n corresponds to the PLCC correlation of the observation and forecast vectors for a feature n and the other metrics are defined in Tab. 7.1. The weights need to be assigned by the user based on the application requirement. In our application, based on the observed performances, we realised that setting all the weights to 1 lead to the best results as the obtained models were not biased in favor of a specific metric rather than others. Note that in (7.1), the absolute value is taken as we are not interested in evaluating the direction of bias, i.e. under or over-estimation. Likewise, we are not interested in evaluating if the correlation is positive

⁵⁴The interested reader is referred to [120] for more information about the PLCC.

⁵⁵Recall that PLCC values range from -1 to +1, where -1 corresponds to negative correlation while +1 corresponds to positive correlation.

or negative. Finally, the *best-fit* is chosen as the set of models of the approach that leads to: (i) the smallest FE, *and* (ii) a Two-sample Kolmogorov-Smirnow test result that is lower than a user-defined critical value of 5% significance level⁵⁶.

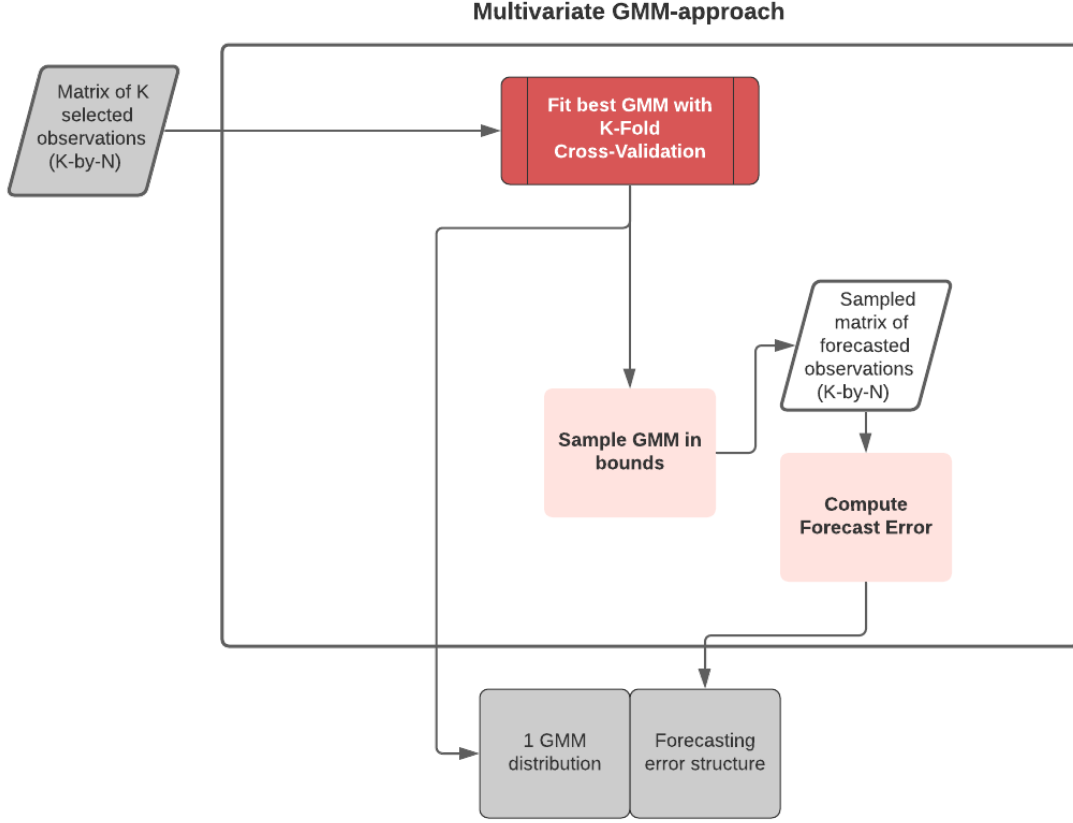


Figure 7.3: Flowchart of the multi-variate GMM approach block

Combining non-EV injections and EV user models into scenarios

Following the non-EV injections and EV user models presented above, it is natural to define a non-EV injection scenario as a day-long power injection profile and, an EV user scenario as the set of all charging sessions for a specific day, where each charging session is described by (i) the EV's arrival and departure times, (ii) initial and desired EV battery SoCs, (iii) the EV's battery capacity and (iv) minimum and maximum active power injection limits. Each uncontrollable resource would, therefore, have at least two associated non-EV injection scenarios (active and reactive power injections) and each EVCS would have one associated EV user scenario. The total number of scenarios would be the total combinations of all generated scenarios for all uncontrollable resources and EVCSs. This, clearly, can lead to a high complexity if the method of selecting the number of scenarios, presented in Rem. 3, is used without any assumptions. Therefore, first, we conservatively assume that the non-EV load and generation injection scenarios are *all* either at their 5 or 95% percentiles when inverse-sampling from the constructed models. Namely, this would lead to the four non-EV injection scenarios described in

⁵⁶We refer the interested reader to [121] for more information about the Two-sample Kolmogorov-Smirnow test.

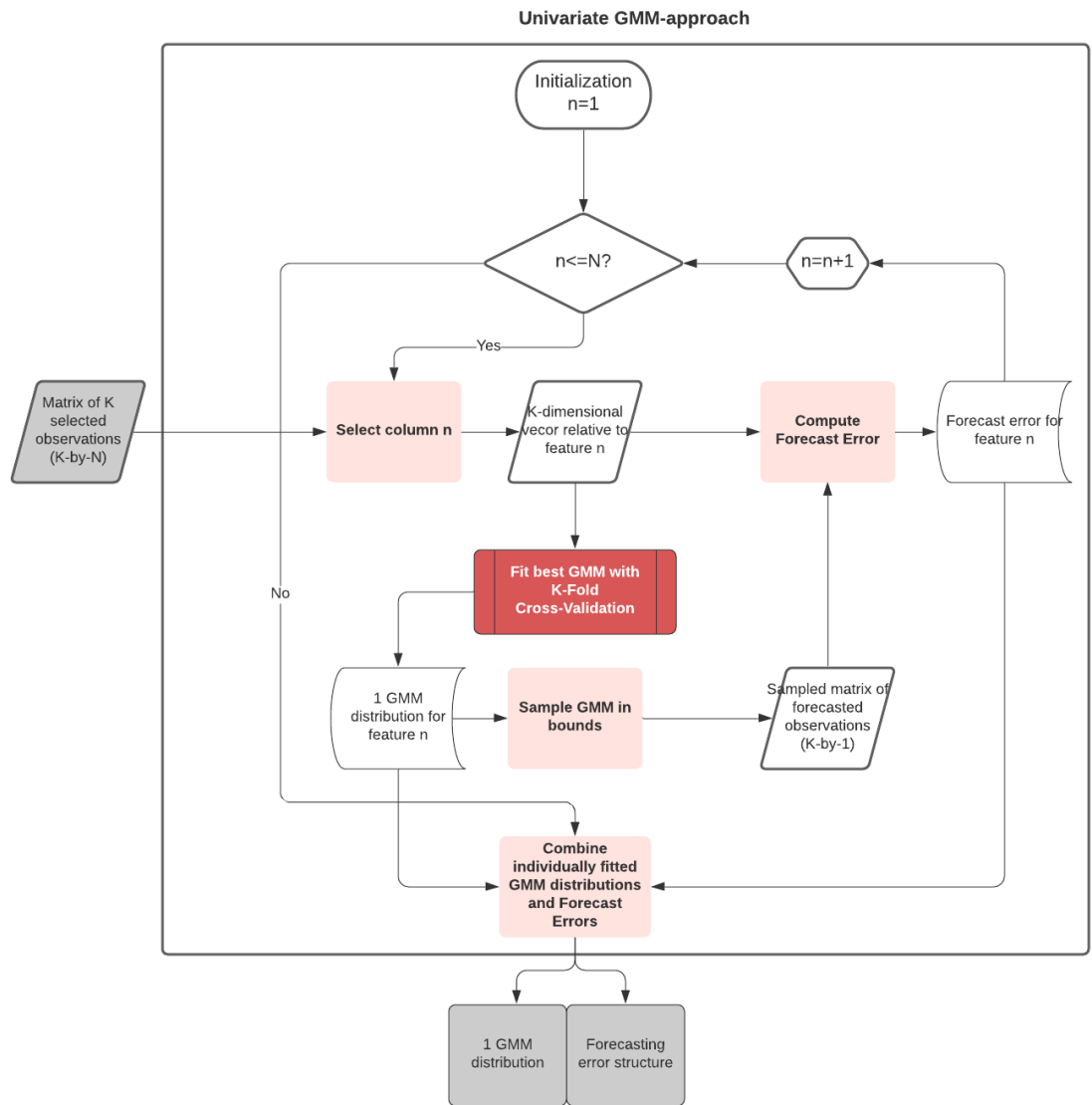


Figure 7.4: Flowchart of the univariate GMM approach block

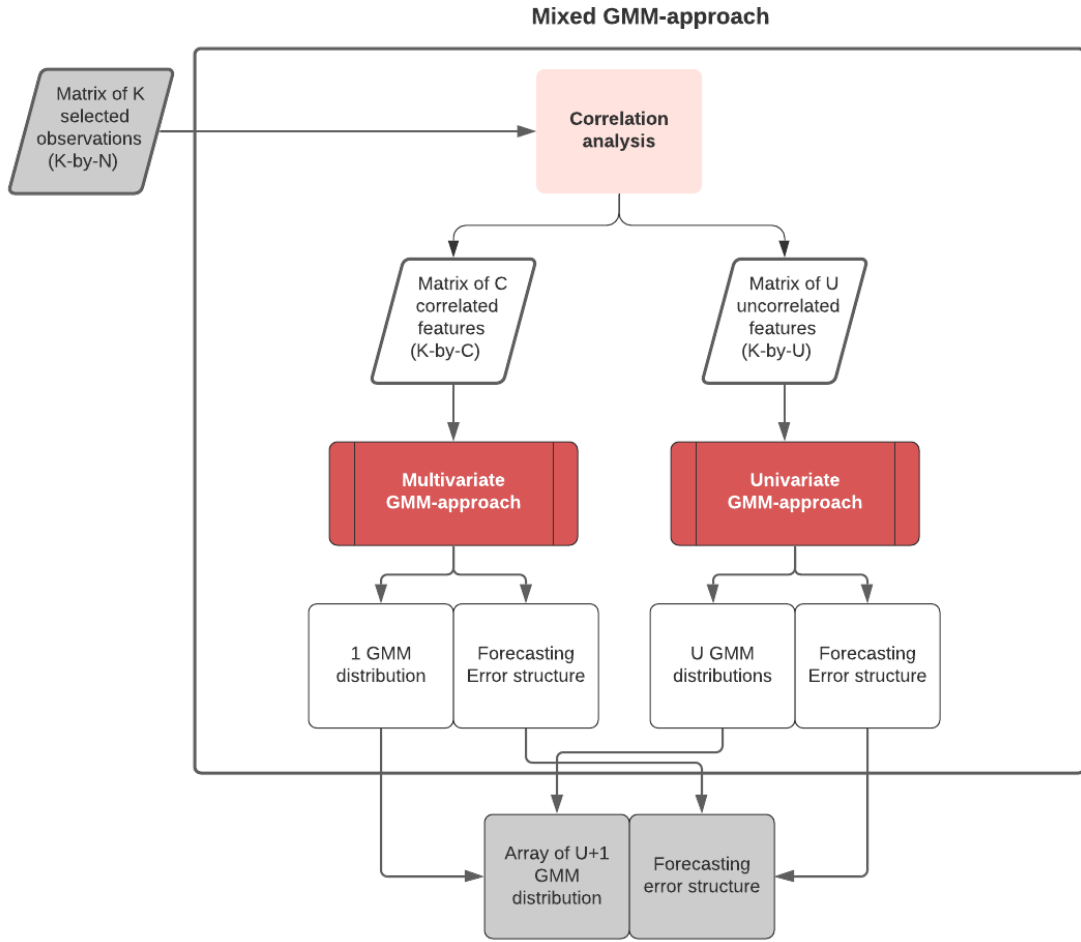


Figure 7.5: Flowchart of the mixed GMM approach block

Table 7.1: Metrics to compare different approaches and choose the *best-fit*

(a) Accuracy metrics

Metric	Unit	Formula
Mean absolute percentage error (MAPE)	[%]	$\frac{100}{K} \sum_{k=1}^K \left \frac{\epsilon_k}{x_k} \right $
Symmetric mean absolute percentage error (sMAPE)	[%]	$\frac{100}{K} \sum_{k=1}^K \frac{\epsilon_k}{0.5(x_k + y_k)}$
Median symmetric accuracy (MSA)	[%]	$100 \left(e^{\text{MEDIAN}(\log_e Q_k)} - 1 \right)$

(b) Bias metrics

Metric	Unit	Formula
Mean percentage error (MPE)	[%]	$\frac{100}{K} \sum_{k=1}^K \frac{\epsilon_k}{x_k}$
Median log accuracy ratio (MdLQ)	different	$\text{MEDIAN}(\log_e Q_k)$
Symmetric signed percentage bias (SSPB)	[%]	$100 \text{sign}(MdLQ) \left(e^{ MdLQ } - 1 \right)$

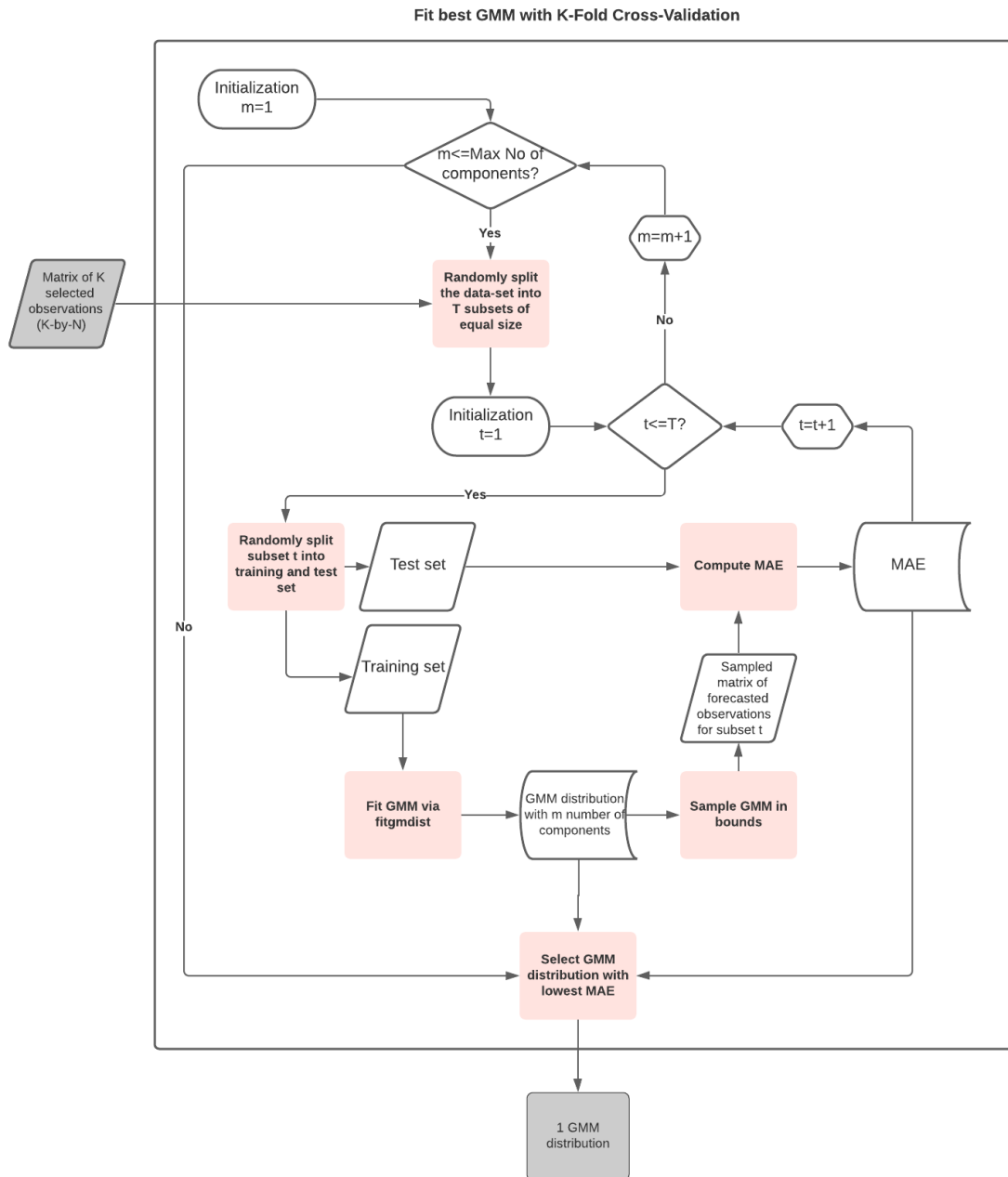


Figure 7.6: Flowchart of the mixed GMM approach block

Tab. 7.2. With this assumptions the total number of scenarios would be four times the total number of considered EV user scenario.

Since that reduced number still led to an OP with high complexity, we went a step further by trying to reduce the number of considered EV user scenarios. To do so, we leveraged the *k-means* clustering algorithm [122] together with the scenario number selection method explained in Rem. 3⁵⁷. Namely, first the number of needed scenarios to achieve statistically meaningful results is computed. Then, after generating the needed EV user scenarios, the scenarios are partitioned and stored into a user-defined number of clusters (NUM_CLUSTERS) using the *k-means* clustering algorithm. Then, the medoid, i.e. the original scenario with the lowest probability distance from the centroid of a cluster, of each cluster is selected as a representative EV user scenario for the ones stored in that cluster. The reason the medoid is selected rather than the centroid, i.e. cluster analytical center, is that the centroid of a cluster is an artificial scenario that might not have any physical meaning. Finally, the output are the *representative* EV user scenarios, i.e. the cluster medoids. Naturally, this means that the reduced total number of considered EV user scenarios is equal to the user-defined number of desired clusters for the *k-means* algorithm (i.e. NUM_CLUSTERS).

As a concluding note, it is important to note that, in their natural form, EV user scenarios are not easy to input into the *k-means* clustering algorithm. This is due to the complexity of their forecasting models, e.g. it is difficult to compare, for instance, a scenario that has 2 morning charging sessions w.r.t a scenario that has 3 evening charging sessions. As a result, *extra-features* needed to be defined to describe each EV user scenario. These features are listed in Tab. 7.3 and were used as input to the *k-means* clustering algorithm.

Table 7.2: Considered non-EV injection scenarios

Scenario number	Percentile of all uncontrollable loads [%]	Percentile of all uncontrollable generation (P-V plants) [%]
1	5	5
2	5	95
3	95	5
4	95	95

7.3.2 Optimization Problem

As previously explained, the second process of the day-ahead stage is to solve a stochastic scenario-based security-constrained OP that outputs an optimal DP. Compared to the one in [6], the proposed OP (i) accounts for EVCSs⁵⁹ as controllable resources with specific objectives and constraints, (ii) does not include minimum PCC power factor hard-constraints but a minimization of the absolute reactive power flow at the PCC in the OP objective, and (iii) is solved iteratively in order to reduce potential power-flow linearization inaccuracies. In the following, the OP objective are first presented. Then, the constraints are listed. Finally, the full OP formulation is given together with its resolution algorithm.

⁵⁷For the interested reader, a similar yet more complex method of leveraging the *k-means* clustering algorithm to reduce the number of needed scenarios in a stochastic OP can be found in [123].

⁵⁸For a given time interval, the occupancy rate is defined as the ratio of the number of control time-steps where a plug is used, over the total number of control time-steps.

⁵⁹In the following, all types of three-phase EVCSs are considered, i.e. Type-2 AC plugs and DC plugs.

Table 7.3: Considered *extra-features* to describe an EV user scenario

Feature number	Description
1	Total number of charging sessions
2	Sum of all stay duration of all charging sessions
3	Sum of all energy demands of all charging sessions
4	Average maximum active power injection limits of all charging sessions
5	Occupancy rate ⁵⁸ from 00:00 to 03:59
6	Occupancy rate ⁵⁸ from 04:00 to 07:59
7	Occupancy rate ⁵⁸ from 08:00 to 11:59
8	Occupancy rate ⁵⁸ from 12:00 to 15:59
9	Occupancy rate ⁵⁸ from 16:00 to 19:59
10	Occupancy rate ⁵⁸ from 20:00 to 23:59

Objective

The OP objective is threefold. The first aim consists in minimizing the deviation between the active power flow at the PCC for all scenarios $d = 1, \dots, D$ and the optimally computed DP $P_{s,t}^{\text{dispatch}}$ where $t = 1, \dots, T$ is the timestep and $s \in \mathcal{S}$ is the slack node index. Formally, this is given by,

$$\frac{1}{DT} \sum_{d=1}^D \sum_{t=1}^T \left| P_{s,t}^d - P_{s,t}^{\text{dispatch}} \right|, \quad (7.2)$$

where the norm-1 operator was used instead of the euclidean norm to avoid quadratic terms and, consequently, decrease computation times. The second aim consists in minimizing the absolute reactive power flow at the PCC for all scenarios and timesteps. Formally, this is given by,

$$\frac{1}{DT} \sum_{d=1}^D \sum_{t=1}^T \left| Q_{s,t}^d \right|. \quad (7.3)$$

The third objective consists in minimizing all resource-specific cost functions that, as explained in [6], reflect the controllable resources' willingness to provide regulating power. Tab. 7.4 lists the different considered resources with their respective cost functions. As can be seen, for a BESS the cost function tries to simply minimize its usage, i.e. absolute injections ($|P_{i,\text{BESS},t}^d|$), to prevent its ageing due to cycling. On the other hand, for EVCSs the cost functions aims are twofold. First, they try to guarantee that each EV's departure SoC ($\text{SoC}_{k,i}^{\text{Leave}^d}$, for plug $k \in K_i$ ⁶⁰, node $i \in \mathcal{C}$ and scenario $d = 1, \dots, D$) is close to its desired SoC ($\text{SoC}_{k,i}^{\text{Target}^d}$ for plug $k \in K_i$, node $i \in \mathcal{C}$ and scenario $d = 1, \dots, D$). The max function is used in order to *penalize* EVs only until they reach their target SoC without limiting extra charging/discharging when applicable (i.e. grid-secure). Second, they try to minimize EV battery wearing by avoiding large deviations of EV injections ($P_{t,k,i}^d$ for plug $k \in K_i$, node $i \in \mathcal{C}$ and scenario $d = 1, \dots, D$ at timestep $t = 1, \dots, T$) between subsequent time-steps [115]. All the factors scaling all the presented cost functions, e.g. $\frac{3600}{\Delta t D K_i}$ where Δt is the DP time-resolution, are included in order to render all objective terms of the same nature (i.e. here, powers). The final OP objective is a weighted sum of all presented cost functions.

⁶⁰Recall that K_i is the total number of plugs of the EVCS connected to node $i \in \mathcal{C}$. Furthermore, at each node $i \in \mathcal{C}$, there's an EV aggregator that can send active and reactive power setpoints to all EVCSs (or plugs).

Table 7.4: Cost functions of all considered controllable resources

Resource	Objective
BESS connected at node $i \in \mathcal{K}$	$\frac{1}{DT} \sum_{d=1}^D \sum_{t=1}^T P_{i,\text{BESS},t}^d \quad (7.4)$
EVCS connected at node $i \in \mathcal{C}$	$\frac{3600}{\Delta t D K_i} \sum_{d=1}^D \sum_{k=1}^{K_i} \max \left\{ \text{SoC}_{k,i}^{\text{Target}^d} - \text{SoC}_{k,i}^{\text{Leave}^d}, 0 \right\} +$ $\frac{1}{10(T-1)DK_i} \sum_{d=1}^D \sum_{k=1}^{K_i} \sum_{t=2}^T P_{t,k,i}^d - P_{t-1,k,i}^d \quad (7.5)$

Constraints

The OP constraints are twofold. The first set of constraints are the ADN operational constraints. As the ADN is assumed balanced in the day-ahead stage, the operational constraints are, formally, given by

$$|\bar{\mathbf{E}}_t|^d \in [E_{\min}, E_{\max}], |\bar{\mathbf{I}}_{ij,t}|^d \leq \mathbf{I}_{ij,\max}, |\bar{\mathbf{S}}_{s,t}|^d \leq \mathbf{S}_{s,\max} \quad (7.6)$$

where, E_{\min} and E_{\max} are, again, the allowed extremes of the nodal voltage magnitudes, $\bar{\mathbf{I}}_{ij,\max}$ is the vector of branch ampacity limits, $\bar{\mathbf{S}}_{s,\max}$ is the substation transformer apparent power limit and the superscript d refers to a given scenario. $|\bar{\mathbf{E}}_t|$, $|\bar{\mathbf{I}}_{ij,t}|$ and $|\bar{\mathbf{S}}_{s,t}|$ are generically linearly approximated by,

$$\begin{aligned} \mathbf{\Gamma}_t^d \approx & \tilde{\mathbf{\Gamma}}_t^d(\tilde{\mathbf{S}}_t^d) + \frac{\partial \mathbf{\Gamma}_t}{\partial \mathbf{P}_t} \Big|_{\tilde{\mathbf{S}}_t^d}^{61} \left(\mathbf{p}_{t,\text{Control}}^d - \mathbf{p}_{t,\text{Control}}^{d, \nu-1} \right) \\ & + \frac{\partial \mathbf{\Gamma}_t}{\partial \mathbf{Q}_t} \Big|_{\tilde{\mathbf{S}}_t^d}^{61} \left(\mathbf{q}_{t,\text{Control}}^d - \mathbf{q}_{t,\text{Control}}^{d, \nu-1} \right) \end{aligned} \quad (7.7)$$

where, $\mathbf{\Gamma} \in \{|\bar{\mathbf{E}}_t|, |\bar{\mathbf{I}}_{ij,t}|, |\bar{\mathbf{S}}_{s,t}|\}$, $\tilde{\mathbf{\Gamma}}_t^d(\tilde{\mathbf{S}}_t^d)$ is the electrical quantity resulting from the system-state obtained from a LF computation with nodal injections $\tilde{\mathbf{S}}_t^d = \tilde{\mathbf{S}}_t^d + \tilde{\mathbf{s}}_{t,\text{Control}}^{d, \nu-1}$, where $\tilde{\mathbf{S}}_t^d$ are the sampled non-EV injection scenarios and $\tilde{\mathbf{s}}_{t,\text{Control}}^{d, \nu-1} = \mathbf{p}_{t,\text{Control}}^{d, \nu-1} + j\mathbf{q}_{t,\text{Control}}^{d, \nu-1} = \tilde{\mathbf{S}}_{\text{BESS},t}^{d, \nu-1} + \tilde{\mathbf{S}}_{\text{EV},t}^{d, \nu-1}$ are the optimal injections of all controllable resources (i.e. $\tilde{\mathbf{S}}_{i,\text{BESS},t}^d = P_{i,\text{BESS},t}^d + jQ_{i,\text{BESS},t}^d$ for a BESS connected to node $i \in \mathcal{K}$ and $\tilde{\mathbf{S}}_{i,\text{EV},t}^d = P_{i,\text{EV},t}^d + jQ_{i,\text{EV},t}^d$ for the EVCSs aggregator of node $i \in \mathcal{C}$) at the previous resolution iteration $\nu - 1$.

The second set of constraints are the controllable resources operational constraints. Tab. 7.5 lists the different considered resources with their respective constraints. The BESS constraints consist in: (i) SoC energy bounds (c.f. (7.8)), where E_i^{\max} is the BESS's maximum energy capacity, and (ii) apparent power limits (c.f. (7.9)). The EVCS constraints consist in: (i) per EV SoC evolution constraints (c.f. (7.10)⁶²), (ii) per EV SoC bounds (c.f. (7.11)), (iii) per EV definitions of the SoCs at departure $\text{SoC}_{k,i}^{\text{Leave}^d}$ (c.f. (7.12)⁶³),

⁶¹Recall that the SCs $\partial \mathbf{\Gamma}_t / \partial \mathbf{P}_t|_{\tilde{\mathbf{S}}_t^d}$ and $\partial \mathbf{\Gamma}_t / \partial \mathbf{Q}_t|_{\tilde{\mathbf{S}}_t^d}$ are, respectively, the partial derivatives of the electrical quantity $\mathbf{\Gamma}$ with respect to nodal active and reactive power injections, computed with the injections $\tilde{\mathbf{S}}_t^d$ using the method of Sec. 2.3.

⁶²Recall that $t_{0,k,i}^d$ is the arrival time of an EV at plug $k = 1, \dots, K_i$ and node $i \in \mathcal{C}$ for scenario $d = 1, \dots, D$. Also, $E_{k,i}^{d,\max}$ were defined as the battery capacity of the EV connected to plug $k = 1, \dots, K_i$ and node $i \in \mathcal{C}$ for scenario $d = 1, \dots, D$. In the day-ahead stage, the arrival times and EV battery capacities are forecasted.

⁶³Recall that $t_{f,k,i}^d$ is the departure time of an EV at plug $k = 1, \dots, K_i$ and node $i \in \mathcal{C}$ for scenario $d = 1, \dots, D$. In

Chapter 7. EV-aware Day-Ahead Power-Grid-Dispatch: Theory and Experimental Validation

(iv) per plug maximum/minimum active⁶⁴ (c.f. (7.13)), reactive⁶⁵ (c.f. (7.14)) and apparent (c.f. (7.15)) power constraints, and (v) constraints linking the per plug variables to the per node aggregate EVCSs injections (c.f. (7.16)).

As a final note, observe that in the SoC constraints (i.e. (7.8) and (7.10)) the efficiency is assumed unitary. However, since in practice this is not true for both BESSs and EVs, we account for power losses by integrating the latter's equivalent series resistance into the network admittance matrix as explained in [6].

Table 7.5: Constraints of all considered controllable resources

Resource	Constraint
BESS connected at node $i \in \mathcal{K}$	$\text{SoC}_{i,\min} \leq \text{SoC}_{t-1,i}^d - \frac{P_{i,\text{BESS},t}^d \Delta t}{E_i^{\max}} \leq \text{SoC}_{i,\max}$ (7.8)
	$\left(P_{i,\text{BESS},t}^d\right)^2 + \left(Q_{i,\text{BESS},t}^d\right)^2 \leq S_{i,\max}$ (7.9)
EVCS connected at node $i \in \mathcal{C}$	$\text{SoC}_{t,k,i}^d = \begin{cases} \text{SoC}_{t_0,k,i}^d & \text{if } t = t_{0,k,i}^d \\ \text{SoC}_{t-1,k,i}^d - \frac{P_{t,k,i}^d \Delta t}{E_{k,i}^{\max}} & \text{otherwise} \end{cases}$ (7.10)
	$0 \leq \text{SoC}_{t,k,i}^d \leq 1$ (7.11)
	$\text{SoC}_{k,i}^{\text{Leave}^d} = \text{SoC}_{t_f,k,i}^d$ (7.12)
	$-\omega_{t,k,i}^d P_{k,i}^{d,\min} \geq P_{t,k,i}^d \geq -\omega_{t,k,i}^d P_{k,i}^{d,\max}$ (7.13)
	$-\omega_{t,k,i}^d Q_{k,i}^{d,\min} \geq Q_{t,k,i}^d \geq -\omega_{t,k,i}^d Q_{k,i}^{d,\max}$ (7.14)
	$\left(P_{t,k,i}^d\right)^2 + \left(Q_{t,k,i}^d\right)^2 \leq \left(S_{k,i}^{d,\max}\right)^2$ (7.15)
	$\bar{S}_{i,\text{EV},t}^d = \sum_{k=1}^{K_i} P_{t,k,i}^d + j Q_{t,k,i}^d$ (7.16)

7.3.3 Recap & Problem Resolution

The final OP of the day ahead-stage is given by (7.17). The variables of the OP are all the apparent power injections of all controllable resources together with the optimal DP ($\mathbf{P}_s^{\text{dispatch}}$). The different α_\bullet are user-tunable weights. Finally, for clarity and completeness, Alg. 7 summarises all the needed steps for both processes of the day-ahead stage, where t_p and t_c are, respectively, maximum tolerances for

the day-ahead stage, the departure times are forecasted.

⁶⁴Recall that $\omega_{t,k,i}^d$ is a *known* Boolean expressing whether, or not, an EV is connected to plug $k = 1, \dots, K_i$.

⁶⁵As explained in Sec. 6.2.2, reactive power limits depend on the plug type. Namely, if the EV plugs are DC-Typed plugs, the reactive power injections are non-null and are only limited by the plug's apparent power bound, otherwise, they are null.

control variable and cost function variations between consecutive OP resolutions.

$$\begin{aligned}
 \mathbf{p}_s^{\text{dispatch}} = \operatorname{argmin} & \left\{ \alpha_{\text{Disp}}(7.2) + \alpha_{\text{PF}}(7.3) + \sum_{\substack{i \in \mathcal{K} \\ \text{where BESS is connected}}} \alpha_{i,\text{BESS}}(7.4) + \sum_{i \in \mathcal{C}} \alpha_{i,\text{EV}}(7.5) \right\} \\
 \text{s.t.} & \\
 & (7.6), \quad \forall d = 1, \dots, D, \forall t = 1, \dots, T \\
 & (7.8) - (7.9), \quad d = 1, \dots, D, \forall t = 1, \dots, T, \forall i \in \mathcal{K} \text{ where a BESS is connected} \\
 & (7.10) - (7.16), \quad \forall d = 1, \dots, D, \forall t = 1, \dots, T, \forall i \in \mathcal{C}, \forall k = 1, \dots, K(i)
 \end{aligned} \tag{7.17}$$

Algorithm 7 Day-ahead stage

1. Create forecasting models using historical data;
 2. Generate next-day scenarios;
 - 3 **Do:** starting from $v = 1$, with $\mathbf{p}_{t,\text{Control}}^d{}^0 = \mathbf{q}_{t,\text{Control}}^d{}^0 = \mathbf{0}$;
 - 3.a Solve (7.17);
 - 3.b Store $\mathbf{p}_{t,\text{Control}}^d{}^v$ and Final objective^v = Objective of (7.17);
 - Until:** $\max \left\{ \left| \frac{\mathbf{p}_{t,\text{Control}}^d{}^v - \mathbf{p}_{t,\text{Control}}^d{}^{v-1}}{\mathbf{p}_{t,\text{Control}}^d{}^{v-1}} \right| \right\} \leq t_p$ and $\max \left\{ \left| \frac{\text{Final objective}^v - \text{Final objective}^{v-1}}{\text{Final objective}^{v-1}} \right| \right\} \leq t_c$;
 4. Store final iteration optimal DP ($\mathbf{p}_s^{\text{dispatch}}$).
-

7.3.4 Numerical Simulations

In order to showcase the advantages of considering EVCSs as controllable resources in the day-ahead stage, two sets of numerical simulations are performed. All simulations were performed on MATLAB using the same electrical grid that contains one BESS and two EVCSs aggregators (see Sec. 7.3.4). The main difference between the two sets of simulations is that the second set of simulations performs a sensitivity analysis w.r.t. to the BESS's energy and apparent power capacities. In the following, first the simulation setup is described, then, both sets of simulations are presented.

Simulation Setup

All simulations were performed using a virtual twin (single-phase equivalent) of the low-voltage electrical-grid of the ELL building at the EPFL Lausanne campus. A schematic depiction of the grid can be found in Fig. 7.7 where the greyed-out resources were not used for the simulations and node B01 corresponds to the unique slack node. EVCS2 corresponds to the CS described in Tab. 5.3. EVCS1 is a commercial EV fast-charger whose photographic depiction and technical specifications can be found in Fig. 7.8. B1 is a commercial BESS whose photographic depiction and technical specifications can be found in Fig. 7.9. Tabs. 7.6, 7.7 & 7.8 give, respectively, the branch, nodes and transformers parameters of the network in Fig. 7.7. The latter parameters were used as is in all the simulations of this section. Tab. 7.9 lists the used resource parameters. Tab 7.10 lay-out the used simulation parameters. Finally, Tab 7.11 describes the origin of the historical data used for every resource in the *forecast & scenario generation* block of Fig. 7.1.

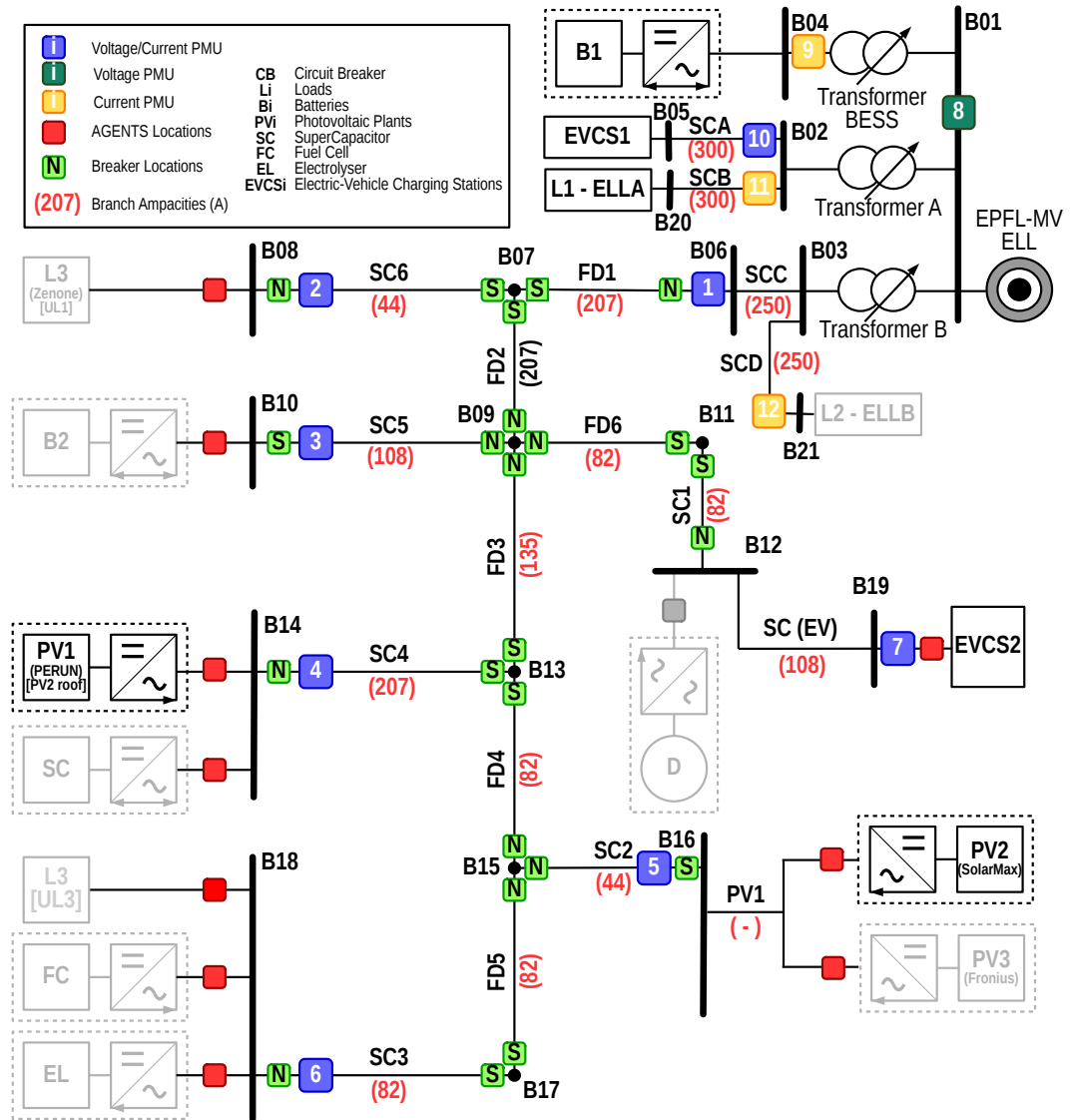





Figure 7.7: Low-Voltage ADN of the ELL building at the EPFL Lausanne campus.

Chapter 7. EV-aware Day-Ahead Power-Grid-Dispatch: Theory and Experimental Validation



(a) EPFL-Lausanne Campus GoFast EVCS

Technical Specifications				
Input AC	Grid connection	AC 3 - phase + N + PE		
	Input voltage range	400V _{AC} +/- 10%		
	Nominal input current 3 x 32 A	3 x 32 A _{AC} - 3 x 300 A		
	Input frequency	45 - 65Hz		
AC Output Connector	AC Plug	IEC 62196 Mode 3, Type 2		
	Plug Nominal AC output power	43kW		
	Nominal AC output voltage	400V _{AC}		
	Nominal AC output current	3 x 63 A _{AC}		
	Safety	<ul style="list-style-type: none"> - Residual current operated device (type B) - Overcurrent circuit protection - Earth monitoring 		
AC Output Socket	AC Socket	IEC 62196 Mode 3, Type 2		
	Socket Nominal AC output power	22 kW		
	(option) Nominal AC output voltage	400V _{AC}		
	Nominal AC output current	3 x 32 A _{AC}		
	Safety	<ul style="list-style-type: none"> - Residual current operated device (type B) - Overcurrent circuit protection - Earth monitoring 		
DC Output	DC Plug	Plug 1	Plug 2	Plug 3
		 CSS IEC 62196-3	 CHAdeMO JEVS G105	 Type 2 DC IEC 62196
	Maximum DC Output power	20kW - 150kW		
	DC Output voltage range	170 - 940V _{DC} (under load: 50 - 940 V _{DC})		
	Maximum DC Output current	50 - 400A _{DC}		
	Power factor (50% load)	> 0.99		
	Efficiency	93% at full load		
	Safety	<ul style="list-style-type: none"> - Short circuit protected output - Overcurrent circuit breaker - Overvoltage protection 		
		<ul style="list-style-type: none"> - Low-voltage protection - Insulation protection - Grounding protection 		
	General			
	Operating temperature	-20°C to +45°C		
	Storage temperature	-40°C to +85°C		
	Relative humidity	5% to 95% (without condensation)		
	Protection	IP 54 (indoor / outdoor use)		
	Dimensions (B x H x T)	1000 x 870 x 2000mm		
	Mass	350 - 500kg (depending on version)		

(b) Technical hardware specifications [124]

Figure 7.8: EVCS1



(a) EPFL-Lausanne Campus Leclanché BESS

Parameter	Value	Unit
Rated Power	720	kVA
Energy Capacity	560	kWh
Voltage at the AC connection point	20	kV
Number of racks	9 in parallel	-
Number of modules per rack	15 in series	-
Cells configuration per module	20s3p	-
Total number of cells	8100	-
Cell minimum voltage	1.7	V
Cell nominal voltage	2.3	V
Cell maximum voltage	2.7	V
Cell nominal capacity	16	Ah
Cell chemistry	Lithium-titanate	-

(b) Technical hardware specifications (Re-adapted from [125])

Figure 7.9: B1

Table 7.6: Day-ahead numerical simulation: branch parameters.

(a) Branches parameters: line data					
From	To	Length [km]	Configuration	Ampacity (from-to) [A]	Ampacity (to-from) [A]
B01	B02	1.000	10	17.32	866.03
B01	B03	1.000	9	17.32	866.03
B01	B04	1.000	8	17.32	1212.44
B02	B05	0.037	6	300.00	300.00
B03	B06	0.037	7	250.00	250.00
B06	B07	0.070	5	207.00	207.00
B07	B08	0.030	1	44.00	44.00
B07	B09	0.035	5	207.00	207.00
B09	B10	0.030	3	108.00	108.00
B09	B11	0.105	2	82.00	82.00
B11	B12	0.030	2	82.00	82.00
B09	B13	0.070	4	135.00	135.00
B13	B14	0.030	5	207.00	207.00
B13	B15	0.105	2	82.00	82.00
B15	B16	0.030	1	44.00	44.00
B15	B17	0.035	2	82.00	82.00
B17	B18	0.030	2	82.00	82.00
B12	B19	0.038	3	108.00	108.00
B02	B20	0.010	6	300.00	300.00
B03	B21	0.010	7	250.00	250.00

(b) Branches parameters: configurations			
Configuration	Longitudinal impedance [Ω/km]	Shunt admittance (from-to) [$\mu S/km$]	Shunt admittance (to-from) [$\mu S/km$]
1	$3.300 + j0.141$	$0.000 + j23.562$	$0.000 + j23.562$
2	$1.210 + j0.132$	$0.000 + j36.128$	$0.000 + j36.128$
3	$0.780 + j0.126$	$0.000 + j32.987$	$0.000 + j32.987$
4	$0.554 + j0.123$	$0.000 + j40.841$	$0.000 + j40.841$
5	$0.272 + j0.119$	$0.000 + j50.266$	$0.000 + j50.266$
6	$0.225 + j0.070$	$0.000 + j27.332$	$0.000 + j27.332$
7	$0.146 + j0.070$	$0.000 + j27.332$	$0.000 + j27.332$
8	$7.944 + j43.877$	$3.923 + j5.884$	$0.000 + j0.000$
9	$5.027 + j40.358$	$1.383 + j1.445$	$0.000 + j0.000$
10	$5.004 + j40.290$	$1.365 + j1.652$	$0.000 + j0.000$

Table 7.7: Day-ahead numerical simulation: node parameters.

Node	Base Voltage [V]	Base Power [MVA]
B01	21000	1
B02	420	1
B03	420	1
B04	300	1
B05	420	1
B06	420	1
B07	420	1
B08	420	1
B09	420	1
B10	420	1
B11	420	1
B12	420	1
B13	420	1
B14	420	1
B15	420	1
B16	420	1
B17	420	1
B18	420	1
B19	420	1
B20	420	1
B20	420	1

Table 7.8: Day-ahead numerical simulation: transformer parameters.

	Transformer A	Transformer B	Transformer BESS
MV rated Voltage [kV]	21	21	21
LV rated Voltage [V]	420	420	300
Rated power [kVA]	630	630	630
Short-circuit voltage [% of MV rated voltage]	5.8	5.81	6.37
Winding losses [W]	4504	4524	7150
Core losses [W]	602	610	1730
Zero-load current [% of MV nominal current]	0.15	0.14	0.495

Table 7.9: Day-ahead numerical simulation: controllable resource parameters.

Name	Parameters
B1	$S_{4,max} = 200$ kVA, $SoC_{4,min} = 0.1$, $SoC_{4,max} = 0.9$, $E_4^{max} = 200$ kWh
EVCS1	$K_5 = 6$ (2 AC-Type-2 and 4 DC [unidirectional])
EVCS2	$K_3 = 3$ (2 AC-Type-2 and 1 DC [bidirectional])

Table 7.10: Day-ahead numerical simulation: simulation parameters.

Parameter	Value	Unit
Objective weights:		
α_{Disp}	100	-
α_{PF}	1	-
$\alpha_{4,\text{BESS}}$	0.01	-
$\alpha_{5,\text{EV}}$	1	-
$\alpha_{19,\text{EV}}$	1	-
Timing:		
Δt	5	minutes
Scenarios:		
Number of EV scenarios	20	-
Total number of scenarios D	80	-
ADN tolerances:		
E_{\min}	0.9	p.u.
E_{\max}	1.1	p.u.
$S_{s,\max}$	1	p.u.
Alg. 7 tolerances:		
t_p	1	%
t_c	1	%

Table 7.11: Day-ahead numerical simulation: inputted historical data.

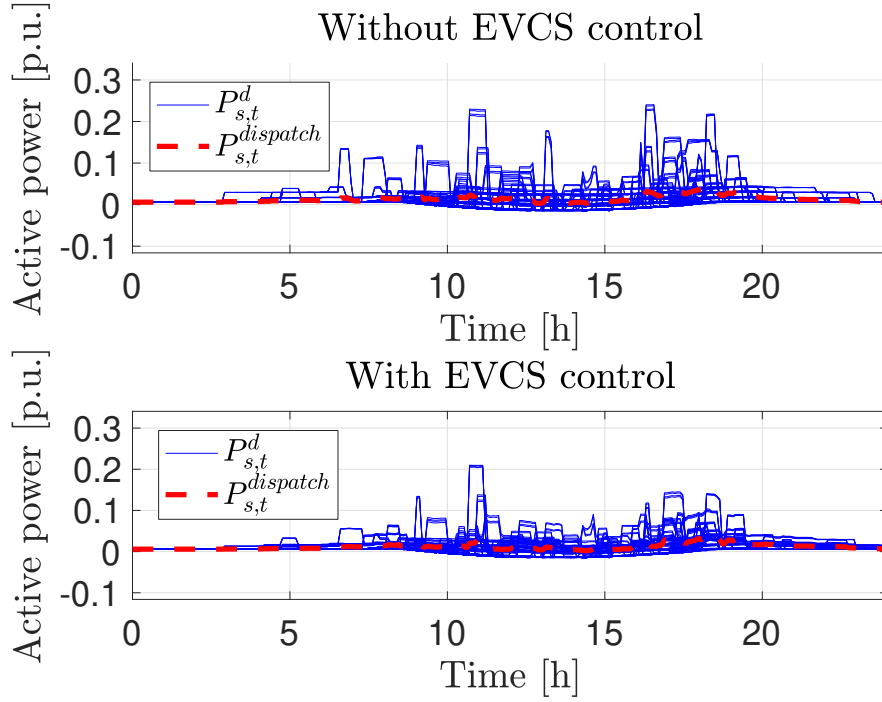
Resource	Description
PV1 & PV2	Same as data used in [6].
L1 - ELLA	Measured data coming from PMU 11 of Fig. 7.7.
EVCS1 & EVCS2	Combination of measured and public data coming from (i) Local back-end logger of EVCS1, and (ii) a confidential dataset provided by GoFAST [126] that contains information about many EV plugs situated in different parts of Switzerland.

Simulation 1: EVCSs as the only day-ahead controllable entities

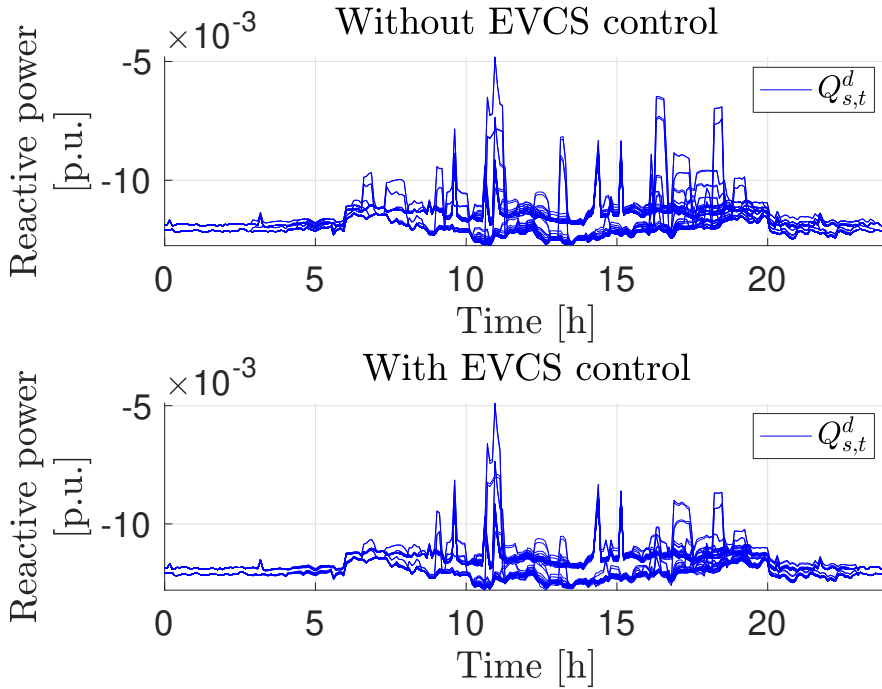
The first set of simulations considers the case where the BESS is not connected to the grid of Fig. 7.7 (i.e. B1). Namely, the only controllable entities in the day-ahead stage are EVCS1 and EVCS2. Using the same scenarios, the idea of these simulations is to compare the obtained DPs when (i) EVCSs are not controlled and plugged EVs simply charge at their maximum rated power, and (ii) EVCSs are considered controllable. It is clear that since there are no controllable entities in the latter case (i), the resulting DP is nothing more than the average over all scenarios of the active power injections at the PCC. In order to compare DPs, we define a set of metrics that are given in Tab. 7.12. First, as defined in [127], the UEE^+ and UEE^- represent the cumulative *worst-case*, respectively upper- and lower-bound of the energy discrepancy needed to merge all PCC nodal active power into the unique DP (i.e. for the PCC active power injections for all scenarios to be equal to the DP). Then, as previously explained, the MAE quantifies the maximum absolute error, in terms of power, between the DP and the PCC active power injection realizations. Then, the MPP is equal to the maximum absolute PCC active power injection realizations. Finally, the MEVUS metric represents the worst ratio, over all charging sessions of all scenarios, of received over best *feasible* energies, where the best *feasible* energy is the minimum between what the EV user requested, i.e. the forecasted quantity given by $E_{k,i}^{\text{desired}^d} = E_{k,i}^{d,\max} \left(\text{SoC}_{k,i}^{\text{Target}^d} - \text{SoC}_{t_{0,k,i}^d, k, i}^d \right)$ for $i \in \mathcal{C}$, $k = 1, \dots, K_i$ and $d = 1, \dots, D$, and, the maximum energy an EV can receive if it was charging at its maximum power – i.e. no control – for its whole plugged duration, i.e. the forecasted quantity given by $E_{k,i}^{\text{best}^d} = P_{k,i}^{d,\max} (t_{f,k,i}^d - t_{0,k,i}^d)$ for $i \in \mathcal{C}$, $k = 1, \dots, K_i$ and $d = 1, \dots, D$.

The results of the simulations are depicted in Figs. 7.10 & 7.11 and Tab. 7.13. Figs. 7.10a & 7.10b show, respectively, the active and reactive nodal power injections at the PCC. Fig. 7.11 shows the time evolution of the UEE. All results lead to the same conclusion: controlling EVCSs in the day-ahead stage (i) improves the merger of all PCC active power scenario realizations into a unique DP, (ii) reduces the untracked energy error and (iii) shaves the peak PCC injections, without penalizing EV users satisfaction. However, it is clear that, in practice, having *only* EVCSs as controllable entities in the day-ahead stage is not enough to fully merge the PCC active power realizations into the DP as they do not have enough *bidirectional energy storage* capabilities⁶⁶. Finally, note that, no voltage, branch current or slack power plots are shown as there were no grid operational constraint violations for any scenario in both simulations, i.e. with and without EVCSs control. Indeed, as the grid-awareness of the developed method was already showcased in [6], our goal was not to stress-test Alg. 7 by tightening the grid operational constraints tolerances, but to illustrate how EVCS can help merge the PCC active power realizations into a unique DP.

⁶⁶Indeed, this could change in the future with the potential penetration of large quantities of bidirectional public chargers which would render the aggregate usable storage of plugged EVs comparable to BESSs used in grid-applications.



(a) Active Power Nodal Injections



(b) Reactive Power Nodal Injections

Figure 7.10: PCC nodal power injections

Table 7.12: Metrics used to quantify the performance of the result of Alg. 7.

Metric	Formula
Uncovered Energy Error (UEE ⁺) [kWh]	$UEE^+(t) = \frac{\Delta T}{3600} \sum_{\tau=1}^t \max_d \{P_{s,\tau}^d\} - P_{s,\tau}^{\text{dispatch}}$
Uncovered Energy Error (UEE ⁻) [kWh]	$UEE^-(t) = \frac{\Delta T}{3600} \sum_{\tau=1}^t \min_d \{P_{s,\tau}^d\} - P_{s,\tau}^{\text{dispatch}}$
Maximum Absolute Error (MAE) [kW]	$MAE = \max_{d,t} \left\{ \left P_{s,t}^{\text{dispatch}} - P_{s,t}^d \right \right\}$
Maximum PCC Power (MPP) [kW]	$MPP = \max_{d,t} P_{s,t}^d $
Minimum EV User Satisfaction (MEVUS) [%]	$MEVUS = 100 \min_{k,i,d} \left\{ \frac{E_{k,i}^{\text{desired}^d}}{E_{k,i}^{\text{best}}} \right\}$

Table 7.13: Simulation 1 - results

Metric	without control	with EVCSs control
UEE ⁺ ($t = T$) [kWh]	1280.93	860.32
UEE ⁻ ($t = T$) [kWh]	-316.10	-284.26
MAE [kW]	214.09	188.59
MPP [kW]	240.64	208.94
MEVUS [%]	100	100

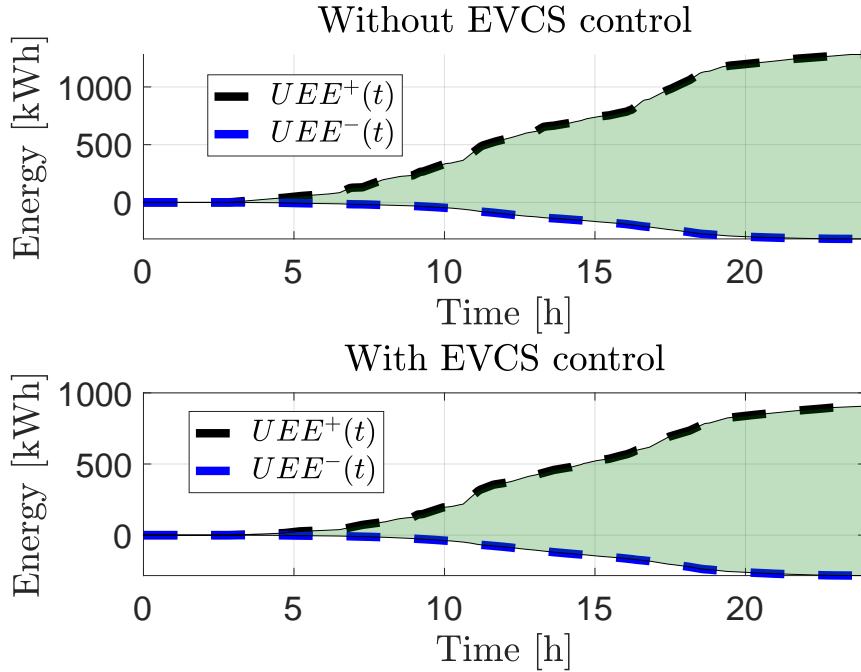


Figure 7.11: UEE time evolution

Simulation 2: EVCSs and BESSs as day-ahead controllable entities

In the second set of simulations, the BESS is considered connected to the grid of Fig. 7.7 (i.e. B1). Namely, the controllable entities in the day-ahead stage are the BESS, EVCS1 and EVCS2. As in the previous simulations, the same scenarios are used and the idea is to compare the obtained DPs when (i) neither EVCSs nor the BESS are controlled, (ii) only the EVCSs are controlled and (iii) both EVCSs and the BESS are controlled. The novelty, w.r.t Simulation 1, is that the comparison is done for different sizes – in terms of maximum apparent power *and* energy capacity – of the BESS. All simulations assume that for all scenarios the BESS's beginning of day SoC is 0.5. Since the BESS is considered, two extra metrics are introduced: the *maximum BESS usage (MBU)* and the *Maximum absolute BESS injections (MABI)*. The MBU is defined as the ratio of (i) the largest energy usage of the BESS over all scenarios, and, (ii) the total usable capacity of the BESS. It is given by $100 \frac{\max_d \left\{ \max_t \text{SoC}_{t,A}^d - \min_t \text{SoC}_{t,A}^d \right\}}{(\text{SoC}_{4,\max} - \text{SoC}_{4,\min}) E_4^{\max}}$. The MABI is defined as the absolute maximum BESS active power injections over all scenarios and timesteps. The results of all simulations are summarized in Tabs. 7.14 & 7.15. In terms of merging the PCC active power realizations into a unique DP, Tabs. 7.14a, 7.14b & 7.14c confirm that (i) the BESS decreases the UEE more than EVCSs, (ii) increasing the BESS size decreases the UEE, (iii) controlling EVCSs always further decreases the UEE, and (iv) the PCC active power realizations are only *perfectly* merged when the BESS is sufficiently large *and* the EVCSs are controlled. As in the previous simulation, there were no grid operational constraints violations. As a result, in terms of EV user satisfaction, all simulations lead to perfect satisfaction (c.f. Tab. 7.15a). Tab. 7.15b shows the BESS's MBU for different BESS sizes and simulation configurations. It can be seen that increasing the BESS's apparent power limit had little-to-no influence as the maximum active power injections were practically all equal. This behavior is due to: (i) the scenarios used for the simulations that did not require extra BESS injections, and (ii) the lack of ADN operational constraints violations. Finally, Tab. 7.15c proves again the advantages of controlling EVCSs as it always lead to less utilization of the BESS for the same EV user satisfaction (c.f. Tab. 7.15a).

Table 7.14: Simulation 2 - results

(a) $UEE^-(t = T)$ - kWh

Controllable Entities \ $S_{4,max}$ [kVA] & E_4^{max} [kWh]	200 & 200	300 & 300	500 & 500	1000 & 1000
None	-316.10	-316.10	-316.10	-316.10
EVCSs	-284.26	-284.26	-284.26	-284.26
BESS	-178.93	-145.35	-74.37	-5.73
EVCSs+BESS	-136.48	-97.51	-20.95	-0.02

(b) $UEE^+(t = T)$ - kWh

Controllable Entities \ $S_{4,max}$ [kVA] & E_4^{max} [kWh]	200 & 200	300 & 300	500 & 500	1000 & 1000
None	1280.93	1280.93	1280.93	1280.93
EVCSs	860.32	860.32	860.32	860.32
BESS	222.46	154.00	66.88	13.92
EVCSs+BESS	165.45	110.77	14.12	0.03

(c) MAE - kW

Controllable Entities \ $S_{4,max}$ [kVA] & E_4^{max} [kWh]	200 & 200	300 & 300	500 & 500	1000 & 1000
None	214.09	214.09	214.09	214.09
EVCSs	188.59	188.59	188.59	188.59
BESS	58.13	48.19	38.71	38.62
EVCSs+BESS	8.39	5.09	0.93	0.02

(d) MPP - kW

Controllable Entities \ $S_{4,max}$ [kVA] & E_4^{max} [kWh]	200 & 200	300 & 300	500 & 500	1000 & 1000
None	240.64	240.64	240.64	240.64
EVCSs	208.94	208.94	208.94	208.94
BESS	117.27	119.12	115.55	109.64
EVCSs+BESS	57.24	50.83	48.59	50.26

Table 7.15: Simulation 2 - results - continued

(a) MEVUS - %

Controllable Entities \ $S_{4,max}$ [kVA] & E_4^{max} [kWh]	200 & 200	300 & 300	500 & 500	1000 & 1000
None	100	100	100	100
EVCSs	100	100	100	100
BESS	100	100	100	100
EVCSs+BESS	100	100	100	100

(b) MBU - %

Controllable Entities \ $S_{4,max}$ [kVA] & E_4^{max} [kWh]	200 & 200	300 & 300	500 & 500	1000 & 1000
None	N/A	N/A	N/A	N/A
EVCSs	N/A	N/A	N/A	N/A
BESS	100	99.60	92.71	67.57
EVCSs+BESS	98.73	76.22	84.06	43.69

(c) MABI - kW

Controllable Entities \ $S_{4,max}$ [kVA] & E_4^{max} [kWh]	200 & 200	300 & 300	500 & 500	1000 & 1000
None	N/A	N/A	N/A	N/A
EVCSs	N/A	N/A	N/A	N/A
BESS	178.72	178.07	172.45	164.05
EVCSs+BESS	198.88	206.42	197.50	198.14

7.4 Real-time stage

As previously mentioned, the main goal of the real-time stage is to track the optimal DP determined by the day-ahead stage. To do so we use the same problem formulation and distributed solution method⁶⁷ described in [6]. However, since we consider EVCSs as controllable entities, extra objectives and constraints are added to the centralised OPF (11) of [6]. Indeed, we leverage the EV-subproblem objectives and constraints presented in Sec. 6.2.2. However, as the OP in [6] is expressed as an MPC problem, the latter are expanded for a given time horizon (denoted by t_H as in [6]). Furthermore, as the real-time controller developed in [6] assumes balanced operation for the ADN, the unbalanced constraints are here omitted. In practice, as explained in Sec. 3.5.1, this assumption also matches the experimental setup used to validate the algorithms of this chapter (c.f. Sec. 7.5). This leads to the objectives and constraints described in Tab. 7.16. As previously explained, the objective is twofold (c.f. Sec. 6.2.2). The first one tries to reach the target EVs SoCs as soon as possible (c.f. (7.18)). The second minimizes the EV battery wearing by penalising large setpoint variations (c.f. (7.19)). All objectives are weighted⁶⁸ in a way to favor plugged EVs with shorter remaining connection times and higher remaining energy demands. In terms of constraints, the first set of constraints guarantee that an EVs' SoCs⁶⁹ do not surpass users requested target (c.f. (7.20)). The second set of constraints guarantee that the computed setpoints are within the EVCS and plugged EVs operational constraints (c.f. (7.21)). Note that, compared to the constraints presented Sec. 6.2.2, there is a minimum charging power constraint that is explicitly added. This is because, in practice, the IEC-61851 [97] protocol does not allow EV charging with currents below 6A per phase. Additionally, we consider the maximum and minimum EV power limitations as time-dependent and known at time t . Finally, compared to Sec. 6.2.2, the last set of constraints (c.f. (7.22)) were added to guarantee the knowledge of the inputted data at time t over the MPC time horizon (i.e. from t to t_H). Indeed, as the problem is formulated using MPC, proper forecasting is required to predict the evolution of the inputted EV user behavior, e.g. the Boolean $\omega_{t,k,i}$ expressing whether, or not, an EV is plugged to plug $k = 1, \dots, K_i$ of node $i \in \mathcal{C}$ at timestep t . As a result, the constraints impose persistent forecast of the latter over the considered horizon. This is acceptable as the horizon is usually selected to be in the order of minutes and the EV user behavior usually does not drastically change during these time-scales.

⁶⁷c.f. Sec. IV-b of [6] for more details about the ADMM-based solution algorithm.

⁶⁸See Sec. 6.2.2 for weights definitions.

⁶⁹Recall that the present SoC is assumed known by either direct measurement or estimation as explained in Sec. 6.2.2.

Chapter 7. EV-aware Day-Ahead Power-Grid-Dispatch: Theory and Experimental Validation

Table 7.16: Real-time stage objectives and constraints of an EVCS aggregator connected to node $i \in \mathcal{C}$

(a) Objectives	
Description	Equation
Reach Target SoC	$\sum_{\tau=t}^{t_H} \sum_{k=1}^{K_i} \kappa_{\tau,k,i} \left(\text{SoC}_{t_f,k,i} - \text{SoC}_{\tau,k,i} + \frac{\eta_{k,i} P_{\tau,k,i} \Delta t}{E_{k,i}^{\max}} \right) \quad (7.18)$
Minimize EV battery wearing	$\sum_{\tau=t}^{t_H} \sum_{k=1}^{K_i} \lambda_{\tau,k,i} \kappa_{\tau,k,i} P_{\tau,k,i} - P_{\tau-1,k,i} \frac{\Delta t}{E_{k,i}^{\max}} \quad (7.19)$
(b) Constraints	
Description	Equation
SoC Limitations	$\text{SoC}_{\tau,k,i} - \frac{\eta_{k,i} P_{\tau,k,i} \Delta t}{E_{k,i}^{\max}} \leq \text{SoC}_{t_f,k,i}, \forall \tau = t, \dots, t_H \quad (7.20)$
Power Limitations	$(P_{\tau,k,i}, Q_{\tau,k,i}) \in \begin{cases} \{ (P, Q) \mid & \omega_{\tau,k,i} = 1 \\ P^2 + Q^2 < (S_{k,i}^{\max})^2, & \\ -P_{\tau,k,i}^{\min} \geq P \geq -P_{\tau,k,i}^{\max} \} & , \forall \tau = t, \dots, t_H \\ \{(0, 0)\} & \omega_{\tau,k,i} = 0 \end{cases} \quad (7.21)$
Persistent Forecasting	$\begin{cases} \omega_{\tau,k,i} = \omega_{\tau-1,k,i} \\ \kappa_{\tau,k,i} = \kappa_{\tau-1,k,i} \\ \lambda_{\tau,k,i} = \lambda_{\tau-1,k,i} \\ P_{\tau,k,i}^{\max} = P_{\tau-1,k,i}^{\max} \\ P_{\tau,k,i}^{\min} = P_{\tau-1,k,i}^{\min} \end{cases}, \forall \tau = t+1, \dots, t_H \quad (7.22)$

7.5 Experimental Validation

This section presents an experimental validation of both the day-ahead and real-time stages. More specifically, first an optimal day-ahead DP is calculated. Then, the real-time controller is used in order to track the DP while accounting for ADN and resources operational constraints. The goal of the experiment is twofold. First, we show that the integration of EVCSs in both the day-ahead and real-time stages improves the tracking of an optimally computed DP. Second, we experimentally prove the aptness of the proposed real-time EVCS controller to best satisfy EV user demands. In the following, first the experimental setup is described. Then, some notes on the experiment are given. Finally, the results of the experiment are shown.

7.5.1 Experimental Setup: EPFL-DESL microgrid

The experimental validation of the proposed algorithms is performed on the EPFL-DESL microgrid. The experiment uses: (i) the same IT infrastructure described in Sec. 3.5.1, (ii) the branch and node parameters listed, respectively, in Tabs. 7.6 & 7.7, and (iii) the PMU-aided monitoring infrastructure shown in Fig. 7.7 (see Sec. 3.5.1). As explained in [6], the microgrid interfaces several resources, however, for the purpose of this experiment, only a subset is considered. More specifically, a load emulator (L3 (Zenone) of Fig. 7.7) is used to reproduce daily demand profile, two controllable P-V plants (PV1 (Perrun) and PV2 (SolarMax) of Fig. 7.7), a controllable battery (B2 of Fig. 7.7) and a controllable EVCS (EVCS2 of Fig. 7.7). The resource parameters are given in Tab. 7.17.

7.5.2 Experimental Notes

As the goal of the experiment was not to stress test the algorithms in terms of ADN and resources operational constraints, all resources were used at full-capacity and the ADN operational limits were set to the values in the EN-50160 standard [48]. However, as in the simulations of Sec. 7.3.4, the maximum and minimum allowable SoCs for the BESS are limited to 0.9 and 0.1 respectively.

Furthermore, as explained in Sec. III-C of [102], power-to-current lookup tables are needed to enable explicit active power control of Type-2 plugs⁷⁰. As a result, power-to-current lookup tables were precomputed for every available Type-2-EV at the DESL. The tables are shown in graphical format in Fig. 7.12. It can be seen that, for the Renault Zoe, when the setpoint – i.e. per-phase current maximum allowable current – is lower than 7A, the car does not consume any active power. This, in practice, means that the EVCS controller could ask this car to not consume power while remaining plugged. This is not the case for the Tesla Model S as it consumes power even when setpoint is set to the IEC-61851 standard's [97] minimum allowable setpoint of 6A. As a result, a plugged Tesla Model S will always consume around 3kW⁷¹.

Additionally, as discussed in Sec. 3.5.2 and to match the hypothesis of [6], the experiment assumes

⁷⁰Recall that Type-2 plugs are controlled through an analog pulsed signal that dictates to the EV the RMS value of the maximum per-phase current it can consume.

⁷¹Note that, in practice, the Tesla Model S's power could be reduced to zero if, as explained in the IEC-61851 standard, the duty-cycle of the control pilot signal is set to a value higher than 95%. However, through testing, it was observed that this created issues for the EV's on-board controller as the car was constantly locking and unlocking its plug. As a result, the look-up table was deliberately started from a minimum three-phase power of 3kW.

Table 7.17: Experiment: resource parameters

	Value	Unit
B2		
Rated Power	25	kVA
Maximum Energy Capacity	25	kWh
Number of racks	1	-
Number of modules per rack	13 in series	-
Cells configuration per module	20s3p	-
Total number of cells	780	-
Cell minimum voltage	1.7	V
Cell nominal voltage	2.3	V
Cell maximum voltage	2.7	V
Cell nominal capacity	16	Ah
Cell chemistry	Lithium-titanate	-
Active power flow	bi-directional	-
Reactive power flow	bi-directional	-
L3 (Zenone)		
Rated power per phase	10	kVA
Active power flow	uni-directional (load)	-
Reactive power flow	bi-directional	-
PV1 (Perrun)		
Rated Power of P-V cells	13	kWp
Active power flow	uni-directional (generator)	-
Reactive power flow	bi-directional	-
PV2 (SolarMax)		
Rated Power of P-V cells	16	kWp
Active power flow	uni-directional (generator)	-
Reactive power flow	none/not allowed	-
EVCS2		
Miscellaneous	See Tab. 5.3	-

balanced operation of the EPFL-DESL microgrid. Consequently, the phase superscript is omitted for the remainder of this chapter. Furthermore, the control time-step is set to 1min with an MPC-horizon the real-time controller of 5mins.

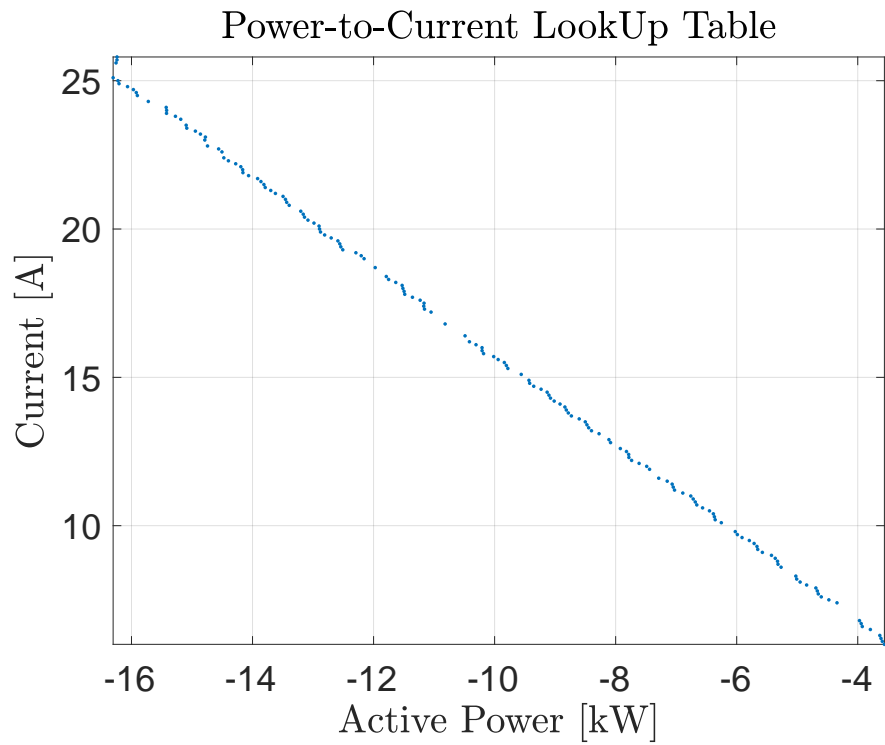
Moreover, as our goal was not to test the validity of our forecasting tools, the models developed in [6] to forecast the P-V generation and L3 (Zenone) load were reused as is. Furthermore, the same EV user behaviour model developed for the day-ahead stage was used to compute a random next-day realization – i.e. an EV day-long scenario with several charging sessions – for the EVCS⁷². The EV-user behaviour scenario is described in Tab. 7.18, where, as previously explained, power-to-current lookup tables are leveraged to control EVs connected to the Type-2 plug, while explicit power setpoints are leveraged to control EVs connected to the CHAdeMO plug.

Finally, even though the DP is day-long, the real-time controller is deployed on a portion of the day, specifically from $t_{0,exp} = 10:30:00$ to $t_{f,exp} = 18:40:30$. This is due to the facts that: (i) the real-time realizations were inferred from the forecasting tools used in the day-ahead stage, (ii) our main focus is the addition of EVCSs in both control stages, and, as seen in the next subsection, the next-day EV scenario realization contains EV charging sessions only from around 11:30:00 to 18:38:00, and (iii) the UEE evolution of the day-ahead optimal DP, shown in Fig. 7.13, shows that most the energy uncertainty is concentrated around the time of the experiment. In this respect, for the sake of fairness, the BESS's initial SoC was set to 0.46, representing the average day-ahead SoC realization over all scenarios at 10:30:00.

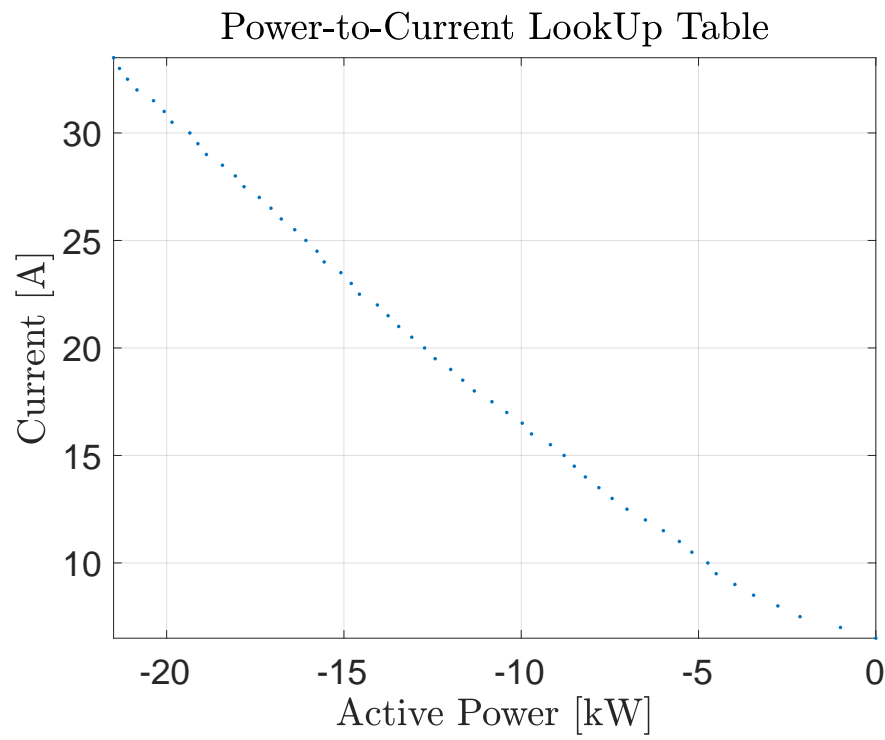
Table 7.18: Day-long EV-scenario used for the experiment

	Charging Session 1	Charging Session 2
Used EV [-]	Peugeot Ion	Renault Zoe
Plug Type [-]	CHAdeMO	Type-2
Initial SoC [%]	29	20
Target SoC [%]	91	55
UsableEV Battery Capacity [kWh]	14	45
Arrival Time [hh:mm:ss]	11:35:00	15:45:00
Scheduled Departure Time [hh:mm:ss]	13:15:00	18:35:00
Actual Departure Time [hh:mm:ss]	13:15:00	18:40:00

⁷²In practice, the generated scenario was adapted to an equivalent scenario that matches the battery capacities of the EVs available at the DESL.



(a) Tesla Model S 90D



(b) Renault Zoe

Figure 7.12: Power-to-current setpoint lookup tables

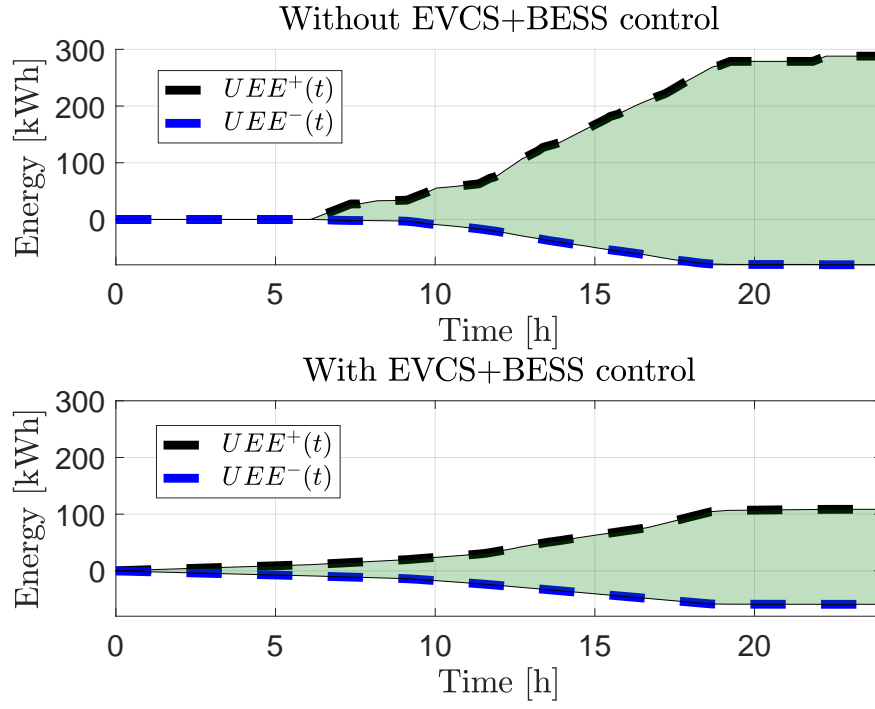


Figure 7.13: Experimental validation: day-ahead UEE time evolution over 24 hours

7.5.3 Results

The results of the experiment are shown in Figs. 7.14, 7.15 and 7.16 and Tab. 7.19. As in the numerical simulations section, neither nodal voltages nor branch currents are shown as there were no ADN operational constraints violations. In the following, the shaded green rectangles in the plots represent the time of the day when the experiment was running, i.e. the real-time controller, with the DP tracking functionality, was active.

Fig. 7.14 shows the day-ahead vs. real-time nodal active power injections of all non-slack resources. It can be seen that all next-day realization were within their forecasted intervals with the exception of two unforeseen passing-clouds for the P-V resources.

Fig. 7.15 shows the evolution the nodal active power slack injections (*Realized (instantaneous)* or $P_{s,t}$) w.r.t. the optimal DP (*Day-Ahead DP* or $P_s^{Dispatch}$). It also shows the nodal active power slack injections averaged over blocks of 5 minutes (*Realized - mean over 5 mins*). The plot shows that in terms tracking the real-time controller *generally* tracks the day-ahead optimal DP with a $\sim 1\text{kW}$ error. More specifically, from 11:12:00 to 11:18:00 and from 17:39:00 to 17:47:30 the BMS of B2, i.e. the BESS used in the experiment, went into error due to unforeseen reasons and the BESS got disconnected from the microgrid. As the disconnection was not planned, the real-time controller tries to follow as best as it can the DP. At 11:37:30, the Peugeot Ion is connected and the CHAdeMO charger decides to start charging even though it was not instructed to. As a result, for one control-period, there's a discrepancy between the DP and the nodal slack power injection. From 12:54:00 to 13:13:00, as the Peugeot-Ion's SoC reaches 85%, its on-board controller decides to decrease its consumption due to internal constraints of the EV BESS. As a result, the EV consumes less than the sent setpoint and that discrepancy leads to a loss in DP tracking. From 13:46:30 to 13:54:00 and 14:52:30 to 15:06:00 there were day-ahead unforeseen passing clouds that further led to erroneous real-time solar irradiance forecast. Consequently, the real-time controller sent setpoints to both P-V resources that were not compatible with the available maximum power of the P-V plants. From 13:54:00 to 14:13:00 the PV2 (SolarMax)'s controller started acting erroneously by injecting only half its potential capacity even when asked by the real-time controller to inject at full-capacity. The time it took to restart the converters led to a temporary loss in dispatch tracking. From 17:48:00 to 18:00:00, the Renault Zoe's on-board controller stopped implementing setpoints which led to tracking issues during the period when the problem was spotted and the EV was unplugged then re-plugged.

Fig. 7.16 shows the evolution of the UEE for both the day-ahead and real-time stages for the duration of the experiment. For the day-ahead plot, the UEE is referred to the one at the starting time of the experiment. For the real-time plot, the UEE is computed directly using the realization measured at the microgrid PCC. The Figure shows that, even with the unforeseen failures listed in the previous paragraph, the real-time UEE remains within the bounds of the day-ahead stage. Furthermore, after further investigation, the previously mentioned resource and forecasting failures account for 25% of the UEE. Additionally, part of the remaining UEE was due to setpoint implementation errors. Indeed, the previously mentioned $\sim 1\text{kW}$ error offset between the nodal active power injections at the slack and the optimal DP is due to setpoint-implementation errors, where each resource implemented on average a power that was $\sim 250\text{W}$ different than the requested one. For instance, the Type-2 power-to-current lookup table of the Renault Zoe exhibits discrete steps of 500W leading to a discrepancy of around 200-300W between the requested active power setpoint and its implementation. Finally, the rest of the remaining UEE is due to two reasons. The first being that the real-time controller fails from time-to-time to converge to a solution that would satisfy both EV users and the DP tracking objective.

This is due to the fact that after a few⁷³ iterations the tracking objective weight is reduced w.r.t to the EV objective to favour EV user satisfaction and guarantee convergence within the control time-step. The second being that the BESS (B2)'s BMS was unexpectedly limiting the usage of the full battery capacity which led to discrepancies between the day-ahead foreseen BESS energy capacity and the effective one available in the real-time stage.

Tab. 7.19 shows the KPI metrics – used to evaluate the performance of the day-ahead stage in the numerical simulations of Sec. 7.3.4 – applied to both day-ahead and real-time stages. The most interesting aspect to note is that the real-time controller fully satisfies the requested EV user needs even though, as can be seen in Fig. 7.14, it rarely charged the EV at full-power.

In summary, the real-time controller was able to successfully track the day-ahead DP even with unforeseen resource hiccups. It is clear that: (i) without the resource hiccups, and (ii) by accounting for resources' setpoint-implementation-inaccuracies in the controller decision-making process, one could achieve a better tracking performance.

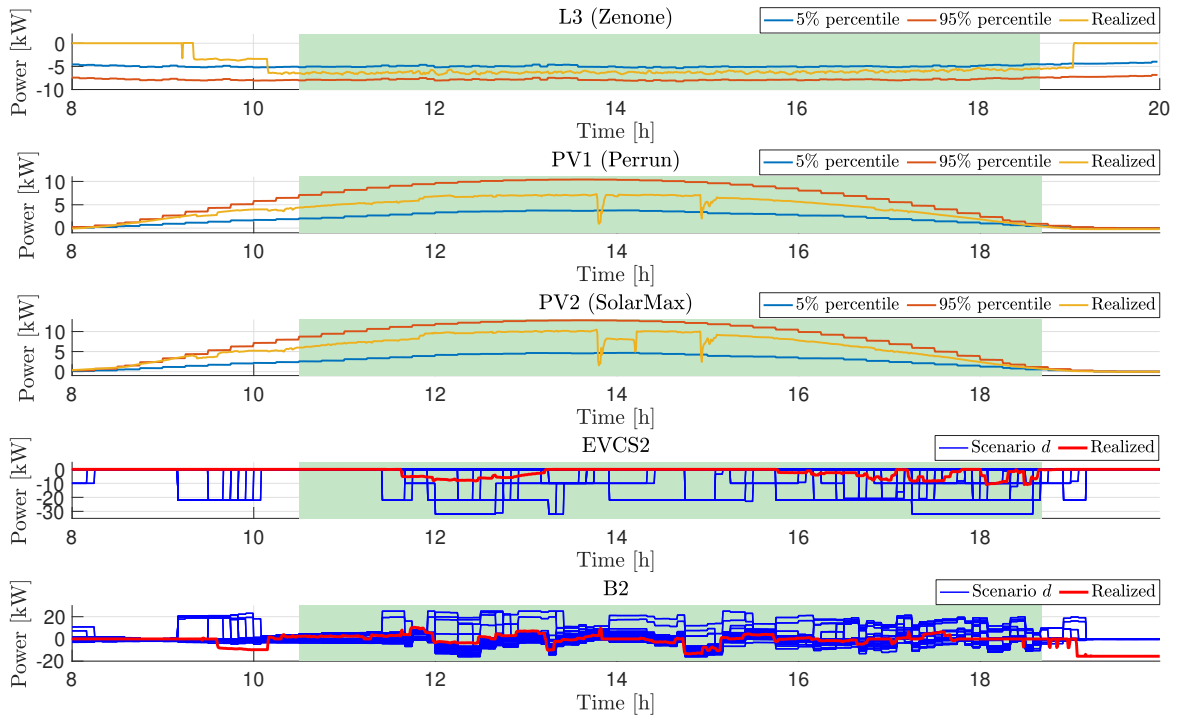


Figure 7.14: Experimental validation results - non-slack active power injections: forecast (day-ahead) vs. realization (real-time)

⁷³In this experiment we set that number to 15.

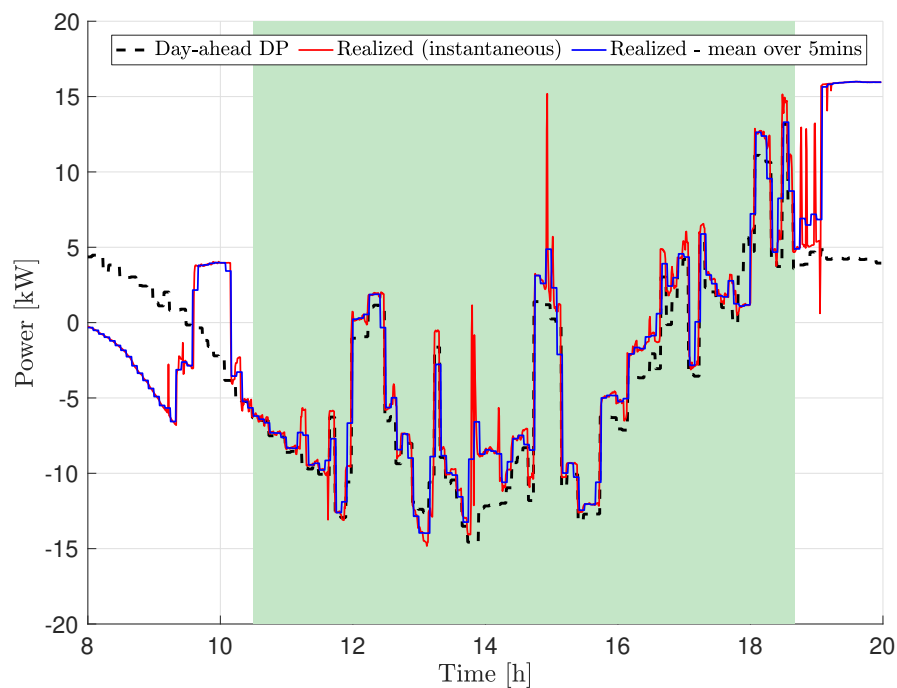


Figure 7.15: Experimental validation results - slack active power injections: DP (day-ahead) vs. realization (real-time)

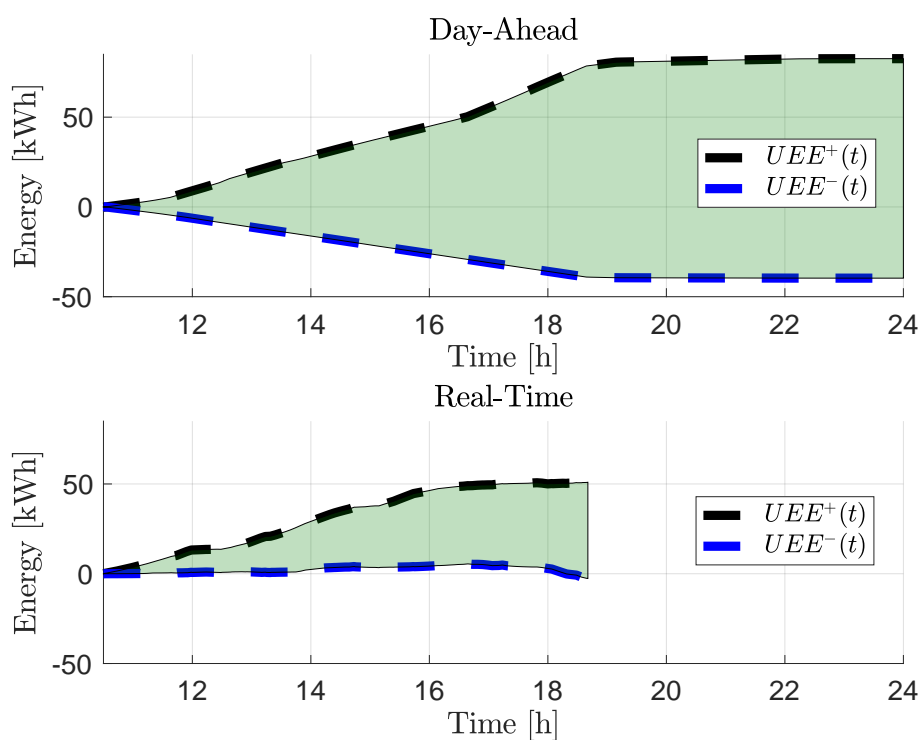


Figure 7.16: Experimental validation results - UEE over experiment horizon: day-ahead vs. real-time

Table 7.19: Experimental Validation Results: KPI metrics

	Day-Ahead Stage (with BESS and EVCS control)	Real-Time Stage
$UEE^+(t = t_{f,exp}) - UEE^+(t = t_{0,exp})$ [kWh]	78.83 ⁷⁴	50.89
$UEE^-(t = t_{f,exp}) - UEE^-(t = t_{0,exp})$ [kWh]	-39.14 ⁷⁴	-2.63
MAE [kW]	14.64	9.85
MPP [kW]	26.99	13.97
MEVUS [%]	100.00	94.55
MBU [%]	100.00	100.00
MABI [kW]	25.00	13.45

7.6 Conclusion

This chapter proposed an extension to the work presented in [6] by accounting for EVCSs' power and energy demand flexibilities in both day-ahead and real-time stages. More specifically, in the day before scheduling, the stochastic OP, computing an aggregated DP at the PCC, is extended to account for EVCSs as controllable entities. The OP in the day-ahead stage accounts for: (i) demand/generation forecasting errors using scenarios, (ii) resource constraints, (iii) grid operational constraints by leveraging SCs, and (iv) next-day EV user behaviour through forecasted scenarios. The advantages of considering EVCSs as controllable entities in the day-ahead stage were showcased through a set of numerical simulations. The simulations revealed that, in terms of UEE, it is always advantageous to control EV charging. In the real-time phase, the grid-aware MPC-based distributed control algorithm proposed in [6] was extended with an MPC-augmented-version of the EV-subproblem model presented in Sec. 6.2.2. The controller accounts for resource and grid operational constraints and aims to compute active and reactive power set-points for heterogeneous resources so that their aggregated contributions track the day-ahead optimally computed DP. Both day-ahead and real-time controllers were experimentally validated using the EPFL-DESL-microgrid. The results of the experiment showed that, even with hardware issues, the DP tracking was within the day-ahead UEE bounds and EV user needs were satisfied. Furthermore, if resources' setpoint-implementation inaccuracies are accounted for in the real-time controller, the DP tracking would have been even better. Future works will focus on the latter by means of experimental validations using the full ELL grid shown in Fig. 7.7.

⁷⁴The values are referenced to the UEE at the starting time of the experiment (i.e. $t_{0,exp}$).

Thesis Conclusions

This thesis numerically and experimentally validated real-time ADN control methodologies accounting for resources and grid operational constraints. The thesis is split in two parts. Part I focused on a general, i.e. resource-agnostic, methodology to linearize the power-flow equations and showcased its real-time control-enabling advantages through realistic sub-second control examples. Then, part II focused on the operational challenges raised by the large presence of EVCSs in ADNs. In the following, the main findings, limitations and future works associated to each chapter are listed.

Chapter 2 This chapter illustrated an analytical method to compute all-node type (i.e. PQ, PV and slack) nodal voltage SCs w.r.t. to *all* possible control variables in a power grid (i.e. nodal active and reactive power injections at PQ nodes, nodal voltage magnitudes and nodal active power injections at PV nodes and nodal voltage magnitudes and phase-angles at slack nodes). The proposed method relies on the knowledge of the grid model and state and the solution of a linear system of equations to determine nodal voltage SCs w.r.t a *user-defined* control variable. Furthermore, since the grid model is assumed to be known, the user can directly infer other (c.f. section 2.2.4) SCs. The chapter also included numerical benchmarks (performed on the IEEE-34 feeder), a complexity analysis and a MATLAB implementation of the proposed method. Results confirmed that the proposed method is accurate, scalable and easy to implement. Investigations on the needed accuracy for grid model were not discussed in the chapter, however, the interested reader is invited to read the work in [18] where the propagation of grid model uncertainties to the computation of SCs was investigated. As a final note, future works will involve investigating the properties of the matrix \mathbf{A} (see Sec. 2.11) in order to: (i) explore matrix factorization to potentially increase computational speeds, and, (ii) find the conditions (if any) that guarantee the uniqueness of the solutions of the linear systems of equations in step 4.ii of Alg. 1 (i.e. conditions that \mathbf{A} is full-rank).

Chapter 3 This chapter tackled the problem of actively resynchronizing (i.e. reconnecting) an islanded ADN to its upstream grid. More specifically, it proposed: (i) a centralised PCC-control in the form of an algorithm that approximately solves a three-phase-unbalanced linearized OPF aiming to steer an ADN's downstream PCC nodal voltages towards their upstream counterparts while guaranteeing ADN and resources' operational constraints, and (ii) a synchrocheck algorithm relying on e-IpDFT phasor extraction to determine whether two three-phase phasors are aligned or not. Both contributions were experimentally validated on the EPFL-DESL microgrid. The proposed synchrocheck was further benchmarked against the Schneider Electric Micom P143 grid-relay with synchronism check [43]. Unlike the proposed methods, the Micom P143 is designed to *only* detect synchronization between the islanded and external grid without any resources' control. Furthermore, it relies on the assumption that the PCC upstream nodal voltages are perfectly balanced. The experimental validation showed that within 1.5 s the resynchronization of PCC nodal-voltages was achieved by the proposed algorithm even if the process was launched when the islanded-microgrid was in an infeasible state. Furthermore, due

Thesis Conclusions

to its present configuration, the tested microgrid was operating in a balanced three-phase condition, lacking the possibility to showcase the ability of the proposed PCC-control algorithm to deal with unbalances. As a result, future works will involve experimental validations to showcase the ability to *securely* resynchronize an ADN to its upstream grid in case both systems operate in unbalanced conditions.

Chapter 4 In this chapter, methods accounting for the uncertainty of the implementation of setpoints at resource controllers have been proposed. First, a tractable *admissibility test* checking whether a control setpoint is admissible or not, was presented. Second, an iterative algorithm was presented with the following features: (i) it accounts for the grid and resource operational constraints, (ii) it leverages SCs to linearize the power-flow equations, and (iii) it is capable to determine the closest admissible control setpoint to its input. At each algorithm iteration, an admissibility test is performed to verify the validity of the OP's output and, ergo, the validity of the approximations used to linearize the constraints of the OP. The performed simulations show that the algorithms: (i) converge, (ii) satisfy the validity of the posed assumptions and, (iii) are compliant with real-time, i.e. sub-second, control. Note that, even though the performed simulations assumed balanced three-phase operation, the method is capable to control grids operating in generic unbalanced conditions as all grid operational constraints are dealt with in the same manner. Finally, as previously mentioned, no code optimization was performed at this point. Therefore, future works are planned to: (i) optimize the code implementation and, (ii) perform an experimental validation on the EPFL-DESL microgrid by integrating the developed algorithms into a real-time control framework (e.g. COMMELEC [54]).

Chapter 5 presented two sub-contributions that motivate the focus on EVs in the second part of the thesis.

The first sub-contribution leveraged LFMCSs to statically quantify the influence of uncontrolled EV charging on low-voltage ADNs' operational constraints. Numerical simulations were performed on two real low-voltage grids situated in the western part of Switzerland (denoted as Rolle-Gare and Rolle-Hoptial). The input data was synthesized using real information concerning the infrastructure of the grid (e.g. number of inhabitants, geographical location, etc.). Both sets of simulations revealed that EV loads put at risk the grid operational security. Indeed, simulations showcased that non-negligible *control* actions are needed if a full electrification of private transport is reached. In the first analysed LV grid (i.e. Rolle-Gare), minor branch ampacity issues and mostly under-voltages have been quantified. Therefore, one can conclude that minor grid reinforcement, coupled with suitable voltage regulation, are enough to handle the private mobility full electrification in that grid. On the other hand, the Rolle-Hospital network presented major branch ampacity violations, under-voltages and transformer overloads, thus, needed grid reinforcements might implicate major economical expenses. Therefore, in such cases, a smart charging algorithm can be used to satisfy EV user needs while steering the electrical grid to operate in a safe state (c.f. Sec.6). As a final note, it is clear that every grid will behave differently and simulations using the tool presented in this chapter can give insights on the strategy to be adopted in order to prepare the grid for the 100% electrification of private transport. In terms of future works, a large-scale, e.g. country-wide, simulation might be of interest using an approach inspired by [128].

The second sub-contribution is a set of two experiments performed using the EPFL-DESL-microgrid's EVCSS (c.f. Tab. 5.3 for technical specifications). Both sets of experiments revealed that (i) EVs have non-negligible local effects on ADNs' operational constraints, and (ii) EVs' on-board chargers cannot be controlled in sub-second time-scales. More specifically, even though an individual single-phase charging EV does not heavily violate the local power-quality grid operational constraints, as soon as a few EVs simultaneously charge at full-power on the same grid node, the EN-50160 [48] negative sequence constraint would not be satisfied. Generally speaking, it seems that each car manufacturer

designs its EV to safely charge in case it is the only grid-connected resource. However, since in practice multiple other resources and EVs are simultaneously grid-connected, their real impact on grid operational constraints is expected to be way higher. In terms of controllability, the experiments revealed that: (i) not all cars behave exactly the same way when it comes to setpoint tracking, and (ii) independently of the EV, on-board chargers have response-times in the order of seconds or tens of seconds. Therefore, again, it is clear that there is a need for different real-time (i.e. seconds-to-minutes scales) smart charging control frameworks if EVs will be used in time-deterministic real-time controls (e.g. frequency containment reserve or local grid voltage/line congestion controls). In terms of future works, it would be interesting to test a fleet of different EV models and categorise their controllability in terms of response times and setpoint implementation inaccuracies.

Chapter 6 This chapter proposed a grid-aware distributed controller (GADC) for EVCSs connected to ADNs of generic topologies. It uses the ADMM to distribute a separably formulated OPF problem into local ones. The latter are solved at the EV aggregators level while a central grid aggregator problem ensures the non-violation of the grid operational constraints while taking into account all the solutions coming from the EV aggregators. The grid aggregator problem takes into account the stochastic nature of various resources by means of scenarios, it relies on a linearization of the power-flow equations and is formulated for generic three phase ADNs. Therefore, it also takes into account voltage unbalances and guarantees proper power quality subject to the EN-50160 std. bounds [48]. Furthermore, as previously explained, as the control time-step is chosen to be in the seconds-to-minutes scale to match the results presented in Sec. 5.2.2, scenario-based optimization was crucial to render the optimally computed setpoints robust against the stochasticity of non-EV nodal power injections. The performance of the method was numerically quantified on the IEEE-34 feeder by comparing it with two grid-unaware controllers. It is shown that the grid-unaware controllers may provide a better service to EV users in terms of matching the desired battery SoC levels. However, this is at the expense of severely violating the grid's static and power quality constraints. From the grid perspective, the proposed GADC kept the ADN within safe operational bounds and, in most cases, was capable to satisfy the needs of EV users. It is clear that the developed method can help grid operators to manage *weak* grids that accommodate heavy EV loads. Future works may involve the integration of more realistic EV models into the problem formulation as this was not done in the presented algorithms. The latter models can, for instance, encapsulate the dependency of charging power limits on the EVs' SoC and/or the setpoint-implementation inaccuracies of EVs' on-board controllers. They can then be included in the EV sub-problem of Sec. 6.2.2 to compute optimal setpoints that are more realistic.

Chapter 7 This chapter proposed an extension to the work presented in [6] by accounting for EVCSs' power and energy demand flexibilities in both day-ahead and real-time stages. More specifically, in the day before scheduling, the stochastic OP, computing an aggregated DP at the PCC, is extended to account for EVCSs as controllable entities. The OP in the day-ahead stage accounts for: (i) demand/-generation forecasting errors using scenarios, (ii) resource constraints, (iii) grid operational constraints by leveraging SCs, and (iv) next-day EV user behaviour through forecasted scenarios. The advantages of considering EVCSs as controllable entities in the day-ahead stage were showcased through a set of numerical simulations. The simulations revealed that, in terms of UEE, it is always advantageous to control EV charging. In the real-time phase, the grid-aware MPC-based distributed control algorithm proposed in [6] was extended with an MPC-augmented-version of the EV-subproblem model presented in Sec. 6.2.2. The controller accounts for resource and grid operational constraints and aims to compute active and reactive power set-points for heterogeneous resources so that their aggregated contributions track the day-ahead optimally computed DP. Both day-ahead and real-time controllers were experimentally validated using the EPFL-DESL-microgrid. The results of the experiment showed

Thesis Conclusions

that, even with hardware issues, the DP tracking was within the day-ahead UEE bounds and EV user needs were satisfied. Furthermore, if resources' setpoint-implementation inaccuracies are accounted for in the real-time controller, the DP tracking would have been even better. Future works will focus on the latter by means of experimental validations using the full ELL grid shown in Fig. 7.7.

Appendix

A - Affine-Transformable-Functions

Affine transformable functions (ATFs) are non-affine mathematical functions that can be expressed as affine functions if they are included in an OP. In other words, if within an OP there are many ATFs, they can all be transformed into linear constraints and objectives in order to preserve the OP's linearity. In the following we give two examples.

A.1 - $\min\{a, b\}$

Starting from $m_1 = \min\{a, b\}$ one can write an equivalent OP (7.23).

$$\begin{aligned} m_1 &= \underset{t}{\operatorname{argmax}}\{t\} = \underset{t}{\operatorname{argmin}}\{-t\} \\ \text{s.t.} \\ t &\leq a \\ t &\leq b \end{aligned} \tag{7.23}$$

It is clear that (7.23) is a linear OP.

A.2 - $\max\{a, b\}$

Starting from $m_2 = \max\{a, b\}$ one can write an equivalent OP (7.24).

$$\begin{aligned} m_2 &= \underset{t}{\operatorname{argmin}}\{t\} = \underset{t}{\operatorname{argmax}}\{-t\} \\ \text{s.t.} \\ t &\geq a \\ t &\geq b \end{aligned} \tag{7.24}$$

It is clear that (7.24) is a linear OP.

Bibliography

- [1] Bo Liu and Yufei Wang. Energy system optimization under uncertainties: A comprehensive review. *Towards Sustainable Chemical Processes*, pages 149–170, 2020.
- [2] Line Roald, David Pozo, Anthony Papavasiliou, Daniel Molzahn, Jalal Kazempour, and Antonio Conejo. Power systems optimization under uncertainty: A review of methods and applications. *Electric Power Systems Research*, 211, 2022.
- [3] Rachna Dhir, Rachana Garg, and Priya Mahajan. A review of microgrid control strategies. In *2022 IEEE Delhi Section Conference (DELCON)*, pages 1–5. IEEE, 2022.
- [4] Linus A Alwal, Peter K Kihato, and Stanley I Kamau. A review of control strategies for microgrid with pv-wind hybrid generation systems. In *Proceedings of the Sustainable Research and Innovation Conference*, pages 243–250, 2022.
- [5] Subhashree Choudhury. Review of energy storage system technologies integration to microgrid: Types, control strategies, issues, and future prospects. *Journal of Energy Storage*, 48:103966, 2022.
- [6] Rahul Gupta, Fabrizio Sossan, and Mario Paolone. Grid-aware distributed model predictive control of heterogeneous resources in a distribution network: Theory and experimental validation. *IEEE Transactions on Energy Conversion*, 36(2):1392–1402, 2020.
- [7] Sherif Fahmy and Mario Paolone. Analytical computation of power grids' sensitivity coefficients with voltage-dependent injections. In *2021 IEEE Madrid PowerTech*, pages 1–6. IEEE, 2021. © 2021 IEEE. Reprinted, with permission, from myself.
- [8] Sherif Fahmy, Quentin Walger, and Mario Paolone. Resynchronization of islanded unbalanced adns: Control, synchrocheck and experimental validation. *Electric Power Systems Research*, 190:106697, 2022.
- [9] William H Kersting. Radial distribution test feeders. In *Power Engineering Society Winter Meeting, 2001. IEEE*, volume 2, pages 908–912. IEEE, 2001.
- [10] John Peschon, Dean S Piercy, William F Tinney, and Odd J Tveit. Sensitivity in power systems. *IEEE Transactions on Power Apparatus and Systems*, PAS-87(8):1687–1696, 1968.
- [11] Qiong Zhou and J Bialek. Simplified calculation of voltage and loss sensitivity factors in distribution networks. In *Proc. 16th Power Syst. Comput. Conf.(PSCC2008)*, 2008.
- [12] Konstantina Christakou, Jean-Yves Le Boudec, Mario Paolone, and Dan-Cristian Tomozei. Efficient computation of sensitivity coefficients of node voltages and line currents in unbalanced radial electrical distribution networks. *IEEE Transactions on Smart Grid*, 4(2):741–750, 2013.

Bibliography

- [13] Thiago RF Mendonca, Mark E Collins, Milena F Pinto, and Timothy C Green. Decentralisation of power flow solution for facilitating active network management. *CIREN-Open Access Proceedings Journal*, 2017(1):1669–1672, 2017.
- [14] Carl Mugnier, Konstantina Christakou, Joel Jatón, M De Vivo, M Carpita, and Mario Paolone. Model-less/measurement-based computation of voltage sensitivities in unbalanced electrical distribution networks. In *2016 Power Systems Computation Conference (PSCC)*, pages 1–7. IEEE, 2016.
- [15] Gustavo Valverde, Thierry Zufferey, Stavros Karagiannopoulos, and Gabriela Hug. Estimation of voltage sensitivities to power injections using smart meter data. In *2018 IEEE International Energy Conference (ENERGYCON)*, pages 1–6. IEEE, 2018.
- [16] Hanchen Xu, Alejandro D Domínguez-García, and Peter W Sauer. A data-driven voltage control framework for power distribution systems. In *2018 IEEE Power & Energy Society General Meeting (PESGM)*, pages 1–5. IEEE, 2018.
- [17] Rahul Gupta, Fabrizio Sossan, and Mario Paolone. Model-less robust voltage control in active distribution networks using sensitivity coefficients estimated from measurements. *arXiv preprint arXiv:2201.04192*, 2022.
- [18] Rahul Kumar Gupta. Methods for grid-aware operation and planning of active distribution networks. Technical report, EPFL, 2022.
- [19] Jos Arrillaga and Neville R Watson. *Power system harmonics*. John Wiley & Sons, 2004.
- [20] Andreas Martin Kettner and Mario Paolone. On the properties of the power systems nodal admittance matrix. *IEEE Transactions on Power Systems*, 33(1):1130–1131, 2017.
- [21] WW Price, HD Chiang, HK Clark, C Concordia, DC Lee, JC Hsu, S Ihara, CA King, CJ Lin, Y Mansour, et al. Load representation for dynamic performance analysis. *IEEE Transactions on Power Systems (Institute of Electrical and Electronics Engineers);(United States)*, 8(2), 1993.
- [22] Saran Satsangi and Ganesh Balu Kumbhar. Effect of load models on energy loss reduction using volt-var optimization. In *2016 National Power Systems Conference (NPSC)*, pages 1–6. IEEE, 2016.
- [23] Seyed Ali Arefifar and Wilsun Xu. Online tracking of voltage-dependent load parameters using ultc created disturbances. *IEEE Transactions on Power Systems*, 28(1):130–139, 2012.
- [24] Mehdi Kabiri and Nima Amjadi. A hybrid estimation and identification method for online calculation of voltage-dependent load parameters. *IEEE Systems Journal*, 13(1):792–801, 2018.
- [25] Álvaro Ortega and Federico Milano. Estimation of voltage dependent load models through power and frequency measurements. *IEEE Transactions on Power Systems*, 35(4):3308–3311, 2020.
- [26] Nasser Tleis. *Power systems modelling and fault analysis: theory and practice*. Elsevier, 2007.
- [27] Cong Wang, Andrey Bernstein, Jean-Yves Le Boudec, and Mario Paolone. Existence and uniqueness of load-flow solutions in three-phase distribution networks. *IEEE Transactions on Power Systems*, 32(ARTICLE):3319–3320, 2017.
- [28] Peng Wang, Shaoshuai Mou, Jianming Lian, and Wei Ren. Solving a system of linear equations: From centralized to distributed algorithms. *Annual Reviews in Control*, 47:306–322, 2019.
- [29] IEEE Standards Coordinating Committee 21. Ieee guide for design, operation, and integration of distributed resource island systems with electric power systems. *IEEE Std 1547.4-2011*, pages 1–54, 2011.

- [30] IEEE Standards Coordinating Committee 21. Ieee standard for interconnecting distributed resources with electric power systems. *IEEE Std 1547-2003*, pages 1–28, 2003.
- [31] IEEE Power System Relaying Committee et al. Ieee guide for automatic reclosing of line circuit breakers for ac distribution and transmission lines. *IEEE Power Engineering Society, USA*, 2003.
- [32] Di Shi, Yusheng Luo, and Ratnesh K Sharma. Active synchronization control for microgrid reconnection after islanding. In *IEEE PES innovative smart grid technologies, Europe*, pages 1–6. IEEE, 2014.
- [33] Thakul Uten, Chalie Charoenlarnopparut, and Prapun Suksompong. Synchronization control for microgrid seamless reconnection. In *2019 14th International Joint Symposium on Artificial Intelligence and Natural Language Processing (iSAI-NLP)*, pages 1–6. IEEE, 2019.
- [34] Muhammed Y Worku, Mohamed A Hassan, and Mohamed A Abido. Power management, voltage control and grid synchronization of microgrids in real time. *Arabian Journal for Science and Engineering*, 46(2):1411–1429, 2021.
- [35] Changhee Cho, Jin-Hong Jeon, Jong-Yul Kim, Soonman Kwon, Kyongyop Park, and Sungshin Kim. Active synchronizing control of a microgrid. *IEEE Transactions on Power Electronics*, 26(12):3707–3719, 2011.
- [36] Fen Tang, Josep M Guerrero, Juan C Vasquez, Dan Wu, and Lexuan Meng. Distributed active synchronization strategy for microgrid seamless reconnection to the grid under unbalance and harmonic distortion. *IEEE Transactions on Smart Grid*, 6(6):2757–2769, 2015.
- [37] Di Shi, Xi Chen, Zhiwei Wang, Xiaohu Zhang, Zhe Yu, Xinan Wang, and Desong Bian. A distributed cooperative control framework for synchronized reconnection of a multi-bus microgrid. *IEEE Transactions on Smart Grid*, 9(6):6646–6655, 2017.
- [38] Tao Xu, Jiabin Zhou, Han Yang, Peng Li, Li Yu, and Xiaobin Guo. Consensus based distributed angle droop control for islands resynchronization. In *2020 IEEE Power & Energy Society General Meeting (PESGM)*, pages 1–5. IEEE, 2020.
- [39] Ali Peiravi. Design and prototyping of a microcontroller based synchrocheck relay for improved reliability. *Journal of American Science*, 5, 2009.
- [40] Carter Lassetter, Eduardo Cotilla-Sanchez, and Jinsub Kim. A learning scheme for microgrid reconnection. *IEEE Transactions on Power Systems*, 33(1):691–700, 2017.
- [41] Ragab Abd Allah. Correlation-based synchro-check relay for power systems. *IET Generation, Transmission & Distribution*, 12(5):1109–1120, 2018.
- [42] P NASPI. Pmu data quality: A framework for the attributes of pmu data quality and quality impacts to synchrophasor applications. Technical report, North American Synchrophasor Initiative, 2017.
- [43] Schneider Electric. Easergy micom p14x. shorturl.at/csYZ9. Accessed last: 2021-09-29.
- [44] IEEE Distribution Resources Integration Working Group. Ieee standard for the specification of microgrid controllers. *IEEE Std 2030.7-2017*, pages 1–43, 2018.
- [45] Mario Paolone, Trevor Gaunt, Xavier Guillaud, Marco Liserre, Sakis Meliopoulos, Antonello Monti, Thierry Van Cutsem, Vijay Vittal, and Costas Vournas. Fundamentals of power systems modelling in the presence of converter-interfaced generation. *Electric Power Systems Research*, 189:106811, 2020.

Bibliography

- [46] H. Jiayi, J. Chuanwen, and X. Rong. A review on distributed energy resources and microgrid. *Renewable and Sustainable Energy Reviews*, 12:2472–2483, 2008.
- [47] Á. Ortega and F. Milano. Estimation of voltage dependent load models through power and frequency measurements. *IEEE Transactions on Power Systems*, pages 1–1, 2020.
- [48] EN Standard. 50160. *Voltage characteristics of public distribution systems*, 18, 2010.
- [49] S. Boyd and L. Vandenberghe. *Convex optimization*. Cambridge university press, 2004.
- [50] S. Agmon. The relaxation method for linear inequalities. *Canadian Journal of Mathematics*, 6:382–392, 1954.
- [51] Paolo Romano and Mario Paolone. Enhanced interpolated-dft for synchrophasor estimation in fpgas: Theory, implementation, and validation of a pmu prototype. *IEEE Transactions on instrumentation and measurement*, 63(12):2824–2836, 2014.
- [52] Paolo Romano. Dft-based synchrophasor estimation algorithms and their integration in advanced phasor measurement units for the real-time monitoring of active distribution networks. Technical report, EPFL, 2016.
- [53] Kenneth E Martin, G Benmouyal, MG Adamiak, M Begovic, RO Burnett, KR Carr, A Cobb, JA Kusters, SH Horowitz, GR Jensen, et al. Ieee standard for synchrophasors for power systems. *IEEE Transactions on Power Delivery*, 13(1):73–77, 1998.
- [54] Lorenzo Reyes-Chamorro, Andrey Bernstein, Niek J Bouman, Enrica Scolari, Andreas M Kettner, Benoit Cathiard, Jean-Yves Le Boudec, and Mario Paolone. Experimental validation of an explicit power-flow primary control in microgrids. *IEEE Transactions on Industrial Informatics*, 14(11):4779–4791, 2018.
- [55] Lorenzo Enrique Reyes Chamorro. Real-time control framework for active distribution networks theoretical definition and experimental validation. Technical report, EPFL, 2016.
- [56] Stavros Papathanassiou, Nikos Hatziargyriou, Kai Strunz, et al. A benchmark low voltage micro-grid network. In *Proceedings of the CIGRE symposium: power systems with dispersed generation*, pages 1–8. CIGRE, 2005.
- [57] Schneider Electric. Nsx250f micrologic 2.2 250a 4p4d. shorturl.at/hzCKS. Accessed last: 2021-09-29.
- [58] E. Scolari, L. Reyes-Chamorro, F. Sossan, and M. Paolone. A comprehensive assessment of the short-term uncertainty of grid-connected pv systems. *IEEE Transactions on Sustainable Energy*, 9(3):1458–1467, July 2018.
- [59] S Surender Reddy, Vuddanti Sandeep, and Chan-Mook Jung. Review of stochastic optimization methods for smart grid. *Frontiers in Energy*, 11(2):197–209, 2017.
- [60] Adriano Arrigo, Christos Ordoudis, Jalal Kazempour, Zacharie De Grève, Jean-François Toubéau, and François Vallée. Optimal power flow under uncertainty: An extensive out-of-sample analysis. In *2019 IEEE PES Innovative Smart Grid Technologies Europe (ISGT-Europe)*, pages 1–5. IEEE, 2019.
- [61] Fabrizio Sossan, Emil Namor, Rachid Cherkaoui, and Mario Paolone. Achieving the dispatchability of distribution feeders through prosumers data driven forecasting and model predictive control of electrochemical storage. *IEEE Transactions on Sustainable Energy*, 7(4):1762–1777, 2016.

- [62] Zhao Yuan, Antonio Zecchino, Rachid Cherkaoui, and Mario Paolone. Real-time control of battery energy storage systems to provide ancillary services considering voltage-dependent capability of dc-ac converters. *IEEE Transactions on Smart Grid*, 12(5):4164–4175, 2021.
- [63] Luca Fabietti, Tomasz T Gorecki, Emil Namor, Fabrizio Sossan, Mario Paolone, and Colin N Jones. Enhancing the dispatchability of distribution networks through utility-scale batteries and flexible demand. *Energy and Buildings*, 172:125–138, 2018.
- [64] Lorenzo Reyes-Chamorro, Mario Paolone, Andrey Bernstein, and Jean-Yves Le Boudec. A super-capacitor agent for providing real-time power services to the grid. In *2015 IEEE PES Innovative Smart Grid Technologies Latin America (ISGT LATAM)*, pages 332–337. IEEE, 2015.
- [65] G Juberias, R Yunta, J Garcia Moreno, and C Mendivil. A new arima model for hourly load forecasting. In *1999 IEEE Transmission and Distribution Conference (Cat. No. 99CH36333)*, volume 1, pages 314–319. IEEE, 1999.
- [66] Bowen Li, Maria Vrakopoulou, and Johanna L Mathieu. Chance constrained reserve scheduling using uncertain controllable loads part ii: Analytical reformulation. *IEEE Transactions on Smart Grid*, 10(2):1618–1625, 2017.
- [67] Line Roald and Göran Andersson. Chance-constrained ac optimal power flow: Reformulations and efficient algorithms. *IEEE Transactions on Power Systems*, 33(3):2906–2918, 2017.
- [68] Andreas Venzke, Lejla Halilbasic, Uros Markovic, Gabriela Hug, and Spyros Chatzivasileiadis. Convex relaxations of chance constrained ac optimal power flow. *IEEE Transactions on Power Systems*, 33(3):2829–2841, 2017.
- [69] Tillmann Mühlpfordt, Timm Faulwasser, Veit Hagenmeyer, Line Roald, and Sidhant Misra. On polynomial real-time control policies in stochastic ac optimal power flow. *Electric Power Systems Research*, 189:106792, 2020.
- [70] Jeremias Schmidli, Line Roald, Spyros Chatzivasileiadis, and Göran Andersson. Stochastic ac optimal power flow with approximate chance-constraints. In *2016 IEEE Power and Energy Society General Meeting (PESGM)*, pages 1–5. IEEE, 2016.
- [71] Emiliano Dall’Anese, Kyri Baker, and Tyler Summers. Chance-constrained ac optimal power flow for distribution systems with renewables. *IEEE Transactions on Power Systems*, 32(5):3427–3438, 2017.
- [72] Eleni Stai, Lorenzo Reyes-Chamorro, Fabrizio Sossan, Jean-Yves Le Boudec, and Mario Paolone. Dispatching stochastic heterogeneous resources accounting for grid and battery losses. *IEEE Transactions on Smart Grid*, 9(6):6522–6539, 2017.
- [73] Haiteng Han, Shan Gao, Qingxin Shi, Hantao Cui, and Fangxing Li. Security-based active demand response strategy considering uncertainties in power systems. *IEEE Access*, 5:16953–16962, 2017.
- [74] Philipp Fortenbacher, Martin Zellner, and Göran Andersson. Optimal sizing and placement of distributed storage in low voltage networks. In *2016 Power Systems Computation Conference (PSCC)*, pages 1–7. IEEE, 2016.
- [75] Vivek Mohan, Reshma Suresh, Jai Govind Singh, Weerakorn Ongsakul, and Nimal Madhu. Microgrid energy management combining sensitivities, interval and probabilistic uncertainties of renewable generation and loads. *IEEE Journal on Emerging and Selected Topics in Circuits and Systems*, 7(2):262–270, 2017.

Bibliography

- [76] Ji Hyun Yi, Rachid Cherkaoui, and Mario Paolone. Optimal allocation of esss in active distribution networks to achieve their dispatchability. *IEEE Transactions on Power Systems*, 36(3):2068–2081, 2020.
- [77] Maria Vrakopoulou, Bowen Li, and Johanna L Mathieu. Chance constrained reserve scheduling using uncertain controllable loads part i: Formulation and scenario-based analysis. *IEEE Transactions on Smart Grid*, 10(2):1608–1617, 2017.
- [78] Andréa A Sousa, Geraldo L Torres, and Claudio A Canizares. Robust optimal power flow solution using trust region and interior-point methods. *IEEE Transactions on Power Systems*, 26(2):487–499, 2010.
- [79] Raphael Louca and Eilyan Bitar. Robust ac optimal power flow. *IEEE Transactions on Power Systems*, 34(3):1669–1681, 2018.
- [80] Daniel Molzahn and Line A Roald. Grid-aware versus grid-agnostic distribution system control: A method for certifying engineering constraint satisfaction. In *Proc. 2019 Hawaii International Conference on System Sciences*, 2019.
- [81] Daniel K Molzahn and Line A Roald. Towards an ac optimal power flow algorithm with robust feasibility guarantees. In *2018 Power Systems Computation Conference (PSCC)*, pages 1–7. IEEE, 2018.
- [82] Cong Wang, Jean-Yves Le Boudec, and Mario Paolone. Controlling the electrical state via uncertain power injections in three-phase distribution networks. *IEEE Transactions on Smart Grid*, 10(2):1349–1362, 2017.
- [83] J. L. Mathieu, S. Koch, and D. S. Callaway. State estimation and control of electric loads to manage real-time energy imbalance. *IEEE Transactions on Power Systems*, 28(1):430–440, Feb 2013.
- [84] Erlend Arge, Are Magnus Bruaset, Phillip B Calvin, Joseph F Kanney, Hans Petter Langtangen, and Cass T Miller. On the numerical efficiency of c++ in scientific computing. In *Numerical Methods and Software Tools in Industrial Mathematics*, pages 91–118. Springer, 1997.
- [85] Action Plan et al. Communication from the commission to the european parliament, the council, the european economic and social committee and the committee of the regions. *European Commission*, 2011.
- [86] European Commission. A european strategy for low-emission mobility, 2016.
- [87] Roadmap Elektromobilität 2022. Roadmap elektromobilität 2022: Was bisher geschah, 2022.
- [88] Unknown. Switzerland sets ambitious new electric vehicle targets for 2025. *SwissInfo*, 2022.
- [89] Douglas A Reynolds. Gaussian mixture models. *Encyclopedia of biometrics*, 741, 2009.
- [90] Marco Liu. Optimal number of trials for monte carlo simulation. *VRC–Valuation Research Report*, 2017.
- [91] Giacomo Pareschi, Lukas Küng, Gil Georges, and Konstantinos Boulouchos. Are travel surveys a good basis for ev models? validation of simulated charging profiles against empirical data. *Applied Energy*, 275:115318, 2020.
- [92] Office of Energy Efficiency and Renewable Energy (EERE). Commercial and residential hourly load profiles for all tmy3 locations in the united states. <https://cutt.ly/Nh43kKM>. Accessed: 2020-12-28.

-
- [93] RWTH Aachen University. Smart energy data: Terni power demand/ supply profiles. <https://cutt.ly/Lh43cSo>. Accessed: 2020-12-28.
 - [94] CoSSMic Adrian Minde. Detailed household load and solar generation in minutely to hourly resolution. <https://cutt.ly/Th43ms2>. Accessed: 2020-12-28.
 - [95] Martin Rüdisüli, Christian Bach, Christian Bauer, Didier Beloin-Saint-Pierre, Urs Elber, Sherif Fahmy, Gil Georges, Robert Limpach, Giacomo Pareschi, Ramachandran Kannan, and Sinan Teske. Electricity based mobility. <https://www.empa.ch/web/s313/electricity-based-mobility>. Accessed: 2022-08-01. Restricted access contact details available on website.
 - [96] National Instruments. crio-9068. <https://www.ni.com/fr-ch/support/model.crio-9068.html>. Accessed last: 2022-08-15.
 - [97] International Electrotechnical Commission et al. Iec 61851-1: 2017-02 “electric vehicle conductive charging system—part 1: General requirements”. *International Electrotechnical Commission: Geneva, Switzerland*, 2017.
 - [98] EvTec. move&charge 1in1, 2in1, 3in1, multiplug. <https://www.evtec.ch/produkte/movecharge>. Accessed last: 2022-08-15.
 - [99] Schneider Electric. Disjoncteur, acti9 ic60h, 4p, 32 a, courbe c, 10000 a (iec 60898-1), 15 ka (iec 60947-2). <https://www.se.com/ch/fr/product/A9F84432/disjoncteur-acti9-ic60h-4p-32-a-courbe-c-10000-a-iec-608981-15-ka-iec-609472/>. Accessed last: 2022-08-15.
 - [100] Schneider Electric. Acti9 iid - interrupteur différentiel - 4p - 40a - 30ma - type b - si - 400v. <https://www.se.com/fr/fr/product/A9Z61440/acti9-iid-interrupteur-diff%C3%A9rentiel-4p-40a-30ma-type-b-si-400v/>. Accessed last: 2022-08-15.
 - [101] Katarina Knezović, Sergejus Martinenas, Peter Bach Andersen, Antonio Zecchino, and Mattia Marinelli. Enhancing the role of electric vehicles in the power grid: Field validation of multiple ancillary services. *IEEE Transactions on Transportation Electrification*, 3(1):201–209, 2016.
 - [102] Roman Rudnik, Jean-Yves Le Boudec, Sherif Fahmy, and Mario Paolone. Experimental validation of the real-time control of an electric-vehicle charging station. In *2021 IEEE Madrid PowerTech*, pages 1–6. IEEE, 2021.
 - [103] Sherif Fahmy, Rahul Gupta, and Mario Paolone. Grid-aware distributed control of electric vehicle charging stations in active distribution grids. *Electric Power Systems Research*, 189:106697, 2020.
 - [104] GA Putrus, Pasist Suwanapingkarl, David Johnston, EC Bentley, and Mahinsasa Narayana. Impact of electric vehicles on power distribution networks. In *2009 IEEE Vehicle Power and Propulsion Conference*, pages 827–831. IEEE, 2009.
 - [105] Yifeng He, Bala Venkatesh, and Ling Guan. Optimal scheduling for charging and discharging of electric vehicles. *IEEE transactions on smart grid*, 3(3):1095–1105, 2012.
 - [106] Sara Deilami, Amir S Masoum, Paul S Moses, and Mohammad AS Masoum. Real-time coordination of plug-in electric vehicle charging in smart grids to minimize power losses and improve voltage profile. *IEEE Transactions on Smart Grid*, 2(3):456–467, 2011.
 - [107] Peter Richardson, Damian Flynn, and Andrew Keane. Optimal charging of electric vehicles in low-voltage distribution systems. *IEEE Transactions on Power Systems*, 27(1):268–279, 2011.

Bibliography

- [108] Mingxi Liu, Phillippe K Phanivong, Yang Shi, and Duncan S Callaway. Decentralized charging control of electric vehicles in residential distribution networks. *IEEE Transactions on Control Systems Technology*, 27(1):266–281, 2017.
- [109] Liang Zhang, Vassilis Kekatos, and Georgios B Giannakis. Scalable electric vehicle charging protocols. *IEEE Transactions on Power Systems*, 32(2):1451–1462, 2016.
- [110] Thomas Allen Short. *Electric power distribution handbook*. CRC press, 2014.
- [111] Rahul Gupta, Fabrizio Sossan, and Mario Paolone. Performance assessment of linearized opf-based distributed real-time predictive control. In *2019 IEEE Milan PowerTech*, pages 1–6. IEEE, 2019.
- [112] SS-EN ISO 15118-1: 2019. Road vehicles—vehicle to grid communication interface—part 1: General information and use-case definition (iso 15118-1: 2019), 2019.
- [113] T Hofman and CH Dai. Energy efficiency analysis and comparison of transmission technologies for an electric vehicle. In *2010 IEEE vehicle power and propulsion conference*, pages 1–6. IEEE, 2010.
- [114] Numa Gueissaz, Konstantina Christakou, Jean-Yves Le Boudec, and Mario Paolone. Fair control of distributed pv plants in low voltage grids. In *2017 IEEE PES Innovative Smart Grid Technologies Conference Europe (ISGT-Europe)*, pages 1–6. IEEE, 2017.
- [115] Leehter Yao, Wei Hong Lim, and Teng Shih Tsai. A real-time charging scheme for demand response in electric vehicle parking station. *IEEE Transactions on Smart Grid*, 8(1):52–62, 2016.
- [116] Rahul Gupta, Fabrizio Sossan, Enrica Scolari, Emil Namor, Luca Fabietti, Colin Jones, and Mario Paolone. An admm-based coordination and control strategy for pv and storage to dispatch stochastic prosumers: Theory and experimental validation. In *2018 Power Systems Computation Conference (PSCC)*, pages 1–7. IEEE, 2018.
- [117] Stephen Boyd, Neal Parikh, Eric Chu, Borja Peleato, Jonathan Eckstein, et al. Distributed optimization and statistical learning via the alternating direction method of multipliers. *Foundations and Trends® in Machine learning*, 3(1):1–122, 2011.
- [118] Saskia Lavrijssen, Anna-Alexandra Marhold, and Ana Trias. The changing world of the dso in a smart energy system environment: Key issues and policy recommendations. *CERRE*, 2016.
- [119] Payam Refaeilzadeh, Lei Tang, and Huan Liu. Cross-validation. *Encyclopedia of database systems*, 5:532–538, 2009.
- [120] Philip Sedgwick. Pearson's correlation coefficient. *Bmj*, 345, 2012.
- [121] Vance W Berger and YanYan Zhou. Kolmogorov–smirnov test: Overview. *Wiley statsref: Statistics reference online*, 2014.
- [122] Aristidis Likas, Nikos Vlassis, and Jakob J Verbeek. The global k-means clustering algorithm. *Pattern recognition*, 36(2):451–461, 2003.
- [123] David Arthur and Sergei Vassilvitskii. k-means++: The advantages of careful seeding. Technical report, Stanford, 2006.
- [124] EvTec. espresso&charge - 6in1. https://www.evtec.ch/download_file/view/356. Accessed last: 2022-09-01.

- [125] Emil Namor, Fabrizio Sossan, Enrica Scolari, Rachid Cherkaoui, and Mario Paolone. Experimental assessment of the prediction performance of dynamic equivalent circuit models of grid-connected battery energy storage systems. In *2018 IEEE PES innovative smart grid technologies conference Europe (ISGT-Europe)*, pages 1–6. IEEE, 2018.
- [126] GoFast. Le plus grand réseau de recharge rapide en suisse. <https://www.gofast.swiss/fr>. Accessed last: 2022-09-01.
- [127] Rahul Gupta, Sherif Fahmy, and Mario Paolone. Coordinated day-ahead dispatch of multiple power distribution grids hosting stochastic resources: An admm-based framework. *Electric Power Systems Research*, 212:108555, 2022.
- [128] Rahul Gupta, Fabrizio Sossan, and Mario Paolone. Countrywide pv hosting capacity and energy storage requirements for distribution networks: The case of switzerland. *Applied Energy*, 281:116010, 2021.

Curriculum Vitae



Sherif Fahmy
01.01.1994 – Egyptian
B-Permit

Rue de la Blancherie 17
1022, Suisse

+41 78 631 71 32
sherif.alaa.fahmy@gmail.com

in

Young PhD student (master's graduate) described by others as *honest, ambitious, smart and hardworking*.

I enjoy working in teams. I am interested in pursuing my career in any *engineering* inspired job. However, I also admire basic human sciences (e.g. *economics, finance, psychology* etc.), which constantly helps push forward my *problem solving* and *communication* skills.

Programming

MATLAB, C/C++, Java,
LabView, Simulink, SQL* &
Python*

Applications

MS Office, PLECS & EMTF

Languages

Arabic – C2
English – C2
French – C2
German – A1 => A2*

Interests

Leadership

Prospective project manager

Entrepreneurship

Prospective MBA and/or
start-up creation

Sports

I practice many. I believe that:
A healthy mind can only exist
in a healthy body.

*Meeting new people,
Travelling & Exploring new
cultures*

* in progress

Education

PhD in Electrical Engineering ♦ [EPFL](#)

Researching the real-time control of unbalanced & uncertain electrical power grids that include *electric vehicle charging stations, energy storage*, etc. [Publications](#)

Master's of Sc. in Electrical Engineering ♦ [EPFL](#)

Majored in *smart grids science & technology* with a specialization in *advanced control and communication for power grids*.

Bachelor of Sc. in Electrical Engineering ♦ [EPFL](#)

Specialized in *power & energy, electronics and information technology*.

Achievements 1. *EPFL Excellence Fellowship*,

2. *Texas Instruments Student Prize 2015 - 3rd place*.

IB Diploma ♦ [École Oasis Internationale](#)

Projects 1. *Miniature solar-boat: theory and proof of concept*,

2. *Extended Essay: The role of subsidies in Egypt's economy from 2007 to 2011*.

Work Experience

Technical Advisor ▀ [Ergodic](#)

Ergodic is a startup aiming to use data analytics in the domain of power grids.

I accompanied them, as a technical advisor, in an InnoSuisse funding quest.

Master Thesis Intern ▀ [ABB Corporate Research Center](#)

I explored the topic of incorporating software defined networking (SDN) in substation automation networks (SAN).

I researched the topic and coded a proof of concept to show-off my findings.

Summer Intern ▀ [Technis](#)

Technis offers smart flooring solutions.

I joined as a summer intern and helped develop their 1st prototype. As they were still a very young company, I was also involved in the business and administration-side of the company.

Extracurricular Activities

Various ▀ [The Consulting Society \(EPFL\)](#)

The consulting society (TCS) is an EPFL student association aiming to bridge students and the world of consulting.

1. **Sponsoring**, I was in charge of procuring financial support for the association.
2. **External Relations (ER)**, I was the contact of TCS with 8 consulting companies.
3. **ER team leader**, I lead the the ER team (4 members including myself).
4. **Vice president**, I lead both the ER (3 members – TCS/Company contacts) & Events (3 members – Organizers of 2-4 on-campus consulting events per semester) teams.
5. **President**. During my mandate, I restructured the association structure and with the help of the executive team successfully proposed new services to students.

Volunteer Fire-Fighter ▀ [SDIS Chamberonne](#)

I am a volunteer fire-fighter for three communes in Vaud, CH.

PhD Student Representative ▀ [EPFL](#)

Acted as a connecting channel between the students of my doctoral program (EDEE) and my university's board of education. I raised any concern they used to have and mitigated conflicts.

Student Teaching Assistant ▀ [EPFL](#)

During my studies, for several courses, I was charged with helping students to solve exercises, understand the course material and, in some cases, correct their assignments.

Class delegate ▀ [EPFL](#)

For all my university years, I connected my classmates to professors and university administration. I raised any concern they had and mitigated conflicts when needed.

ECOSOC Chair ▀ [École Oasis Internationale](#)

During high-school, I co-organized our annual model united nations conference (OISMUN). I also chaired the ECOSOC committee consisting of ~30 delegates during the conference.

Extracurricular Certifications

IBM Data Science Professional Certificate ♦ [Coursera](#)

Online course covering the basics of Data Science & Machine learning. It introduces Python, SQL, data analytics and data visualization.

Leadership Essentials ♦ [IMD](#)

Personalized course showing essential competencies to become a better leader.

References Upon Request

Lausanne, CH
2018-Present

Lausanne, CH
2015-2017

Lausanne, CH
2011-2015

Cairo, EG
1996-2011

Lausanne, CH
2020-2020

Dättwil, CH
2017-2017
6 months

Lausanne, CH
2015-2015
2 months

Lausanne, CH
2018-2021

6 months
9 months

3 months
10 months

6 months

Lausanne, CH
2018-Present
Lausanne, CH
2018-2020

Lausanne, CH
2014-2017

Lausanne, CH
2012-2017

Cairo, EG
2010-2011

Online
2022-Present

Online
2020-2020